Passive Control of Shock Wave Turbulent Boundary Layer Interaction over a Perforated Wall

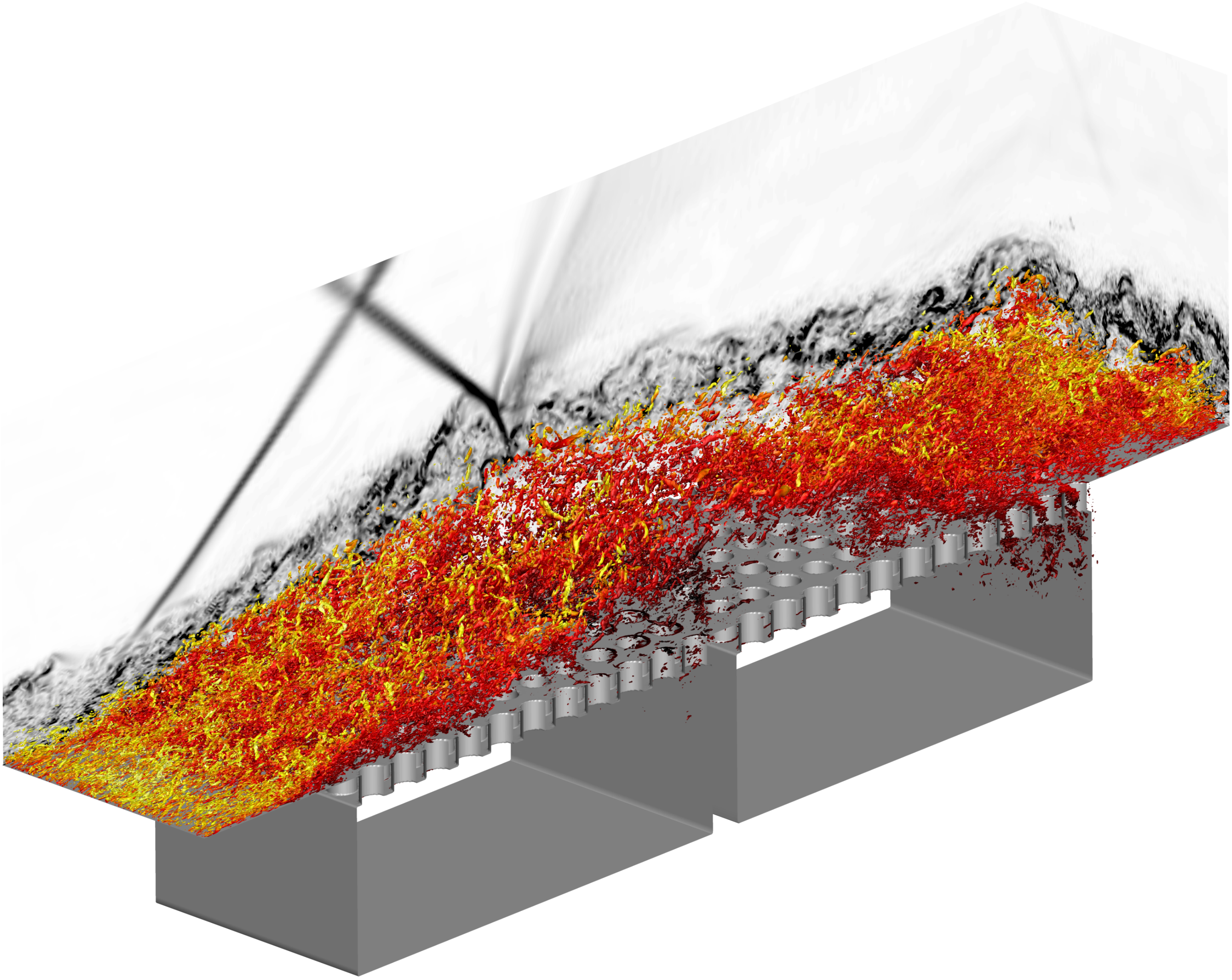

Francisco Dores

Passive Control of Shock Wave Turbulent Boundary Layer Interaction over a Perforated Wall

Master of Science Thesis

by

Francisco de Jesus Jorge Dores

to obtain the degree of Master of Science
at the Delft University of Technology
to be defended publicly on 18th December 2024

Student Number: 5852021
Supervisors: Prof. Stefan Hickel & Dr. Luis Laguarda

Preface

The moments of greatest learning often come unanticipated, arriving without warning to broaden the horizons of our being. When I embarked on this thesis, I expected to gain knowledge about high-speed compressible flows, STBLIs, and advanced post-processing techniques. Thanks to my supervisors, Prof. Stefan Hickel and Dr. Luis Laguarda, I have achieved this and much more. Their generosity in sharing their knowledge and experience in every interaction was invaluable.

What I did not anticipate was the deeper lessons I would learn about professionalism, openness to new ideas, positivity, and problem-solving efficiency, as exemplified by Prof. Stefan Hickel. At every challenge, he always came up with solutions and guided me toward success. His calm and considerate approach taught me the importance of patience and clarity in achieving goals. Equally transformative were the interactions I had with Dr. Luis Laguarda. His dedication, availability, and genuine commitment to others set a remarkable example for me. Time seemed to vanish during our discussions - ranging from technical to personal topics. He consistently inspired confidence and offered new perspectives that enriched my journey. His warmth and encouragement from the very beginning gave me the assurance that I was on the right path.

Most surprising of all, however, were the discoveries I made about myself. Over these ten months, I learned more about who I am and my place in the world than I could have imagined. At a pivotal moment, these revelations shook the core of my being, ultimately leaving me more confident and prepared to embrace future challenges, no matter where they might lead me.

I am deeply grateful to the colleagues and friends who shared this journey of effort and dedication with me. Their constant support made me feel at home even during the most challenging moments. A special thanks to Alex, Marco, João, and Edoardo, each of whom helped me grow as both a student and a person in unique ways.

Among all those who have supported me, my sister was one of the most important influences on this journey. Her unwavering belief in me, often stronger than my own, continuously encouraged me to rise above mediocrity and strive to be the best version of myself. Her example has always inspired me as she is the biggest reference in my life. Thank you for knowing me better than myself, for helping me see reality through the lens of my idealism, and for making me proud to call you my sister.

None of this would have been possible without the love and sacrifices of my parents, who are the true inspiration of my life. Words cannot capture my gratitude for their endless support, all the sacrifices, all the hours awaken, and each one of the shared uncertainties and achievements. Thank you for ensuring that the only limit to my dreams is my imagination. Thank you for all the hugs, the words, and the smiles, often from afar, but that still offered me the strength and the reassurance needed throughout this journey. Thank you for teaching me what life is truly about.

Finally, I thank God for being the guiding light of my life, for never letting me feel lonely, and for making everything happen in His perfect time. Science, after all, is but a path to understanding God, as Louis Pasteur once said: ”Science brings men nearer to God.”

Francisco Dores
Technical University of Delft, December 2024

Contents

List of Figures

List of Tables

Nomenclature

Symbols

Symbol	Definition	Unit
a	Speed of Sound	[m/s]
d	Diameter	[m]
f	Frequency	[Hz]
h	Height	[m/s]
k	Turbulent Kinetic Energy	[$\mathrm{m}^2/\mathrm{s}^2$]
l	Length	[m]
m	Mass	[kg]
n	Number of	[-]
p	Pressure	[$\mathrm{N/m}^2$]
q	Heat Flux	[$\mathrm{W/m}^2$]
r	Recovery Factor	[-]
t	Time	[s]
u	Streamwise Velocity	[m/s]
u_τ	Friction Velocity	[m/s]
v	Wall-Normal Velocity	[m/s]
w	Spanwise Velocity	[m/s]
x	Streamwise Coordinate	[m]
$\langle x \rangle$	Time- and span-wise average of x	
y	Wall-Normal Coordinate	[m]
z	Spanwise Coordinate	[m]
A	Area	[m^2]
C	Mixing Length Proportionality Constant	[-]
C_f	Skin-Friction Coefficient	[-]
E	Total Energy	[J]
$\mathcal{F}$	Flat Plate Configuration (Reference Case)	
$\mathcal{G}$	Correlation Function (Free-Interaction Theory)	
H	Shape Factor	[-]
K	Kurtosis	[-]
L	Length	[m]
M	Mach Number	[-]
M_c	Isentropic Convective Mach Number	[-]
N	Number of	[-]
$\mathcal{P}$	Perforated Wall Configuration (Study Case)	
Pr	Prandtl Number	[-]

R	Specific Gas Constant	[J/(kg $\cdot$ K)]
Re	Reynolds Number	[-]
Re_δ	Boundary Layer thickness-based Reynolds Number	[-]
Re_θ	Momentum thickness-based Reynolds Number	[-]
Re_τ	Friction Reynolds Number	[-]
S	Cross-sectional Area	[m^2]
St	Strouhal Number	[-]
$St_{L_{sep}}$	Separation length-based Strouhal Number	[-]
T	Temperature	[K]
U	Velocity Magnitude	[m/s]
V	Volume	[m^3]
α	Correction Coefficient (Helmholtz Resonator)	[-]
γ	Specific Heat Ratio	[-]
δ	Boundary Layer Thickness	[m]
δ_ν	Viscous Length Scale	[m]
δ^*	Boundary Layer Displacement Thickness	[m]
ϵ	Turbulent Dissipation Rate	[m^2/s^3]
ε	Plateau Pressure Ratio	[-]
θ	Boundary Layer Momentum Thickness	[m]
ϑ	Deflection Angle	[-]
λ	Wavelength	[m]
λ_{ci}	Swirling Strength Criterion	[1/s]
κ	Thermal Conductivity	[W/(m $\cdot$ K)]
μ	Dynamic Viscosity	[kg/m $\cdot$ s]
ν	Kinematic Viscosity	[m^2/s]
ξ	Pressure Gradient Parameter	[-]
ρ	Density	[kg/m^3]
σ	Standard Deviation	[-]
σ^2	Variance	[-]
τ	Shear Stress	[Pa]
ϕ	Shock Angle	[rad]
χ	Probability of Reverse Flow	[-]
Ω	von Karman Constant	[-]

Abbreviations

Abbreviation	Definition
ALDM	Adaptive Local Deconvolution Method
BFS	Backward-Facing Step
BL	Boundary Layer
CFD	Computational Fluid Dynamics
CFL	Courant-Friedrichs-Lewy
DMD	Dynamic Mode Decomposition
DNS	Direct Numerical Simulation

FTT	Flow-through Time
IQR	Interquartile Range
IR	Irregular Reflection
IS	Incident Shock
K-H	Kelvin-Helmholtz
LES	Large-Eddy Simulation
MR	Mach Reflection
MVG	Micro-vortex Generator
PD	Pressure-deflection
PIV	Particle Image Velocimetry
PM	Prandtl-Meyer
PSD	Power Spectral Density
RMS	Root-Mean-Square
RR	Regular Reflection
RS	Reflected Shock
RSWBLI	Regular Shock Wave Boundary Layer Interaction
SGS	Subgrid Scale
STBLI	Shock Turbulent Boundary Layer Interaction
SWBLI	Shock Wave Boundary Layer Interaction
SWTBLI	Shock Wave Turbulent Boundary Layer Interaction
TBL	Turbulent Boundary Layer
TKE	Turbulent Kinetic Energy
TV	Thick Vane

Subscripts

Subscript	Definition
0	Stagnation Conditions
∞	Freestream Conditions
χ	Probability of Reverse Flow-based
$\langle x \rangle_t$	Time average of x
bub	Bubble
ds	Dividing Streamline
e	Edge
i	Inflow
imp	Inviscid Impingement
int	Interaction
l	Laminar
m	Mean
min	Minimum
n	Normal
p	Plateau
rea	Reattachment
s	Sampling
sep	Separation

t	Turbulent
u	Upstream
ui	Upstream Influence
w	Wall
x	Streamwise
y	Wall-normal
z	Spanwise
VD	van-Driest

Superscripts

Superscript	Definition
$\overline{x}$	Mean of x (Reynolds Average)
$\tilde{x}$	Mean of x (Favre Average)
x'	Fluctuation part of x (Reynolds Average)
x''	Fluctuation part of x (Favre Average)
x^+	x represented in wall units
$x^{\mathcal{F}}$	Referring to the flat plate case
$x^{\mathcal{P}}$	Referring to the perforated wall case

Abstract

Wall-resolved large-eddy simulations are performed to study the interaction between a supersonic turbulent boundary layer and an impinging shock over a wall. The freestream conditions used were Mach 2 and a moderate friction Reynolds number of $Re_\tau = 950$. A passive control method was implemented using perforations in the interaction region of influence of the reference case (flat plate), with the addition of two separated cavities beneath the perforations. The cavities were designed to work as Helmholtz-like resonators at a separation length-based Strouhal number of $St_{L_{sep}} \approx 0.03$. For the reference case results consistent with the literature were obtained and a time analysis, based on the cross-correlations between dynamic properties allowed to suggest a sequence of events driving the unsteadiness of the interaction. The controlled case, resulted in a larger region of influence of the interaction, with the blowing-suction mechanism inside the cavities allowing a reduction of the separation length. Large oscillations were found close to the wall for thermodynamic properties, but also skin friction and wall-normal velocity. The topology of the recirculation bubble changed to become less symmetric resulting in a stronger reattachment compression fan. Regarding the unsteadiness of the controlled interaction, a tonal behaviour was found (at $St_{L_{sep}} \approx 0.3$) for the reflected shock motion associated with the resonant frequency found inside the cavities and also for the bubble volume variation. In general, the resonance within the cavities seemed to be able to affect the dynamics of the interaction, despite maintaining its global topology.

CHAPTER 1

Introduction

Every time an object flies faster than the speed of sound it is subjected to two phenomena that, as of today, cannot be avoided. These are (1) the development of a boundary layer, established due to the no-slip condition at the wall and (2) the generation of shocks waves, resulting from the coalescence of the acoustic waves that no longer can outrun the object speed. Having these two structures cohabiting the same domain around the object leads to what is known as shock wave boundary layer interactions (SWBLIs).

Shock wave boundary layer interactions can be found in numerous locations on an aircraft: from its nose, to the wings, control surfaces and most critically, on its engines, particularly on the inlets. When a shock impinges on a boundary layer (see Figure 1.1), it introduces a strong adverse pressure gradient that, if strong enough, leads to flow separation. A separation shock is produced due to the flow curvature around the reverse-flow region. The shear layer that detached after the separation shock interacts with the impinging shock close to the bubble apex, which triggers its reattachment and the formation of a compression fan. If the streamlines curvature around the recirculation bubble is accentuated enough, the compression fan may coalesce into a shock.

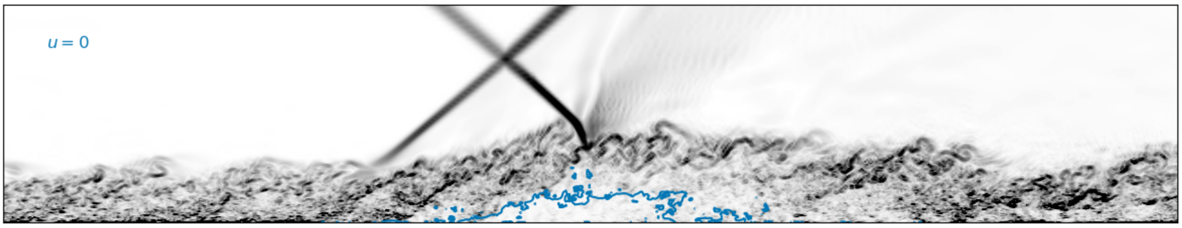

Figure 1.1: Schlieren visualisation of shock wave boundary layer interaction.

The detrimental aspects associated with SWBLIs are largely related to two main occurrences: the separation of the boundary layer from the wall, resulting in a reverse-flow region, and the low-frequency unsteadiness, associated with the large-scale motion of the reflected shock and the breathing motion of the separation bubble.

Because of the previously mentioned phenomena, SWTBLIs can have detrimental effects on the performance of the aircraft. On the one hand, the exterior interactions can lead to a decrease in lift, increased drag, and possibly loss of control effectiveness. Furthermore, unsteady phenomena such as buffet is also associated with these interactions (D'Aguanno, 2023). On the other hand, the interior interactions, such as those happening inside the engines can induce total pressure losses while diminishing the homogeneity of the flow entering the combustion chamber and changing the turbulence content of the flow. Instabilities can also occur due to the displacement of the reflected shock within the interaction region inside the inlet (buzz condition) (Sepahi-Younsi & Esmaeili, 2023).

At Delft University of Technology (TUDelft) SWTBLIs have been studied for the past few years (Pasquariello et al., 2017; Hu et al., 2021; Laguarda et al., 2022, 2024b). These studies have focused on understanding the fundamentals of the interactions as well as their dependence on flow properties, such as Reynolds number and Mach number. Some research has also focused on the control of the SWTBLIs by using steps or channels (Pasquariello et al., 2017; Laguarda and Hickel, 2024). However, no satisfactory mechanism has been found that can successfully avoid flow separation while mitigating the low-frequency unsteadiness. Mitigating these two phenomena is important to reduce mechanical and thermal loads on structures, that may ultimately result in structural failure (Gaitonde, 2015). Likewise, with the higher demand for sustainable solutions and the prospective return of civil supersonic aviation, it is pivotal to address any detrimental aspects that are still preventing a faster concretization of these global goals.

This thesis studies the impact of having a supersonic SWTBLI at $M = 2$ over a perforated wall with Helmholtz-like resonator cavities beneath it. The goal of this passive control method is to reduce the separation region and mitigate the low-frequency unsteadiness by dissipating the energy associated with these frequencies through resonation. To carry out this study, wall-resolved large-eddy simulations (LES) were performed at a moderate friction Reynolds number ($Re_\tau = 950$) for which other experimental and numerical results are available for comparison. The results for the perforated wall case were compared against a reference case, consisting of an SWTBLI over a flat plate. The thesis aims to answer the following research question:

Can a passive control method consisting of a perforated wall with resonant cavities beneath it mitigate the detrimental effects of a shock wave turbulent boundary layer interaction?

- In terms of flow separation?
- In terms of low-frequency unsteadiness?

Extensive review of the literature on SWBLIs can be found in Chapter 2 as well as the theory behind these interactions. A section on the boundary layer is also included. A combination of some of the already well-established 'theoretical' knowledge on SWTBLIs with the most relevant results from the literature in characterising these interactions is presented, in terms of wall properties, turbulence content and unsteadiness, the most likely mechanisms for causing the unsteadiness and some of the most common control methods that have been implemented in the past.

Chapter 3 describes the methodology followed. The equations used for modelling the flow are presented first, followed by the computational domain chosen, the boundary conditions imposed and the grid used. The numerical method is described and the rationale for the selected dimensions of the geometry is provided.

The results obtained are discussed in Chapter 4 starting with a validation of the method applied by examining the behaviour of the undisturbed turbulent boundary layer. Next, the different aspects concerning the SWTBLI are considered and compared across the two proposed configurations: from instantaneous to mean flow configurations, wall properties, reverse flow characterisation and unsteadiness mechanisms. The effect of adding perforations to the wall and cavities beneath it is studied. Lastly, the main conclusions of the work and recommendations for future studies are presented in Chapter 5.

CHAPTER 2

Theoretical Background

In this chapter the theoretical background necessary to understand the discussion of the results is introduced. Section 2.1 focus on turbulent boundary layers (TBLs), their structure, the main parameters governing them, how they depend on the Reynolds number and the scalings used to compare incompressible and compressible boundary layers. Section 2.2 explores the shock wave turbulent boundary layer interactions (SWTBLIs) from a steady perspective and discusses how the main flow parameters evolve throughout the interaction. Lastly, Section 2.3 focuses on the SWTBLI unsteadiness and its control, presenting a literature review on the phenomenon itself and the main control techniques implemented so far.

2.1 Turbulent Boundary Layer

When a flow is convected along a no-slip surface a boundary layer (BL) is formed (represented in Figure 2.1), which is a region of the flow where the velocity transitions from the external outer value ($u = u_e$) to stagnation at the wall (no-slip condition, $u = 0\,\mathrm{m/s}$). The boundary layer thickness, δ, is defined as the wall-normal position where the streamwise velocity reaches 99% of the external outer velocity ($u = 0.99u_e$).

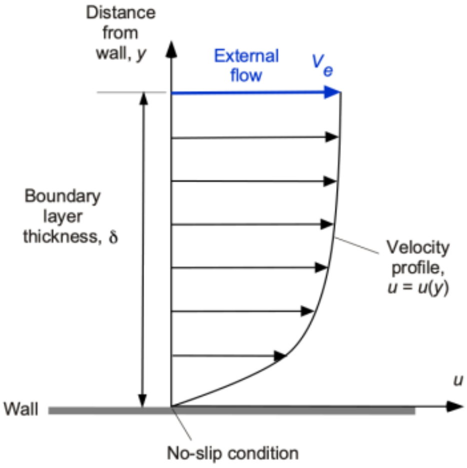

Figure 2.1: The concept of a boundary layer as it forms adjacent to a solid surface or "wall," where the flow velocity increases smoothly and asymptotically with distance away from the wall. (Leishman, 2022)

Depending on the flow history as well as on the flow conditions the boundary layer can be either laminar or turbulent. In this section, an emphasis will be put on turbulent boundary layers given the scope of this study.

Turbulent boundary layers and turbulent flow in general are characterised by the presence of fluctuations in the flow properties, usually related to vortices and eddies that are generated and that enhance mixing between the different layers of the flow (as represented in Figure 2.2).

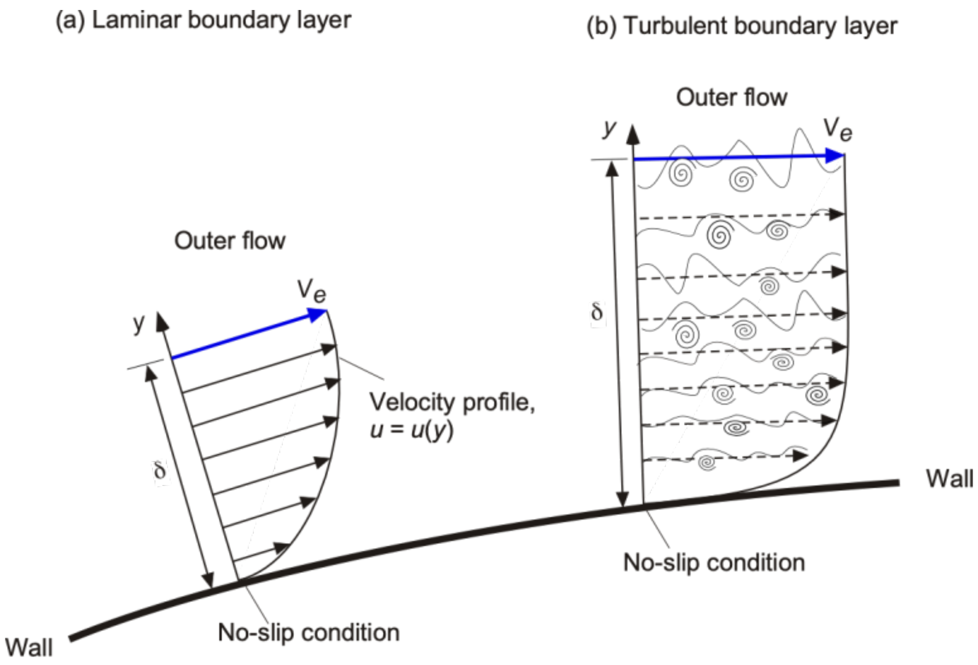

Figure 2.2: Fundamental differences in the characteristics between a laminar boundary layer and a turbulent boundary layer. (Leishman, 2022)

As a result of the mixing of the flow turbulent boundary layers are usually thicker and fuller. These properties are related to the integral parameters presented in Subsection 2.1.2 and have a big impact on how the boundary layer and consequently the flow in general reacts to different disturbances, namely shock wave boundary layer interactions (SWBLIs).

2.1.1 Structure (Law of the Wall)

The characterisation of a boundary layer is commonly done through its velocity profile. The velocity profile can be defined as varying only with the wall-normal coordinate in the form $u = u(y)$. When compared to its laminar counterpart, the velocity profile of a turbulent boundary layer is fuller, meaning that it has a steeper velocity gradient at the wall $\left(\frac{\partial u}{\partial y}\Big|_l < \frac{\partial u}{\partial y}\Big|_t \right)$ and that it can withstand stronger adverse pressure gradients, since the flow near the wall transports more momentum, brought from the outer flow through the mixing mechanism. This steeper gradient also means a higher wall shear stress (Equation 2.1) and skin friction coefficient (Equation 2.2) assuming a constant dynamic viscosity, μ:

$$\tau_w = \mu_w \left. \frac{\partial u}{\partial y} \right|_w , \tag{2.1}$$

$$C_f = \frac{\tau_w}{\frac{1}{2}\rho_\infty u_\infty^2} . \tag{2.2}$$

A graphical representation of the different shear stresses is shown in Figure 2.3.

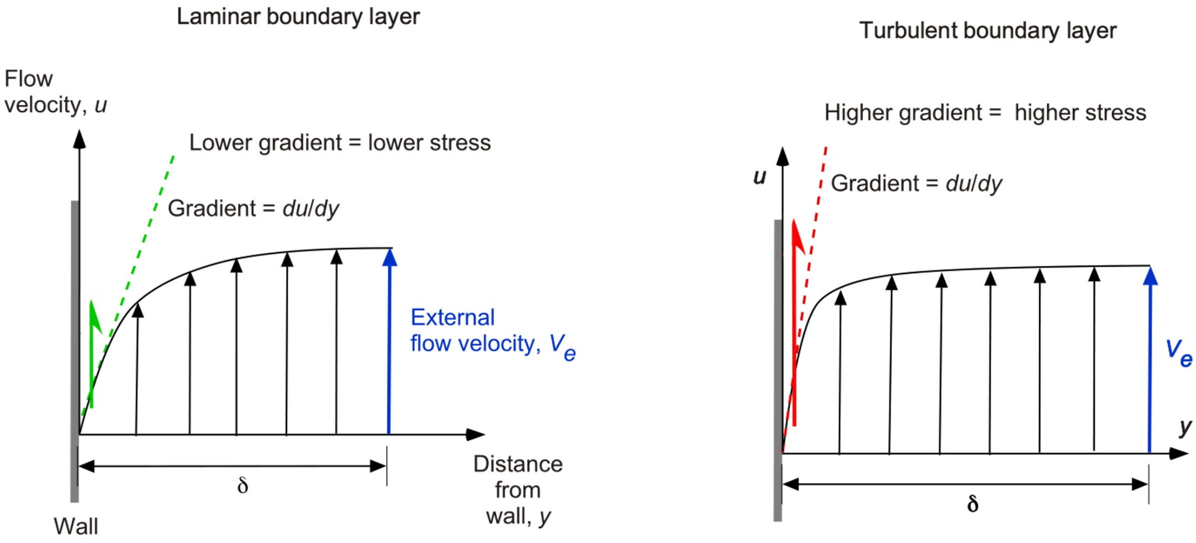

Figure 2.3: The shear stress on a surface produced by a flowing laminar boundary layer is much lower than that produced by a turbulent boundary layer. (Leishman, 2022)

The velocity profile can be divided into 3 different regions: the inner, the overlap and the outer layers. Each of these regions can be scaled based on different quantities. Closer to the wall the friction velocity (Equation 2.3) and viscous length scale (Equation 2.4) are used for the non-dimensionalisation. These quantities can be computed as

$$u_\tau = \sqrt{\frac{\tau_w}{\rho_w}}, \tag{2.3}$$

$$\delta_\nu = \nu\sqrt{\frac{\rho_w}{\tau_w}} = \frac{\nu}{u_\tau}, \tag{2.4}$$

where ν is the kinematic viscosity.

Based on either of the quantities defined above one can also define the viscous Reynolds number as:

$$Re_\tau = \frac{u_\tau \delta}{\nu} = \frac{\delta}{\delta_\nu}. \tag{2.5}$$

Inner Layer

The inner layer can be subdivided into the viscous sub-layer, the buffer layer and the overlap layer. As indicated by its name it depends on the 'inner' conditions at the wall. Using dimensional analysis one can argue that the mean velocity depends on the shear stress at the wall, the density, the dynamic viscosity and the wall-normal coordinate: $\bar{u} = f(\tau_w, \rho, \mu, y)$.

Based on the definition of the friction velocity (Equation 2.3) and using the Buckingham π theorem, one finds that

$$\frac{\overline{u}}{u_\tau} = f\left(\frac{y u_\tau}{\nu}\right). \tag{2.6}$$

Introducing the *wall units* defined as:

$$\begin{aligned} u^+ &= \frac{\overline{u}}{u_\tau}, \\ y^+ &= \frac{y u_\tau}{\nu} = \frac{y}{\delta_\nu}, \end{aligned} \tag{2.7}$$

the overall result is that for the inner layer the condition $u^+ = f(y^+)$ holds. This condition given in wall units is also known as the *Law of the Wall*.

Outer Layer

Opposing to the inner layer, the outer layer is not directly affected by the wall conditions, but by the freestream conditions instead. Following the same reasoning as before a dimensional analysis can be carried out. The only difference is that in this case also the pressure gradient is considered as one of the parameters affecting the flow velocity: $u_e - \overline{u} = g(\tau_w, \rho, \mu, y, \frac{dp_e}{dx})$.

The result of the analysis gives rise to the *Defect Law*:

$$\frac{u_e - \overline{u}}{u_\tau} = g\left(\frac{y}{\delta}, \xi\right), \tag{2.8}$$

where $\xi = \frac{\delta}{\tau_w}\frac{dp_e}{dx}$ is the pressure gradient parameter.

Logarithmic (Overlap) Layer

The region in between the inner and the outer layers is called the overlap layer. In this region both the viscous and the freestream conditions are important.

As may be expected both the law of the wall and the defect law must agree in this region. Hence, by equaling Equation 2.6 and Equation 2.8 one arrives to the conclusion that both functions f and g must be logarithmic functions, which gives the name to this layer also known as *Logarithmic Layer*. Expressed in inner variables (or wall units), the general relation found for the logarithmic layer is:

$$u^+ = \frac{1}{\Omega} \ln y^+ + B, \tag{2.9}$$

with $\Omega \approx 0.41$ being known as the von Karman constant and $B \approx 5.0$ a fitting constant.

Overview

Having defined the different regions and its 'laws' one can further develop the velocity characterisation based on the contributions of both the molecular and turbulent viscosity (based on the Reynolds stresses $\overline{u'v'}$) for the total shear stress as a function of the distance to the wall. As plotted in Figure 2.4, near the wall (inner layer) the molecular or viscous shear stress is more important, given the fact that close to the wall velocity fluctuations tend to zero (and therefore, the Reynolds stresses are negligible). As one moves away from the wall (overlap layer), velocity fluctuations become more important and the turbulent viscosity becomes predominant for the total shear stress. In the buffer layer both contributions are important.

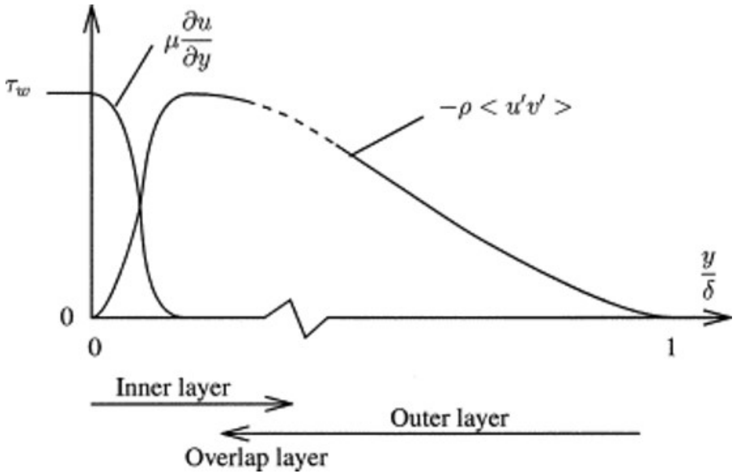

Figure 2.4: Shear stresses in a flat plate turbulent boundary layer. The boundary layer has a two-layer structure. The inner layer thickness is exaggerated in this figure. The inner layer and the outer layer overlap to give a logarithmic velocity law. (Cousteix, 2003)

Given this evolution of the character of the shear stress, the law of the wall is then adapted to each of the sub-layers within the inner layer depending on shear stress considerations and its dominant components, resulting in:

- **Viscous sub-layer** $y^+ \leq 5 : u^+ = y^+$
- **Buffer layer** $5 \leq y^+ \leq 30$
- **Logarithmic (overlap) layer** $y^+ \geq 30 : u^+ = \frac{1}{\Omega} \ln y^+ + B$

If represented in a semi-logarithmic plot the turbulent velocity profile has the form shown in Figure 2.5, where the above relations are plotted in dashed lines.

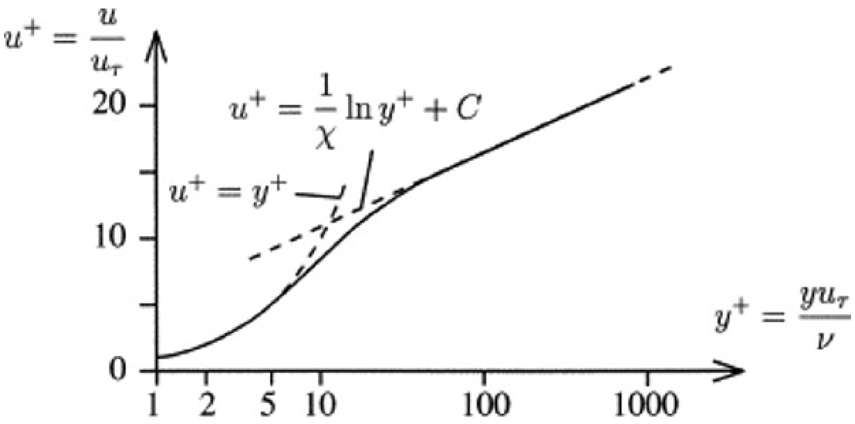

Figure 2.5: Law of the wall in semi-logarithmic coordinates. (Cousteix, 2003).

The buffer layer has no expression attached to it. Nonetheless, there are a number of analytical expressions that represent the entire velocity profile, being one of the most common the one from Spalding (1961):

$$y^+ = u^+ + e^{-\Omega B} \left(e^{\Omega u^+} - 1 - \Omega u^+ - \frac{(\Omega u^+)^2}{2!} - \frac{(\Omega u^+)^3}{3!} \right). \tag{2.10}$$

Figure 2.6 shows how this expression fits into experimentally measured velocity profiles on pipe flows. The agreement is very good except in the wake region where a divergence is noticed.

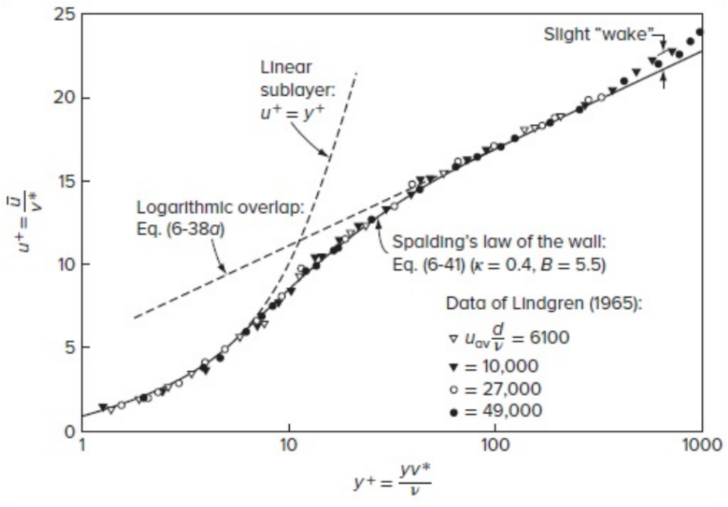

Figure 2.6: Comparison of Spalding's inner law expression with the pipe-flow data of Lindgren (1965). (White & Majdalani, 2021)

Despite its convenience, Spalding's relation is not commonly used in practical applications, with the comparisons being made directly between the velocity profiles of interest and the relations for the viscous sub-layer and the log-layer.

2.1.2 Integral Parameters

Based on the boundary layer velocity and density one can define two important integral parameters: the displacement and the momentum thickness.

The displacement thickness (Equation 2.11) is the distance from the wall that a full constant velocity profile must be displaced by to have the same mass flow deficit as the real boundary layer profile (as shown in Figure 2.7) and, for compressible flows is given by

$$\delta^* = \int_0^\delta \left(1 - \frac{\rho u}{\rho_e u_e}\right) dy. \tag{2.11}$$

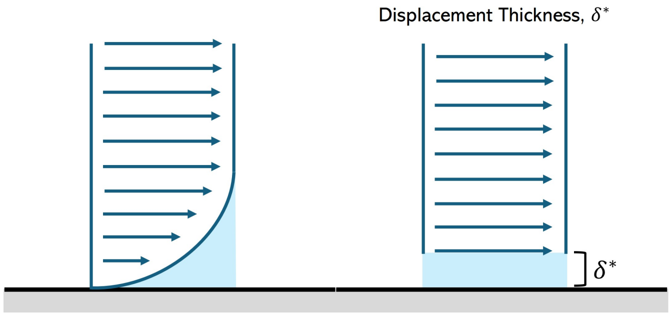

Figure 2.7: Displacement thickness representation.

The momentum thickness (Equation 2.11) is the distance from the wall that a full constant velocity profile must be displaced by to have the same momentum deficit as the real boundary layer profile (as shown in Figure 2.7) and, for compressible flows is given by

$$\theta = \int_0^\delta \frac{\rho u}{\rho_e u_e}\left(1 - \frac{u}{u_e}\right) dy. \tag{2.12}$$

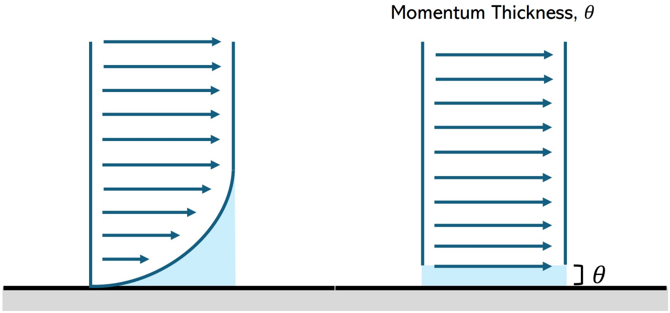

Figure 2.8: Momentum thickness representation.

Using both the previously defined integral parameters one can define a third parameter, the shape factor H, which is commonly used to have an idea of the nature of the flow, whether it is laminar ($H \approx 2.6$), turbulent ($H \approx 1.3$), transitional or close to separation. It is given by the ratio between the displacement and the momentum thicknesses, as expressed in Equation 2.13,

$$H = \frac{\delta^*}{\theta}. \tag{2.13}$$

2.1.3 Turbulence Content & Reynolds Number Effects

Regarding their turbulence content, turbulent boundary layers are very complex. Just like any other turbulent flow, they are highly three-dimensional, characterized by a general anisotropy, and despite their chaotic appearance, coherent structures can be found.

In this section results from Laguarda et al. (2024a) will be used to illustrate the most important features of this kind of flow and its dependency on the Reynolds number. Laguarda et al. (2024a) have performed this study using wall-resolved LES for a $M = 2$ flow, which is the same Mach number targeted in this thesis.

The first and second-order velocity statistics are shown in Figure 2.9. As discussed in Subsection 2.1.1 the mean velocity of TBLs follows the law of the wall with a near-wall viscous sub-layer and a logarithmic region clearly visible, particularly for the higher Reynolds number cases. For the smallest value of Re_τ presented the log-layer is almost nonexistent (meaning, it is not fully established). The higher Re_τ the bigger the extension of the log-layer before the wake region. This observation is also related to the overall size of the BL which, for the same freestream conditions and fluid properties, is bigger for higher Re_τ.

In terms of the Reynolds stress components, the intensity of the fluctuations increases with the Reynolds number. Apart from this trend, it is always verified that the fluctuations with the highest intensity are the streamwise fluctuations, followed by the spanwise and finally the wall-normal fluctuations. The cross fluctuations (streamwise - wall-normal) are the only negative ones. Note that all of them start at zero near the wall, due to the physical restriction imposed by the surface and tend to zero outside the boundary layer, where freestream flow (approximately turbulence-free) is present.

Two important behaviours were identified by Laguarda et al. (2024a) for increasing Reynolds numbers: as Re_τ increases a plateau for the shear stresses starts establishing and the wall-normal component of the velocity variance peak moves closer to the boundary layer edge.

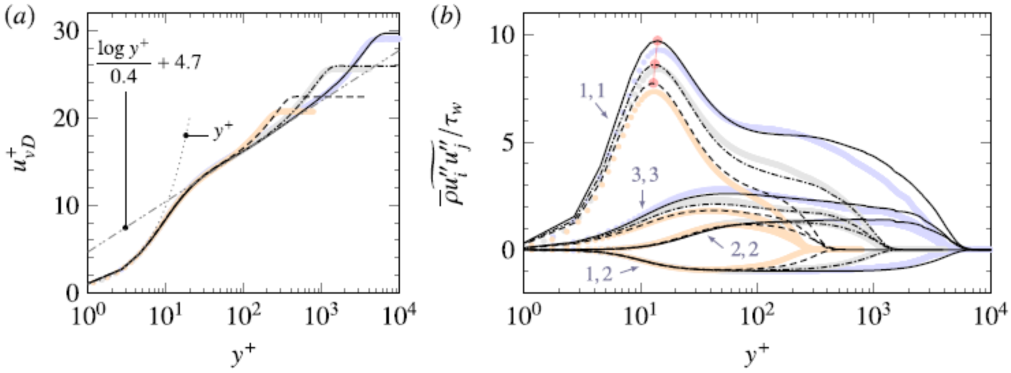

Figure 2.9: First and second-order velocity statistics: $(a) - (b)$ van Driest transformed mean velocity and density-scaled Reynolds stresses over the inner-scaled wall-distance y^+. For reference, DNS data of Pirozzoli and Bernardini (2011, 2013) at Mach 2.0 and $Re_\tau \approx [250, 1100, 4000]$ is respectively indicated in panel (b) with orange, gray and blue markings. The indices i, j for the Reynolds stresses are indicated in panel (b), as well as the peak value of the streamwise stress represented by the red circles. (Laguarda et al., 2024a)

Another important feature of turbulent flows and TBLs in particular are their turbulent structures and correspondent characteristic lengths. As demonstrated by Laguarda et al. (2024a) and shown in Figure 2.10 the bigger the Reynolds number, the smaller the scales near the wall. These near-wall structures are influenced by the outer-layer structures which become larger with increasing Re_τ (see the discussion in Laguarda et al. (2024a) on the spanwise spectra of the spanwise velocities correlation functions). The coupling between inner and outer fluctuations can be clearly seen in Figure 2.10 $(e)-(f)$ where regions of dark and light colour coincide between the two wall-normal stations. Moreover, also thermodynamic properties and the wall-pressure in specific present higher intensity fluctuations for higher Re_τ. Note, however, that the mean pressure is approximately constant throughout the BL.

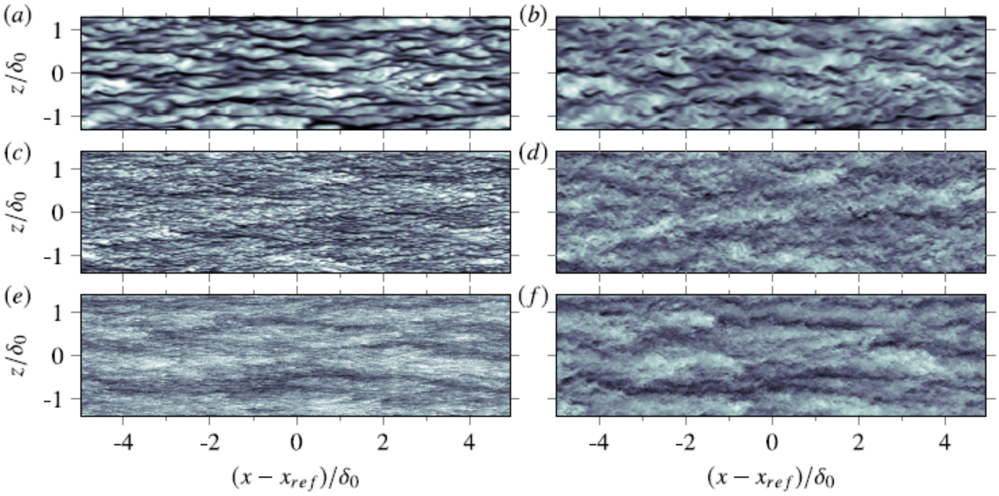

Figure 2.10: Instantaneous streamwise velocity field at $y^+ \approx 15$ (left panels) and $y/\delta_0 \approx 0.1$ (right panels): $(a) - (b)$ Re_τ : $242 - 402$; $(c) - (d)$ Re_τ : $949 - 1338$; $(e) - (f)$ Re_τ : $3897 - 5554$. Contour levels from $u'/u_\infty = -0.25$ (dark shade) to $u'/u_\infty = 0.25$ (light shade).(Laguarda et al., 2024a)

Furthermore, as observed by Laguarda et al. (2024b) for increasing Reynolds number, the separation between inner and outer structures becomes more evident (note their similar size for the low-Reynolds number case in Figure 2.10 and how they are different for higher Re_τ). Likewise, the structures present in both cases differ. At low Re_τ hairpin vortices are easily identified, but they are not visible for higher Reynolds numbers (Laguarda et al., 2024a). In general, there is a decrease in space and time scales of near-wall turbulence with increasing Reynolds number. Also, for higher Re, the agreement of the spanwise spectra at $y \approx 0.1\delta$ becomes more evident (Laguarda et al., 2024b).

2.1.4 Morkovin's Hypothesis / Scaling

When analysing boundary layers one wants to be able to compare them regardless of their Mach number. However, for moderate Mach numbers compressibility starts having an effect and density variations within the boundary layer must be taken into account to obtain an accurate comparison.

In 1962 Morkovin suggested that "the essential dynamics of [supersonic boundary layer flows]... will follow the incompressible pattern" (Smits & Dussauge, 2006). This similarity is also known as *Morkovin's Hypothesis*.

Based on this idea, Morkovin assumed that the time scales for the mean and fluctuating fields are of the same order (meaning $t_t \approx \mathcal{O}(t_m)$). The turbulent time scale is defined based on the turbulent kinetic energy and the turbulent dissipation rate as $t_t \approx k/\epsilon$. Furthermore, it is assumed to be a function of several parameters, namely, mean time scale (t_m), Reynolds (Re) and Mach (M) numbers, distance to the wall (y) and characteristic length scale (L), among others:

$$t_t = g(t_m, Re, M, y, L, ...). \tag{2.14}$$

Using Morkovin's hypothesis one can conclude that $g \approx \mathcal{O}(1)$. Further analysing the mechanisms of turbulence amplification and assuming constant shear stress as well as equal production and dissipation of turbulence one can find a scaling for the compressible Reynolds stress components defined as:

$$\overline{u'v'}^{+} = \frac{1}{u_\tau^2}\frac{\bar{\rho}}{\rho_w}\overline{u'v'}, \tag{2.15}$$

where the symbol $^+$ represents the scaled quantity in wall units. For more details on the derivation refer to Smits and Dussauge (2006). The Morkovin hypothesis infers that the turbulence characteristics are essentially not affected by the fluctuations of the thermodynamic properties, while the mean properties are responsible for the divergence between the compressible and incompressible states.

2.1.5 Similarity Transformations for Compressible Flows

For small Mach numbers, the law of the wall allows scaling all incompressible boundary layers into one single profile (DiGregorio et al., 2019). However, it is known that for $M \gtrsim 0.3$ compressibility starts being relevant in the development of flows and in particular, boundary layers. Hence, if one wants to compare boundary layers at different Mach numbers one has to correct (transform) the velocity profiles to account for the compressibility effects. Considering Morkovin's insight on the similarity between patterns for both compressible and incompressible flows this should be possible.

van Driest Transformation

In 1951, van Driest (van Driest, 1951) developed a way of relating density to velocity in compressible flows that would become one of the most successful velocity transformations.

He did it by anticipating Morkovin's insight in accounting for variable density in his near wall-mixing theory and using Prandtl's assumption that $\tau \approx \tau_t$ (White & Majdalani, 2021) while neglecting the sublayer:

$$\tau \approx \tau_t \overline{\rho} l^2 \left(\frac{\mathrm{d}\overline{u}}{\mathrm{d}y}\right)^2, \quad l \approx Cy, \tag{2.16}$$

where C is the proportionality constant in the mixing length (l) formula. Furthermore, an ideal gas with unit Prandtl number ($Pr = 1$) was also assumed. Using Crocco-Busemann approximation van Driest (1951) found:

$$u_{VD}^+ = \frac{u_e}{u_\tau A}\left\{\sin^{-1}\left(\frac{2A^2\left(\overline{u}/u_e\right) - B}{\sqrt{B^2 + 4A^2}}\right) + \sin^{-1}\left(\frac{B}{\sqrt{B^2 + 4A^2}}\right)\right\}, \tag{2.17}$$

where

$$A = \left(\frac{\gamma - 1}{2} M_e^2 \frac{T_e}{T_w}\right)^{1/2}, \quad B = \frac{1 + \frac{\gamma-1}{2} M_e^2 r}{T_w/T_e} - 1,$$

which is the equivalent of modifying the velocity by the square root of the integrated density ratio (White & Majdalani, 2021):

$$u_{VD}^+ = \int_0^{\overline{u}} \left(\frac{\overline{\rho}}{\rho_w}\right)^{1/2} d\overline{u}. \tag{2.18}$$

As would be noticed years later by DiGregorio et al. (2019) the van Driest transformation success in collapsing the velocity profiles for high Mach numbers is confined to adiabatic wall conditions cases. Moreover, the fact that van Driest scales $\overline{u}$ and the wall-normal coordinate separately, results in a disagreement between the true velocity gradients and the scaled gradients ($\frac{\mathrm{d}u_{VD}^+}{\mathrm{d}y^+}$). Given the preponderance of these gradients for the shear stress and skin friction estimations, it is expected that a bad scaling results in poor predictions for these quantities. In their paper DiGregorio et al. (2019) focus on a new transformation proposed by Trettel and Larsson (2016) known as the *Trettel-Larson Transformation*. Trettel and Larsson (2016) compared their scaling with the van Driest transformation for both supersonic channel flows and boundary layer DNS and experiments with heat transfer. Trettel transformation performs particularly better than van Driest's in the prediction of the viscous sub-layer slope. For channel flow the overlap with DNS and experimental results was also very good, with some mismatch verified for the boundary layer cases in the log-layer.

DiGregorio et al. (2019) concluded that the Trettel transformation was superior in comparison to the van Driest transformation, particularly in the viscous sublayer and the buffer region and in the prediction of gradients. They concluded that this improvement was independent of the heat transfer status at the wall (adiabatic or isothermal). More recently, Laguarda et al. (2024a) concluded in their study on supersonic boundary layers that this transformation led to increased scatter, in comparison with DNS data, in both the buffer layer and the quasi-logarithmic layers. This effect has been reported before by other authors (Griffin et al., 2021; J. Huang et al., 2022; Cogo et al., 2022) being related to the mean shear over-prediction in the logarithmic layer, due to the assumption of constant viscous stress in the entire boundary layer (Griffin et al., 2021). Given the disagreement in performance for both transformations considered, the van-Driest transformation will be used, following the most common practice in the literature.

2.2 Shock Wave Turbulent Boundary Layer Interaction

Many are the applications where one can find interactions between shocks and boundary layers. In both external and internal aerodynamics, shock waves are generated every time a flow moves faster than the speed of sound. At the same time, a boundary layer is always present around any geometry subject to the incoming flow. Hence, these interactions can be observed very often in high-speed flows. SWTBLIs have been studied for a long time in their most canonical forms: incident shocks on flat plates and compression corners. They are usually studied separately. Threadgill and Bruce (2016) studied both canonical configurations in the same wind-tunnel facility for the same flow conditions.

Despite their importance, only more recently focus has been given to the research in this field with the development of supersonic and hypersonic engines and aircraft. Hence, being able to fully understand and control this phenomenon is imperative for the next big developments in the aerospace industry.

From a macro perspective it is possible to separate these interactions into two types: weak and strong interactions. The main difference between the two is that strong interactions are capable of inducing flow separation near the impingement location.

2.2.1 Weak Interactions

In weak interactions, the shock is not strong enough to induce separation. In this case the incident shock penetrates the boundary layer at a given angle. As it goes deeper it starts bending, due to the velocity gradient characteristic of boundary layer flow, until it vanishes at the BL's sonic line ($M = 1$ line).

The impinging shock introduces a pressure gradient on the BL that is felt upstream of the shock impingement location. This is because the gradient is transmitted through the subsonic part of the BL. This gradient leads to a dilatation of the subsonic part of the BL. In turn, this dilatation will be felt by the supersonic part, which is forced to curve around it. This will result in compression waves (necessary to curve the flow) that depending on the strength of the shock may coalesce into a reflected shock (Babinsky & Harvey, 2011).

This phenomenon is very similar in both the flat plate (Figure 2.11a) and the compression ramp (Figure 2.11b) cases as can be seen in the representations shown below. The main difference is that in the compression ramp, the pressure gradient is imposed by the wall deflection, which also forces the flow to change direction, originating the shock.

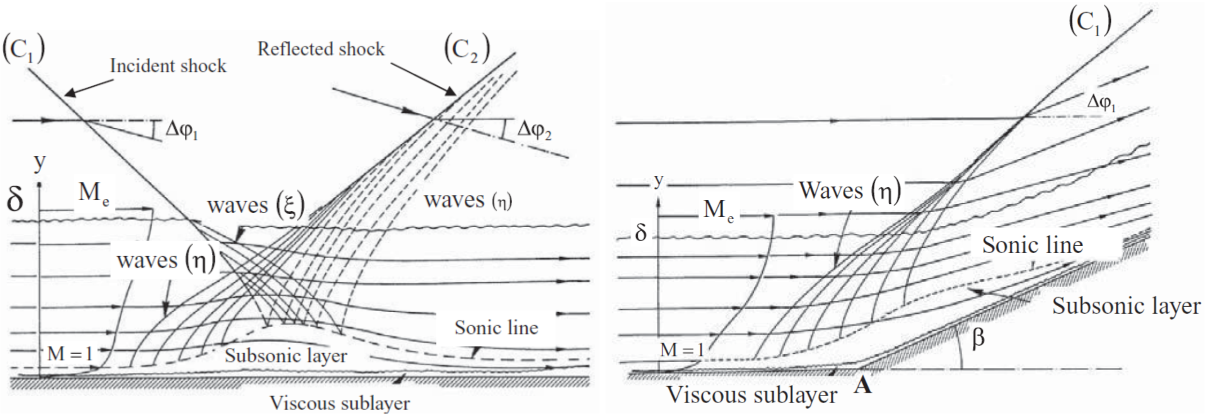

(a) Flat plate

(b) Compression ramp

Figure 2.11: Representation of weak STBLI's. (Babinsky & Harvey, 2011)

2.2.2 Strong Interactions

These kinds of interactions are characterised by strong enough shocks that cause the separation of the boundary layer. To understand them, the starting point is a shock impinging on the wall (for the flat plate case). For the compression ramp, the shock is generated by the necessity to deflect the flow near the wall. The generated shock due to flow turning then causes separation followed by a similar interaction as observed for the flat plate case. The same is true for other canonical SWTBLIs configurations. Comprehensive reviews can be found on the dynamics of SWTBLIs (Gaitonde & Adler, 2023). Focus will be given to the impinging shock configuration in the following sections.

When a shock - incident shock (IS) - impinges on the flat plate it will impose a pressure gradient sufficiently strong to cause separation. This separation is identified by the appearance of a recirculation bubble in which the flow direction is reversed. As reported by Laguarda et al. (2024b), the higher the Reynolds number, the more the bubble resembles a triangle, which justifies the approximation made in Figure 2.13. Given a certain mean bubble, one can also define the mean separation, S and the mean reattachment, R points (see Figure 2.12). The bubble itself, through streamline curvature, is responsible for the generation of the reflected shock (RS) C_2. At separation, a shear layer is formed and spanwise-oriented vortices originate through a mechanism similar to Kelvin-Helmhotz type of instability with scale of order $0.2\delta_\infty$ (Priebe & Martín, 2012). The separation bubble is separated from the remaining flow by the detached turbulent shear layer, formed near separation (Pasquariello et al., 2017).

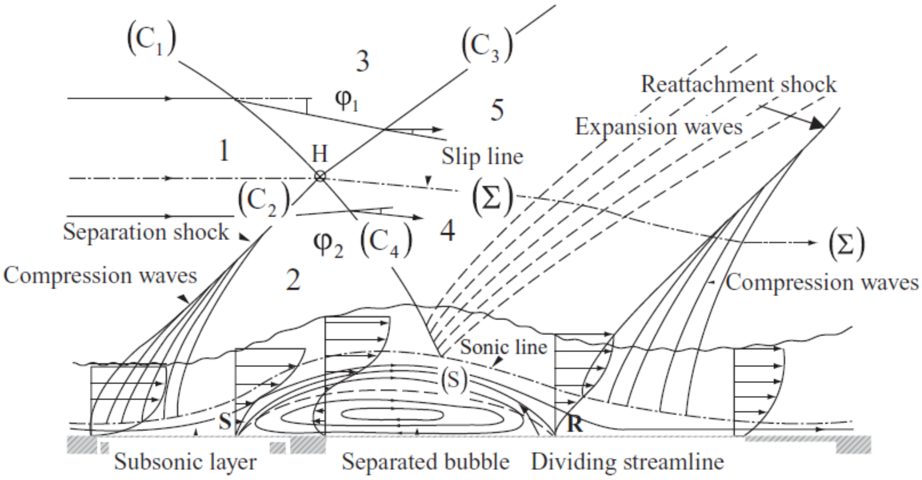

Figure 2.12: Impinging shock configuration. (Babinsky & Harvey, 2011)

The transmitted shock, C_4 is reflected as expansion waves. This will cause the shear layer to bend towards the wall promoting reattachment of the flow. At the same time, the bending of the flow is accompanied by a series of compression waves that may coalesce into a reattachment shock (Babinsky and Harvey, 2011; Pasquariello et al., 2017). Meanwhile, throughout the interaction, the boundary layer thickness increases significantly (Dupont et al., 2006). In their study, Pasquariello et al. (2017) found a maximum of about $3\delta_\infty$ for the boundary layer height close to the bubble apex.

For low Reynolds numbers the RS does not penetrate as deeply into the boundary layer (Pasquariello et al., 2017; Laguarda et al., 2024b). This is directly linked to the properties of the sonic curve, from which compression waves emanate and is Reynolds number dependent (D. S. Dolling and Murphy, 1983; Babinsky and Harvey, 2011; Laguarda et al., 2024b). Furthermore, the increased viscous effects associated with low Reynolds numbers contribute to a broader range of frequencies and attenuated shock intermittency due to the diffusion of the shock foot into a compression fan (Ringuette et al., 2009). In Laguarda et al. (2024b) the intersection between shock C_1 and C_2 was found to occur at approximately $2.5\delta_{imp}$, independently of the Reynolds number and the inviscid ”virtual” impingement point was located at approximately $1\delta_{imp}$ upstream of the reattachment point.

Dupont et al. (2006) suggested a linear relation between the interaction length L_{int} (defined as the distance between the RS mean position and the virtual IS impingement location) and shock intensity $\Delta p/2\tau_w$ (defined as the normalized pressure jump, where τ_w is the wall shear stress upstream of the interaction - strong shock $\Rightarrow \Delta p/2\tau_w > 40$, Dupont et al. (2006)). More recently, Helm and Martín (2021) suggested a different relation for the two quantities previously mentioned, based on a modification of the scaling method proposed by Souverein et al. (2013). The relation by Helm and Martín (2021) takes into account heat transfer. They concluded that for incipient separation a linear relation is indeed observed. For fully separated SWTBLIs, however, no collapse is found in the data. They suggested that the physical mechanisms governing incipient and fully separated SWTBLIs are different, which also requires different scalings.

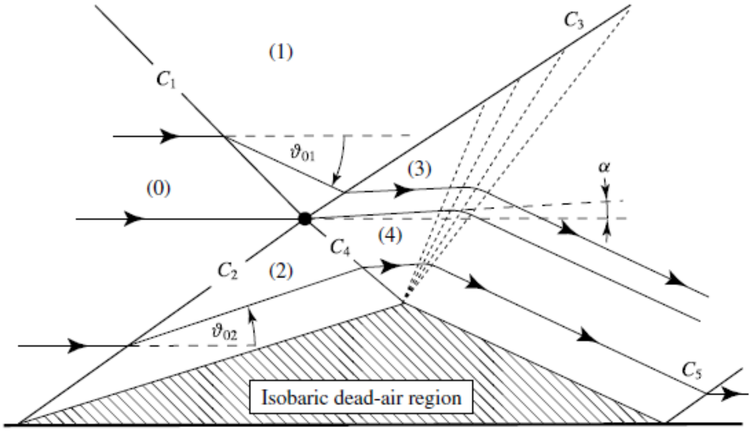

Figure 2.13: Inviscid flow model of the strong RSWBLI. (Matheis & Hickel, 2015)

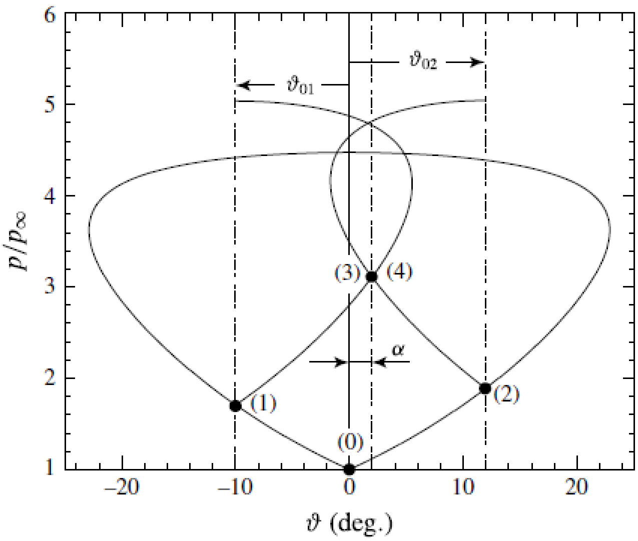

Figure 2.14: Shock polar representation of the inviscid flow model of the strong RSWBLI. (Matheis & Hickel, 2015)

By assuming inviscid flow (Figure 2.13), one can study the interaction using standard oblique shock relations (Appendix A), which allows for estimates of the flow properties after the interaction.

The interaction can also be further represented by its respective polar (Figure 2.14), which gives an indication of the kind of interaction that one may expect, either a regular SWTBLI (RSWTBLI) or an irregular interaction. The occurrence of each type of interaction is mainly dependent on the freestream Mach number and the initial flow deflection. For a more extensive understanding of the different types of interaction (regular and irregular) refer to Matheis and Hickel (2015).

2.2.3 Wall Properties

The skin-friction coefficient and the wall pressure are some of the most analysed parameters in SWTBLIs. Their trends and Reynolds number dependency will be discussed.

Skin-Friction

The skin friction distribution starts at a freestream value, which decreases with increasing Reynolds number. As the interaction region is approached it starts decreasing steeply due to the upstream influence of the interaction. It then crosses the $\langle C_f \rangle = 0$ line at both the separation and reattachment points that are defined in this way. In between these two points there is the recirculation region. It can be identified in the $\langle C_f \rangle$ distribution as the region with negative values. Laguarda et al. (2024b) concluded that the distance between the separation and reattachment points, also known as the separation length L_{sep} is not very sensitive to Reynolds number variations.

For SWTBLIs, a global minimum is always present. The location of this minimum is not dependent on the Reynolds number (Laguarda et al., 2024b). For low Reynolds numbers, however, a W shape can be identified in the separation region (Priebe et al., 2009; Aubard et al., 2013), with an additional local minimum right after separation upstream of the global minimum (see Figure 2.15). On the other hand, high Reynolds number interactions present a plateau in the region after separation before the peak (see the illustrative high Reynolds example in Figure 2.15).

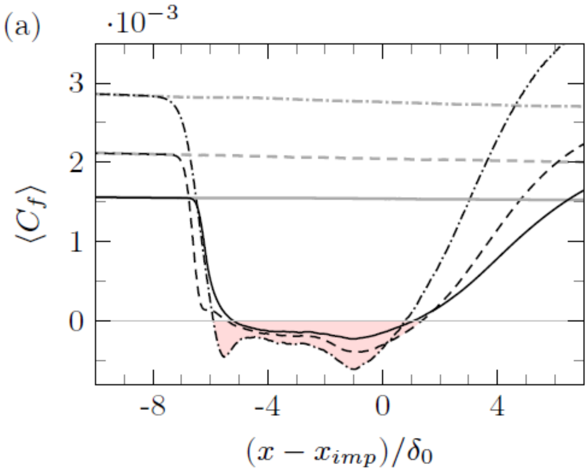

Figure 2.15: Time- and spanwise-averaged skin-friction evolution: (-·-·) low-, (·····) moderate-, (—) high-Reynolds number. Separated regions are shaded in red and the gray lines denote the corresponding skin friction distribution for the undisturbed TBL. Laguarda et al. (2024b)

Pressure

The wall pressure evolution across the interaction is characterised by a smooth, but steep increase that starts at the foot of the RS. Note that the curve of the mean wall pressure presents three inflection points, more prominent for strong interactions (Delery and Marvin, 1986; Matheis and Hickel, 2015

- see Figure 2.17): at the RS foot (at the start of separation), within the separation region (due to the onset of reattachment) and close to the reattachment position (related to the reattachment compression).

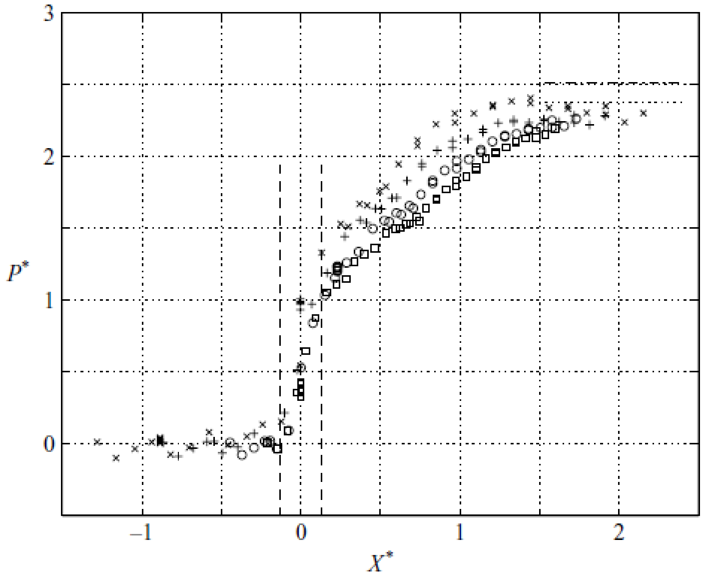

Figure 2.16: $P^* = (\overline{P} - p_1)/(p_2 - p_1)$ mean pressure distribution along the interaction; $X^* = (x - X_0)/L$, X_0 mean position of the reflected shock, L interaction length, p_1 and p_2 the inviscid pressure upstream and downstream of the incident shock, respectively; the symbols represent different IS angles; the horizontal lines dashed lines correspond to the inviscid theoretical values: (-·-·), 9° incidence; (······), 7° incidence; $Re_{\delta_\infty} = 59.3 \times 10^3$. (Dupont et al., 2006)

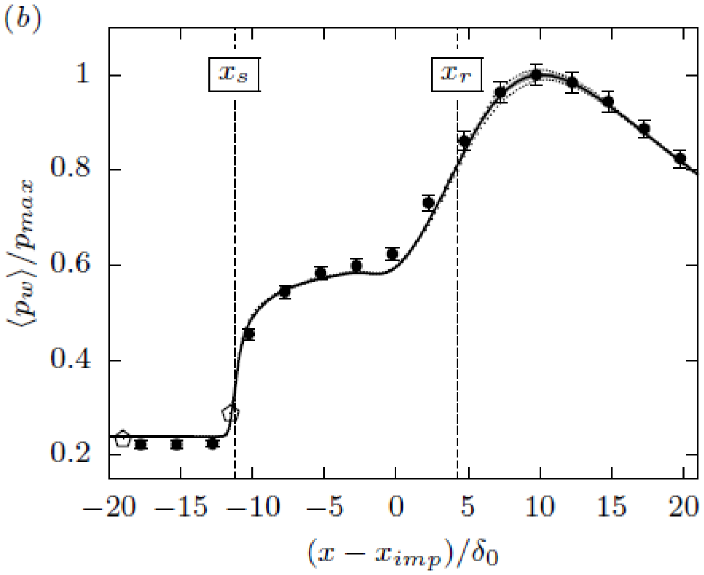

Figure 2.17: Pressure distribution - high Reynolds number, $Re_{\delta_\infty} = 203 \times 10^3$. (Pasquariello et al., 2017)

For even stronger interactions, a plateau forms in the recirculation region, followed by another increase, due to the reattachment of the boundary layer. The plateau pressure can be predicted using the free interaction theory (Subsection 2.2.5) and it becomes more pronounced the bigger the Reynolds number. For low Reynolds numbers, it is smeared and almost non-existent.

The mean pressure then tends to the inviscid, post-shock value. However, this convergence with the inviscid solution can be affected by the presence of expansion waves generated by the trailing edge of the shock generator. When expansion waves are present the post-interaction mean wall pressure is lower than the inviscid prediction. An illustrative example of the mean wall pressure can be seen in Figure 2.16 and Figure 2.17 for low and high Reynolds numbers interactions, respectively.

The root-mean-square (RMS) pressure (see illustrative Figure 2.18) shows a different evolution. Until the interaction, its value is close to zero. At the start of the interaction, at the RS foot, it has a peak (D. S. Dolling and Or, 1985; D. S. Dolling and Murphy, 1983; Pasquariello et al., 2017). Dupont et al. (2006) reported that the jump was approximately $p'_2/p'_1 \approx 9$. Downstream of this first bump the fluctuations remain higher than upstream, with a small decrease close to reattachment due to the compression of the flow in this region, followed by another smaller peak downstream of the mean reattachment point related to the reattachment of the shear layer, which was found at about $2.4\delta_\infty$ by Pasquariello et al. (2017).

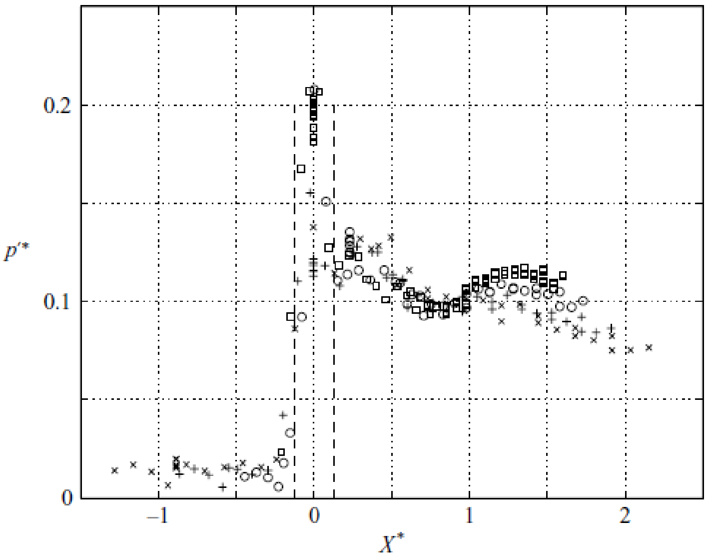

Figure 2.18: Dimensionless RMS wall pressure fluctuations, $p'^* = \sqrt{\overline{p'^2}}/(p_2 - p_1)$, symbols as in Figure 2.16; $Re_{\delta_\infty} = 203 \times 10^3$. (Dupont et al., 2006)

It is important to note that the wall-pressure fluctuations become more intense as the Reynolds number increases, which coadunate with the fact that for higher Reynolds numbers the shock originates from deeper within the boundary layer. Also, the passage of coherent structures contributes to the pressure fluctuations, particularly, in the spanwise direction, as observed by Laguarda et al. (2024b). Also, more recently, W. Wu et al., 2024 observed that using ridge-type roughness can reduce the wall pressure fluctuation peak in the separation onset region.

2.2.4 SWTBLIs Turbulence Content

In terms of turbulence content, one can focus the discussion into three different categories: the TKE distribution, the Reynolds stress tensor components and turbulent structures. Regarding TKE, Priebe and Martín (2012) observed large values of TKE originating at the shock foot, extending in the downstream direction, above the recirculation region and along the shear layer. Also, near reattachment, large values were registered. For a more detailed analysis of the TKE budgets of SWTBLIs the works of Vyas et al. (2016) and Laguarda et al. (2024b) are suggested.

The characterisation of the Reynolds stress components is made based on the work of Pasquariello et al. (2017) for which the streamwise, wall-normal and spanwise components are shown in Figure 2.19 (a), (b) and (c), respectively. Note that the distributions presented in Figure 2.19 were obtained for a moderate Reynolds number of $Re_{\theta_\infty} = 14 \times 10^3$. For different Reynolds numbers, the same kind of trends are expected. Nonetheless, the reader should keep this fact in mind when comparing it with other cases.

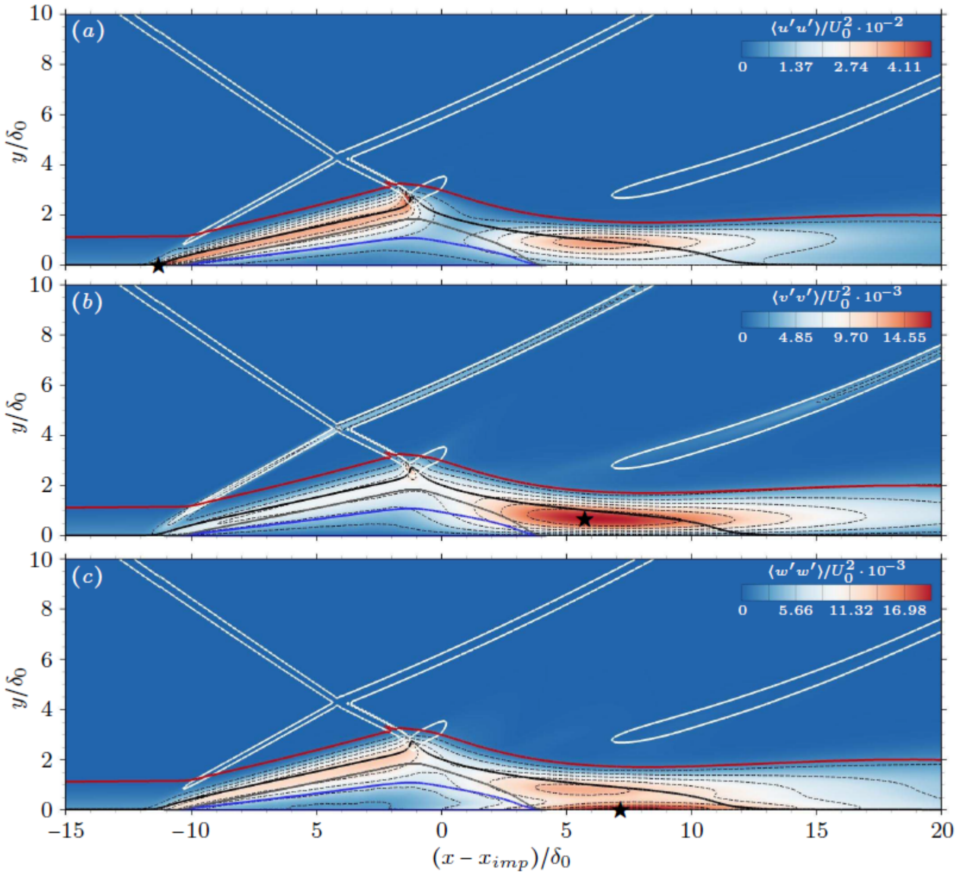

Figure 2.19: Time- and spanwise-averaged Reynolds normal stress components. The shock system is visualised by isolines of pressure gradient magnitude $|\nabla p|\delta_\infty/p_\infty = \{1.08; 3.28\}$. (—)$\delta$, (—) $\langle M \rangle = 1$, (—) $\langle u \rangle = 0$, (—) dividing streamline y_{ds}. A star (⋆) indicates the location of maximum contour level. Eight discrete contour levels are shown by dashed lines. (Pasquariello et al., 2017)

In general, the streamwise Reynolds stress $\langle u'u' \rangle$ has higher intensity along the detached shear layer (with its maximum near the point of maximum stress production (Laguarda et al., 2024b) in the separation point region close to the wall as reported in previous studies such as the ones by Pasquariello et al. (2017) or Kang and Lee (2024)) and close to the reattachment point further from the wall. According to Pasquariello et al. (2017) the region of high $\langle u'u' \rangle$ near the reattachment location has to do with the interaction of the reattachment point with the convected vortices. Close to the bubble apex, the convexity of the streamlines dampens this component of the Reynolds stress, which is the most affected by the streamline curvature (Sandham, 2016). Laguarda et al. (2024b) reported that the peak location shifts from the reflected shock foot to the core of the detached shear layer as the Reynolds number increases. Based on their study of the TKE budget, they propose that this shift is related to the increased pressure transport in the separation-shock excursion domain.

For $\langle v'v' \rangle$, the maximum is observed far from the wall in the reattachment region, but high levels are also visible along the separation and reattachment shocks, associated with their unsteadiness (Pasquariello et al., 2017).

Lastly, the spanwise component has a similar distribution to that found for the streamwise component. Nonetheless, its maximum is found at the wall in the reattachment area about $3\delta_\infty$ downstream, below another high-level region (Pasquariello et al., 2017). A different location for the maximum was found by Laguarda et al. (2024b) who reported that location to be in the first half of the detached shear layer away from the wall.

2.2.5 Free Interaction Theory

When analysing SWTBLIs one of the most useful tools for initial predictions of flow displacement/deflection and pressure distributions is the *free interaction* concept. This concept was first introduced by Chapman et al. (1958) and further reviewed by others such as Delery and Marvin (1986) or Babinsky and Harvey (2011). The general idea of this concept is that the interaction is entirely determined by the properties of the flow at the onset of the interaction.

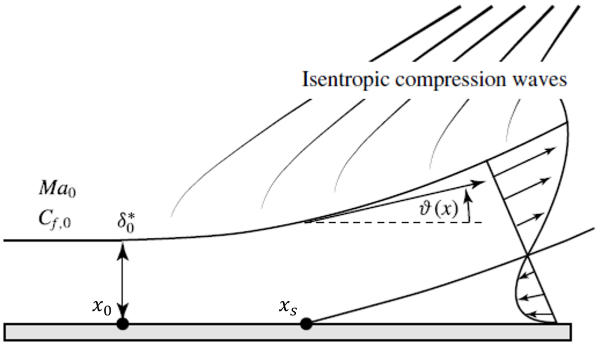

Figure 2.20: Free interaction region of RSWBLI - boundary layer displacement. (Matheis & Hickel, 2015)

Based on free interaction theory one can determine the flow deflection at separation. Figure 2.20 shows a schematic of the interaction close to the separation point. In this subsection, the subscript $_0$ indicates the onset conditions. One can assume that the deflection of the inviscid outer flow is exactly the same as the one imposed by the displacement of the boundary layer

$$\frac{\mathrm{d}\delta^*}{\mathrm{d}x} = \vartheta(x) - \vartheta_0. \tag{2.19}$$

By normalizing the streamwise coordinate and the BL displacement thickness and assuming similarity for both the BL profile as well as for the pressure rise one finds a universal correlation function $\mathcal{G}$ that is independent of both the Reynolds and the Mach number given by

$$\begin{aligned} \mathcal{G}(s) = \sqrt{f_1(s) f_2(s)} &= \sqrt{\frac{p(s) - p(0)}{q_0} \frac{\vartheta(s) - \vartheta_0}{C_{f_0}}} \\ &\approx \frac{p(s) - p_0}{q_0} (M_0^2 - 1)^{0.25} (2C_{f_0})^{-0.5}. \end{aligned} \tag{2.20}$$

The expression presented for $\mathcal{G}$ in Equation 2.20 uses the linearised wave equation to express the pressure variation induced in the outer flow as proposed by Chapman et al. (1958). Carrière et al. (1969) generalized the theory presented by Chapman et al. (1958) to take into account non-uniformities in the incoming flow. Hence they proposed a universal correlation function $\widehat{\mathcal{G}}$ of the form

$$\widehat{\mathcal{G}}(s) = \sqrt{\frac{p(s) - p_0}{q_0} \frac{\overline{\nu}(s) - \widehat{\nu}(s)}{C_{f_0}}}, \tag{2.21}$$

where $\overline{\nu}$ is the Prandtl-Meyer angle for the actual pressure at s and $\widehat{\nu}$ is the value that it would have in the absence of separation (Delery & Marvin, 1986). The Prandtl-Meyer angle is computed as presented in Equation A.15.

Depending on the applications and the method used for its determination $\mathcal{G}$ and $\widehat{\mathcal{G}}$ can take different values. The value of $\widehat{\mathcal{G}_p} = 6.2$ assumed by Matheis and Hickel (2015) will be used here for the plateau value. Knowing the values of C_{f_0} and M_0, together with the assumption $\widehat{\mathcal{G}} = \widehat{\mathcal{G}_p}$ one can iteratively determine the plateau pressure ratio $\varepsilon = p_p/p_0$. To do so, one must further assume no curvature (flat plate) and isentropic compression, which yield Equation 2.22 and Equation 2.23, respectively,

$$\overline{M}^2(s) = M_0^2, \tag{2.22}$$

$$\widehat{M}^2(s) = \frac{2}{\gamma - 1} \left[\left(\frac{p_0}{p(s)} \right)^{(\gamma-1)/\gamma} \left(1 + \frac{\gamma - 1}{2} M_0^2 \right) - 1 \right]. \tag{2.23}$$

The coordinate s is given by $s = (x - x_0)/(x_{ref} - x_0)$, with x_{ref} being the coordinate where $\widehat{\mathcal{G}} = 4.22$ and x_0 the position for which $dp/dx|_w(\delta_0(x)/p_w(x)) = 3.5 \times 10^{-3}$.

Having determined the plateau pressure ratio, the flow deflection across the RS can be determined as

$$\vartheta_{02} = \arctan \left[\frac{(\varepsilon - 1)^2 [2\gamma(M_0 - 1) - (\gamma - 1)(\varepsilon - 1)]}{[\gamma M_0^2 - (\varepsilon - 1)]^2 [2\gamma + (\gamma - 1)(\varepsilon - 1)]} \right]^{0.5}. \tag{2.24}$$

According to the study made by Laguarda et al. (2024b) both the incipient plateau pressure and the separation-shock angle are rather insensitive to variations in the Reynolds number.

For a more comprehensive derivation and understanding of the free interaction theory refer to Chapman et al. (1958), Delery and Marvin (1986) and Matheis and Hickel (2015).

2.3 SWTBLI Unsteadiness

SWTBLIs are characterised by low-frequency unsteadiness, particularly, on the reflected shock. There are a number of different mechanisms that have been pointed out throughout the years as the sources for this unsteadiness. From upstream to downstream mechanisms and also an inherent instability have been observed to be correlated with the shock motion. A comprehensive review on these can be found in the work of Dussauge et al. (2006), or more recently Clemens and Narayanaswamy (2014).

A growing body of evidence suggests that downstream mechanisms drive the low-frequency unsteadiness, with the upstream mechanism and the inherent instability being also considered as contributing to the low-frequency shock motion, despite being more prominent for low Reynolds numbers and when the shock is in the extremes of its excursion range.

2.3.1 Upstream Mechanisms

Large eddy simulations of Hunt and Nixon (1995) showed an approximately one-to-one relationship between the shock velocity and the incoming turbulent velocity fluctuations, supporting Erengil (1993) conclusions.

Ünalmis and Dolling (1994) suggested that low-frequency variations in the incoming boundary layer thickness might induce the large-scale shock motion based on the comparison of the mean pitot pressure at a fixed vertical position in the boundary layer upstream and downstream of the shock foot. Moreover, Ganapathisubramani et al. (2007) suggested that *superstructures*, regions of alternating low- and high-speed fluid in the logarithmic layer, would be responsible for the shock motion. These superstructures were also identified in DNS simulations (Ringuette et al., 2007). Their longitudinal extension is of the order of $\mathcal{O}(10\delta_\infty)$ (Priebe & Martín, 2012) and can go up to $30\delta_\infty$ (Piponniau et al., 2009).

S. Beresh et al. (1997, 1998), on the other hand, found no significant correlation between the upstream boundary layer thickness and the shock foot location. The correlation between the incoming TBL fluctuations and the shock foot velocity did not show any relation between the two quantities (S. Beresh et al., 1998). S. J. Beresh et al. (2002) reported evident correlations between positive/negative fluctuations close to the wall in the incoming boundary layer and downstream/upstream movements of the shock, respectively, consistent with the principle wherein positive velocity fluctuations contribute to a momentarily fuller velocity profile, which in turn is more resistant, postponing separation to a downstream position and vice-versa (see Figure 2.21). Nonetheless, S. J. Beresh et al. (2002) concluded once more that a thickening/ thinning boundary layer mechanism is probably not the cause of the shock unsteadiness.

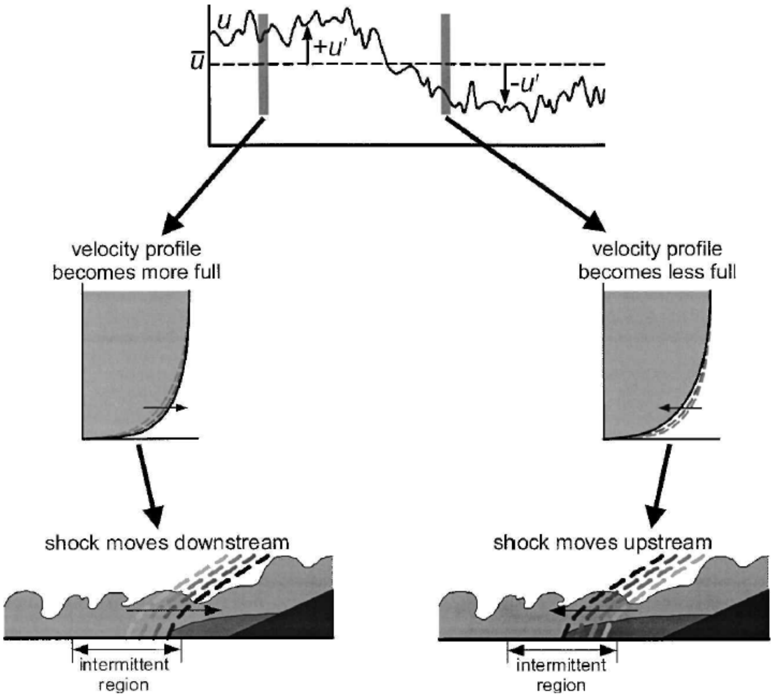

Figure 2.21: Relation between the incoming boundary layer and the separation shock foot unsteadiness. (S. J. Beresh et al., 2002)

M. Wu and Martín (2007) in their DNS of a Mach 2.9 compression ramp found ”no significant difference in the properties of the incoming boundary layer when the shock location is upstream or downstream” concluding that the incoming boundary layer structures have a minimal impact on the shock unsteadiness. Also Priebe and Martín (2012) observed weak statistical link between the two parameters.

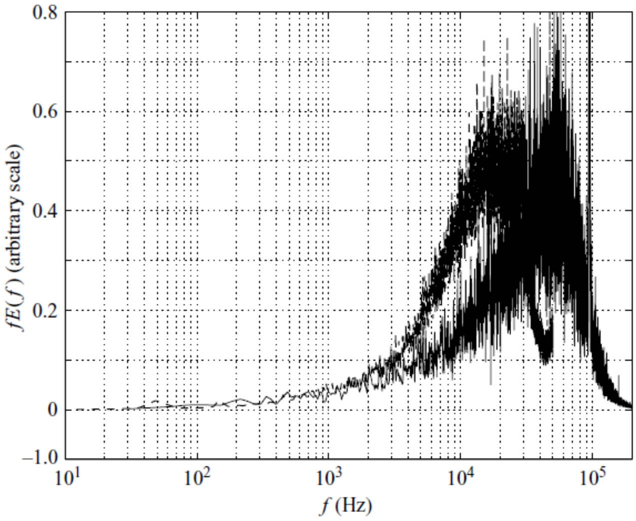

Figure 2.22: Power spectral density in the upstream boundary layer - $M_\infty = 2.3$; (—) momentum fluctuations: $y/\delta = 0.2$; (- - -) wall pressure fluctuations, low pass = 50 kHz. (Dupont et al., 2006)

Regarding the incoming boundary layer, Dupont et al. (2006) analysed its power spectral density (PSD) spectrum for a Mach 2.3 flow in the wind tunnel where they observed the characteristic high-frequency content of TBLs ($\mathcal{O}(u_\infty/\delta_\infty)$) with no low-frequency content present as seen in Figure 2.22.

This shows that the low frequencies found in SWTBLIs are related to the dynamics of the interaction itself. Overall, these findings provided little support for the thickening/ thinning boundary layer mechanism, despite being admitted that according to the correlations found between incoming fluctuations and the shock unsteadiness, they might have some minor influence in the low-frequency motion (Priebe & Martín, 2012). Regarding the upstream mechanism, a Reynolds-independent statistical link between the shock motion, the velocity streaks and large-scale vortices at low frequencies was found by Laguarda et al. (2024b) indicating that the incoming turbulence may influence the dynamics of the interaction.

2.3.2 Downstream Mechanisms

Dupont et al. (2006) mentioned that they found a strong correlation between the IS foot motion and the second half of the interaction/separation zone. Furthermore, they reported a phase shift of π between the two pressure signals measured at each of those locations.

Similar results were obtained by M. Wu and Martín (2007) and Priebe and Martín (2012) who found a negative correlation between the mean separation and reattachment points locations, which indicates a *breathing motion* of the separation bubble. Further analysis from M. Wu and Martín (2007) not only found that the mass (and hence, size) of the bubble is correlated with the mean shock location (with a correlation peak of 0.7), but that the shock motion lags the motion of the separation bubble by $\approx 13\delta_\infty/u_\infty$. Based on these observations they concluded that "the separation bubble drives the shock motion". Priebe and Martín (2012) also supported this conclusion in their DNS of a compression ramp in Mach 2.9 flow. Likewise, Hu et al. (2021) argued to have "evidence" relating the unsteady low-frequency with the breathing of the separation bubble and the flapping motion of the shock.

Pirozzoli and Grasso (2006) proposed an acoustic feedback mechanism as the driver for the unsteadiness. Acoustic disturbances would propagate upstream through the subsonic part of the boundary layer, feeding the loop. Evidence was found of this acoustic propagation by Laguarda et al. (2024b) who reported a lag of the separation shock motion concerning the bubble volume variations, consistent with the time required for an acoustic wave to travel from the reattachment to the separation point. Likewise, M. Wu and Martín (2007) further hypothesised a *feedback-loop* between the separation bubble, the shear layer and the shock. They propose that the shear layer entrainment, caused by the generated vortices, and the injection near the reattachment point are responsible for negative and positive fluctuations in the bubble mass, respectively. Priebe and Martín (2012) supported this hypothesis and reported a low-frequency flapping of the shear layer that they linked to the shock motion. When the bubble expands, the separation and reattachment point move, upstream and downstream, respectively. This causes the RS to also move upstream following the separation point. The movement of the shock alleviates the pressure gradient and streamlines curvature in the separation region, reducing the entrainment of fluid. The bubble becomes unstable and breaks, bursting fluid outside the bubble, and making it shrink. The shrinking causes the shock to move downstream and its effect on the pressure gradient and streamline curvature is now the opposite feeding the feedback loop.

Piponniau et al. (2009) admitted M. Wu and Martín (2007) hypothesis and developed a simple model for the separation and bubble dynamics that aimed to relate the subsonic and supersonic bubble motions. The characteristic Strouhal numbers as defined in Subsection 2.3.4 do not match for both conditions being approximately 0.03 and 0.12 for supersonic and subsonic detached flows, respectively. Hence, they came up with a Strouhal number that is weighted by two functions: the first considering density and reverse flow intensity $g(r, s)$ and the second accounting for compressibility effects $\Phi(M_c)$, where r and s are the external velocity and density ratios across the mixing layer, while M_c is the isentropic convective Mach number. By plotting the quantity $St \times \{g(r, s)\Phi(M_c)\}^{-1}$ they found a collapse of the data for a representative mean value of $6 \pm 20\%$ (see Figure 2.23), which made them conclude that the previously verified difference in Strouhal numbers must be related to the Mach dependence on the mixing layer entrainment ($\Phi(M_c)$).

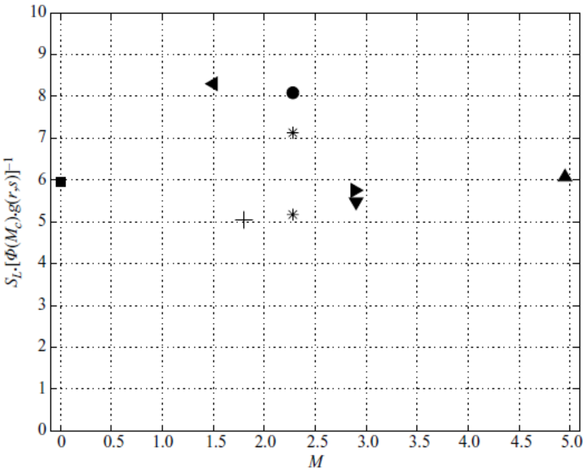

Figure 2.23: Scaled Strouhal number of the shock oscillation. (Piponniau et al., 2009)

Adding to M. Wu and Martín (2007) proposed downstream mechanism, Piponniau et al. (2009) further observed an asymmetric behaviour of the shock motion. Its movement downstream is somewhat confined when the bubble contracts while it almost doubles the displacement upstream when the bubble expands. Priebe and Martín (2012) further mentioned a "sawtooth-like" trajectory of the reattachment point, moving downstream at almost constant velocity with rapid relaxations when moving upstream. This behaviour of the reattachment point was also observed by Hu et al. (2021).

Piponniau et al. (2009) also analysed the influence of upstream disturbances on the bubble breathing motion and even though they found a correlation between the two, they concluded that upstream fluctuations are unlikely to be the cause of the breathing and that they may only interfere with the development of the extreme states of the bubble.

2.3.3 Inherent Instability

A third mechanism proposed for the characteristic SWTBLIs low-frequency unsteadiness is an inherent instability. Touber and Sandham (2009) performed LES on a flat plate shock reflection Mach 2.3 flow and observed an unstable global mode based on a linear stability analysis of the mean flow. According to them this could be the driving mechanism for the unsteadiness. One should keep in mind, however, that the spanwise domain extension used by Touber and Sandham (2009) was very small, which could have introduced artificial numerical coupling between the spanwise periodic boundaries. In fact, for a very similar case, Laguarda et al., 2024b showed that a domain as wide as $3-4\delta$ was needed to avoid artificial correlations between fluctuating quantities at the spanwise boundaries.

According to Guiho et al. (2016) the most unstable global mode is located along the line $u = 0$, especially around the reattachment point. Priebe and Martín (2012) found similar skin-friction distributions throughout the interaction as Touber and Sandham (2009), associated with the burst of the bubble or the enhancement of separation, which made them also consider the global instability as the source of the unsteadiness. Figure 2.24 shows a schematic of the mechanism and flow structure as observed by Priebe and Martín (2012).

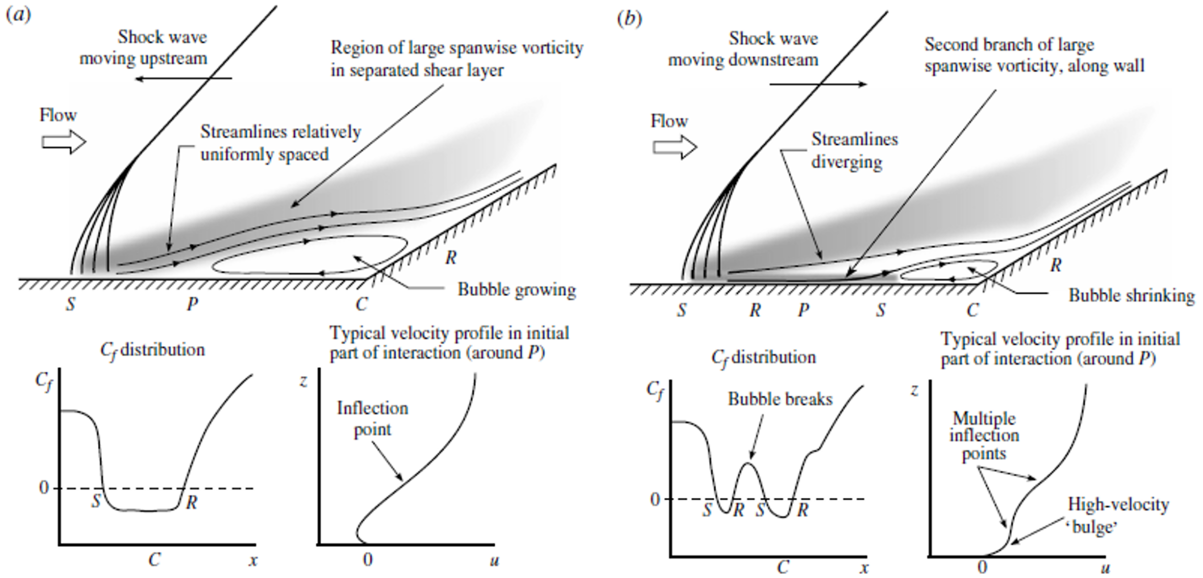

Figure 2.24: Schematics of the different flow structure observed depending on the phase of the low-frequency motion: (a) bubble growth phase; and (b) bubble collapse phase. (Priebe & Martín, 2012)

Touber and Sandham (2011) proposed that some forcing should be present for the unsteadiness to exist since, according to them, the low-frequency motion is an intrinsic low-pass filter due to the interaction and not necessarily due to any upstream or downstream mechanisms. Pasquariello et al. (2017) obtained results consistent with the inherent instability mechanism in the interaction zone through their PSD and sparsity-promoting dynamic mode decomposition (SPDMD). They suggested that Götler-like vortices can be the ”continuous (coherent) forcing” for strong SWTBLIs. Furthermore, they suggest a centrifugal instability to be the plausible mechanism of generation of the vortices. These vortices have also been identified in Loginov et al. (2006) LES on a compression ramp flow. Both experimental and numerical results agree that the spanwise extension of each vortex pair is $\approx 2\delta_\infty$.

The numerical work from Grilli et al. (2013) and Priebe et al. (2016) for compression ramps observed streamwise-elongated Götler-like vortices originating around the reattachment point. Also Pasquariello et al. (2017) found them in their dynamic mode decomposition (DMD) analysis for an impinging shock configuration. These vortex pairs have an intrinsic spanwise wavelength of about $\lambda_z \approx 2\delta_\infty$ (Schülein and Trofimov, 2011; Priebe et al., 2016; Hu et al., 2021).

According to Pasquariello et al. (2017) the counter-rotating vortices do not have a fixed spanwise position as reported by Loginov et al. (2006). They induce up- and downwash in alternating spanwise regions. In the upwash regions, the shear stress at that spanwise location is reduced moving the reattachment point downstream. The opposite is true for the induced downwash regions. Despite considering the Götler-like vortices as a possible driving mechanism to the unsteadiness, Pasquariello et al. (2017) also reported that the vortices ”appear and disappear, coalesce and separate in an apparently random manner”. Hu et al. (2021) made similar observations. These observations of randomness suggests that the average effect of these vortices might be diminished and not ”constant” enough to be responsible for the unsteadiness observed in SWTBLIs. Hence, even though Götler-like vortices may impact the low-frequency unsteadiness, given the different temporal scales, they are most likely not its source.

2.3.4 Frequency Content

To address the topic of frequency content one must first define the Strouhal number St as $St = fL/u_\infty$. The length in the Strouhal number definition can vary with some authors proposing the separation length L_{sep} while others prefer to use the interaction length L_{int}.

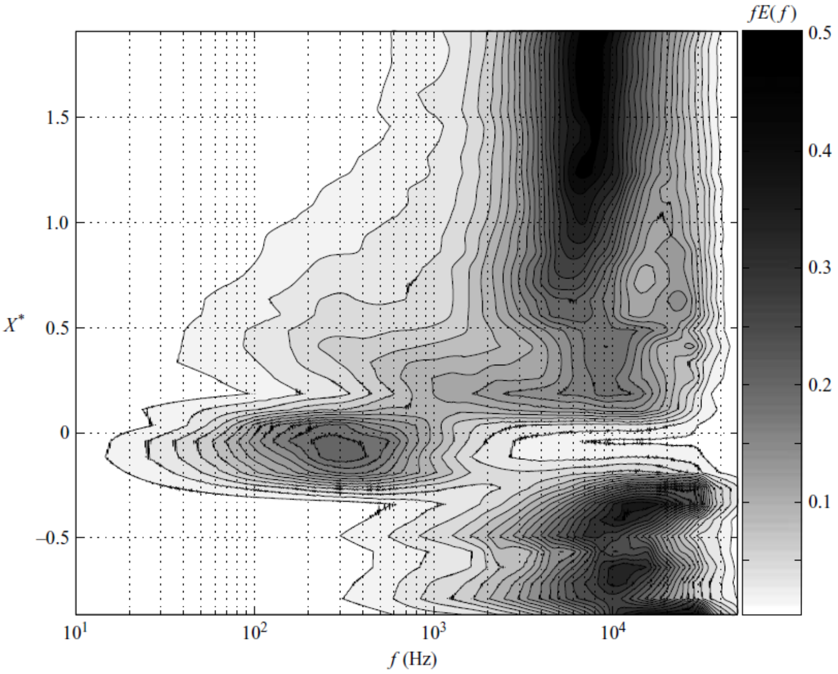

Figure 2.25: PSD along the interaction. (Dupont et al., 2006)

Following the representative example published by Dupont et al. (2006) presented in Figure 2.25 one can analyse the evolution of the frequency spectrum across the interaction. This evolution was also observed by other authors such as Priebe and Martín (2012). Four regions can be identified. The first (upstream of the interaction) is related to the incoming boundary layer. As seen in Figure 2.22 it is characterised by energetic high frequencies (above 10 kHz) with no low-frequency content. The second region is located around the separation shock. There is a clear shift to low frequencies in this region (some hundreds of Hz - of the order of $0.007 - 0.013u_\infty/\delta_\infty$, M. Wu and Martín (2007)) attributed to the RS unsteadiness, which has a displacement of the order of the initial boundary layer thickness. The third region is the interaction region itself where a range of intermediate frequencies is found ($St_{int} \approx 0.5$, Dupont et al. (2006)). One can still find significant energy for both high and low frequencies associated with the incoming boundary layer and the characteristic low-frequency RS unsteadiness. These frequencies are associated with the convection of large scales over the recirculation zone where vortices in the shear layer formed at the shock foot are shedded close to the separation bubble apex. Laguarda et al. (2022) also found a peak for $St_{sep} \approx 0.1$, which becomes more intense for higher Reynolds numbers. In a different study on the effects of the Reynolds number in SWTBLIs, Laguarda et al. (2024b) observed once more a peak for the same Strouhal number in the bubble-volume spectra. Lastly, a relaxation region is present downstream of the reattachment point where the frequencies are high but lower than for the original incoming boundary layer. This reduction in frequency is due to the growth of the BL across the interaction, but also due to the rearrangement of the vortical structures that become larger.

In agreement with the spectral evolution discussed above and taking into account their locations in the interaction Priebe and Martín (2012) observed that while the separation point has most of its energy in the low-frequency range, the reattachment point, while still presenting some energy at those frequencies, has most of its energy contained in higher frequencies (for $St_{int} \approx 0.5$).

Reflected Shock Properties

As seen before, in SWTBLIs the low-frequency shock foot unsteadiness presents a characteristic frequency that is much lower than the frequency of the incoming boundary layer fluctuations, about two orders of magnitude lower - $\mathcal{O}(0.01u_\infty/\delta_\infty)$ (Kistler, 1964; Gonsalez and Dolling, 1993; Piponniau et al., 2009; Priebe and Martín, 2012). This fact has been observed in several experiments such as the ones carried by D. S. Dolling and Or (1985) or Dupont et al. (2006). The streamwise movement of the shock extends for a range of about $1\delta_\infty$ (M. Wu & Martín, 2007).

The low-frequency motion is related to a Strouhal number in the range $St_{int} = 0.025 - 0.04$, having an average value of 0.03 ($\pm 20\%$) using L_{int} as scaling parameter (Dupont et al., 2006). Other authors (M. Wu and Martín, 2007;Priebe and Martín, 2012) indicate an extended range for the low-frequency Strouhal number of $0.02 - 0.05$. As expected, the shock motion is correlated with the motion of the mean separation point (M. Wu & Martín, 2007).

Adding to the low-frequency the shock motion also exhibits high-frequency content of $\mathcal{O}(u_\infty/\delta_\infty)$ (M. Wu & Martín, 2007). This high frequency, however, becomes decorrelated spanwise with increasing wall distance. The low-frequency, on the other hand, remains spanwise correlated for large values of Δy and in phase across the span. This indicates an approximately 2D motion of the shock. 3D effects are mentioned to be important near reattachment (Priebe & Martín, 2012) and enhanced for higher Reynolds numbers (Laguarda et al., 2024b).

Muck et al. (1988) was one of the first to report a spanwise non-uniformity. Later, M. Wu and Martín (2007) identified it as a spanwise wrinkling (with an amplitude of $\approx 0.5\delta_\infty$), that they attribute, based on their results, to the turbulent structures in the incoming boundary layer, particularly to low-momentum fluid. Also Andreopoulos and Muck (1987) and Erengil and Dolling (1991) had proposed a similar cause. Likewise, they also observe large-amplitude wrinkling with magnitudes of the order of $4\delta_\infty$. Nonetheless, the mean position of the shock foot is similar across the span. Also, Humble et al. (2009) reported the spanwise wrinkling of the shock due to the passage of coherent structures in their PIV measurements of a Mach 2.1 impinging SWTBLI. The spanwise position of the shock is correlated with the edge of the separation bubble, as high-speed flow, displaces the shock foot closer to the wall, postponing separation (Laguarda et al., 2024b).

2.3.5 Unsteadiness Control

Given the recurrence and the impact of SWTBLIs in nowadays engineering applications, it is of the utmost importance to try to control this phenomenon, particularly to reduce its unsteadiness and avoid separation, since these two effects are the most detrimental for aircraft, wing and inlet performances. Throughout the years several control methods have been studied to address these problems: from cavities to micro vortex generators or ramps, to channels and boundary layer bleeding/suction as well as jets, plasma actuators and electrical discharges. Two major categories can be identified: boundary layer control and shock control mechanisms. The first focuses on energising the incoming boundary layer to make it more resistant to adverse pressure gradients, while the second pretends to decrease those pressure gradients by weakening the shock and dampening its unsteadiness. W. Huang et al. (2020) provide a comprehensive review of the most common methods and their impact on the SWTBLI.

Porous/Perforated Wall

Raja sekar et al. (2019) applied perforated walls both upstream and downstream of the separation bubble as well as the combination of the two for a scramjet configuration. Their results showed that having two separate perforated regions up- and downstream of the bubble results in the biggest decrease in the bubble size.

Jana et al. (2020) used the same method in a similar application (see Figure 2.26). They tested walls with different levels of porosity. They observed an increase in performance as the result of a reduction in shock strength and suppression of the separation bubble. The bubble size decreased monotonously with increasing surface perforation for a porosity of up to 17%.

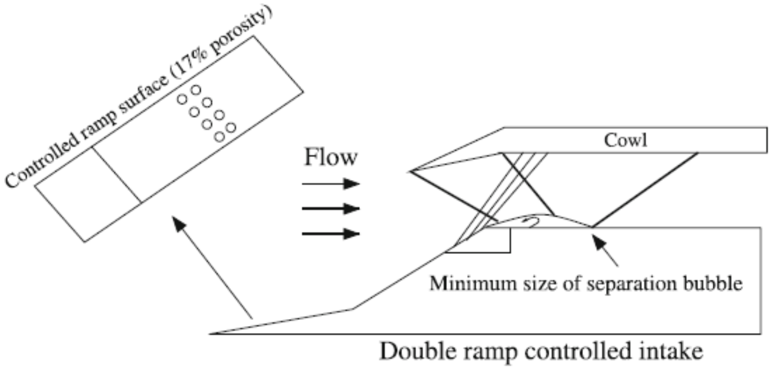

Figure 2.26: Engine intake perforated wall application. (Jana et al., 2020)

Feedback Channel

This control configuration is based on the feedback loop as explained in Subsection 2.3.2. It creates a channel between the downstream and upstream regions of the interaction. In each location, one can impose fluid suction and injection, respectively, with another possibility relaying on the pressure gradient created by the shock to drive the flow through the channel.

Pasquariello et al. (2014) used the suction/blowing method on a Mach 2.3 impinging shock configuration, keeping the flow injection location constant as shown in Figure 2.27. They concluded that the suction reduces the volume of the recirculation bubble, yielding the best results when applied to the rear part of the bubble. Moreover, due to the presence of the suction slots, additional unsteady shocks are generated in their vicinity. On the other hand, the injection of fluid upstream of the interaction leads to an increased subsonic layer for all configurations tested.

Regarding the interaction frequency content, Pasquariello et al. (2014) observed a shift of the high energy low-frequencies to higher frequencies. The energy level, however, was only decreased when the suction was applied to the rear region of the bubble. When suction is applied to the rear part, the mitigated reflected shock dynamics and the acceleration of the flow near the wall (due to suction) contribute to a local increase of the skin friction upstream of the suction slot and a decrease in the turbulence production within the interaction zone. Likewise, also turbulence fluctuations are damped. If suction is applied in the middle of the bubble region, the shock-excursion length increases.

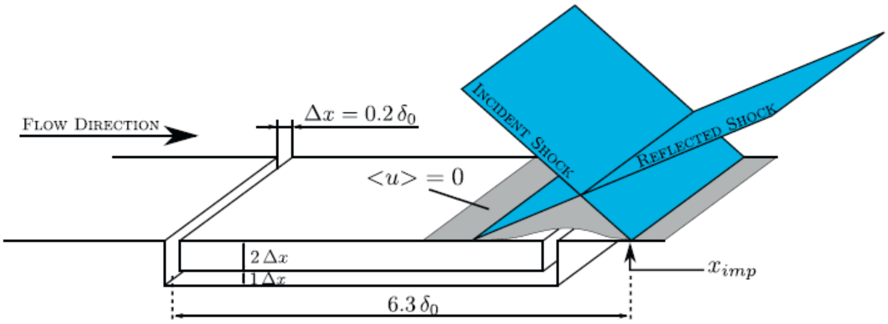

Figure 2.27: Schematic of the control method considered by Pasquariello et al. (2014). Blue planes: reflected shock system. Grey Surface: 2D sketch of the recirculation region.

Also L. Yan et al. (2020) studied this method for an impinging shock configuration using RANS. They tested different suction/bleed positions as well as various channel widths. According to them, the placement of the suction slot on the windward side of the separation zone is advantageous, reducing the separation length as well as the wall pressure peak. Moreover, a secondary separation was observed in the bleeding slot with a secondary shock system being formed. However, this enhanced mixing, which proved beneficial. Lastly, they concluded that the dimensions of the slots have only a small impact on the flow control efficiency.

Step Flows

Step flows have been studied previously in different contexts from a fundamental understanding perspective. Nonetheless, only more recently they have been addressed as possible control mechanisms for SWTBLIs. Laguarda and Hickel, 2024 work pioneered this new perspective. In their work, Laguarda and Hickel, 2024 used a backward-facing step (BFS) with the intent of blocking the acoustic connection between mean separation and reattachment points. The results obtained showed a significant reduction in low-frequency unsteadiness, while maintaining similar separation length. Hence. the outcomes of their study provide strong evidence for the downstream mechanism.

Additionally, other step flows will be discussed next. The following studies were not implemented with the *a priori* intention of controlling the SWTBLI. Nonetheless, they give further insight into the SWTBLI dynamics and its behaviour in this kind of configuration. Hence, they are still regarded as informative of the characteristics of SWTBLI flows over steps.

BFS flows have been tested in various configurations. In general, this approach increases the length of the separation bubble despite decreasing its height. Hu et al. (2021) reported a separation length of about 3 times the height of the step ($L_{sep} \approx 3h$) This is due to the recirculation region formed at the corner of the step (see Figure 2.28).

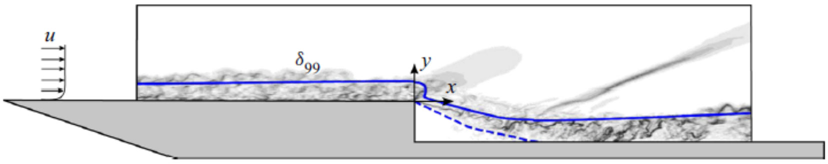

Figure 2.28: Illustrative representation of a BFS SWTBLI configuration. (Hu et al., 2021)

Due to its geometry, a BFS also generates an expansion fan that when interacting with the shocks will weaken them, promoting less severe adverse pressure gradients on the boundary layer. This expansion fan is also responsible for an increase in skin friction upstream of the step (Hu et al., 2021). Regarding pressure, an accentuated drop is present in the corner recirculation region, after which it increases again to its initial value (Hu et al., 2021). As also found in uncontrolled impinging configurations, Hu et al. (2021) reported that the small incoming vortical structures combine into larger coherent structures due to the shear layer instability (Figure 2.29). Hu et al. (2021) also reported similar Reynolds stress components distributions similar to those found by Pasquariello et al. (2017) and shown in Figure 2.19.

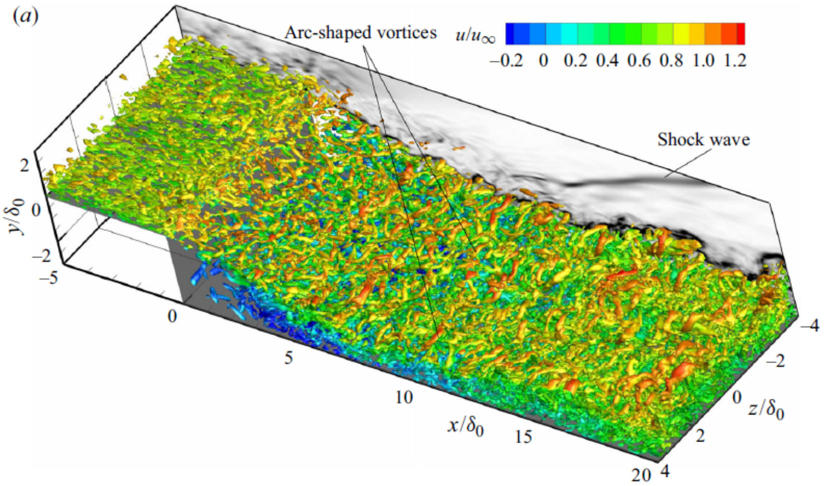

Figure 2.29: Illustrative representation of a BFS instantaneous vortical structures. (Hu et al., 2021)

Moreover, Hu et al. (2021) also observed the spanwise wrinkling of the shock and based on their DMD analysis the low-frequency motion of the shock is coupled with the streamwise-elongated structures that are the signature of Götler-like vortices. According to them, Götler-like vortices are the forcing sustaining the low-frequency motions of the shock and separation bubble. In their study, they found a strong correlation of the vortices with the upstream disturbances. Furthermore, they reported an overall increase in the Strouhal number range, being about 3 times larger than for canonical cases. They attributed this shift to the fixed separation point and confinement caused by the step wall.

The exact effect of the BFS on the flow depends on the flow conditions, but also on its geometry. As found by Li and Liu (2019) the deeper the step, the longer the recirculation region, the bigger the suppression of the mean pressure increase and the smaller the turbulence production in the vicinity of the interaction. The pressure loads, however, remain unaltered. Both step configurations used by Li and Liu (2019) had a height smaller than the boundary layer thickness.

Zhai et al. (2022) used a BFS to mitigate separation on a Mach 5 hypersonic inlet. They placed the step at the shock generator, to create two weak shocks instead of a single stronger one. Using this method they manage to decrease the extent of the recirculation region, with the separation point moving downstream and a fuller BL velocity profile downstream of the interaction. They concluded that having the BFS on the shock generator instead of on the flat plate can decrease the length, height and volume of the separation bubble by at least 60% using the correct parametrical settings for the dimensions and position of the BFS.

Micro vane / vortex generator

A different but related approach to steps is using micro vortex generators (MVGs) applied directly to the impinging surface. This technique has had multiple applications in both research and engineering applications (McCormick, 1993; B. Anderson et al., 2006; Babinsky et al., 2009; Titchener and Babinsky, 2013). These devices work by providing the incoming boundary layer with additional momentum due to the mixing promoted by the vortices generated. Two kinds of vortices are generated: streamwise and Kelvin-Helmholtz (K-H) vortices (see Figure 2.30).

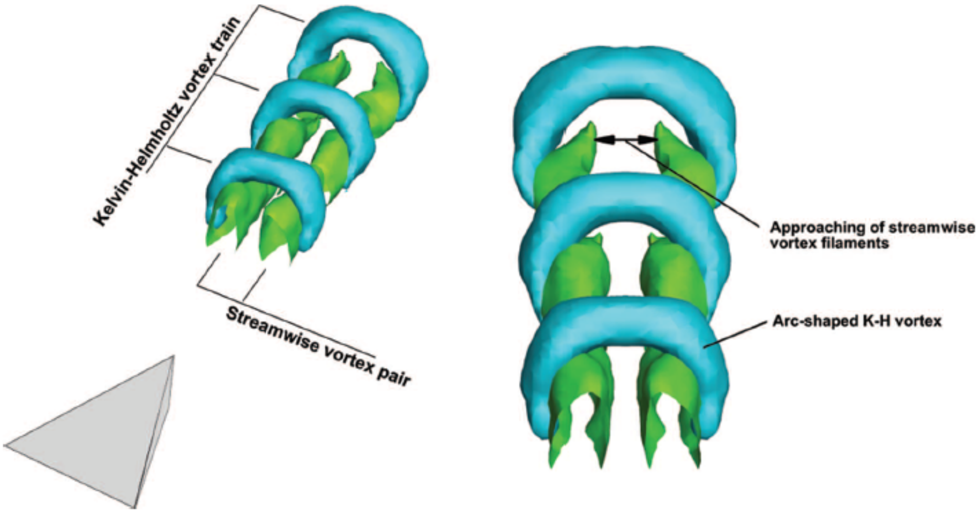

Figure 2.30: Streamwise and K-H vortices visible through vorticity iso-surfaces. (Z. Sun et al., 2012)

According to Y. Yan et al. (2012) the vortex rings are generated due to the inflection points in the shear layer, which contribute to the development of K-H instabilities (see Figure 2.31). The vortices then roll forming a vortex train that will interact with the SWTBLI (see Figure 2.32).

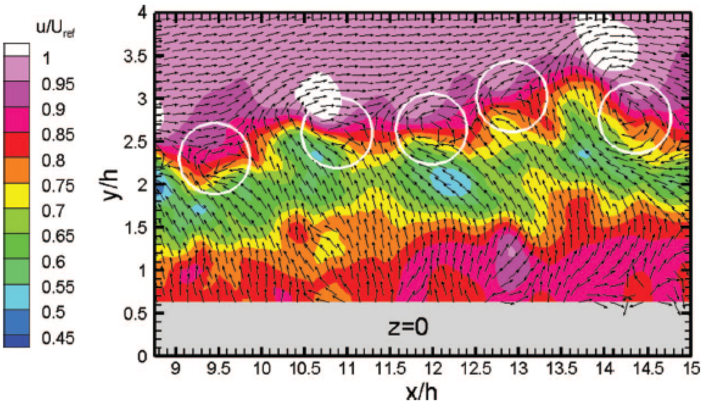

Figure 2.31: K-H vortices in the shear layer (indicated by white cycles). (Z. Sun et al., 2012)

As observed by Z. Sun et al. (2012) while moving downstream, the vortex system moves up in height at an approximately linear rate. Each vortex is accompanied by a momentum deficit (maximum slightly inside and above the position of the vortex core). Due to the local backward flow effect induced below the K-H vortices, the low-speed region develops into several packets. According to Z. Sun et al. (2012) the induced velocities result in a net positive lift force, responsible for the upward shift of the overall wake, which is encompassed by a circular shear layer.

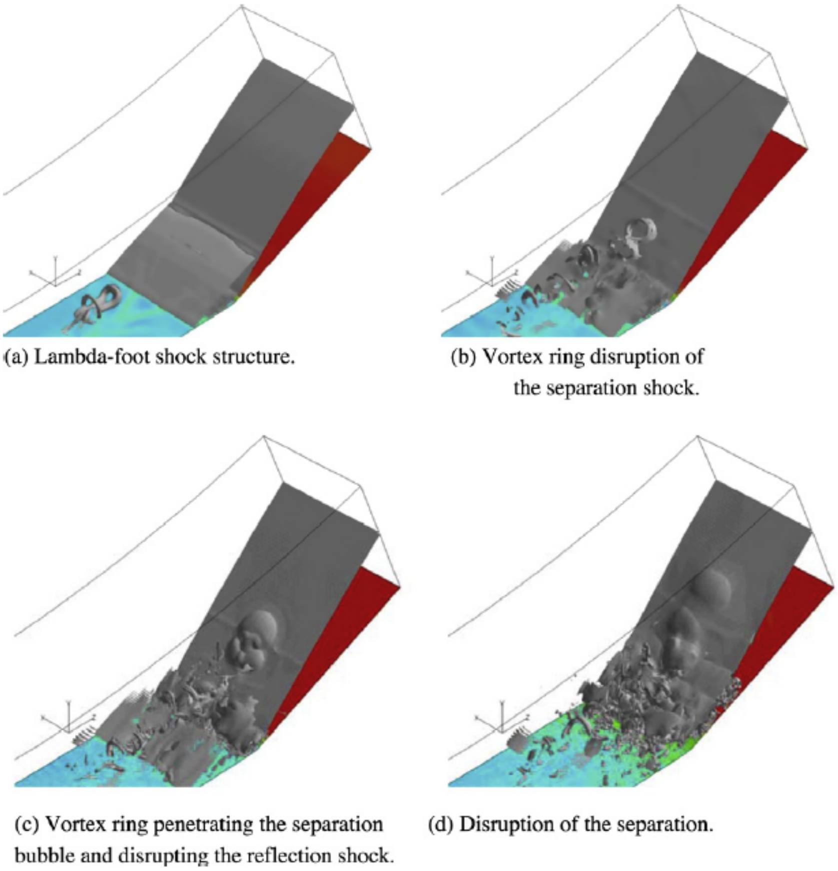
(a) Lambda-foot shock structure.

(b) Vortex ring disruption of the separation shock.

(c) Vortex ring penetrating the separation bubble and disrupting the reflection shock.

(d) Disruption of the separation.

Figure 2.32: Sequence of frames showing vortex ring interaction with the leading and rear legs of the lambda-foot shock. (Y. Yan et al., 2012)

The previously almost 2D flow, becomes highly three-dimensional as the vortices bring high-speed flow closer to the wall, reenergizing the boundary layer, while removing low-speed flow away from the wall. In this way, the boundary layer becomes more resistant to the adverse pressure gradients imposed by downstream geometries or shock interactions. The mean velocity suffers a decrease immediately downstream of the device's centerlines with a slight increase of the separation region in the same area, despite the overall decrease in separation length (Schreyer et al., 2021). Moreover, the turbulence is not very affected by the control method. Instead, a superposition is generally verified, with the enhanced mixing contributing to a faster boundary layer recovery to equilibrium conditions post-interaction (Schreyer et al., 2021).

Based on the results of Lee and Loth (2009) that showed that micro vanes have a better separation control in comparison with micro ramps, Martis and Misra (2013) compared the thick vanes (TVs) proposed by Lee and Loth (2009) with the more common MVGs (see Figure 2.33 for comparison). The advantage of thick vanes is that they have an easier implementation due to their more robust design when compared to thin vanes. In both cases, there is a better total pressure recovery on the sides of the devices than on their trailing edges. This is due to the wake that is generated at the trailing edge.

When implemented in arrays, the total pressure recovery is higher than for the uncontrolled case between different devices, due to the high-speed flow brought close to the wall by the counter-rotating vortices. Martis and Misra (2013) observed that the higher the device the stronger the generated vortices and the bigger the total pressure loss downstream of its trailing edge for both MVGs and TVs. Furthermore, the separation point also moves downstream with increasing height. The reattachment point, on the other hand, remained approximately in the same position.

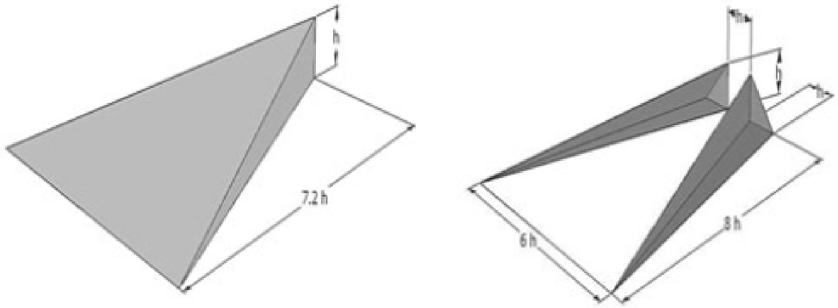

(a) BR (b) TV

Figure 2.33: Micro ramp/vane geometry. (Martis & Misra, 2013)

Martis and Misra (2013) concluded that for a given height MVGs have better performance regarding total pressure recovery, but TVs further delay separation. However, the MVG controlled interaction has a positive effect over a bigger streamwise extension of the interaction up to beyond reattachment. Moreover, they concluded that the interaction between vortices for devices smaller than $50\%\delta$ is detrimental to the individual intensity of each vortex, and more importantly, to the control efficiency. Despite this, an increase in height proved beneficial up until $70\%\delta$ when separation delay staganates.

Other Methods

Another common method for controlling SWTBLIs is flow injection. A lot of different configurations have been tested, most of them using continuous flow injection in the wall-normal direction. Souverein and Debiève (2010) tilted the injection angle to 45 ° (Figure 2.34) which contributed to the generation of counter-rotating vortices, similar to those generated using MVGs. The difference, however, is in the strength of the vortices. While using MVGs one gets a pair of symmetric vortices, in Souverein and Debiève (2010) application the vortices have different strengths. The overall result, nonetheless, is the same, with the mixing of outer high-momentum flow with the BL low-momentum fluid, which energises the BL resulting in a smaller separation bubble, as reported. Moreover, the frequency of the shock unsteadiness increased by about 50% (from $\approx$ 200 Hz to $\approx$ 300 Hz), with the separation-based Strouhal number only increasing by about 1% due to the reduction in the bubble size.

A method with similar results was employed by Holden and Babinsky (2005), who used streamwise slots in a Mach 1.5 engine intake (Figure 2.35). The slots also generate vortices that contribute to the increased resistance of the incoming boundary layer to adverse pressure gradients. They observed a transformation of the almost 2D bubble configuration to a highly 3D distribution of attached and separated regions. A better total pressure recovery was achieved.

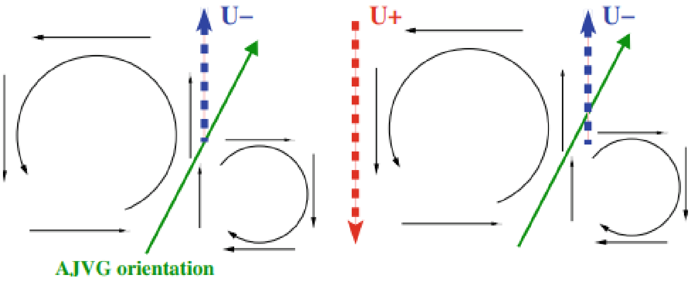

Figure 2.34: Schematic representation of the longitudinal vortices generated by the air jet vortex generators, viewed in the upstream direction. The green arrow represents the jet. (Souverein & Debiève, 2010)

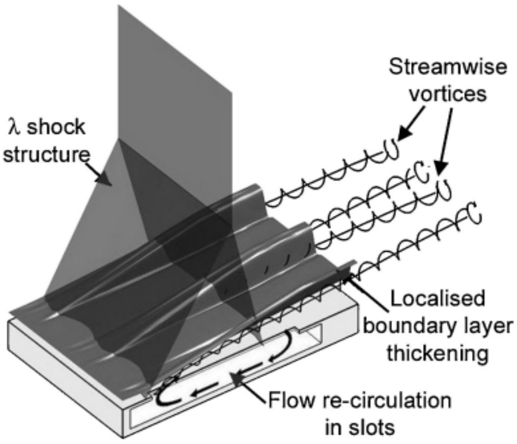

Figure 2.35: Structure of a shock–boundary layer interaction controlled by streamwise slots. (Holden & Babinsky, 2005)

A last method worth mentioning is the plasma actuator (Narayanaswamy et al., 2012; Q. Sun et al., 2014; Kinefuchi et al., 2016; Wang et al., 2022). Wang et al. (2022) employed this method as a discharge generated between two poles on the surface of the interaction. This discharge generates vortices that, by augmented mixing will help the boundary layer withstand the imposed pressure gradient. Wang et al. (2022) studied the effect of this method for an hypersonic compression ramp using different discharge frequencies. They concluded that the control effectiveness correlates with the scale of the energetic eddies. The separation region was reduced particularly for the lower frequency range testes ($\approx 10 - 20\,\text{kHz}$). Experimental work from Q. Sun et al. (2014) found an enlargement of the separation region, despite the downstream displacement of the separation. This enlargement was also verified by Kinefuchi et al. (2016) due to heat generation caused by the discharge in a Mach 2.8 impinging shock flow. On the other hand, the additional vorticity created with the discharge is beneficial for the control.

Narayanaswamy et al. (2012) used plasma jets instead. They observed that using a pulse at $St_{L_{sep}} \approx 0.04 (f = 2\,\text{kHz})$, the separation shock responded with a rapid upstream motion followed by a gradual downstream recovery motion. Furthermore, its unsteadiness was locked to the pulsing frequency of the actuator. They found a 30% decrease in the magnitude of the pressure fluctuations in the low-frequency band. When the injection was from inside the separation bubble there was no noticeable effect, contrary to what was observed when the injection happened upstream.

This method is relatively recent and as shown in the brief discussion above the results show a great variance in terms of control effectiveness, depending mostly on the positioning and frequency of the discharges.

In sum, the exact mechanism driving low-frequency unsteadiness is still not yet fully understood. While upstream mechanisms are still regarded as plausible causes for the low-frequency unsteadiness, convincing evidence has been found more recently that strongly points to a downstream-led mechanism driving the unsteady behaviour of SWTBLIs. Global instability, on the other hand, lacks more evidence to be considered, for now, as a potential driving mechanism. Moreover, just as the exact cause for the unsteadiness is still not fully understood, the way the driving mechanism operates is also still yet to determine. Regarding the different control methods discussed in the literature, so far, it has not been found a method that successfully mitigates the two main detrimental phenomena in SWTBLIs: flow separation and low-frequency unsteadiness. While some of them can reduce separation they fail in preventing unsteadiness and vice-versa. Additional studies are required to identify the control method that will ultimately contribute to solving this increasingly prevalent problem.

CHAPTER 3

Methodology

In this chapter the setups used for the two studied cases are presented. Section 3.1 presents the flow modeling and governing equations, the computational domain, and boundary conditions. Section 3.2 discusses the grid and its adequacy to solving the flow. Section 3.3 presents the numerical method used and Section 3.4 highlights the differences between the reference and the study case setups.

3.1 Flow Configuration

The interaction of an impinging oblique shock wave with an incoming turbulent boundary layer is studied for two different configurations: a flat plate and a perforated wall with a resonant cavity underneath. The isolated flat plate case is simulated as the reference case $\mathcal{F}$ with which the study case $\mathcal{P}$ (cavity - Section 3.4) will be compared. The reference case, $\mathcal{F}$, is similar to the moderate Reynolds number case studied by Laguarda et al. (2024b).

3.1.1 Flow Modelling & Governing Equations

To model the flow the three-dimensional compressible Navier-Stokes equations are used in the conservative form. Equation 3.1, Equation 3.2 and Equation 3.3 represent mass, momentum and energy conservation, respectively:

$$\frac{\partial \rho}{\partial t} + \frac{\partial}{\partial x_i}\left(\rho u_i\right) = 0, \tag{3.1}$$

$$\frac{\partial \rho u_j}{\partial t} + \frac{\partial}{\partial x_i}\left(\rho u_i u_j + \delta_{ij} p - \tau_{ij}\right) = 0, \tag{3.2}$$

$$\frac{\partial \rho E}{\partial t} + \frac{\partial}{\partial x_i}\left(u_i \rho E + u_i p - u_j \tau_{ij} + q_i\right) = 0, \tag{3.3}$$

where p is pressure, ρ is density, u_i is the i^{th} velocity component and E is the total energy defined as

$$\rho E = \frac{p}{\gamma - 1} + \frac{1}{2}\rho u_i u_j. \tag{3.4}$$

Air in supersonic conditions is a Newtonian fluid. Stokes hypothesis is assumed for the viscous stress tensor, τ_{ij},

$$\tau_{ij} = \mu \left(\frac{\partial u_i}{\partial x_j} + \frac{\partial u_j}{\partial x_i} - \frac{2}{3} \delta_{ij} \frac{\partial u_k}{\partial x_k} \right), \tag{3.5}$$

with the dynamic viscosity μ given by the 0.7 Power Law

$$\mu = \mu_{ref} \left(\frac{T}{T_{ref}} \right)^{0.7}, \tag{3.6}$$

where μ_{ref} and T_{ref} are the freestream dynamic viscosity and static temperature, respectively.

The Fourier Law is used for the heat flux determination as

$$q_i = -\kappa \frac{\partial T}{\partial x_i}, \tag{3.7}$$

with the thermal conductivity κ given by

$$\kappa = \frac{\gamma R}{(\gamma - 1) Pr} \mu. \tag{3.8}$$

Both μ and κ are assumed to only depend on the static temperature T. Likewise, the Prandtl number is assumed to be constant $Pr = 0.72$. Lastly, the fluid is assumed to behave as a perfect gas with the specific heat ratio of $\gamma = 1.4$ and a specific gas constant $R = 287.05\,\mathrm{J/(kg \cdot K)}$ following the ideal-gas equation

$$p = \rho R T. \tag{3.9}$$

3.1.2 Computational Domain

The computational domain used for case $\mathcal{F}$ is shown in Figure 3.1. Note that δ_∞ represents the inflow boundary layer thickness, defined based on 99% of the freestream velocity. The domain size was based on the work of Laguarda et al. (2024b) that made a domain sensitivity study, where they concluded that a span of $4\delta_\infty$ was enough to ensure that no confinement effects would influence the results. In other words, turbulent fluctuations are sufficiently decorrelated over the domain half-width for $L_z \geq 4\delta_\infty$.

Based on their study, the dimensions of $L_x, L_y, L_z = [45, 16.5, 6]\delta_\infty$ were used. Every dimension is the same as the ones used by Laguarda et al. (2024b), except the spanwise dimension which was increased by $2\delta_\infty$ to become $6\delta_\infty$. Notice that the streamwise extension of the domain was chosen to ensure enough space for the development and stabilisation of the incoming boundary layer (generated artificially). In the same way, the wall-normal extension was set to prevent the reflection of the reflected shock on the top boundary from interfering with the boundary layer after the interaction. A deeper discussion on these choices is introduced by Laguarda et al. (2024b).

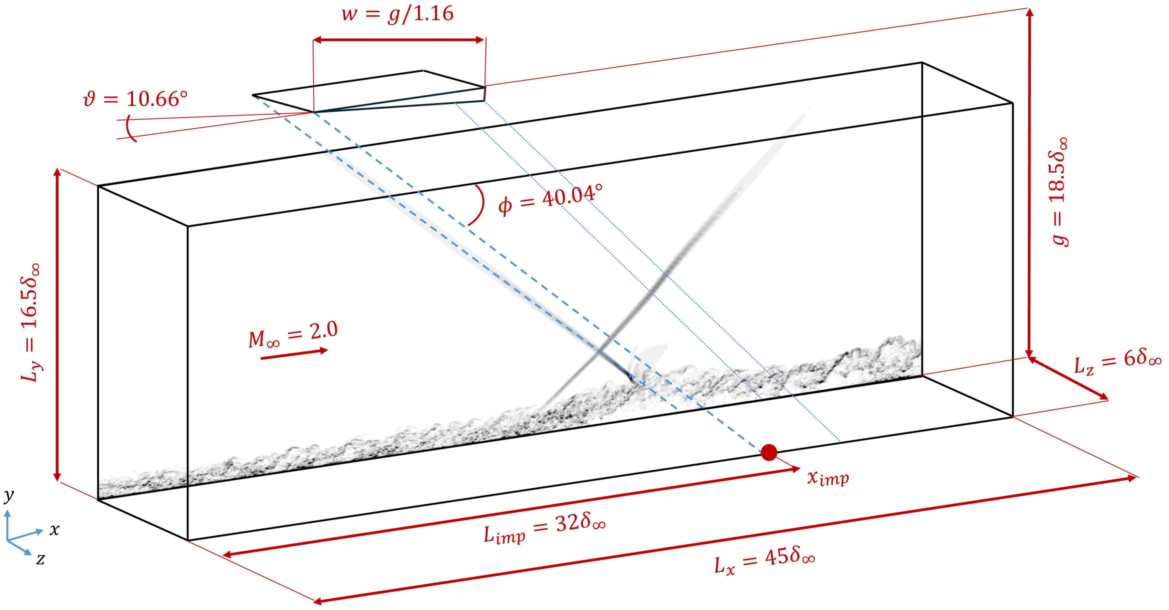

Figure 3.1: Schematics of the computational domain dimensions. (- - -) shock wave, (······) expansion fan.

A virtual shock generator is used, but it is located outside of the computational domain at a distance $g = 18.5\delta_\infty$ from the wall (see Figure 3.1). Its hypotenuse has a length $w = g/1.16$ and deflects the flow by an angle, ϑ, of 10.66°. The resulting shock angles at $\phi = 40.04°$, meaning that the virtual (inviscid) impingement point is located approximately $32\delta_\infty$ downstream of the inflow plane.

3.1.3 Boundary Conditions

The freestream conditions are the same for all the cases and can be consulted in Table 3.1.

Table 3.1: Constant parameters at the inflow plane

u_∞ [m/s]	ρ_∞ [μg/mm^3]	T_∞ [K]	M_∞	$Re_{\delta_\infty,i}$	$Re_{\tau,i}$	$\delta_{\infty,i}$ [mm]
507	0.9886	160.15	2.0	50.1×10^3	950	5.2

The wall was set as adiabatic, i.e., $\dot{q}_w = 0$. The inflow boundary condition was set using the digital filter technique (Xie & Castro, 2008) to generate the required turbulent boundary conditions with the correct time and space statistical correlations. The implementation of this method is detailed in the work of Laguarda et al. (2024a). On the top boundary, the incident shock and the expansion fan were introduced over a range of computational cells using the Rankine-Hugoniot relations and the Prandtl-Meyer theory. Furthermore, at the top and outflow boundaries, non-reflecting boundary conditions based on the Riemann invariants were used (Poinsot & Lelef, 1992). Finally, periodic boundary conditions were used in the spanwise direction.

3.2 Grid Distribution

A structured grid was used. It was divided into blocks as shown in Figure 3.2. Each block has the same number of elements, despite their different dimensions. This was achieved through linear stretching in the wall-normal direction and coarsening in the stream- and spanwise directions. The coarsening was applied only for the blocks above the shocks crossing height, to ensure that the interaction was well resolved within the desired plus units ranges.

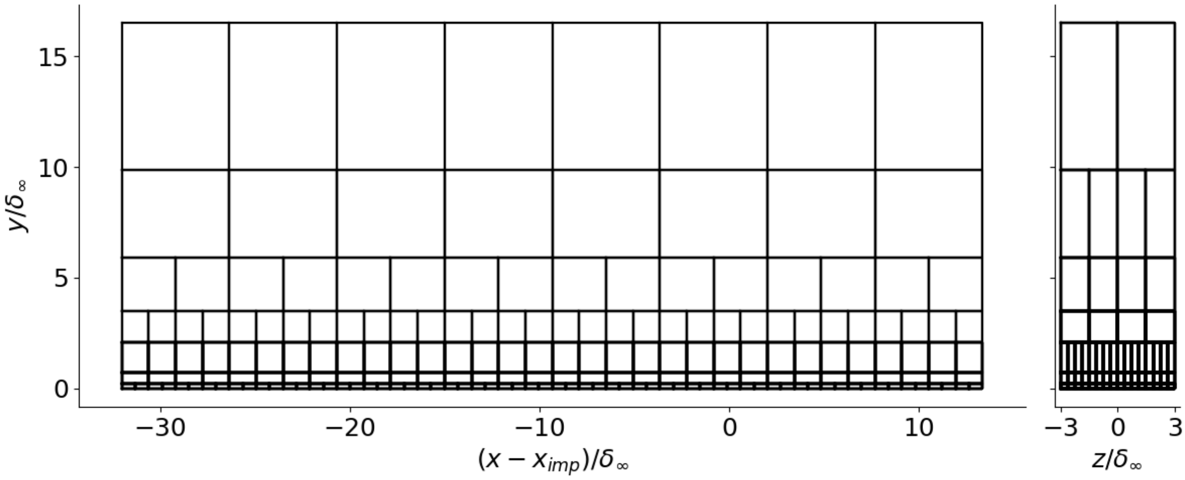

Figure 3.2: Block distribution of the numerical grid.

The adequacy of the elements' sizes was assumed based on the grid sensitivity study carried out by Laguarda et al. (2024b) on a similar grid. Table 3.2 shows the resulting grid parameters. The plus units were computed based on two different values for the viscous length: the time- and span-averaged mean and minimum value along the wall centerline. To ensure that turbulent structures are well-captured, one must aim to plus units grid variations of about $\Delta x^+_{min} \times \Delta y^+_{min} \times \Delta z^+_{min} \lesssim [30, 1, 10]$, being Δy^+_{min} the most critical parameter. As observed in Table 3.2 for $\mathcal{F}$ only in the worst case scenario of using l^+_{min}, Δx^+_{min} shows a much bigger value than desired, but still within the expected order of magnitude. This observation has no significant impact on the results. If the mean inner scale is used, $\langle l^+ \rangle$, all grid spacings fall inside the desired range. The same conclusions could be drawn by using the data from case $\mathcal{P}$.

Table 3.2: Grid parameters based on reference case data.

	$\langle l^+ \rangle_{\mathcal{F}} = 0.01045$	$l^+_{min,\mathcal{F}} = 0.00443$
$N_x^{max} \times N_y \times N_z^{max}$	$\Delta x^+_{min} \times \Delta y^+_{min} \times \Delta z^+_{min}$	$\Delta x^+_{min} \times \Delta y^+_{min} \times \Delta z^+_{min}$
$1088 \times 240 \times 576$	$20 \times 0.45 \times 5.2$	$49.0 \times 1.1 \times 12.2$

An analysis done for the $\langle y^+ \rangle$ value across the domain revealed that in both cases $\langle y^+ \rangle$ slightly exceeds 1 close to the outflow due to the increase in shear stress caused by the effect of the expansion wave, as will be explained in Chapter 4. The results, however, are considered unaffected, since the increase above 1 is minimal and it only happens downstream of the interaction. This means that the mesh is capable of accurately capturing the desired turbulent structures and flow physics, that are spatially well-resolved, validating the mesh used. The plot from which these conclusions were drawn can be find in Appendix B.

3.3 Numerical Method

The simulations were performed in TUDelft's supercomputer DelftBlue ((DHPC), 2024) using the in-house solver INCA (https://www.inca-cfd.com). The solver uses the adaptive local deconvolution method (ALDM) to perform implicit LES (Hickel et al., 2014). This numerical method has successfully been applied to a variety of flow configurations and geometries, particularly to different SWTBLI cases (Grilli et al., 2013; Pasquariello et al., 2017; Laguarda et al., 2024b).

The ALDM is a non-linear finite volume method used in the discretisation of convective fluxes. It provides a physically consistent subgrid scale (SGS) model. Its advantages are related to its capability to capture shock waves while avoiding excessive numerical dissipation for the propagation of turbulence and smooth waves. Unresolved turbulence and shock waves are usually associated with different optimal SGS models. However, in the ADLM the model parameters are controlled based on a shock sensor, allowing a good performance in modelling both phenomena, which results in a non-oscillatory solution at strong discontinuities.

The Courant-Friedrichs-Lewy (CFL) number was set to CFL ≤ 1 everywhere in the domain, for the entire simulation time, which ensures numerical stability. For time integration, the third-order total variation diminishing Runge-Kutta scheme (Gottlieb & Shu, 1998) was employed. Linear second-order schemes were used to compute gradients in the viscous flux tensor.

For the reference case, the initialisation of the domain was based on the inviscid shock reflection solution. Data extraction began after an initial transient of ≈ 15 flow-through times (FTT). This time is determined based on the total streamwise length of the domain and the freestream velocity. The total simulation time, including the transient was ≈ 90 FTTs. For case $\mathcal{F}$, 3D snapshots of the interaction region were collected every $\Delta t \approx 2\delta_{\infty}/u_{\infty}$. Additionally, time- and span-averaged statistics were computed based on data extracted at a sampling rate of $\Delta t \approx 0.02\delta_{\infty}/u_{\infty}$.

3.4 Perforated Wall / Cavity - Study Case ($\mathcal{P}$)

In this section only the differences between the reference ($\mathcal{F}$) and the study ($\mathcal{P}$) cases will be highlighted. Hence, the reader can assume that anything that is not mentioned in this section was made exactly the same as for the reference case.

For the study case $\mathcal{P}$, perforations were added to the wall and a cavity was placed underneath them, within the interaction region. The intended goals of adding the cavity were two: the first was to try to re-energise the boundary layer by creating a suction-blowing mechanism driven by the pressure gradient created by the shock structure above the wall; the second was to dissipate the SWTBLI characteristic low-frequency energy, by creating a Helmholtz resonator (inspired by the mechanism already applied in modern acoustic liners).

The mesh used for the simulations was the same as for the reference case. However, an addition was made in the bottom part (blue cells in Figure 3.3) by mirroring the cells highlighted in red in Figure 3.3.

The schematic in Figure 3.4 shows the 3D geometry used in the simulation, along with its dimensions. As represented in Figure 3.4 the geometry is bigger in every dimension than the grid (see legend). This is to make sure that the ghost cells used in the computation do not cross the geometry limits, which would lead to the calculation of incorrect fluxes between the inside and outside cells, resulting in unphysical solutions. For this reason, care was taken to ensure that the additional cells fully enclosed the cavity in stream- and wall-normal directions. In span, periodic boundary conditions were kept for every boundary.

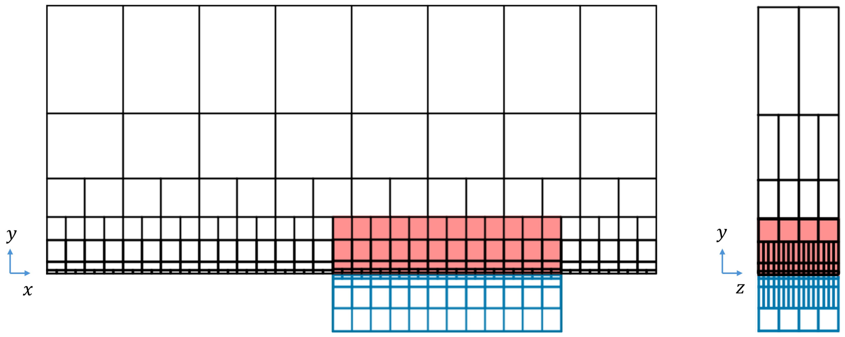

Figure 3.3: Representation of the grid used for case $\mathcal{P}$. In blue, added cells. In red, mirrored cells.

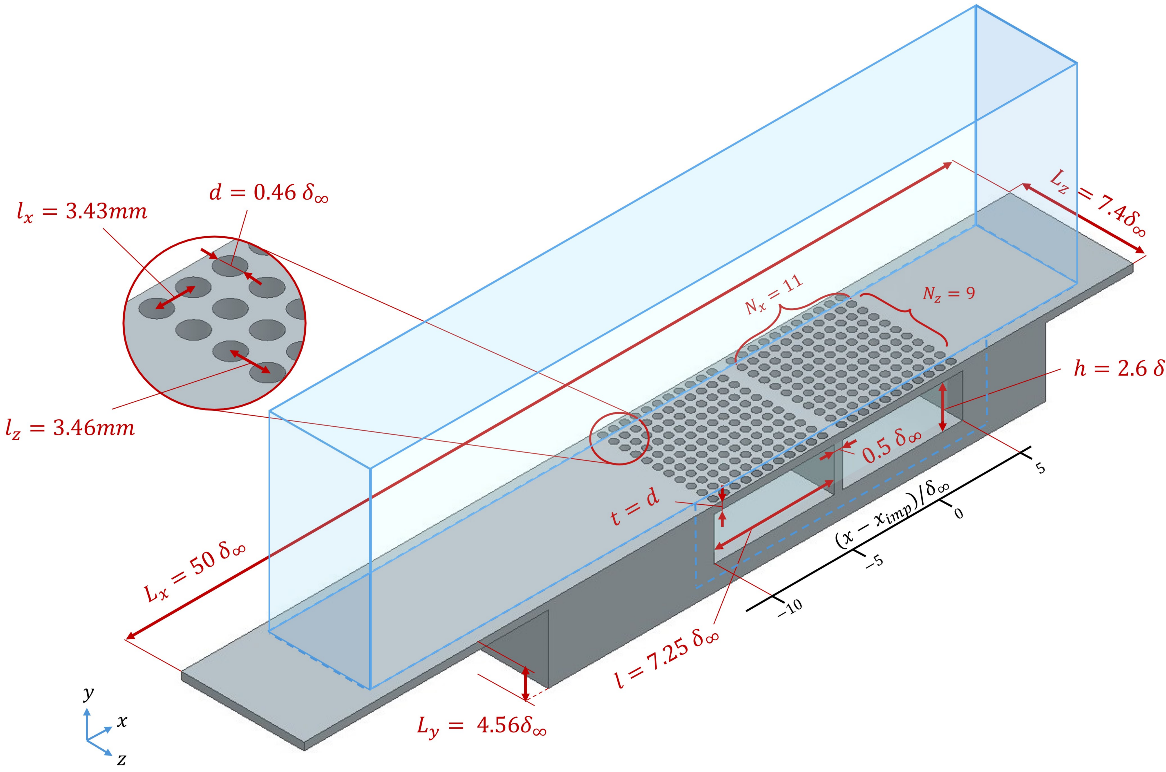

Figure 3.4: Schematics of the perforated wall with the added cavity. The blue box represents the grid boundaries (not to scale). (- - -) blueprint of the grid.

The dimensions and position of the cavity and its holes were determined based on the desired resonant frequency inside the Helmholtz resonator (the cavity). The cavity was placed within the interaction region between $-10 \leq (x - x_{imp})/\delta_\infty \leq 5$. Based on the visual inspection of the mean span-averaged wall pressure, the upstream and downstream ranges of influence of the interaction were determined, which set these values as the ones used for the streamwise location and range of the cavity.

A Helmholtz resonator has two components: the neck and the cavity. The oscillating air in the neck makes the air in the cavity resonate at a natural resonant frequency. Resonator geometry highly impacts this frequency, mainly the volume and the mass of air in the neck. Also, the orifice dimensions are important. On the other hand, orifice shape is not highly significant as long as the largest orifice dimension is much less than the resonance wavelength (Chanaud, 1994). Based on this assumption, circular holes were chosen.

The analytical model developed by Langfeldt et al. (2019) for the resonant frequency inside a multi-neck resonator was used as presented in Equation 3.10. Note that this model assumes constant pressure inside the cavity, which is a strong assumption for the SWTBLI case. The resonant frequency inside the cavity can be computed as

$$f = \frac{a_\infty}{2\pi}\sqrt{\frac{\rho_\infty}{V}\sum_{i=1}^{N}\frac{S_i}{m_i}}, \tag{3.10}$$

a_∞ and ρ_∞ being the freestream speed of sound and air density, V the cavity volume, S_i the cross-sectional area of each neck (hole) and m_i the mass of air inside the i^{th} neck. The mass of air in each neck, m_i, was computed with the expression presented by Fedotov et al. (2018), who developed an end correction coefficient (α) expression to account for the inertia of the air around the orifices:

$$m_i = \rho_\infty\left(t_i + \alpha_i\frac{d_i}{2}\right), \tag{3.11}$$

with l_i the length of each neck (the thickness of the wall), d_i the diameter of each orifice (hole) and α_i the end correction coefficient, which is given by:

$$\alpha(t,d) = 1.821 + 3.338te^{-3.132\frac{d}{2}} - 0.1487\frac{d}{2}, \tag{3.12}$$

according to Fedotov et al. (2018) expression.

The initial extension of the cavity was $15\delta_\infty$. However, Equation 3.10 is more accurate for cavities with a length-to-width ratio close to one, $l/w \approx 1$. Since the width of the cavity, w, (in span) is determined by the width of the grid, $6\delta_\infty$, the initial cavity was divided into two cavities, each with an extension of $l = 7.25\delta_\infty$ and divided by a wall of $0.5\delta_\infty$ thickness. This division not only ensures better accuracy in the resonant frequency obtained but also contributes to a more even pressure throughout each cavity since the individual streamwise pressure gradient imposed by the shock system on each cavity is lower.

With the above-mentioned parameters fixed, the only remaining parameters that can vary are the holes diameter, d, the cavity depth, h, the number of holes, n, in each cavity, $n = N_x \times N_z$ and the thickness of the wall, t, since V, m and S are dependent on them. The number of holes in each direction was chosen freely to $N_x, N_z = [11, 9]$. The holes were then placed evenly spaced in both directions.

The other parameters were computed by solving the following optimization problem, set to obtain a separation length-based Strouhal number inside the cavity of $St_{L_{sep}} = 0.03$:

$$\begin{aligned}
&\boldsymbol{x} = [d, h, t],\\
&St_{L_{sep}}(\boldsymbol{x}) = \frac{a_\infty}{2\pi}\sqrt{\frac{1}{lwh}\frac{n\pi\frac{d^2}{4}}{n\left(t+\alpha\frac{d}{2}\right)}\frac{L_{sep}}{u_\infty}},\\
\min_{\boldsymbol{x}}\quad &0.99 \times |St_{L_{sep}}(\boldsymbol{x}) - 0.03| + 0.01 \times |d - t|,\\
&\boldsymbol{x} \in \mathbb{R}^3,\\
&[0.42, 0.1, 0.05]\delta_\infty \leq \boldsymbol{x} \leq [0.5, 3.5, 1]\delta_\infty.
\end{aligned} \tag{3.13}$$

Following the work of Shahzad et al. (2024) for acoustic liners, the thickness of the plate was set to be as close as possible to the diameter of the holes. This is reflected in the objective of the optimisation where a weighting of the Strouhal number accuracy and the difference between the holes diameter and the plate thickness was set.

Moreover, lower and upper bounds were prescribed to guarantee enough cells inside each perforation, so that the flow inside the holes is resolved well enough. Hence, a minimum of 10 cells in each direction is ensured with the defined bounds ($\approx$ 10 cells in x and $\approx$ 40 cells in z).

The result of the optimisation can be seen in Figure 3.5, where the design space for the optimum cavity depth is shown. The optimum found was $[d, h, t] = [0.46, 2.6, 0.46]\delta_\infty$.

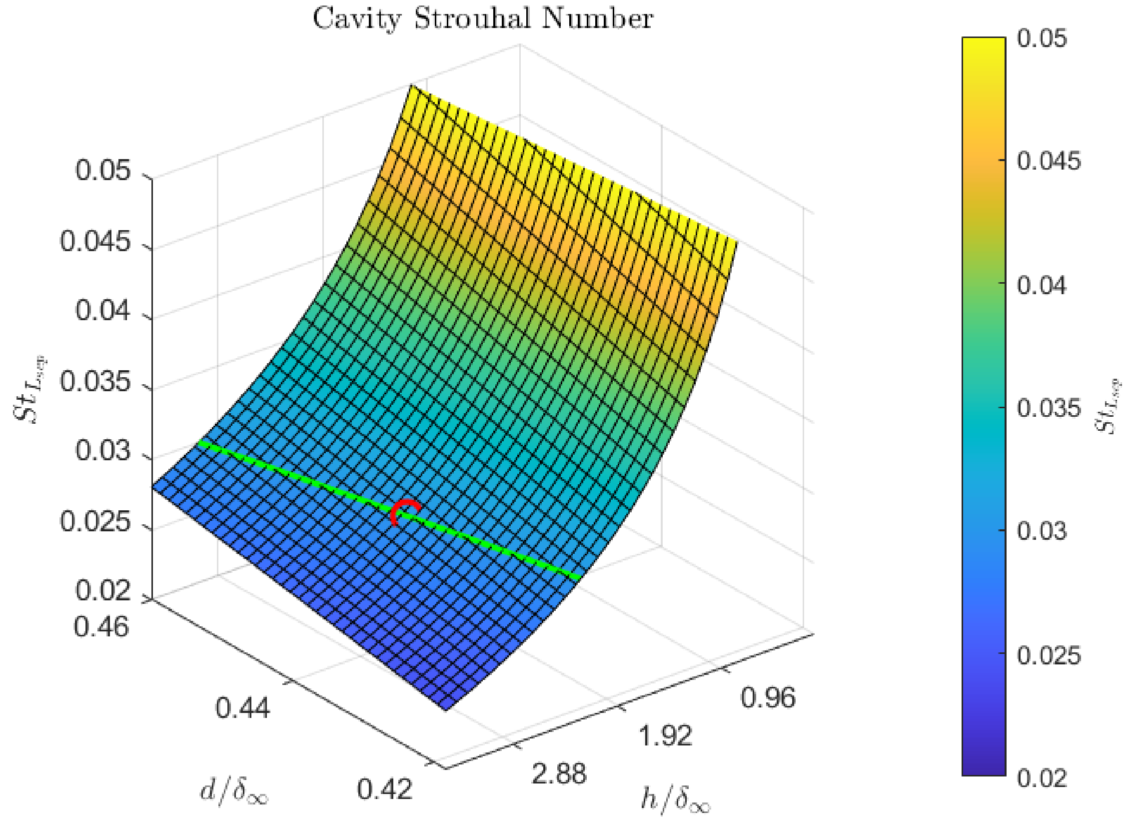

Figure 3.5: Optimisation space for the resonant frequency inside the cavity, based on $St_{L_{sep}}$. Approximate feasible space ($St_{L_{sep}} = 0.03$) for optimum t/δ_∞ in green (t is the wall thickness). Optimum in red.

Lastly, some differences were also implemented in the initialisation of case $\mathcal{P}$. Inside the cavity, velocity was set to zero. The simulation was started without the impinging shock, giving enough time for the flow to stabilise over the holes and cavities, after which the shock was introduced in the domain. The total integration time for the perforated wall case was $\approx$ 20 ms, which is about 40 FTTs.

CHAPTER 4

Results

In this chapter the results are presented. The isolated boundary layer is characterized in Section 4.1. Next, the two studied configurations are compared in terms of mean and instantaneous flow, Reynolds stresses and reverse flow region and wall properties in Section 4.2. Lastly, the unsteadiness is discussed in Section 4.3.

4.1 Boundary Layer Characterisation

In order to ensure that the STBLI results are correct and to further be able to determine the impact of the shock structure in the boundary layer, a characterisation of the isolated boundary layer was made. Figure 4.1 shows both the velocity profile and the Reynolds stress tensor components at the virtual impingement point, x_{imp}. This point was chosen since it is the point that for both numerical and, in particular, experimental results is more accessible for monitorisation. Figure 4.1 presents the time- and span-averaged boundary layer velocity profile and Reynolds stress components at the virtual impingement point. DNS data from Pirozzoli and Bernardini (2011) for a Mach 2 flow at a friction Reynolds number, $Re_\tau = 1110$ is used for comparison of the results.

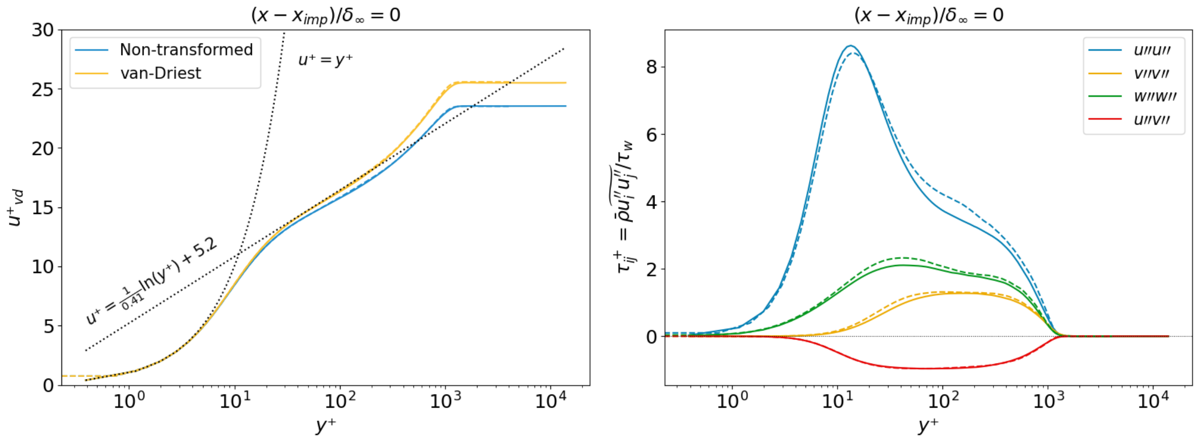

Figure 4.1: (a) Time- and span-wise averaged streamwise velocity profile and (b) density-scaled Reynolds stresses at $x = x_{imp}$. (- - -) DNS data from Pirozzoli and Bernardini (2011) at $M = 2$ and $Re_\tau = 1110$.

The velocity profile was transformed using the van-Driest transformation based on the density variation in the wall-normal direction ($u^+_{vd} = \int_0^{u^+} \left(\frac{\bar{\rho}}{\rho_w}\right)^{1/2} du^+$, as introduced in Subsection 2.1.5).

This allows a direct comparison with incompressible flows and more importantly with the 'universal' law of the wall (Subsection 2.1.1). Note that, as stated by Trettel and Larsson (2016), the van-Driest transformation is more effective for adiabatic wall TBLs, which further strengthens the comparison. As seen in the plot, the profile follows the linear relation between u^+ and y^+ perfectly for the inner viscous sub-layer, before transitioning, at the buffer layer to a logarithmic relation extending over the range $y^+ \approx 200 - 300$. Further away from the wall, the wake region becomes evident by the 'detachment' of the velocity profile from the logarithmic relation and the free stream velocity is reached. The agreement with the reference DNS data is very good for all the regions composing the boundary layer.

The Reynolds stress components were computed using Favre-averaging, which takes into account compressibility effects in the form of density variations. Once again the profiles obtained at the virtual impingement point are as expected for high-speed compressible turbulent boundary layers. Note that all of them start at zero, due to the non-slip boundary condition that ensures zero velocity at the wall and consequently, no fluctuations. Likewise, they also tend to zero away from the wall where freestream flow is reached. As a general trend, all of the components show a good agreement with the reference DNS data, with the cross-flow component showing particularly good agreement.

The streamwise component, $\widetilde{u''u''}$, displays the highest magnitude, reaching a peak of ≈ 8 at $y^+ \approx 10 - 11$, which coincides with the wall distance at which the production of turbulent kinetic energy is higher. For the wall-normal component, $\widetilde{v''v''}$, it is the component that grows the least among the 3 principal components and it is also the one which starts developing further away from the wall. The spanwise component, $\widetilde{w''w''}$ reaches a normalised peak of about 2, starting to develop right after $\widetilde{u''u''}$. Lastly, the cross-term component, $\widetilde{u''v''}$ is the only one represented that is negative. This fact is related to the production of turbulent kinetic energy, which for a turbulent boundary layer is proportional to this component ($P_k \propto -\widetilde{u''v''}$). Before the peak of production is reached at $y^+ \approx 11$, the cross-term component stars increasing in absolute value, feeding the streamwise component, that is then redistributed to the remaining terms throught the velocity-pressure difusion terms in the turbulent kinetic energy equation (Schlichting & Gersten, 2017).

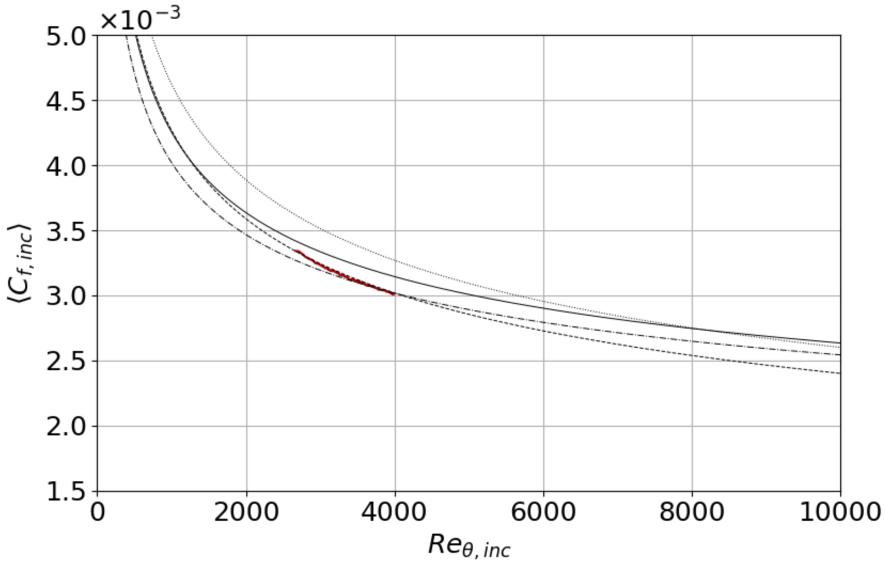

Figure 4.2: van-Driest II transformed incompressible skin-friction coefficient as a function of $Re_{\theta,i}$. (——) present data. (——) Kármán-Schoenherr, as presented by Shahab et al. (2011). (- - -) Smits (Smits et al., 1983). (······) Blasius and Kármán Schoenherr, as presented by Hadjadj et al. (2015). (-·-·) Rotta (Nishioka, 2009).

Additionally, the incompressible equivalent skin-friction coefficient ($C_{f,inc}$) evolution along the wall is plotted against the incompressible momentum-thickness based Reynolds number, Re_θ, in Figure 4.2. The van-Driest II transformation (van Driest, 1956) was used with the formulation presented by Hadjadj et al. (2015). As can be seen in the plot, the curve follows Smits relation (Smits et al., 1983) almost perfectly, showing an excellent agreement also with Rotta's relation (Nishioka, 2009) for higher Reynolds numbers. As expected the converge with Blasius relation is the worst since this relation is best suited for incompressible flows.

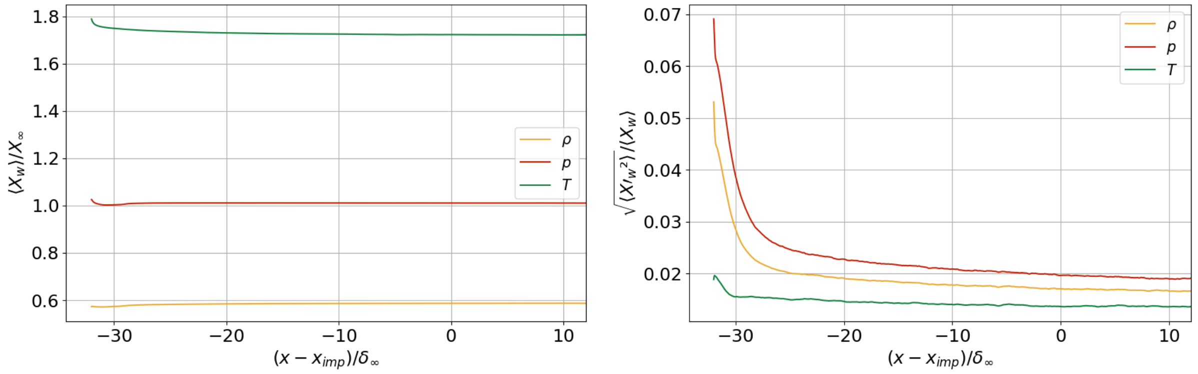

(a) Mean.

(b) RMS.

Figure 4.3: Span- and time-averaged thermodynamic properties at the wall for the undisturbed boundary layer.

The mean thermodynamic properties along the wall are shown in Figure 4.3a. They all display an initial gradient that spans for less than $10\delta_\infty$ into the domain. These gradients are particularly visible in the pressure and density plots. The mean pressure remains approximately constant throughout the entire domain. In the same way, density and temperature show small variations, while monotonically increasing and decreasing, respectively, throughout the domain.

For completeness, the rms (root mean squared) of the same quantities is presented in Figure 4.3b. All the properties present fluctuations in the same order of magnitude (10^{-2}), with the pressure fluctuations being the largest. In the same way, all of the the fluctuations asymptotically decrease to a stable value. The RMS of the temperature is the one with the smallest variation in value, before reaching the asymptotic value.

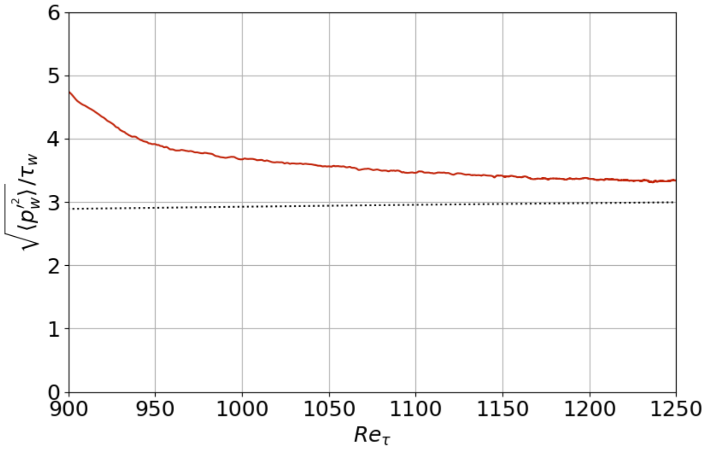

Figure 4.4: Inner-scaled RMS pressure. (⋯⋯) Semi-empirical correlation by Farabee and Casarella (1991)

Additionally, to further verify the validity of the generated boundary layer, the RMS pressure is non-dimensionalised by the wall shear stress and plotted against the friction Reynolds number. This inner-scaling allows a direct comparison with the semi-empirical correlation of Farabee and Casarella (1991) given by $\langle {p_w'}^2 \rangle / \tau_w^2 = 6.5 + 1.8 \ln \left(Re_\tau / 333 \right)$.

As shown in the Figure 4.4 the pressure fluctuations are higher than the ones predicted by Farabee and Casarella (1991) correlation, due to the artificial oscillations induced by the digital filter inflow condition (Laguarda et al., 2024a). Nonetheless, the inner scaled RMS pressure asymptotically converges to the reference correlation within the computational domain.

4.2 SWTBLI Configuration

Having characterised the boundary layer, the results for the interaction between the boundary layer and the shock wave are presented for both the reference and the controlled cases. The line legend and the symbology used to represent the mean separation and reattachment points adopted for each case for the remainder of this chapter can be found in Table 4.1.

Table 4.1: Line Legend for plots in Chapter 4

	Line legend	Mean Separation Point	Mean Reattachment Point
Case $\mathcal{F}$ (reference)	—	$S^{\mathcal{F}}$	$R^{\mathcal{F}}$
Case $\mathcal{P}$ (controlled)	- - -	$S^{\mathcal{P}}$	$R^{\mathcal{P}}$

4.2.1 Instantaneous Flow

Isosurfaces of the swirling strenght criterion are shown in Figure 4.6 coloured by the local streamwise velocity. In the same plot, Schlieren visualisations are shown in both the background and the outflow of the reduced domain considered. For case $\mathcal{P}$ an additional isosurface of wall distance $= 0$ is included.

Before analyzing the turbulence content of each configuration a description of a SWTBLI is presented. By taking Subsection 4.2.1 as a reference, one can understand the structure of a SWTBLI. The incoming turbulent boundary layer faces an adverse pressure gradient imposed by the impinging shock. For the friction Reynolds number considered this adverse pressure gradient is strong enough to cause flow separation. The reverse flow region is characterized by a bubble, in which it is 'contained'. The division of separated and non-separated flow is made by the shear layer that detaches from the wall near the separation point. The upstream flow that was first going parallel to the wall can no longer follow that path. Instead, it must go around the bubble.

At the bubble apex, the flow is accelerated and turned inwards against the wall by an expansion fan, which results from the reflection of the transmitted shock on the detached shear layer. As the shear layer reattaches, a compression fan is formed instead of a fully coalesced shock due to the mild curvature of the streamlines in that region. For the perforated wall case, the more aggressive turning of the flow at reattachment, is still not enough to result in a coalesced shock.

Using the swirling strength isosurfaces one can visualise the turbulent structures within the flow. The same value was used for both cases to allow a direct comparison between them. In the incoming boundary layer, turbulent structures are rather small for both cases. As they cross the shock, the detachment of the shear layer promotes the three-dimensional interaction of the structures (Dores et al., 2024) that become larger and group in alternating *packs* (Adrian, 2007) of low- and high- momentum as suggested by the colors in Figure 4.6.

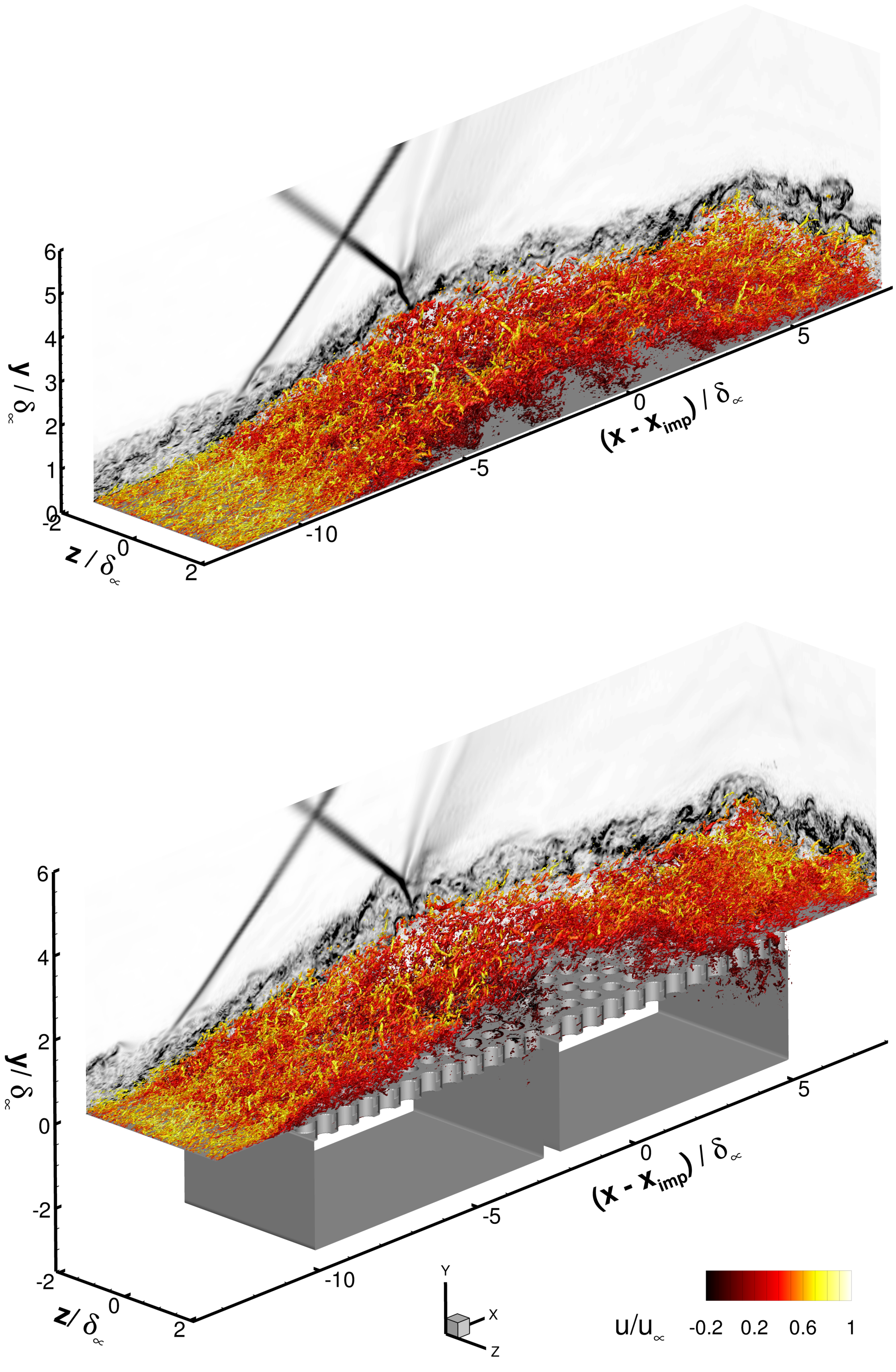

Figure 4.6: Instantaneous snapshots. (Top) Case $\mathcal{F}$. (Bottom) Case $\mathcal{P}$. Vortical structures visualised with the swirling strength criterion (λ_{ci}). Isosurfaces for $|\lambda_{ci}|\delta_\infty/u_\infty = 2.75$ coloured by local streamwise velocity. Schlieren visualisations at $z/\delta_\infty \approx -2$ and $(x - x_{imp})/\delta_\infty \approx 8$.

Close to the separation shock foot, the spanwise *wrinkling* of the shock is also highlighted in both plots by the different streamwise locations at which the structures start detaching from the wall. The turbulent structures continue growing until they reach their maximum size close to the bubble apex. After the interaction with the impinging shock, the turbulent structures break, losing their *pack* coherence. After the reattachment process, the structures slowly regain their coherence. Lastly, note that the growth of the boundary layer across the interaction is also very clear.

By comparing Subsection 4.2.1 and Subsection 4.2.1 two major differences can be observed for the controlled interaction. The first is the more pronounced breaking of the structures close to the bubble apex. The second is the increased height of the instantaneous bubble, which is also found for the averaged flow (as will be seen in Subsection 4.2.4). Finally, note that for the controlled case, small turbulent structures are seen entering the cavities (in particular the second) at its rear portion. This observation is related to the suction existent in this part of the cavities as well as to the 'impingement' of the detached shear layer at the wall. For an animated visualisation of this entrainment into the cavities, please refer to *'Case_P'* animation by Dores et al., 2024.

To complement these observations a second plot (Figure 4.7) is presented for the reference configuration. Figure 4.7 displays a Schlieren visualisation as well as the streamwise velocity fluctuations at five different stations along the interaction region.

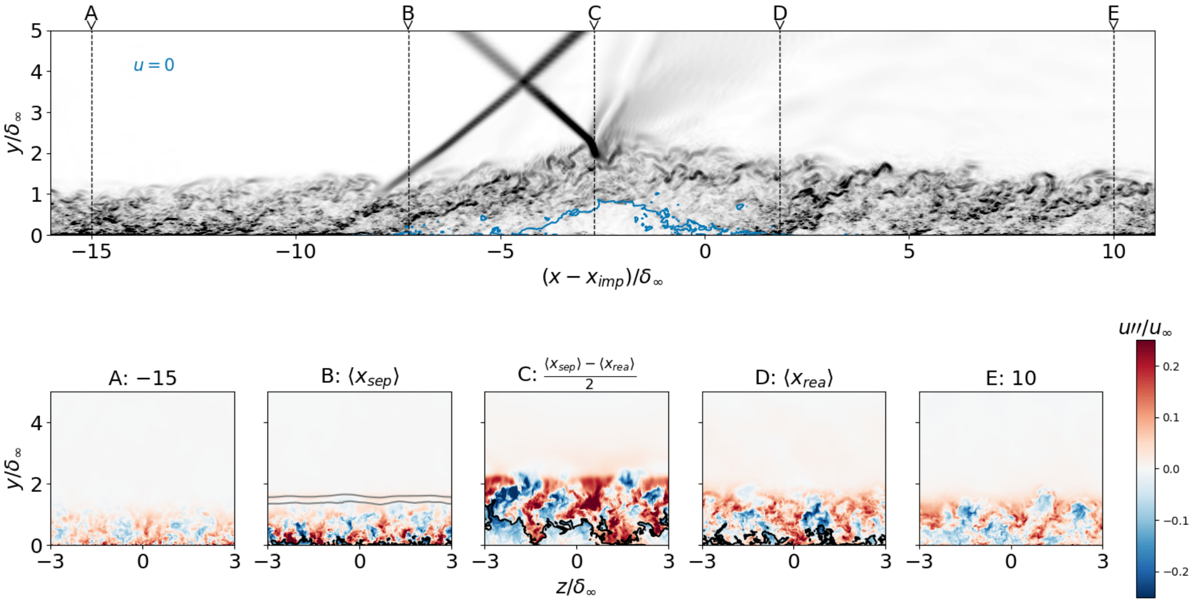

Figure 4.7: Instantaneous snapshot of reference case $\mathcal{F}$. (Top) schlieren visualisation. (Bottom) Favre fluctuations of streamwise velocity. (—) $|\nabla p|\delta_\infty/p_\infty = 1.2$

Analysing the streamwise velocity fluctuations, one can observe that the incoming turbulent boundary layer (station A) exhibits small velocity fluctuations in the outer region. Alternating streaks of low- and high-momentum can be identified close to the wall. As the boundary layer develops these fluctuations develop naturally (station B) becoming bigger and 'more coherent'. The pressure gradient isolines at this station highlight the dependency of the shock penetration depth with the speed of the flow beneath it. This can be seen by the wavy look of the isolines also known as *shock wrinkling*. The depth of penetration of the separation shock in the boundary layer depends on the Reynolds number. For higher Reynolds numbers the sonic line (which is the approximate location from where the separation shock emanates) is closer to the wall. For a constant Reynolds number the penetration depth varies according to the low- and high-momentum fluid movements in the boundary layer. As seen in Figure 4.7 the shock is located further away from the wall when high-momentum flow passes underneath it, while the opposite occurs for low-momentum flow.

However, after crossing the separation shock a further increase in size and intensity is observed that peaks close to the bubble apex location (station C). Note, at this location (station C), that the separation phenomenon, commonly assumed as spanwise homogeneous is not, indeed. As can be seen, there are big spanwise regions in which the flow is not instantaneously separated. At the same time, large portions of high-momentum fluid entrain deep within the boundary layer while low-momentum flow is brought away from the wall in a *sweep-ejection*-like motion characteristic of undisturbed turbulent boundary layers. Afterwards, there is a region downstream of the interaction where the boundary layer stabilizes again (stations D and E). After the interaction, the overall size of coherent regions increases compared to the incoming upstream flow, and the turbulent intensity (in terms of fluctuations magnitude) also increases following the enhanced growth of the boundary layer caused by the interaction with the shocks system (compare stations A and E). Similar conclusions can be drawn for the controlled interaction. Animations of the two different configurations can be consulted in Dores et al., 2024 database.

4.2.2 Mean Flow

Span- and time-averaged fields of u-velocity are shown in Figure 4.8. An accentuated contrast can be found for the STBLI phenomenon between the 3D instantaneous (Figure 4.6) and 2D spanwise-averaged (Figure 4.8) visualisations, which showcases the complex character of these interactions and the non-triviality of their analysis.

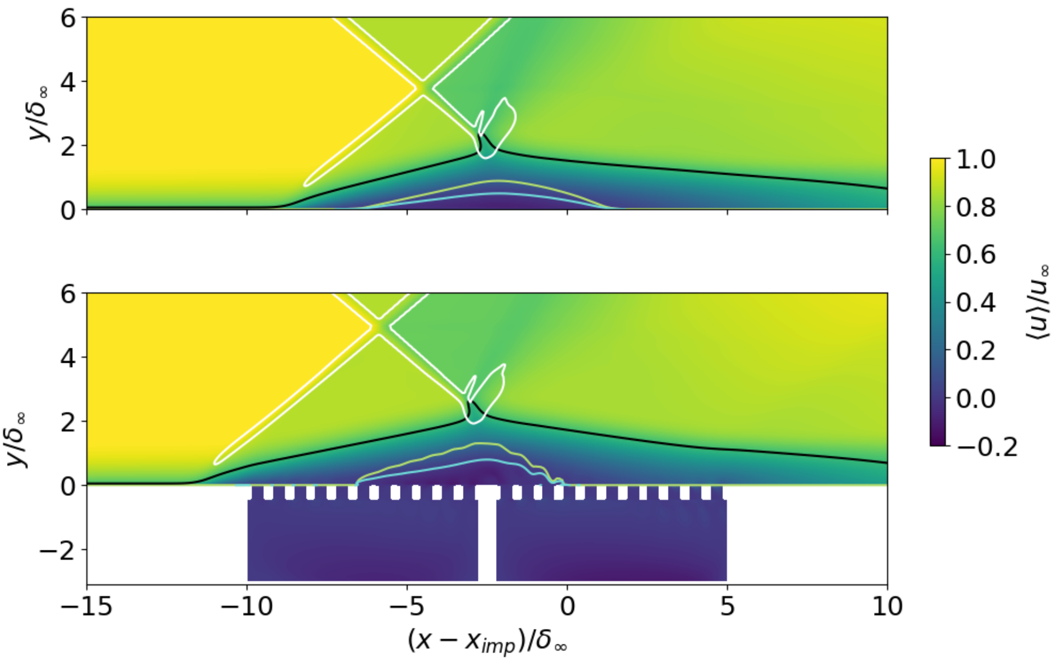

Figure 4.8: Span- and time-averaged streamwise velocity field. (—) $\langle u \rangle = 0$. (—) $\langle M \rangle = 1$. (WHITE) $|\nabla p|\delta_\infty/p_\infty = 1.2$. (—) dividing streamline: $\left\{(x, y_{ds}) \mid \int_0^{y_{ds}} \langle \rho u \rangle \, dy = 0\right\}$.

In Figure 4.8 the boundary layer thickening throughout the interaction is highlighted by the sonic line (in black). Following the mixing layer across the interaction, the sonic line reaches a maximum height of $\approx 2\delta_\infty$, which is less than the one verified by Pasquariello et al. (2017) for a case with a higher Reynolds number. At the same time, the dividing streamline, given by $\left\{(x, y_{ds}) \mid \int_0^{y_{ds}} \langle \rho u \rangle \, dy = 0\right\}$

can be taken as the representation of the lower limit of the shear layer that contains the recirculation region. The decrease in velocity through the shocks is also clear from the plots. The opposite occurs when the flow encounters the expansion fan close to the bubble apex.

Two differences stand out from the comparison between the mean flows. The first is the different intersection heights for the reflected and the impinging shocks. For case $\mathcal{F}$ it occurs at $y/\delta_\infty \approx 4$, while for case $\mathcal{P}$ it can be found higher at $y/\delta_\infty \approx 5$. Also, its streamwise location is shifted upstream for the controlled case, due to the displacement of the separation shock foot location, which is now bounded to the 'leading edge' of the first cavity. Interestingly enough, these variations in the separation shock position do not seem to influence the shock angle (hence, the shock strength), which can be concluded from the contour color after the shock. This may be due to the similar locations of the mean separation points (see Figure 4.18). The fact that the mean separation region is almost unaltered, indicates that the blowing in the front part of the first cavity (see Figure 4.9) helps prevent separation by re-energizing the boundary layer. At the same time, the blowing forces the flow to curve, which triggers the separation shock at the leading edge of the first cavity.

The second observation is related to the development of the boundary layer. Despite achieving similar thicknesses at the outflow plane, the evolution of the two is different, particularly, in the reattachment region. For case $\mathcal{P}$ a kink is present at $(x-x_{imp})/\delta_\infty \approx 4$ in the $\langle M \rangle = 1$ curve, indicating that the reattachment compression fan is stronger when including the passive control method.

A final remark should be made regarding the convergence of the solution for the controlled case. One can notice from the $\langle u \rangle = 0$ and the dividing streamline curves that the results are not fully converged (compare the same two curves between the top and bottom plots in Figure 4.8, for example).

An additional plot is presented showing the wall-normal velocity for the perforated wall configuration (Figure 4.9). The feedback recirculation mechanism inside each cavity is highlighted by the contours in Figure 4.9. One can clearly identify a *blowing-suction* mechanism from downstream to upstream of each of the cavities. This recirculation is driven by the pressure gradient above the wall imposed by the shock system. As will be seen in Figure 4.22a, pressure monotonically increases across the interaction. The monotonicity in pressure is responsible for the variation in the intensity of the suction/blowing between holes. Moreover, it justifies the fact that the more upstream/downstream holes present the largest absolute blowing/suction velocities.

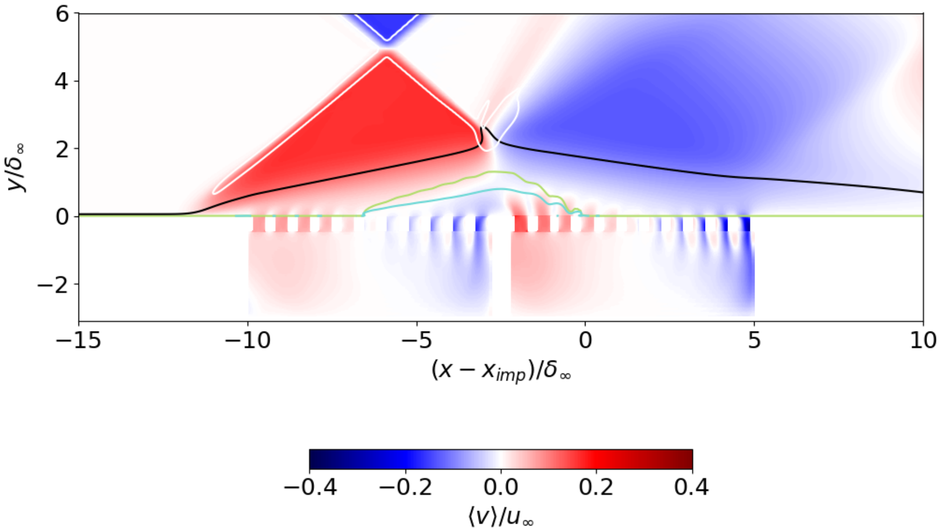

Figure 4.9: Span- and time-averaged wall-normal velocity. (—) $\langle u \rangle = 0$. (—) $\langle M \rangle = 1$. (WHITE) $|\nabla p|\delta_\infty/p_\infty = 1.2$. (—) dividing streamline: $\left\{(x, y_{ds}) \mid \int_0^{y_{ds}} \langle \rho u \rangle \, dy = 0\right\}$.

An important parameter to inspect that has large impact in real world applications is the total pressure recovery across the interaction, in particular, at the outflow plane. Figure 4.10 shows how the total pressure varies along streamwise $y-z$ planes. The total pressure recovery factor presented in Figure 4.10 was weight-averaged with the span-averaged mass flow rate. This ensures that regions of small mass flow (such as the boundary layer) have less impact on the recovery factor than major large-scale dissipative features happening in the outer-region.

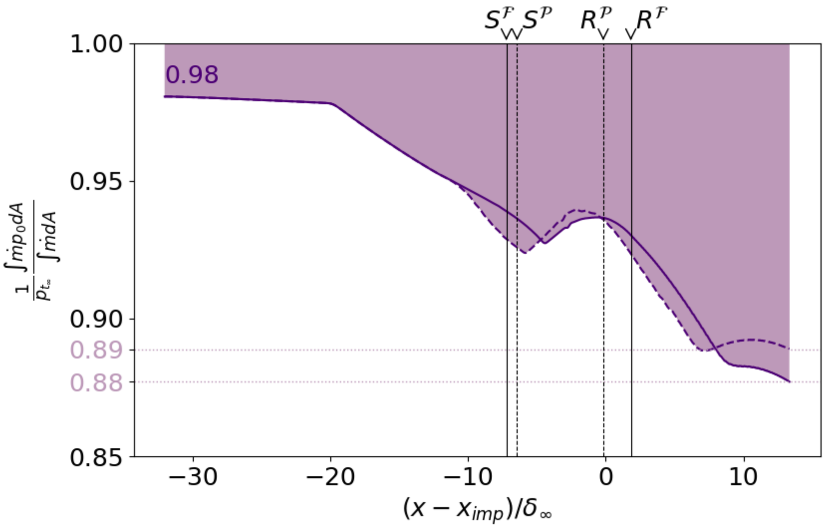

Figure 4.10: Mass-flow rate averaged total pressure recovery.

The presence of the boundary layer is clearly identified in the inflow region before the interaction by the 2% reduction in total pressure recovery observed. After an initial soft descending slope due to the natural growth of the boundary layer, the slope of the curve becomes steeper at $(x-x_{imp})/\delta_\infty \approx -20$. Since no other phenomenon is occurring in the domain, one is led to conclude that this is caused by boundary layer growth and might be related to the stabilization of the inflow conditions. At the shock foot, the slope of the curves changes once again, further decreasing total pressure, before reaching their minima after separation. As the flow crosses the expansion fan at the bubble apex a slight recovery of total pressure is verified, after which it steadily decreases as the flow encounters the reattachment compression fan and a larger boundary layer, resulting from the interaction. The same behaviour is found for both controlled and uncontrolled cases.

Overall the total pressure recovery after the interaction drops to 88% and to 89% for case $\mathcal{F}$ and $\mathcal{P}$, respectively, which indicates a reduction of $\approx 10\%$ in both configurations when compared to the inflow plane where only the incoming undisturbed boundary layer is present. Despite an improvement of 1%, the inclusion of perforations and the cavities underneath the interaction does not seem to have a big impact on total pressure recovery. Moreover, a drop in the mass flow rate at the outflow plane above the wall is observed from 1.28 kg/s in the reference case to 1.25 kg/s for the controlled interaction, which is also not desirable, particularly for propulsion applications.

4.2.3 Reynolds Stresses

The normal Reynolds stress components are shown in Figure 4.11, Figure 4.12 and Figure 4.13. Once again, the shock system, sonic line, dividing streamline and mean bubble are indicated in each figure. Each of the Reynolds stress components is non-dimensionalised by the maximum magnitude found above the wall between the two cases. In this way, one ensures that the qualitative interpretation of the results based on the contour colours is accurate and indicative of the magnitude for each component.

This means, that a darker colour from one plot to another is associated with higher intensity and vice-versa.

For $\tau_{11} = \widetilde{u''u''}$ a region of very high stress is initiated at the shock foot following the upward movement of the detached shear layer before reaching the bubble apex. A second region is observed downstream of the mean reattachment location, but much less prominent. Overall, the introduction of the control method resulted in lower streamwise fluctuations. Likewise, the high-intensity region coinciding with the detached shear layer in $\mathcal{F}$ is slightly attenuated close to the wall due to the blowing in the upstream portion of the first cavity.

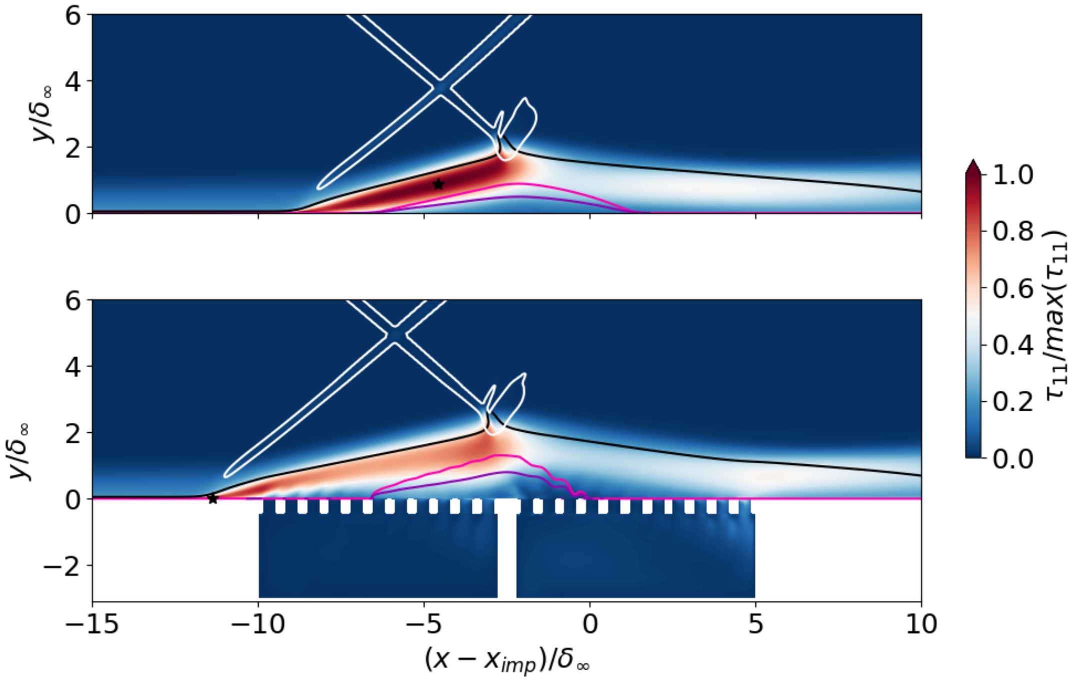

Figure 4.11: Span- and time-averaged streamwise Reynolds stress. (——) $\langle u \rangle = 0$. (——) $\langle M \rangle = 1$. (WHITE) $|\nabla p| \delta_\infty / p_\infty = 1.2$. (——) dividing streamline: $\left\{(x, y_{ds}) \mid \int_0^{y_{ds}} \langle \rho u \rangle \, dy = 0\right\}$. ($\star$) location of maximum.

Contrary to what was found by Pasquariello et al. (2017) and by Laguarda et al. (2024b) (for the same Re_τ), for the reference case, the maximum is located far from the wall downstream of the shock foot location. In both studies, the streamwise stress maximum was placed close to the wall near the shock foot as found for the controlled case. Only for the high-Reynolds number case carried by Laguarda et al. (2024b) the maximum was located away from the wall. Nonetheless, Laguarda et al. (2024b) did find a local maximum at the identified location. The difference in maximum location observed in case $\mathcal{F}$ can be due to the wall boundary condition, which is adiabatic in the present study, while isothermal in Laguarda et al. (2024b) study. On the other hand, the agreement found in $\mathcal{P}$ seems to be a direct consequence of a global intensity decrease everywhere in the domain above the cavities, while a smaller attenuation is felt at the shock foot, outside the cavities/perforations range. Finally, note the small intensity region along the separation shock, due to the streamwise excursions of the shock, resulting in small variations of velocity downstream of the shock system outside of the interaction. A similar contour is still present for $\mathcal{P}$ but is almost insignificant.

Regarding the wall-normal stress, $\tau_{22} = \widetilde{v''v''}$ it shows a large region of high intensity across the entire interaction region. The turning of the previously undisturbed flow caused by the separation shock, makes this component start increasing after the shock, remaining approximately constant across the recirculation region. For $\mathcal{F}$ it reaches its maximum above the wall, near the shear layer reattachment position.

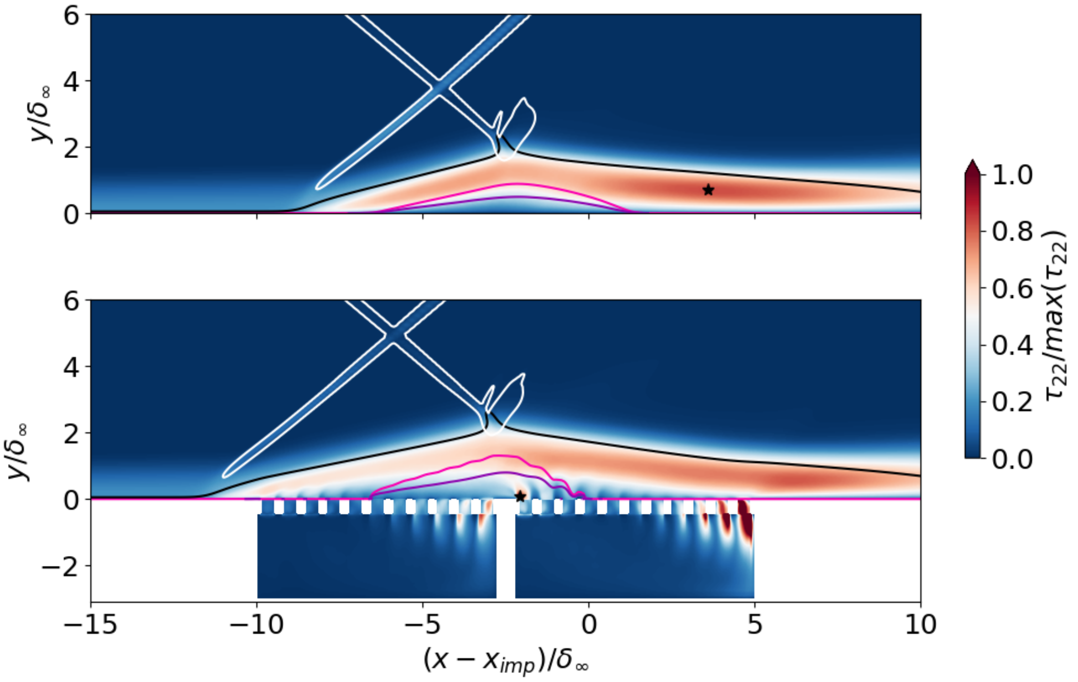

Figure 4.12: Span- and time-averaged wall-normal Reynolds stress. (—) $\langle u \rangle = 0$. (—) $\langle M \rangle = 1$. (WHITE) $|\nabla p|\delta_\infty / p_\infty = 1.2$. (—) dividing streamline: $\left\{(x, y_{ds}) \mid \int_0^{y_{ds}} \langle \rho u \rangle \, dy = 0\right\}$. ($\star$) location of maximum.

Despite displaying a local maximum in the same region as $\mathcal{F}$, the controlled interaction has its above-the-wall maximum inside the recirculation bubble. The cause of this maximum seems to be the global maximum found in the rear portion of the second cavity since the highest pressure gradient inside the cavity is found between the most upstream and the most downstream holes. Hence, the high stress intensities found in the suction portion of the second cavity are expected to influence the region where the blowing is most potentiated, which is where the above-the-wall maxim is found. This finding may indicate a detrimental effect of the wall dividing the two cavities. The pressure gradient that should propagate to a region upstream of the recirculation bubble is now connected to the interior of the bubble which is confined by the shear layer above it. In this way, the bubble may work as a valve with the suction in its upstream portion (connected to the first cavity) enhancing the blowing from the upstream portion of the second cavity, which in terms magnifies the suction in the downstream portion of the second cavity. The animation for the controlled case (*Case_P* - Dores et al. (2024)), shows indeed fluid moving from the second to the first cavity. The suction in the rear portion of the second cavity may be even more magnified by the impingement of the reattaching shear layer, which further contributes to high levels of wall-normal velocity fluctuations. In fact, the global maximum found inside the second cavity below the wall is 1-2 orders of magnitude higher than the above-the-wall maximum. The mentioned mechanism may explain why a maximum is found in the blowing section of the second cavity for $\mathcal{P}$. Contrarily, in the first cavity, the same trend as found for $\widetilde{u''u''}$ is observed, with the region affected by the blowing displaying a decrease in stress. In both configurations, it is also possible to observe an increased magnitude across the separation shock, being higher for the reference configuration. Being v'' associated with the characteristic unsteady shock motion, the observation of lower stress magnitudes in the shock region points to an attenuation of this unsteady behaviour.

Lastly, for the spanwise component of the Reynolds stress tensor, $\tau_{33} = \widetilde{w''w''}$, the maximum is located upstream of the bubble apex above the wall for $\mathcal{F}$ and at the wall close to the edge of the second cavity for $\mathcal{P}$. The spanwise Reynolds stress component presents a similar behaviour to the one verified for τ_{11} up to the bubble apex location. Downstream of the apex, a high-intensity region is observed above the wall following the shear layer path.

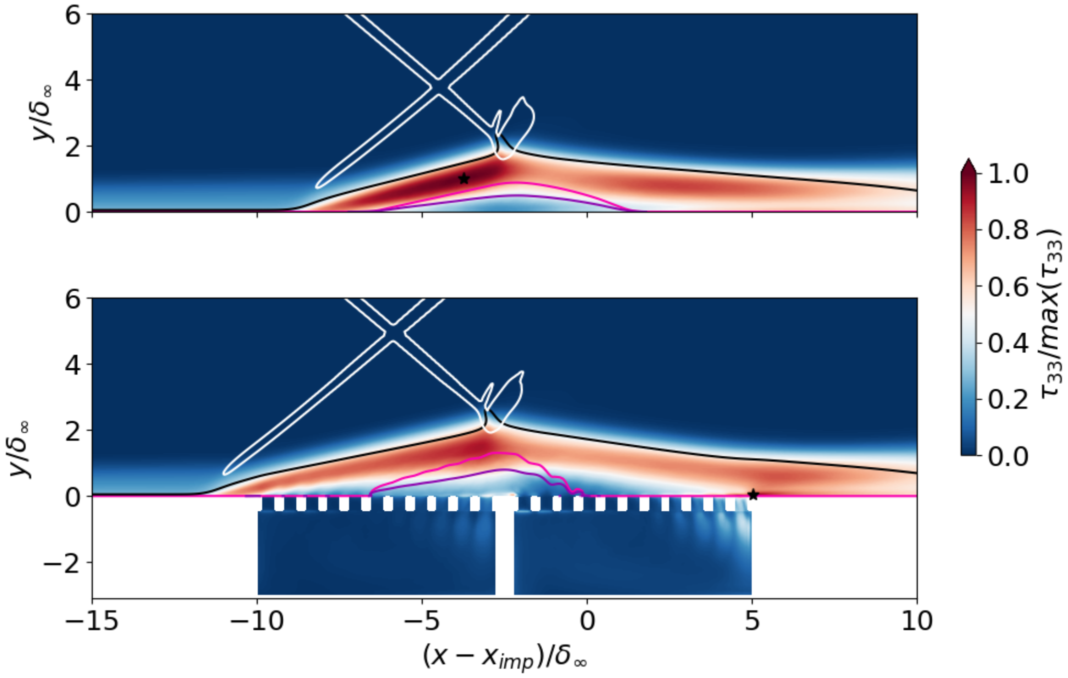

Figure 4.13: Span- and time-averaged spanwise Reynolds stress. (—) $\langle u \rangle = 0$. (—) $\langle M \rangle = 1$. (WHITE) $|\nabla p|\delta_\infty/p_\infty = 1.2$. (—) dividing streamline: $\left\{(x, y_{ds}) \mid \int_0^{y_{ds}} \langle \rho u \rangle \, dy = 0\right\}$. ($\star$) location of maximum.

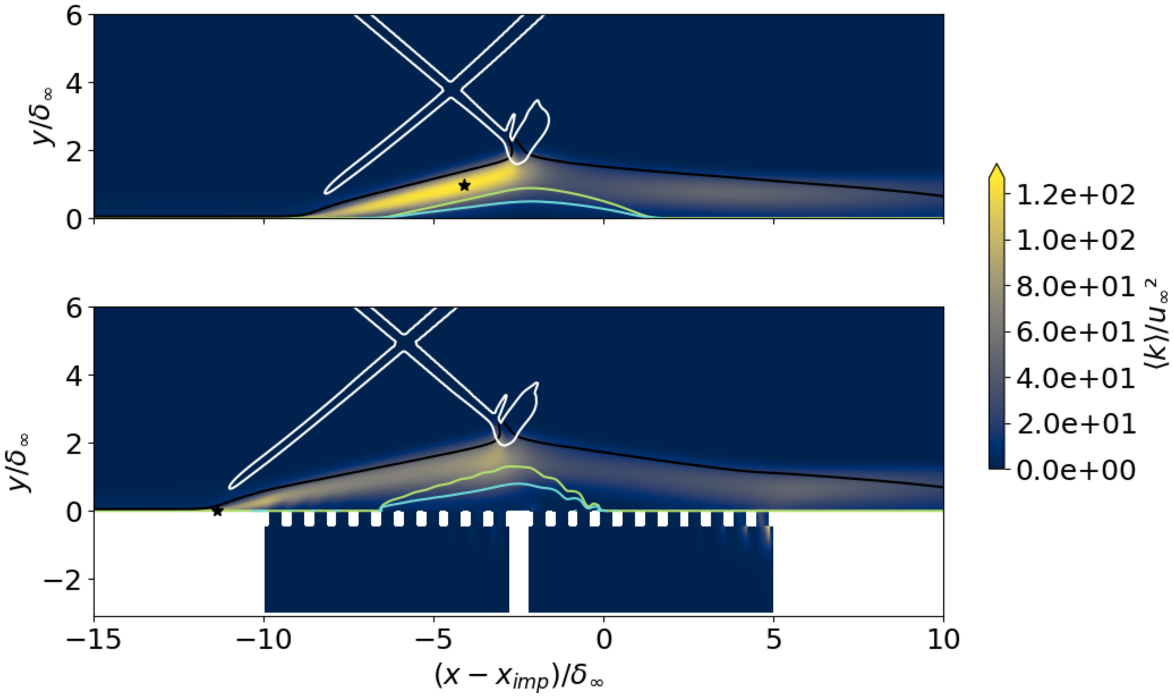

Figure 4.14: Span- and time-averaged turbulent kinetic energy field. (—) $\langle u \rangle = 0$. (—) $\langle M \rangle = 1$. (WHITE) $|\nabla p|\delta_\infty/p_\infty = 1.2$. (—) dividing streamline: $\left\{(x, y_{ds}) \mid \int_0^{y_{ds}} \langle \rho u \rangle \, dy = 0\right\}$. ($\star$) location of maximum $\langle k \rangle$.

As described by Pasquariello et al. (2017) a third additional high-intensity region is also found further downstream close to the wall, where they found the maximum for $\widetilde{w''w''}$, which according to them suggests a centrifugal instability, linked to Görtler-like vortices. For the reference case, given that the same adiabatic wall boundary condition was used, the disagreement with Pasquariello et al. (2017) on the maximum location can be related to the difference in the Reynolds number. On the other hand, the observation of the same location for the maximum in the controlled interaction may be justified in the same way as for τ_{11}: the overall reduction of magnitude within the region covered by the cavities may cause this region to stand out.

Figure 4.14 shows the turbulent kinetic energy, with the mean bubble in blue, the dividing streamline in green and the maximum represented by the star. The turbulent kinetic energy field gives an insight into where the turbulent intensity is higher. In general, the contours are very similar to the ones found for τ_{11}, as expected since the streamwise component of the velocity is the one with the highest magnitude, making it the component that most contributes to the turbulent kinetic energy. Furthermore, also the maxima locations are the same as found for τ_{11}.

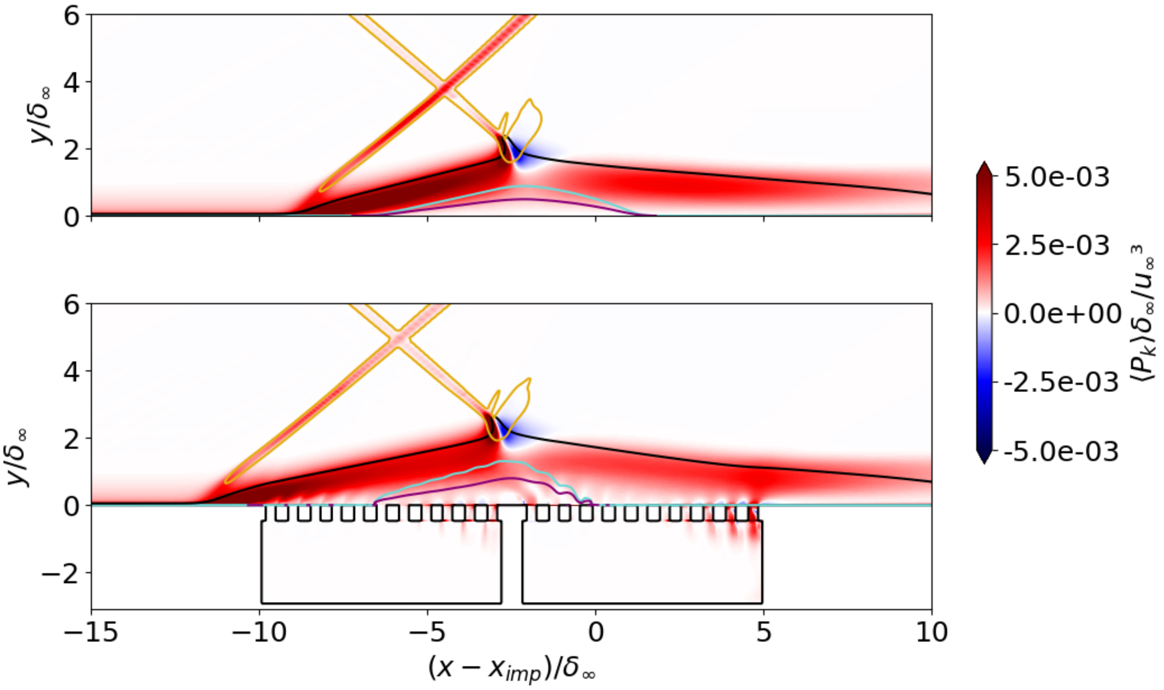

Figure 4.15: Span- and time-averaged turbulent kinetic energy production field. (—) $\langle u \rangle = 0$. (—) $\langle M \rangle = 1$. (—) $|\nabla p| \delta_\infty / p_\infty = 1.2$. (—) dividing streamline: $\left\{ (x, y_{ds}) \mid \int_0^{y_{ds}} \langle \rho u \rangle \, dy = 0 \right\}$.

Turbulent kinetic energy production is shown in Figure 4.15. Similarly to what was found for each of the Reynolds stress components and the turbulent kinetic energy, most of the production occurs along the shear layer, particularly in its upstream portion upon detachment from the wall. Also, along the impingement and separation shocks, regions of high production are found, being higher for the separation shock, due to its excursion movements. Close to the bubble apex a large region of negative production is observed associated with the expansion fan responsible for initiating the reattachment process of the shear layer. Comparing both cases, an overall reduction of turbulent kinetic energy is observed for the controlled case (despite not being very significant), particularly visible in the separation shock region and the upstream portion of the detached shear layer. Moreover, production of turbulent kinetic energy is associated with each one of the perforations, being higher in the suction regions of each cavity.

4.2.4 Reverse Flow Region / Bubble Characterisation

In this section, the topology and the properties of the recirculation region are analysed. Figure 4.16 shows the time-averaged 2D distribution of the skin-friction. The contour for case $\mathcal{F}$ does not introduce any additional information to the one that will be discussed for Figure 4.18. Contrarily, for $\mathcal{P}$, the contour presents some interesting features. It shows that each perforation influences its surrounding area and that this influence depends on the streamwise location of each hole. One can conclude that the presence of the cavities influence the location of the separation shock as discussed in Subsection 4.2.2. The more upstream location of the shock makes all wall-related quantities start varying more upstream as well as seen in Figure 4.16 for the skin-friction in particular.

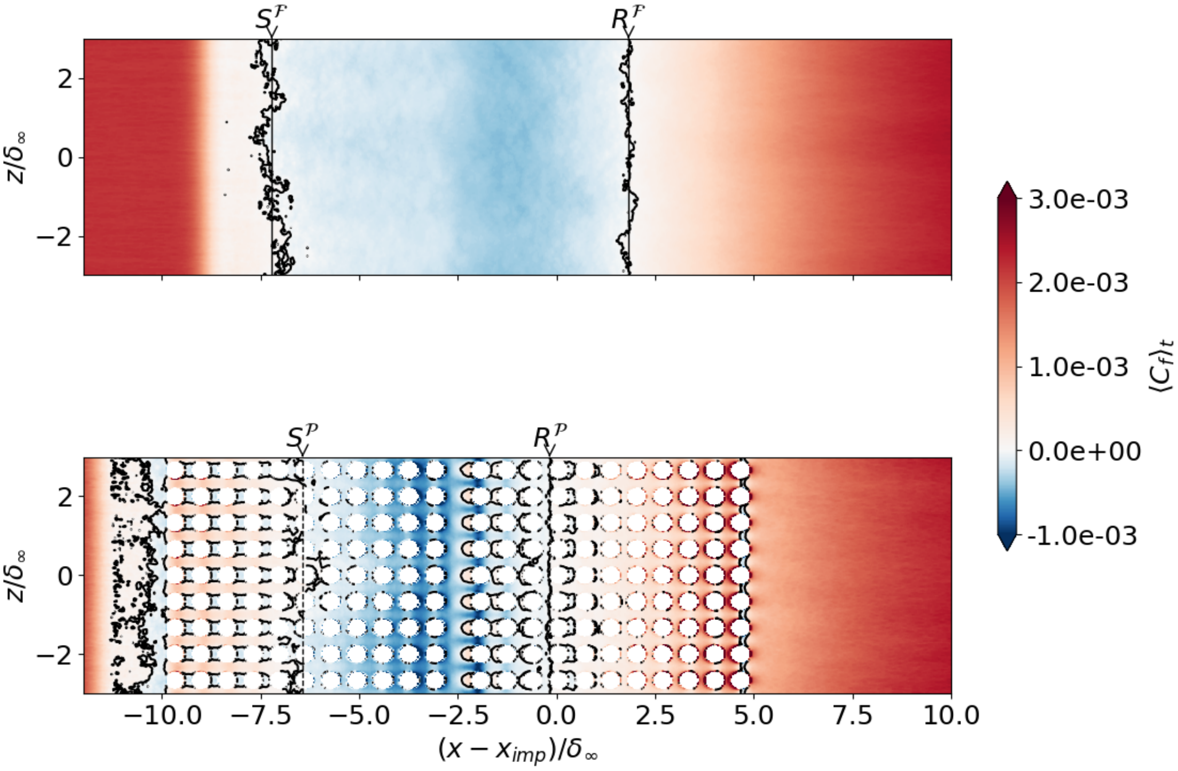

Figure 4.16: Time-averaged skin-friction coefficient. (—) $\langle u \rangle = 0$.

The first observation that can be done is the partial separation that occurs before the first column of perforations. For the first cavity, this separated status is observed in every x-row in the holes line, until the mean separation line is reached. Between the holes, the flow reattaches until it separates at $S^{\mathcal{P}}$. The separation behind each orifice is due to the upward motion of the air triggered by the blowing from inside the cavity. On the other hand, inside the mean bubble in the upstream portion of the second cavity, one can observe regions of positive C_f upstream of the perforations, where the flow is moving from the second cavity to the first (see *'Case_P'* movie by Dores et al. (2024)). Lastly, a stripe of separated flow is found between the holes after the mean reattachment line at $(x - x_{imp})\delta_\infty \approx 5$. The exact cause for this is not clear. However, the most likely reason for it may be the strong suction felt at the rear part of the second cavity (see *'Case_P'* movie by Dores et al. (2024)).

Before interpreting the 1D skin-friction distributions, a small remark is made regarding the convergence of the sampled data. Figure 4.17 shows the skin friction coefficient for the study case $\mathcal{P}$, computed in four different ways: (1) from the statistics (with the highest sampling rate) excluding the holes and from the snapshots, (2) excluding the holes, (3) considering only the x-rows where no holes are present and (4) considering only the z-columns where no holes are present. The number of snapshots collected is enough to make the respective curve collapse with the one computed from the statistics. This indicates that the results are sufficiently converged and that the number of snapshots is adequate. If one only averages the 2D $\langle C_f \rangle$ distribution in the z-columns where no holes are present, setting the columns in between to zero, the orange curve is obtained, which also shows a good agreement with the previously mentioned curves. More interesting is to take only the x-rows that do not include any perforations. By doing so, the curve obtained shows much less oscillations. This finding brings evidence to support the conclusion that the perforations and the flow dynamics related to them are responsible for part of the oscillations observed.

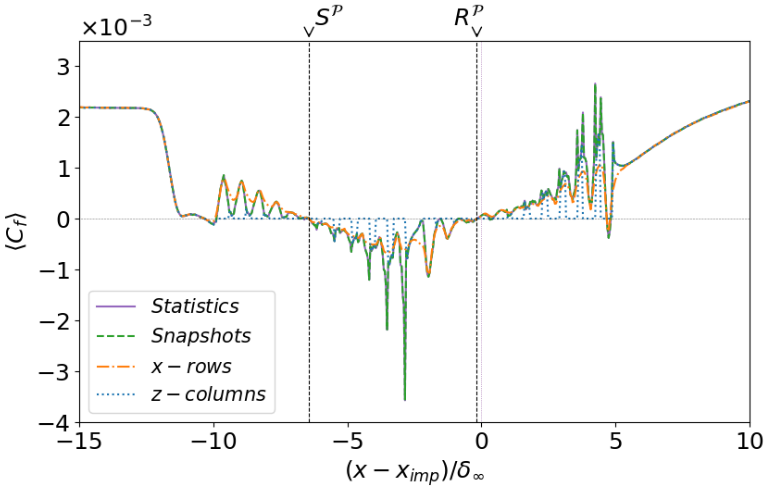

Figure 4.17: Span- and time-averaged skin-friction coefficient along the wall computed for case $\mathcal{P}$. (——) statistics, excluding holes. (- - -) snapshots, excluding holes. (-·-·) snapshots, only 'complete' x-rows. (······) snapshots, only 'complete' z-columns.

The large spanwise variations shown in Figure 4.16 for $\mathcal{P}$, are visible in the 1D distribution of skin-friction at the wall (Figure 4.18), obtained by averaging Figure 4.16 in the spanwise direction. Figure 4.18 shows the span- and time-averaged skin friction along the wall for both $\mathcal{F}$ and $\mathcal{P}$ as well as for the undisturbed boundary layer.

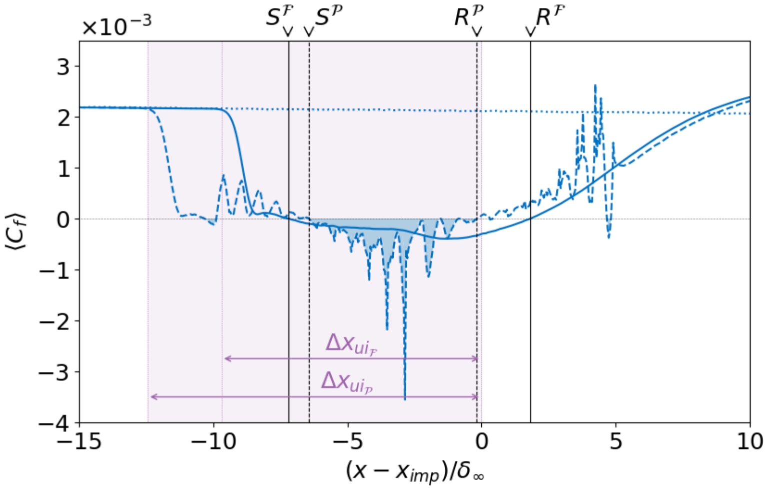

Figure 4.18: Span- and time-averaged skin-friction coefficient along the wall. (······) undisturbed boundary layer.

For each configuration the separation region is defined as the largest region where $\langle C_f \rangle \leq 0$. Positive outliers are ignored, but only if they correspond to at most one computational cell in the streamwise direction. Based on this definition, the definition of the mean separation (x_{sep}) and mean reattachment (x_{rea}) points follow as the first and last points where the $\langle C_f \rangle$ curve crosses the zero line for the determined separation region, respectively. Likewise, the mean separation length is then defined as $L_{sep} = x_{rea} - x_{sep}$. Similarly, one can also define the upstream influence distance as the distance between the streamwise coordinate where the variation of $\langle C_f \rangle$ variation becomes bigger than 1% with respect to the undisturbed boundary layer distribution, and the virtual impingement point, $\Delta x_{ui} = x_{imp} - x_{ui}$.

Regarding case $\mathcal{F}$ distribution one can observe that at $(x - x_{imp})/\delta_\infty \approx -10$, $\langle C_f \rangle$ starts decreasing. After the initial drop, a local maximum is present, indicative of the incipient separation that occurs before the complete establishment of separation. Afterwards, the $\langle C_f \rangle$ distribution presents a shape, which is a transition between the shapes reported by Laguarda et al. (2024b) for high- and low-Reynolds number STBLIs. On the one hand, it has a W-shape characteristic of low-Reynolds interactions (Priebe et al., 2009). On the other hand, it also exhibits a plateau in the first half of the recirculation region, characteristic of high-Reynolds interactions. The global minimum is located in the downstream half of the separation bubble, after the plateau at $\approx 1\delta_\infty$ of the virtual impingement point.

The distribution for $\mathcal{P}$ shows larger oscillations. The previously incipient separation for $\mathcal{F}$ becomes fully established in this case with $\langle C_f \rangle$ becoming negative after the first drop at $(x - x_{imp})/\delta_\infty \approx -10$. As the flow enters the first cavity region a sudden rise in $\langle C_f \rangle$ is observed promoting 'reattachment'. A descent trend in $\langle C_f \rangle$ is then followed until separation occurs. The negative peak verified for $\mathcal{P}$ is almost 4 times higher than the one observed for $\mathcal{F}$. Even if neglecting the oscillatory behaviour of the curve, it is possible to infer that the peak would still be larger in magnitude than for the flat plate (see Figure 4.17). After reattachment, both controlled and uncontrolled cases follow similar trends. However, as the suction portion of the second cavity is reached large fluctuations are visible until the flow exits the cavities region $(x - x_{imp})/\delta_\infty \approx 5$, after which the oscillations are no longer present and a convergence with the flat plate distribution is observed.

From $(x - x_{imp})/\delta_\infty \approx 5$ onwards, both curves start increasing, reaching values bigger than the one for the undisturbed boundary layer, due to the effect of the expansion fan that is generated at the virtual shock generator, interacting with the boundary layer at approximately that streamwise location.

Integrating the span- and time-averaged wall shear stress over the entire flat plate extension one can obtain the average viscous drag, which for case $\mathcal{F}$ is 1.40 N and for $\mathcal{P}$ is 0.46 N. Despite the improvement in viscous drag, for $\mathcal{P}$ one should also consider the pressure drag linked to the different pressures inside each cavity. Since mean pressure is higher in the second cavity, a net drag-like force is felt for $\mathcal{P}$, increasing its total drag to 1.74 N. Hence, despite the overall reduction in skin friction at the wall, the resulting effect of the cavities is detrimental regarding total drag.

Another quantity that is also representative of the reverse flow region is the probability of reverse flow, χ. Figure 4.19 shows the 2D distribution of this quantity. Very high values can be found for both cases inside the mean bubble region (above $\langle \chi \rangle \geq 0.5$, as can also be seen in Figure 4.21). However, the region where reverse flow can be found at any given instant exceeds the separation bubble. Additionally, for $\mathcal{P}$, probabilities of almost 1 are found inside each cavity, which confirms the pressure-driven recirculation. Figure 4.19 also shows that the displacement of air inside the cavities is predominantly located at the bottom, pointing to downward/upward movement in the suction/blowing portions of each cavity as confirmed in the wall-normal velocity contour in Figure 4.9.

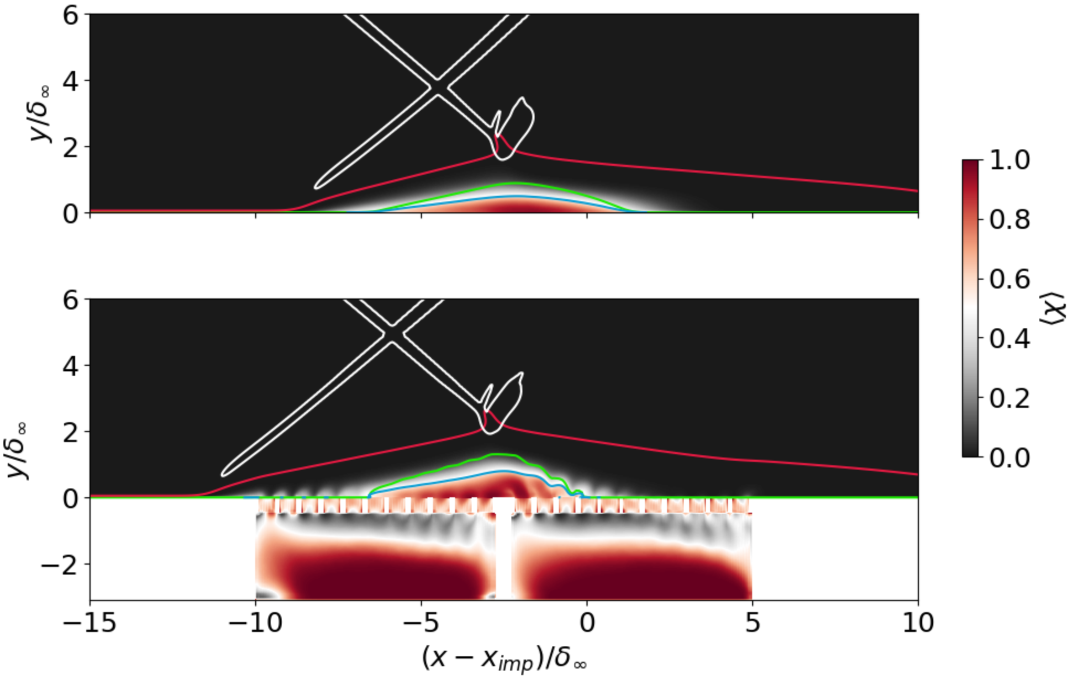

Figure 4.19: Span- and time-averaged probability of reverse flow. (—) $\langle u \rangle = 0$. (—) $\langle M \rangle = 1$. (WHITE) $|\nabla p|\delta_\infty/p_\infty = 1.2$. (—) dividing streamline: $\left\{(x, y_{ds}) \mid \int_0^{y_{ds}} \langle \rho u \rangle \, dy = 0\right\}$.

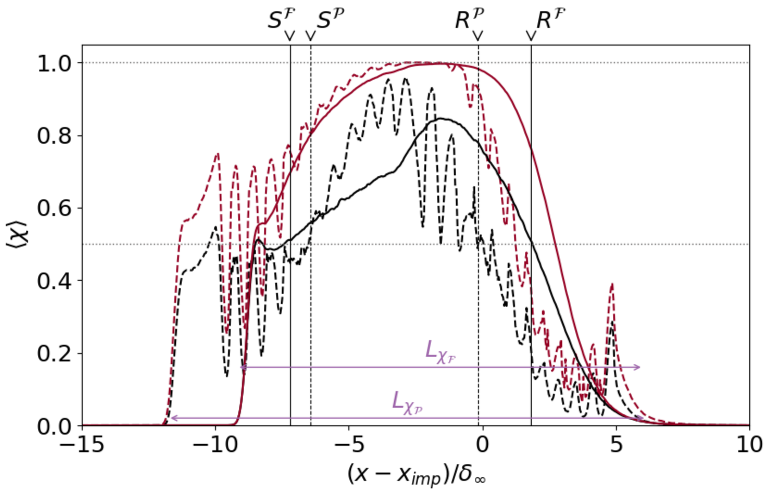

Figure 4.20: Span- and time-averaged probability of reverse flow along the wall. (—) $\langle \chi \rangle$ along the wall. (—) maximum $\langle \chi \rangle$ in wall-normal direction.

Plotting the distribution of $\langle \chi \rangle$ along the wall, one obtains the black lines shown in Figure 4.20. Based on the locations where $\langle \chi \rangle$ crosses 1% the reverse flow based length scale L_χ is defined (see Figure 4.20). In both cases, the probability of reverse flow increases rapidly to values higher than 0.5 right after the upstream influence location, x_{ui}. Afterwards, it presents a local minimum continuing to increase until it reaches the global maximum. Note that the coordinates for the global maximum correspond to the location of the respective global minimum identified for the skin-friction distribution. Moreover, it is important to highlight that the probability never reaches 1, meaning that, at the wall, there are always moments in time where the flow is attached, even within the recirculation region. This observation gains significance, considering that the curve shown is span-averaged. A similar conclusion had been made already for $\mathcal{F}$ based on Figure 4.7, in which non-homogenous separation is observed in the spanwise direction. Moreover, a difference is found in the shape of the curve for $\langle \chi \rangle$. While, for $\mathcal{F}$, the probability of reversed flow is not symmetric (within the recirculation region), with a clear peak closer to reattachment, for $\mathcal{P}$, the distribution is almost symmetric for the same considered region. Also, the maximum value achieved is higher for $\mathcal{P}$. These observations agree with the higher negative values of $\langle C_f \rangle$ found for the study case.

Additional conclusions can be made if instead of plotting the probability of reverse flow at the wall, one computes the probability of having reverse flow ($u < 0$) anywhere above the wall at a given x coordinate. In that case, the distributions are given by the red lines in Figure 4.20. This time, a probability of 1 is found in the downstream portion of the bubbles. Once again, this fact leads to the existence of incipient separation, characterised by the partial reattachment of the flow right after separation, with the separation only becoming completely established further downstream.

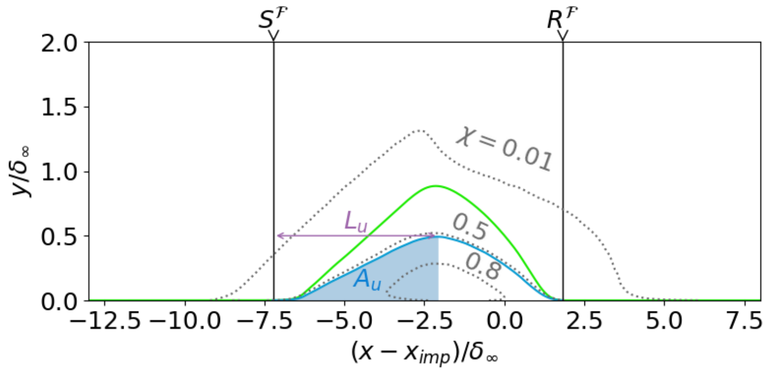

(a) Case $\mathcal{F}$.

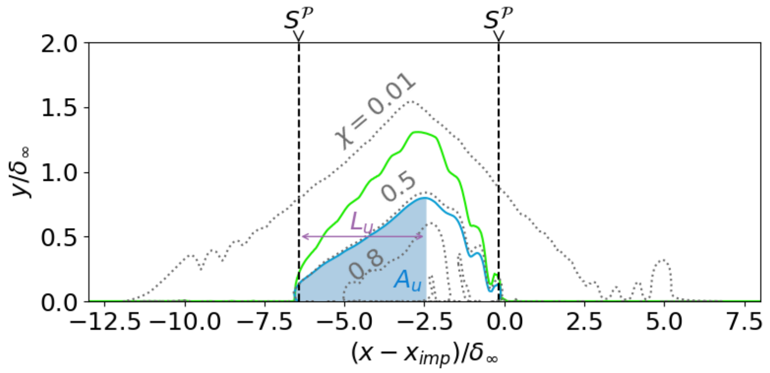

(b) Case $\mathcal{P}$.

Figure 4.21: Span- and time-averaged bubble configuration. (——) $\langle u \rangle = 0$. (——) dividing streamline: $\left\{(x, y_{ds}) \mid \int_0^{y_{ds}} \langle \rho u \rangle \, dy = 0\right\}$. (······) isocontours of probability of reverse flow.

One can now focus on the topology of the mean separation bubbles shown in Figure 4.21 along with the dividing streamline and isolines of reverse-flow probability. Defining the upstream recirculation length, L_u and the mean upstream area, A_u as shown in Figure 4.21 one can have a quantitative indication of the symmetry of the bubble. Their values can be found in Table 4.2. Likewise, also the mean bubble height, h_{sep} is reported. Moreover, the ratio of the bubble area and the area of a perfect triangle is included.

Visually, it is possible to infer that for $\mathcal{F}$ the bubble is almost symmetric in terms of its upstream and downstream portions with respect to the bubble apex, closely resembling a perfect isosceles triangle. Contrarily, for $\mathcal{P}$, the bubble has a non-symmetric shape with most of it being in the upstream portion of the bubble, closer resembling a right triangle. Table 4.2 includes different physical quantities characterising the reverse flow region following the definitions in the work of Laguarda et al., 2024b. The values in the table confirm the change in bubble topology. Also, the more curvilinear shape of the bubble for the flat plate interaction in its downstream portion can be attributed to the presence of a non-coalesced compression fan at reattachment, instead of a shock. Even though no shock is present at reattachment for the porous wall configuration, the reattachment compression fan is stronger as had already been noticed in Figure 4.8. The shape of the $\langle\chi\rangle = 0.01$ isolines also highlights this fact.

For both the controlled and uncontrolled configurations the isoline $\langle\chi\rangle = 0.5$ almost perfectly coincides with the mean bubble shape. Moreover, very high values of reverse-flow probability ($\langle\chi\rangle \geq 0.8$) are confined to a very small inner region inside the bubble, while separation can occur in a much broader region in both streamwise and wall-normal directions (as the isoline $\langle\chi\rangle = 0.01$ indicates).

Overall, the introduction of the control mechanism resulted in a similar interaction, due to the opposite effects of an increased mean bubble height and a decreased mean separation length. However, as can be inferred from Figure 4.21, the interaction influence region increased significantly.

Table 4.2: Reverse flow region properties

	$\frac{L_{sep}}{\delta_\infty}$	$\frac{L_\chi}{\delta_\infty}$	$\frac{\Delta x_{ui}}{\delta_\infty}$	$\frac{h_{sep}}{L_{sep}}$	$\frac{A_{sep}}{\frac{1}{2}h_{sep}L_{sep}}$	$\frac{L_u}{L_{sep}}$	$\frac{A_u}{A_{sep}}$
$\mathcal{F}$	9.09	15.23	9.69	0.054	1.02	0.57	0.54
$\mathcal{P}$	6.26	17.94	12.45	0.128	1.21	0.64	0.64
$\Delta\%$	-31.1	17.8	28.5	137.0	18.6	12.3	18.5

4.2.5 Wall Properties

Plotted in Figure 4.22a and Figure 4.22b are the three main mean thermodynamic properties along the wall for the configurations studied.

Starting with case $\mathcal{F}$, pressure and density showcase very similar distributions. They both start increasing at approximately x_{ui} close to the separation shock foot location. Across the shock, all static thermodynamic properties increase as expected. Inside the upstream portion of the bubble, both pressure and density continue to increase. A fully established plateau is not observed. Nonetheless, one can still identify a region of slower increase in density and pressure, for which this plateau occurs at a ratio of approximately 2, in agreement with the empirical formula by Zukoski (1967): $p_{plateau}/p_\infty = 1 + 0.5M_\infty$. The impingement shock close to the bubble apex is then responsible for initiating the reattachment process while further increasing pressure and density. Only after reattachment, pressure and density begin to drop. Note that both these curves exhibit three inflection points characteristic of separation, reattachment onset and reattachment compression (Delery & Marvin, 1986), as detailed in Subsection 2.2.3.

For $\mathcal{P}$, the undisturbed and post-interaction mean pressure and density values are the same as for $\mathcal{F}$, as expected. The increase in these properties, however, starts further upstream due to the larger upstream influence distance. Apart from this difference, mean pressure and density also exhibit two plateaus instead of one, each connected to one of the cavities. In the wall between cavities, a small jump is observed before the second plateau is established. The increase in pressure and density is therefore made in a more gradual way, being the curves always below the ones for the reference case after separation.

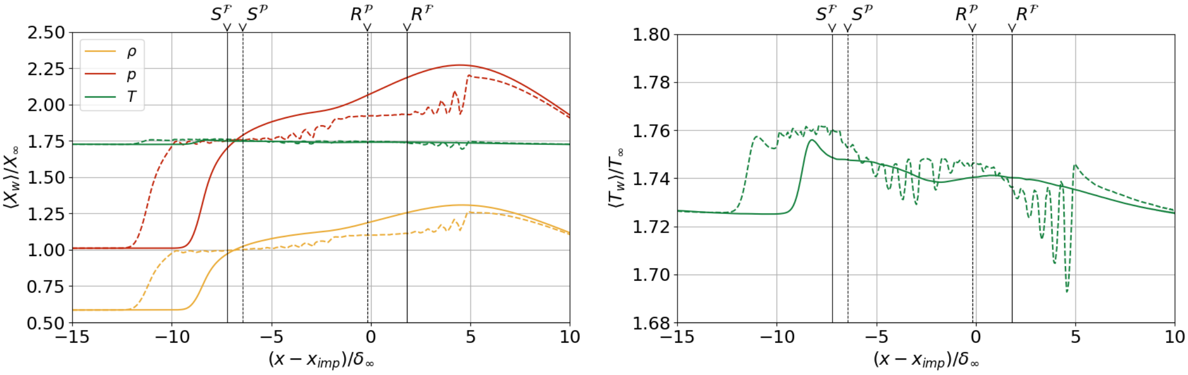

(a) Mean.

(b) Mean temperature (adjusted scale).

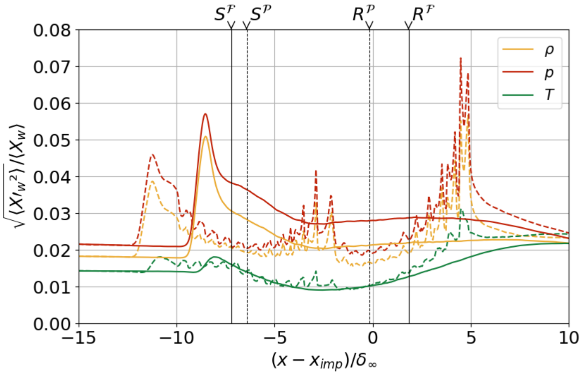

(c) RMS.

Figure 4.22: Span- and time-averaged thermodynamic properties at the wall.

Mean temperature (showed in detail in Figure 4.22b), on the other hand, shows very little variation for either case in terms of its magnitude. Following the ideal gas law, it is expected that it does not show a big variation due to the similar distributions of pressure and density across the interaction. However, its 'profile' is still relevant to analyse. As a general trend, static temperature increases slightly after the separation shock, converging back to the freestream value across the interaction. In reality, and despite not being shown, it is expected that the final value for the mean temperature is lower than the freestream values, due to the interaction of the flow with the expansion fan caused by the virtual shock generator. In the interaction region, for $\mathcal{F}$, it displays a local minimum close to the location of the global minimum found for $\langle C_f \rangle$. For $\mathcal{P}$ a plateau is present within the mean bubble region. Within the first cavity, an abrupt variation is observed between the suction and blowing regions. For the second cavity, a similar variation is found. Nonetheless, the suction portion of the second cavity does not present a plateau. Instead, a descent trend is observed.

Important to note are the oscillations observed for $\mathcal{P}$ close to the end of each cavity. These may be related to the pressure equalisation required between the flow above the wall and the air inside the cavities. Likewise, since the two cavities are isolated from each other by a dividing wall, there must also be an equalisation of pressure for the fluid above the wall that goes from being on top of one cavity to being on top of the other. Moreover, the fact that the pressure and density rise is made more gradually, achieving the same final post-interaction values, requires large variations of these thermodynamic variables upon reattachment of the shear layer at the end of the second cavity (see $\langle p \rangle$ at $(x - x_{imp})/\delta_\infty \approx 5$, for example).

A complementary analysis can be done by looking at the RMS (root-mean-squared) of the same thermodynamic properties (Figure 4.22c). They all have the similar magnitudes when normalized with the mean value of the corresponding quantity at the wall. Nonetheless, pressure fluctuations are the largest while, the temperature seems to be the quantity that is less sensitive to changes in the flow, as can be seen by in Figure 4.22c. Just like for the mean thermodynamic quantities, in the RMS distribution, both pressure and density vary in very similar ways.

For the flat plate configuration all quantities peak at the shock foot location, after which they display a bowl-like shape, decreasing up to the bubble apex streamwise location. From this point onwards, pressure and density plateau while slowly converging to slightly higher values than the freestream in a trend of descent. Temperature, on the other hand, upon reaching the apex location, starts increasing smoothly, until it exceeds the freestream RMS value downstream of the interaction region.

The introduction of the cavities underneath the interaction has both beneficial and detrimental effects in the RMS of the thermodynamic properties. From the dashed lines in Figure 4.22c one can conclude that the control method applied reduces the mean-normalised RMS, in general, while keeping the same trend. The presence of the holes can also be noted by the periodic oscillations of the curves. All quantities peak at the shock foot location as they did for the reference case. The peak value is smaller for pressure and density and remains the same for temperature. Pressure and density show a similar decaying behaviour after the initial peak, but this time the recirculation bubble and the shock system do not seem to be the ones driving the fluctuations. Instead, from the middle of the first cavity until its border, the RMS increases peaking in the region of the wall separating both cavities. The blowing of the second cavity dampens the fluctuations, but again a rising trend is observed as the air changes from the blowing to the suction portion of the second cavity. At the end of the second cavity, the maximum RMS values are reached for all variables, largely surpassing the magnitudes observed for the flat plate. Lastly, a sudden drop brings the RMS to the same post-interaction values as for $\mathcal{F}$. Temperature is the least affected quantity, displaying a very similar behaviour to the one previously found. Peaks are still present at the end of each cavity, and its at the end of the second one that the biggest difference can be found in comparison to the uncontrolled case.

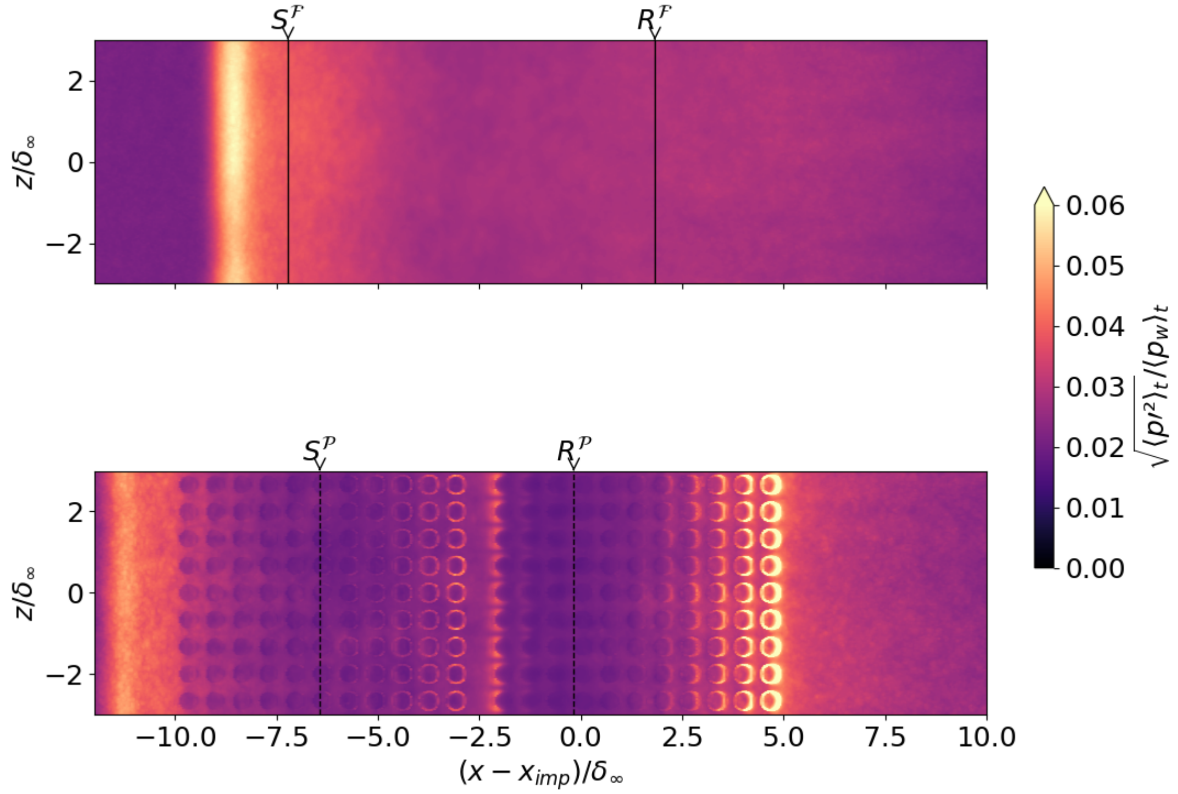

Figure 4.23: Time-averaged RMS pressure.

A better idea of where the pressure RMS is higher can be obtained by analysing the 2D distribution of this quantity at the wall. From Figure 4.23, one can conclude that the trailing portions of each cavity present large RMS magnitudes that can be associated with the impingement of the flow into the orifices walls (the dividing wall, for the first cavity and the end wall for the second cavity). This would explain why increased RMS magnitudes are found mainly in the three last rows of holes above each cavity, and only around the holes' edges, being higher in the rear portion of each perforation.

When analysing the flow inside the two cavities in terms of velocity components, pressure and temperature, both seem to have identical properties. Moreover, as seen in Figure 4.22a for $\mathcal{F}$, the second cavity should experience a less intense pressure gradient than the first cavity. However, all the higher fluctuations are found close to the rear part of the second cavity. This might be related to a combination of four different factors. The first is the difference in pressure gradient imposed from downstream to upstream within each cavity. This results in slower velocities of recirculation inside the cavity, allowing oscillations to 'concentrate' more in specific regions. The second factor is that the suction portion of the second cavity is placed close to the reattachment point, where considerable shear layer dynamics happen, in particular, the 'impingement' of the shear layer at the wall when it reattaches. Contrarily, the first cavity suction portion is placed underneath the recirculation bubble, which can be considered as an isolated portion of the flow that, from a global perspective, is shielded from the dynamics outside, despite still reacting to changes in the flow that affect, in particular, the separation and reattachment onsets. The third factor, which may also justify some of the oscillations in the rear of the first cavity, is the impingement of the flow into the holes walls as explained for Figure 4.23. Lastly, and arguably the most important factor is the presence of an unsteady compression fan at close to the 'trailing edge' of the second cavity as identified in Figure 4.8. Due to both convection and interaction phenomena, the reattachment compression fan displaces in the streamwise direction creating meaningful variations in the thermodynamics properties.

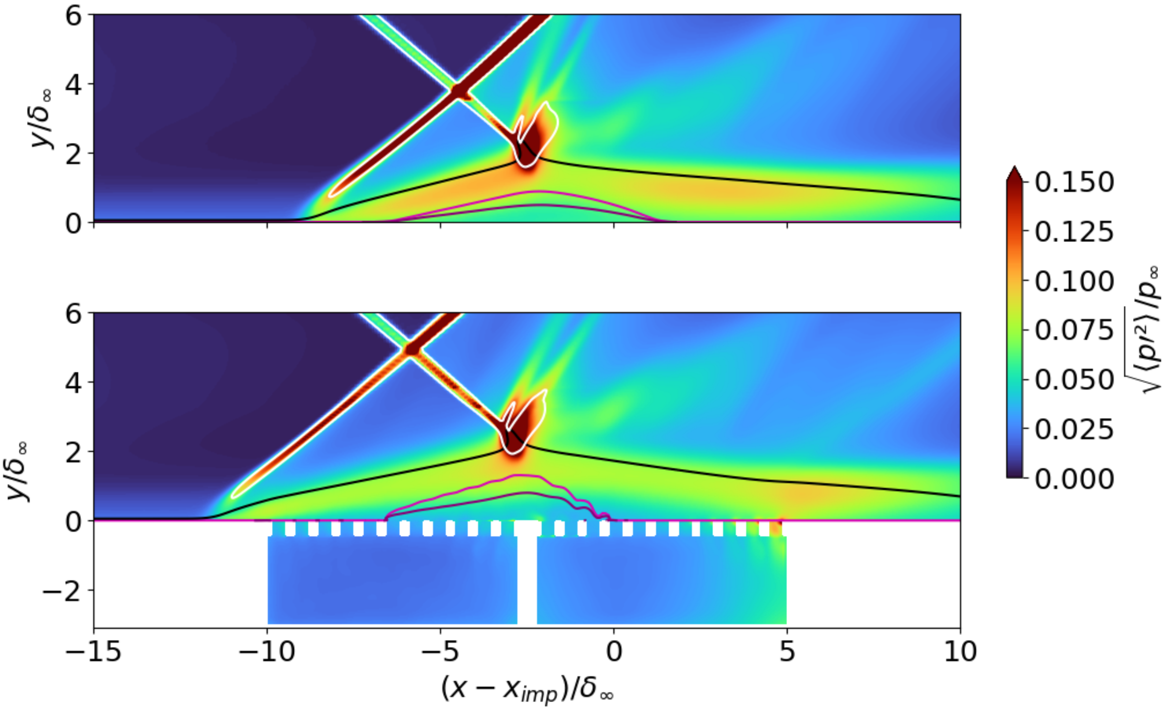

Figure 4.24: Span- and time-averaged pressure RMS. (—) $\langle u \rangle = 0$. (—) $\langle M \rangle = 1$. (WHITE) $|\nabla p|\delta_\infty/p_\infty = 1.2$. (—) dividing streamline: $\left\{(x, y_{ds}) \mid \int_0^{y_{ds}} \langle \rho u \rangle \, dy = 0\right\}$.

A third perspective on pressure RMS can be seen in Figure 4.24. The highest magnitudes are found along the separation shock and in the region of interaction between the transmitted shock and the detached shear layer. Also along the shear layer moderate magnitudes can be observed. In general, case $\mathcal{P}$ shows smaller magnitudes than the reference case, with a similar distribution. Interesting to note is the contour in the region of the reattachment compression fan. While no significant increase in pressure RMS can be found for the reference case, for the controlled case a light shade is observed emanating from the kink in the sonic line. This is indicative of a more coalesced compression fan. An analysis was made based on the solver's shock sensor to determine if this contour was related to the presence of a coalesced shock. The conclusion was that it was not a shock.

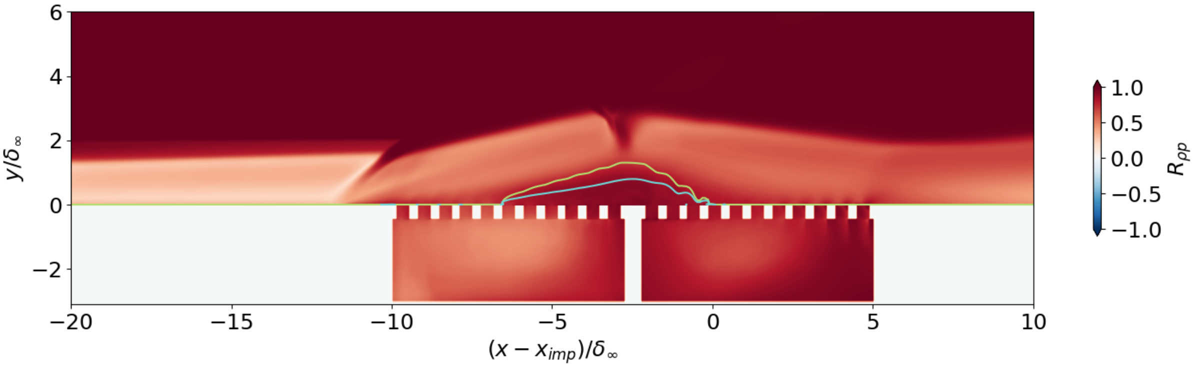

(a) Density - pressure.

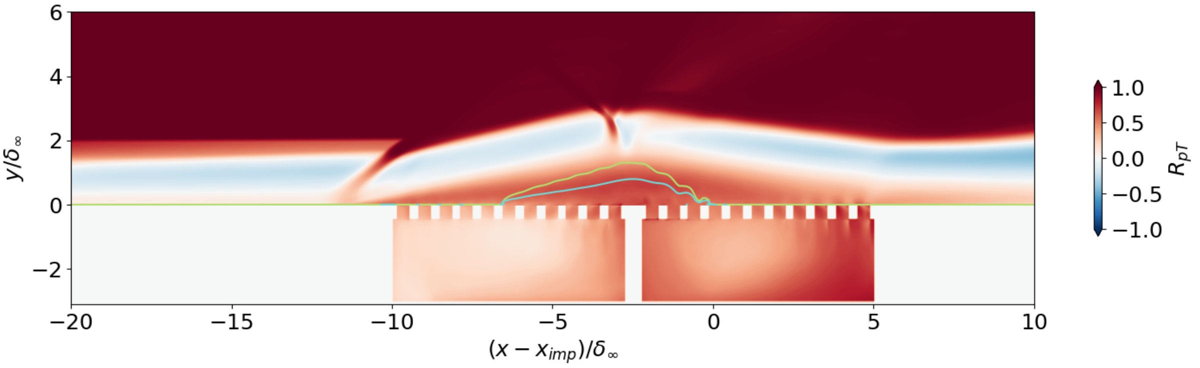

(b) Pressure - temperature.

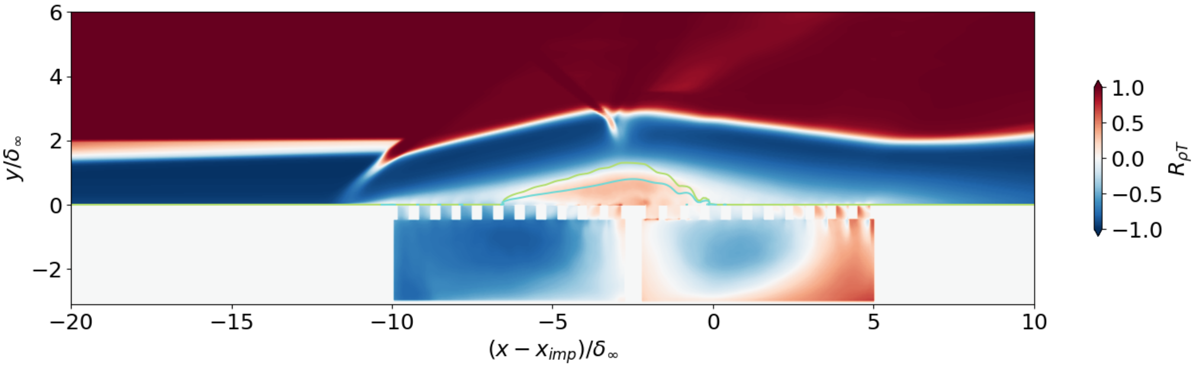

(c) Density - temperature.

Figure 4.25: Time-averaged cross-correlation coefficient between thermodynamic properties fluctuations. (—) $\langle u \rangle = 0$. (—) dividing streamline: $\left\{(x, y_{ds}) \mid \int_0^{y_{ds}} \langle \rho u \rangle \, dy = 0\right\}$.

To better understand how the different thermodynamic properties interact with each other one can look at the cross-correlation coefficient between the thermodynamic properties fluctuations as shown in Figure 4.25. The cross-correlation coefficient can be defined as $R_{xy} = \frac{\langle xy\rangle - \langle x\rangle\langle y\rangle}{\sqrt{\langle x^2\rangle - \langle x\rangle^2}\sqrt{\langle y^2\rangle - \langle y\rangle^2}}$. Both the controlled and the uncontrolled interactions have identical cross-correlation distributions above the wall. Therefore, only the cross-correlations for the controlled case are shown in Figure 4.25. The same plots for the reference interaction can be consulted in Appendix C. One-dimensional visualisations of these quantities for $\mathcal{F}$ and $\mathcal{P}$ in comparison to the undisturbed boundary layer at the virtual impingement point can be found in Appendix D.

The first observation that can be made is that all the plots have a correlation value of 1 for the freestream. This is expected from the ideal gas model assumed. Figure 4.25a confirms what was previously mentioned: pressure and density vary almost in the same way everywhere in the domain ($R_{\rho p} \approx 1$), meaning that an increase in pressure is always associated with an increase in density and vice-versa.

A positive correlation can also be found between pressure and temperature (Figure 4.25b) in the regions of the interaction where the flow is subsonic. The positive correlation between the two quantities near the wall was already visible from 4.22. In opposition, where the flow is supersonic, the correlation between pressure and temperature fluctuations is almost negligible, since the magnitude of the correlation coefficient is mostly below $R_{pT} \lesssim 0.1$.

The assumption of constant pressure inside the boundary layer in the wall-normal direction, helps to explain the almost perfect negative correlation $R_{\rho T}$ in the boundary layer and shear layer regions, represented in Figure 4.25c. Inside the bubble the flow is subsonic and all quantities remain approximately constant resembling static flow conditions. Inside the first cavity, the same negative correlation between density and temperature is found as for the shear layer. Nonetheless, the second cavity displays a region of positive correlation, associated with its suction portion, in the region where (as seen in Figure 4.22c) pressure fluctuations are the highest at the wall. In absolute value, pressure is the thermodynamic quantity that has the largest magnitude. Hence, to compensate for large pressure fluctuations both density and temperature must vary in the same direction ($R = const = \frac{p}{\rho T}$), which could justify the positive correlation found in this region.

4.3 Unsteadiness

In this section the unsteadiness of the STBLI is assessed by analysing the wall pressure signal as well as the bubble volume and the separation shock position signals. Furthermore, a comprehensive study was carried out to determine the times between variations of important quantities to define and characterise the unsteadiness.

Probes were placed along the centerline at the wall: 300 probes registered pressure and the three velocity components at a sampling frequency of $f_s \approx 26.5 u_\infty/\delta_\infty$. In addition of the centerline probes, for case $\mathcal{P}$, probes were also placed in the holes and inside the cavity, immediately above and below the wall, as well as in the middle of the cavity, distributed as shown in Figure 4.26, resulting in a total of 618 probes inside the domain.

All time-dependent analyses were carried considering only the part of the signals that came after the initial transient. The transient was considered to end at 7ms, or 15 FTTs. Figure 4.27 shows the evolution of the pressure fluctuations signals for the centerline probes closer to the mean separation and reattachment points for each configuration. From Figure 4.27 one can clearly conclude that the transient spans for about 4-5 ms for both cases. Hence, the choice of considering data after 7ms is justified.

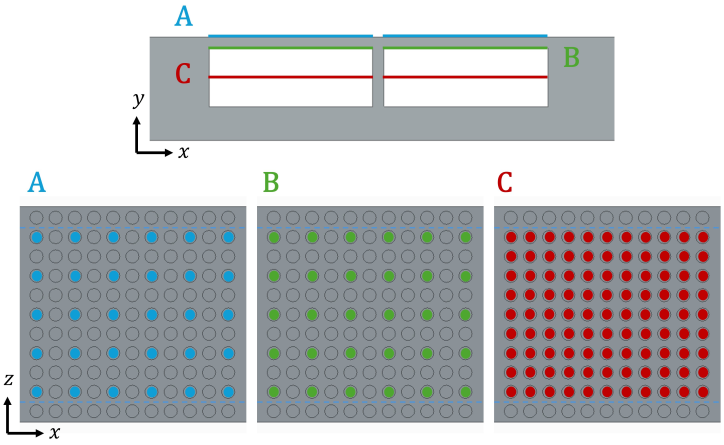

Figure 4.26: Placement of holes / cavity probes for case $\mathcal{P}$.

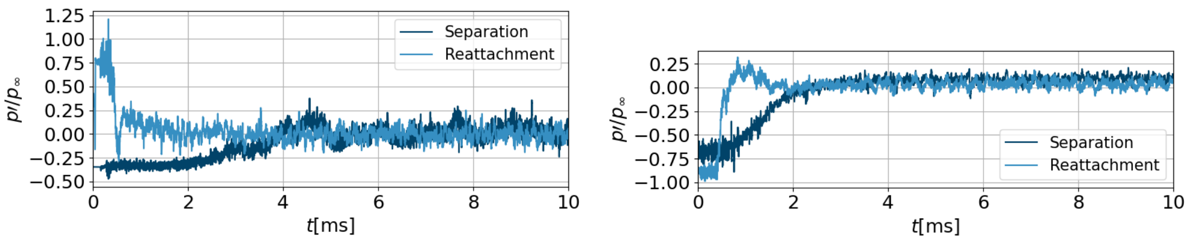

(a) Case $\mathcal{F}$.

(b) Case $\mathcal{P}$.

Figure 4.27: Pressure fluctuations signals evolution over time.

In this section several power spectral density (PSD) plots will be shown as well as coherence plots. All of these quantities have been computed with the Welch method using Hanning windows for better convergence and accuracy of the results, given the non-periodic nature of the signals evaluated. Table 4.3 summarises the parameters used in each case. The goal was to obtain similar window sizes in terms of considered time, by varying the number of segments/windows and the overlap between them, while ensuring that the difference between the captured variance and the real variance ($\Delta\sigma^2$) was as small as possible. Based on an iterative study the values presented in Table 4.3 were chosen. The different sampling rates between probes and snapshots justify the need to use different overlap/# segments.

Table 4.3: Welch parameters for PSD & coherence calculation.

		Overlap [%]	# segments	Δt [ms]	$\lvert\Delta\sigma^2\rvert <$ ... [%]
PSD (**Probes**)	Case $\mathcal{F}$	65	10	8.43	0.5
	Case $\mathcal{P}$	70	5	5.58	0.5
PSD & Coherence (**Snapshots**)	Case $\mathcal{F}$	80	15	4.31	2.5
	Case $\mathcal{P}$	80	12	3.86	10

Figure 4.28 shows how the pre-multiplied power spectral density (PSD) of the pressure fluctuations evolves across the interaction computed from probe data. For a more comprehensive understanding of the unsteadiness and to facilitate comparison with previous literature, the separation length Strouhal number is used instead of frequency, being defined as $St_{L_{sep}} = \frac{fL_{sep}}{u_\infty}$, where L_{sep} is always the mean separation length for the reference case $\mathcal{F}$ to allow a direct comparison between the results.

Before the upstream influence of the shock is felt both configurations show a spectrum composed of high-frequency fluctuations, characteristic of turbulent boundary layers. As soon as the interaction region is reached a sudden shift is verified towards lower frequencies for $\mathcal{F}$, associated with a Strouhal number range of $0.01 \lesssim St_{L_{sep}} \lesssim 0.1$. This broadband low-frequency dynamics is associated with the separation shock motion and the breathing motion of the recirculation bubble (as will be seen in Figure 4.32 and Figure 4.33). This is the same range of low-frequency unsteadiness found by Laguarda et al., 2024b for all the three Reynolds numbers tested. The perforated wall configuration also displays a shift towards lower frequencies. However, they are not as low as the ones verified for the reference case, being limited by a Strouhal number higher than $St_{L_{sep}} \gtrsim 0.3$. Frequencies below these Strouhal numbers do exist. Nonetheless, they are not as significant. The fact that the introduction of the resonant cavities changed the observed low frequencies suggests that it is possible to influence the dynamics of the SWTBLI through resonance. One will see later in Figure 4.29-C_{LEFT} that, indeed, the cavities are resonating at the observed frequencies. This observation also indicates that the dynamics of the SWTBLI are related to acoustic phenomena. The evidence is not enough, however, to indicate acoustics as the only underlying unsteady propagation mechanism, since, despite the verified frequency shift, lower frequencies are still present and were not completely mitigated.

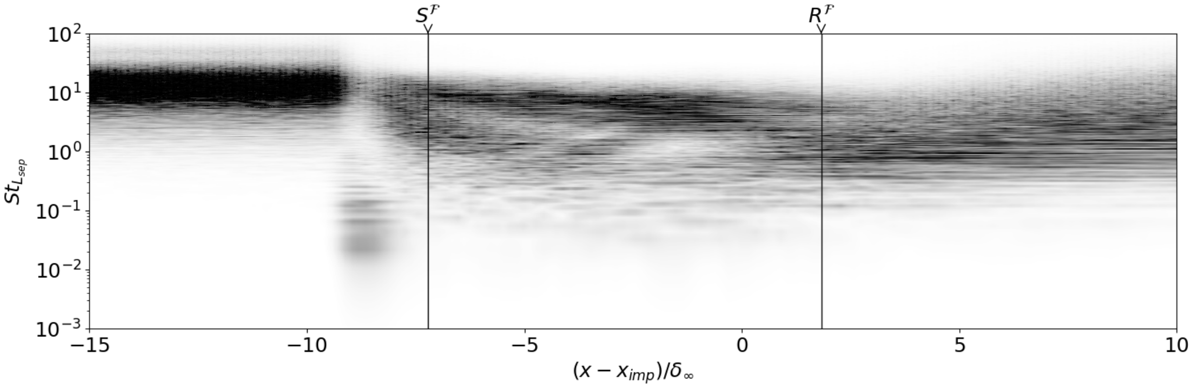

(a) Case $\mathcal{F}$.

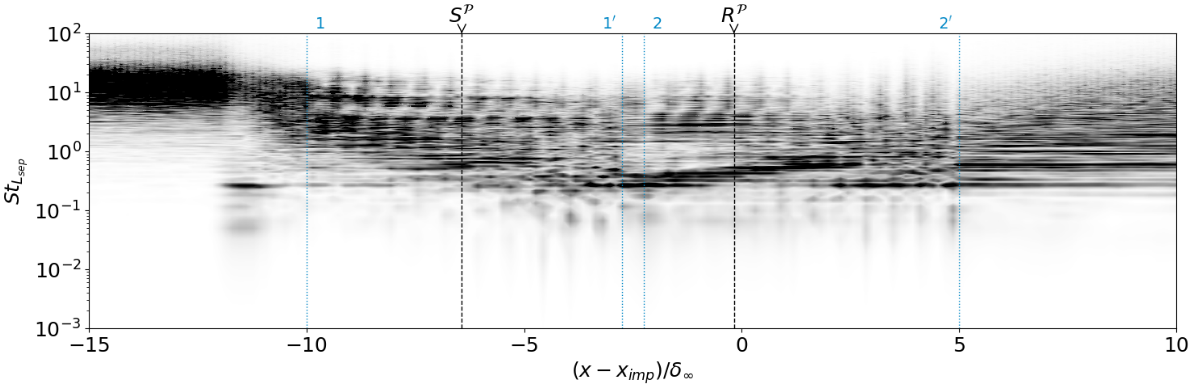

(b) Case $\mathcal{P}$.

Figure 4.28: Frequency-weighted variance-normalised power spectral density map of wall-pressure fluctuations along the centerline. Contour levels range from zero (WHITE) to 0.7 or higher (BLACK).

For the reference configuration a shift towards higher Strouhal numbers is observed inside the reverse flow region between the mean separation and reattachment points, with the lowest frequencies not present anymore. In this part of the interaction, the shear layer unsteadiness domains with oscillations in the order of $St_{L_{sep}} \approx 0.1$. Also, the boundary layer frequency content remains slightly below its undisturbed values. The controlled case shows a similar evolution, but this time, instead of being framed between the mean bubble it is delimited by the leading edge of the first cavity and the mean reattachment point. Another difference is the periodic pattern observed due to the perforations on the wall. Once again a "cut-off" frequency at $St_{L_{sep}} \approx 0.3$ can be noticed. Moreover, while for the reference case the most relevant frequencies within the separation region seem to be the higher frequencies associated with the incoming boundary layer, for the controlled case, even though these higher frequencies are still present, the most significant are the frequencies in the range $0.3 \lesssim St_{L_{sep}} \lesssim 1$, in particular in the front part of the second cavity where blowing occurs.

Inside the second cavity range and most prominently in its front part, there is an almost tonic frequency content at $St_{L_{sep}} \approx 0.3$, which will be later observed in the PSD of the wall-normal velocity fluctuations in Figure 4.29-RIGHT. This frequency slowly shifts to higher frequencies as one moves downstream up to Strouhal numbers of $St_{L_{sep}} \approx 1$. The shift observed may be linked to the different phenomena occurring: at the leading edge of the second cavity, the rear part of the bubble is still present. Hence, it is expected that the frequencies observed are closely related to the breathing motion of the bubble. As one moves downstream and the mean reattachment point is reached, the shear layer vortices reattachment dynamics and the fluid entrainment mechanism become dominant.

Once mean reattachment, for $\mathcal{F}$, and the second cavity edge, $\mathcal{P}$ are reached, the most important frequencies are of the order of $St_{L_{sep}} \approx 0.1 - 1$, associated with the reattachment of the shear layer vortices. Higher frequencies begin to reappear as the boundary layer recovers downstream of the interaction, while all the low-frequency dynamics is no longer observed.

One is also interested in verifying the effectiveness of the cavities in dampening low-frequency oscillations by dissipating energy through resonance. To do so, the pressure fluctuation PSDs of all the probes in a given streamwise location for a specific group of probes (see A, B and C groups in Figure 4.26) are averaged and plotted in the contours presented in Figure 4.29-LEFT.

Figure 4.29-A_{LEFT}, does not introduce any new information in comparison to the one already shown in Figure 4.28b since the probes in this contour are located above the wall. As expected the contour looks similar to the ones presented in Figure 4.28b. As one moves to immediately below the wall (Figure 4.29-B_{LEFT}) a similar contour as for above the wall is obtained for the second cavity, with the lower frequencies becoming more relevant. However, the energy content increases at higher frequencies in the first cavity. The reason for this discrepancy is not clear. Nonetheless, comparing Figure 4.29-B_{LEFT} with Figure 4.28b at $St_{L_{sep}} \approx 0.3 - 0.4$, one can verify that in the same frequency range above the wall, there are small peaks associated with each perforation for the PSD along the centerline probes.

Inside the cavities (Figure 4.29-C_{LEFT}), 'symmetry' is reached as both cavities present similar frequency contents in homonymous regions. This symmetry is indicative of the resonance inside the cavities, with the higher frequencies being related to the harmonics of the fundamental frequency $St_{L_{sep}} \approx 0.3$. Overall, the desired resonance frequency of $St_{L_{sep}} \approx 0.03$ is not observed anywhere in the cavities. This may be related to the accuracy of the formulas used in the geometry-defining optimisation problem or to flow-related features that excite the frequencies observed. However, the most plausible cause is the pressure gradient inside the cavities, which is not considered in the formulas used, where pressure is assumed constant inside the cavities.

In Helmholtz resonators, the resonance is mainly concentrated in the neck of the resonator, while all the air below it works as a dumper. Hence, it is also relevant to analyse the PSD for the wall-normal velocity fluctuations presented in Figure 4.29-RIGHT. Inside the cavities (Figure 4.29-C_{RIGHT}) a broadband of frequencies in the low-medium range can be found with no particular frequency standing out.

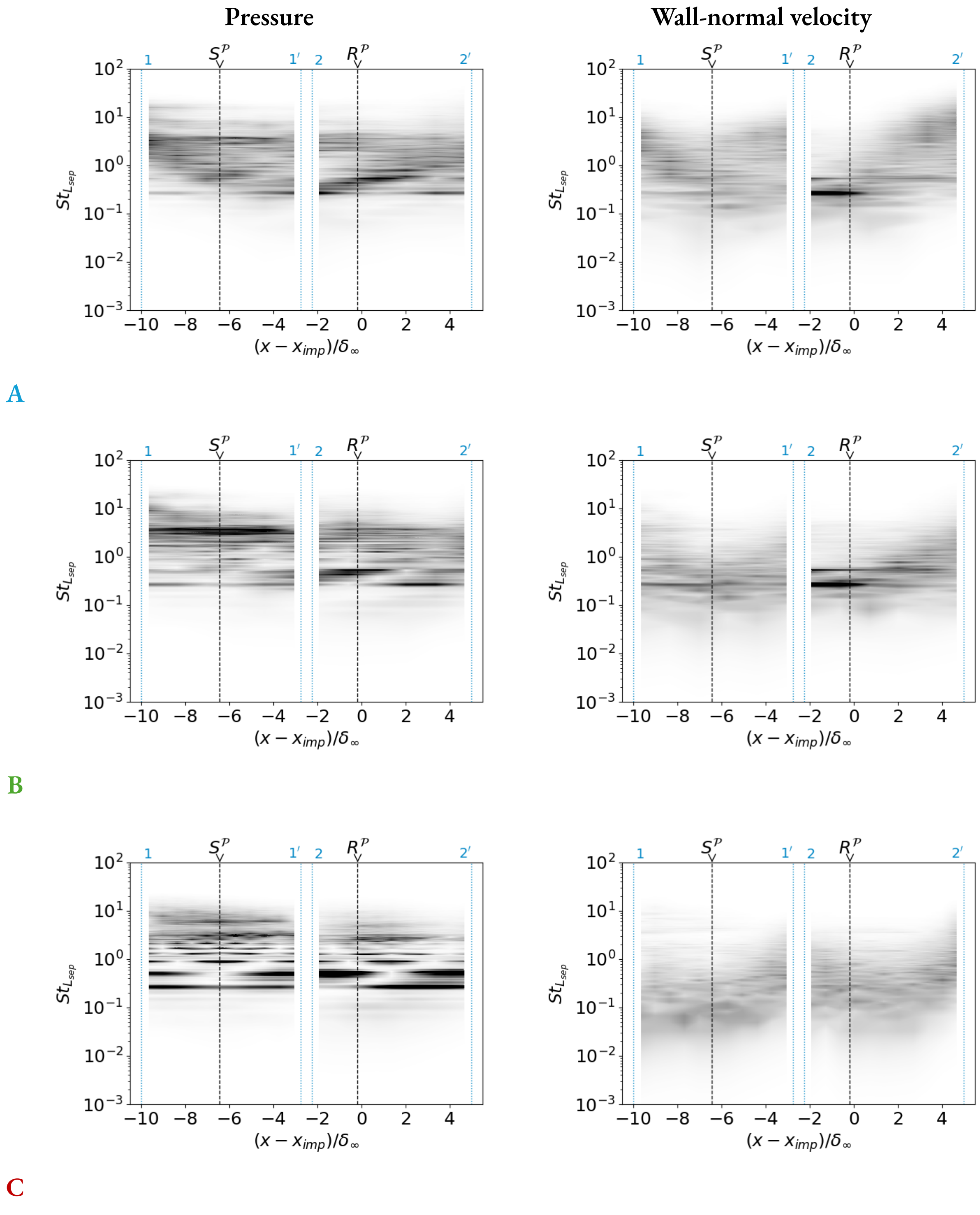

Figure 4.29: Frequency-weighted variance-normalised power spectral density map of (LEFT) wall-pressure fluctuations and (RIGHT) wall-normal velocity fluctuations in the cavities region. Contour levels range from zero (WHITE) to 1 (BLACK). Each row represents a sampling region as identified in Figure 4.26.

Contrarily, above and below the wall (Figure 4.29-A_{RIGHT} and Figure 4.29-B_{RIGHT}, respectively), the frequencies found are, in general, higher than inside the cavities and a region of very high energy is concentrated upstream of the mean reattachment point over the second cavity at a Strouhal number of $St_{L_{sep}} \approx 0.3$. The cause for this peak can be associated with the bubble breathing motion and its variations in volume. In the same way, also the separation shock motion may be responsible for the observed peak. This hypothesis is based on the following discussion on the time signals and PSDs for the bubble volume and the separation shock motion. Lastly, note that for the first cavity, below the wall, the wall-normal fluctuations PSD no longer shows a tonal peak at $St_{L_{sep}} \approx 0.3 - 0.4$ as for the pressure fluctuations PSD in Figure 4.29-B_{LEFT}.

In Figure 4.30 and Figure 4.31 the time signals and the probability density functions (p.d.f.) of the bubble volume variation and the separation shock location are shown, respectively. The p.d.f. plots were computed using the histogram method. The number of bins to use was determined based on the Freedman-Diaconis rule (Freedman & Diaconis, 1981; Scott, 1979), which is given by

$$\text{Bin width} = 2\frac{IQR}{\sqrt[3]{n}}, \tag{4.1}$$

where IQR is the interquartile range and n the number of samples.

The bubble volume was computed as the sum of the volume of all cells in which the condition $u < 0$ was verified at a given time. The shock location, on the other hand, was determined based on the location of the first local maximum of the pressure gradient magnitude, $|\nabla p|$ in the streamwise direction at a wall distance of $2.5\delta_\infty$. By identifying the first local maximum for each spanwise coordinate one obtains a shock front that is then averaged in span to obtain a single x coordinate for each snapshot.

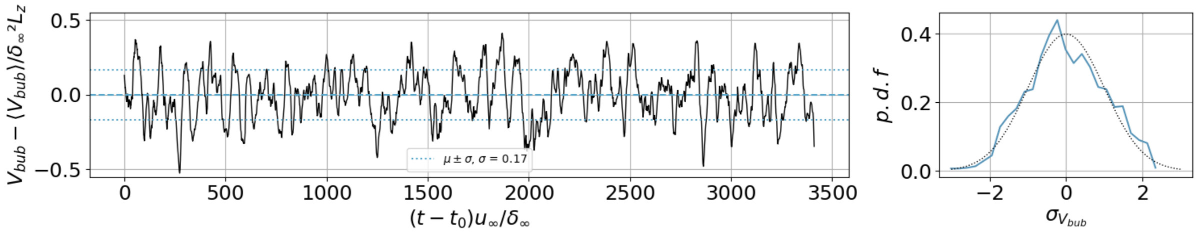

(a) Case $\mathcal{F}$.

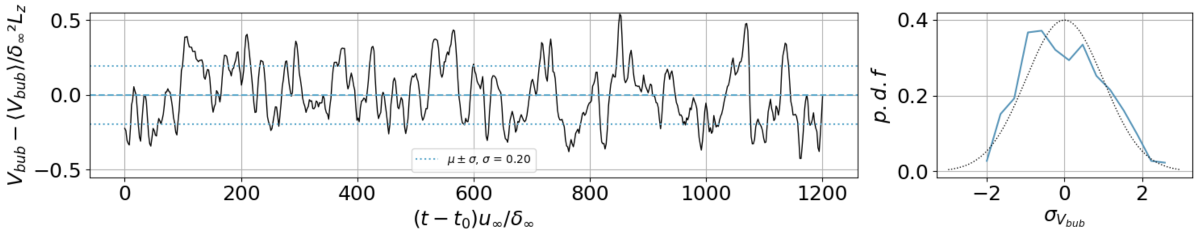

(b) Case $\mathcal{P}$.

Figure 4.30: Bubble volume signal. (LEFT) instantaneous fluctuations signal. (RIGHT) normalised p.d.f., in (——) and Gaussian distribution in (······).

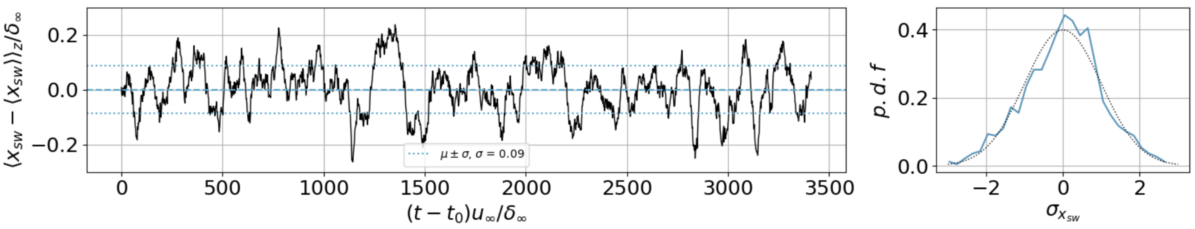

(a) Case $\mathcal{F}$.

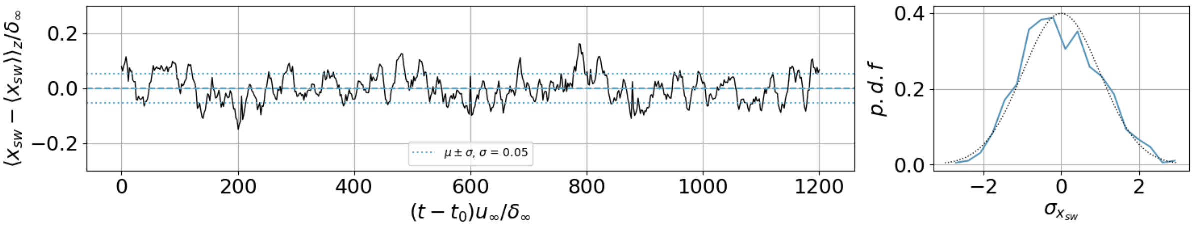

(b) Case $\mathcal{P}$.

Figure 4.31: Separation shock location signal. (LEFT) instantaneous fluctuations signal. (RIGHT) normalised p.d.f., in (——) and Gaussian distribution in (⋯⋯).

By analysing the time signals it is possible to conclude that both signals present both high- and low-frequency oscillations. Regarding the shock excursion range, it can vary up to $0.2\delta_\infty$ in comparison to its average location, with a standard deviation of about half that value. Note that the different time ranges, make the plots related to the controlled configuration appear less oscillatory.

The second to fourth statistical moments of each signal are presented in Table 4.4. The mean is not included, since it is zero for all signals. Variance, skewness and kurtosis are shown. The variance gives an idea of how spread the data is. In this case, it is indicative of how much the quantities evaluated can deviate from the average. One can conclude that the bubble volume can vary more and the shock location less for $\mathcal{P}$, in comparison with the reference case.

Skewness gives an idea of the asymmetry of the probability distribution, with positive skewness meaning a longer right tail. Despite the discrepancies in the values, when analysing the p.d.f. of each signal, it is possible to conclude that all the signals are essentially symmetric. One should highlight, however, a trend in higher skewnesses for the controlled case, with a change in the sign being found for the shock location signal.

Lastly, the kurtosis is an indicative of the tailedness or peakedness of the signal. For a Gaussian distribution, $\mathcal{K} = 3$. The values presented in Table 4.4 are the deviation from that value. All signals have lower kurtosis than a normal distribution, indicating that most of the fluctuations concentrate closer to the mean and extreme oscillations are less likely.

Table 4.4: Statistical moments for bubble volume and shock location fluctuations signals.

		$\sigma^2\,(\mathcal{M}_2)$	$S\,(\mathcal{M}_3)$	$K\,(\mathcal{M}_4)$
V_{bub}	Case $\mathcal{F}$	0.028	0.009	-0.478
	Case $\mathcal{P}$	0.038	0.244	-0.669
x_{sw}	Case $\mathcal{F}$	0.007	-0.135	-0.080
	Case $\mathcal{P}$	0.003	0.195	-0.324

The presence of low-frequency variations in the interest quantities can be further observed in the pre-multiplied normalised PSD plots in Figure 4.32 and Figure 4.33. The PSDs were computed from snapshot data. For completeness, the PSDs for the other dynamic quantities considered in the analysis can be consulted in Appendix E.

The recirculation bubble volume (Figure 4.32) presents a more dispersed spectrum than the shock position (Figure 4.33a). For $\mathcal{F}$ the bubble volume frequencies concentrate at Strouhal numbers smaller than 0.2. While it still shows a peak at $St_{L_{sep}} \approx 0.03 - 0.04$, the most relevant frequencies are concentrated at $St_{L_{sep}} \approx 0.1 - 0.2$. As suggested by Babinsky and Harvey (2011) and Morgan et al. (2013) these frequencies can be associated with the flapping of the shear layer and the large turbulent coherent structures formed upon the lifting of the shear layer from the wall. According to Piponniau et al. (2009) these oscillations can be responsible for the mass entrainment mechanism that allows the *breathing motion* of the bubble, characterised by periodic expansions and contractions. For the perforated wall, a similar distribution is verified. However, the lower frequencies gain preponderance, while the peak at $St_{L_{sep}} \approx 0.2 - 0.3$ is still maintained.

On the other hand, a clear frequency shift is observed for the separation shock position. While in the reference case, the PSD concentrates most of its energy in the low-frequency range (Figure 4.33), associated with Strouhal numbers smaller than 0.1, with its peak being located at $St_{L_{sep}} \approx 0.03 - 0.04$, for $\mathcal{P}$ Strouhal numbers smaller than 0.1 are no longer relevant; a clear isolated peak at $St_{L_{sep}} \approx 0.2 - 0.3$ is present (Figure 4.33b). The peak values observed for $\mathcal{F}$ agree with the ones previously reported as the characteristic unsteady frequency for the separation shock position by M. Wu and Martín (2007), Priebe and Martín (2012), Pasquariello et al. (2017) and Laguarda et al. (2024b).

For the controlled STBLI, the Strouhal number found for the peak is the same as the one observed for the wall-normal velocity and pressure fluctuations in the second cavity as well as for the bubble volume. The fact that this particular frequency, that is found relevant for different quantities, is particularly linked to the second cavity suggests that the STBLI dynamic behaviour in the controlled case is mostly linked to what happens close to the mean reattachment point. While resonance at $St_{L_{sep}} \approx 0.3$ is found in both cavities, clear peaks in the wall-normal and pressure fluctuations PSDs are observed at this frequency only for the second cavity.

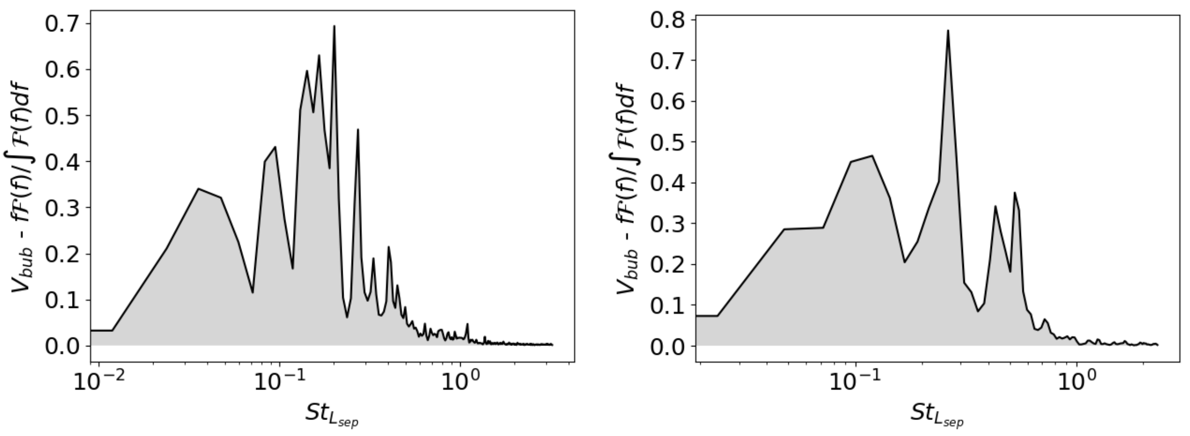

(a) Case $\mathcal{F}$.

(b) Case $\mathcal{P}$.

Figure 4.32: Pre-multiplied normalised power spectral density (PSD) of the bubble volume signal.

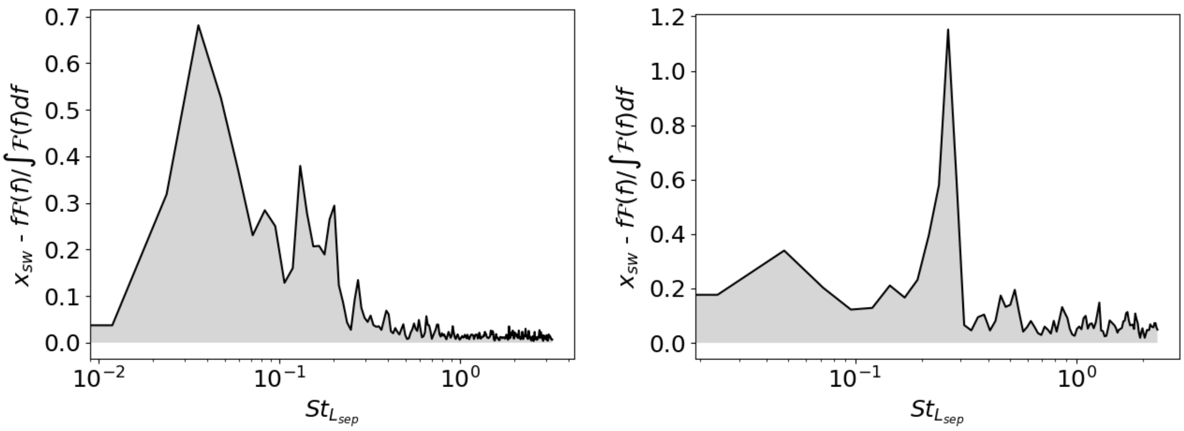

(a) Case $\mathcal{F}$.

(b) Case $\mathcal{P}$.

Figure 4.33: Pre-multiplied normalised power spectral density (PSD) of the separation shock location signal.

Additionally, by comparing the cross-correlation plots between the pressure at the reattachment point and V_{bub} (bubble volume) and x_{sw} (shock location) for both cases (see Figure G.55 and Figure G.57 in Appendix G and Figure H.19 and Figure H.21 in Appendix H), one can conclude that where previously there was virtually no correlation for $\mathcal{F}$, there is now a peak of $\approx$ 0.5 and $\approx$ 0.3 at very small time shifts for $\mathcal{P}$, between the pressure at reattachment and V_{bub} and x_{sw}, respectively. Moreover, the high correlation peaks found for the pressure probes close to the mean reattachment point are no longer found for the probes near the mean separation point, further strengthening the hypothesis that the dynamics at the rear portion of the recirculation bubble are responsible for the unsteady behaviour in the controlled case.

One should stress that for the reference case, the pressure at reattachment is taken locally for a single probe, while for the controlled case, it is averaged over the probes aligned in the spanwise direction. Nonetheless, using only one local probe for $\mathcal{P}$ yields already peaks in the cross-correlations that were not previously found for the reference configuration (as seen in Figure 4.34), which provides further evidence for the observations made.

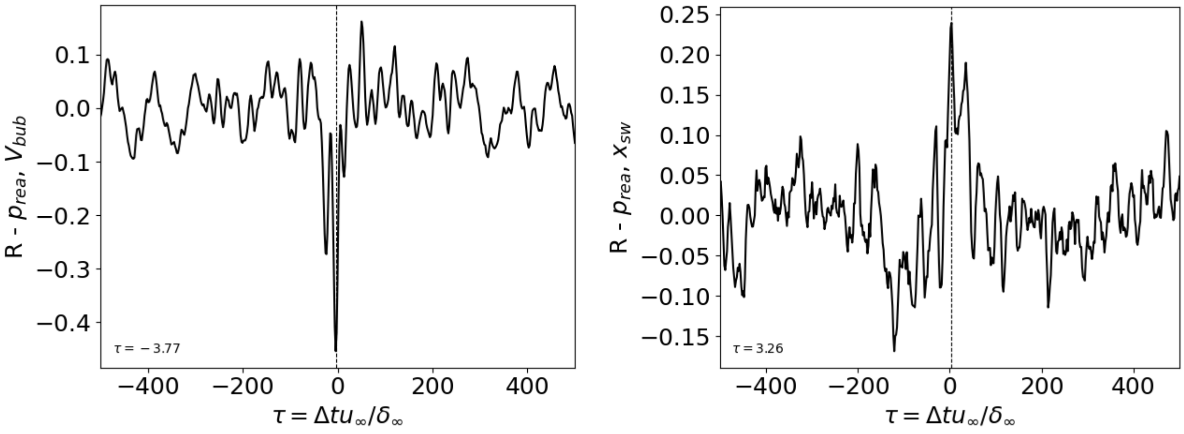

Figure 4.34: Cross-correlation coefficient between pressure close to mean reattachment point and bubble volume/shock location signals for case $\mathcal{P}$ (from single centerline probe).

More information about the mechanism driving the unsteadiness can be derived from the cross-correlation and coherence plots presented in Figure 4.35 and Figure 4.36. A strong negative correlation can be found between the variation of the bubble volume and the shock foot location in both cases. This means, that for a positive variation of the bubble volume, which is associated with an upstream movement of the separation point and a downstream movement of the reattachment point (i.e. an expansion motion), the shock moves upstream. Indicated in the cross-correlation coefficient plots is also the time shift for which this maximum absolute amplitude peak is found. In both cases, the time shift is negative, indicating that the shock motion lags behind the variation of the recirculation region volume, by a non-dimensionalised time of $\tau = \Delta t u_\infty / \delta_\infty \approx 14.4$ and $\tau = \Delta t u_\infty / \delta_\infty \approx 31.0$, for $\mathcal{F}$ and $\mathcal{P}$, respectively.

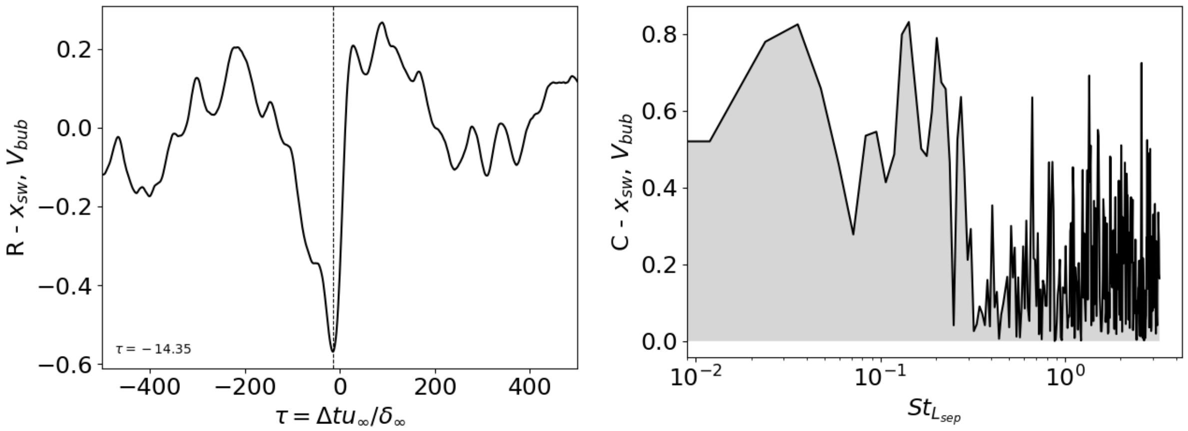

(a) Cross-correlation coefficient.

(b) Coherence.

Figure 4.35: Cross-correlation coefficient and coherence between bubble volume and separation shock location signals for case $\mathcal{F}$.

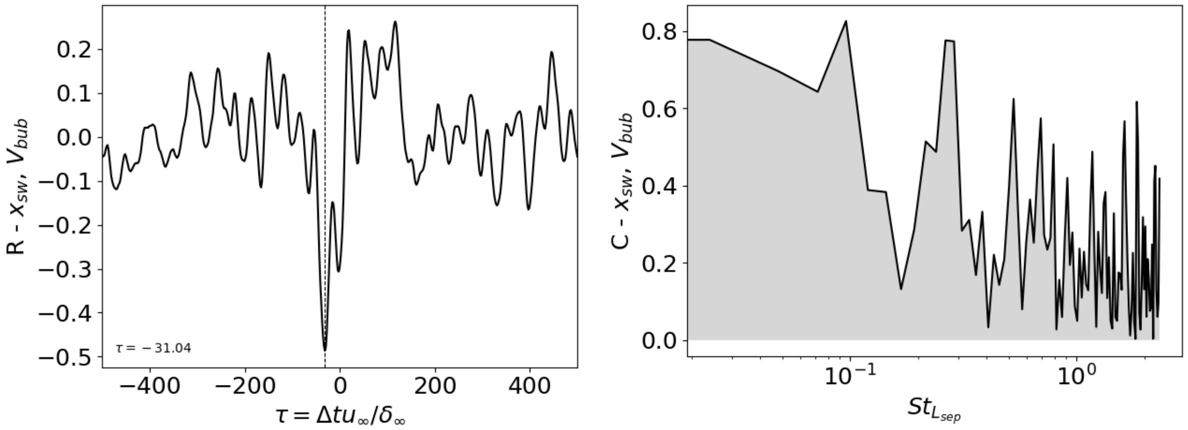

(a) Cross-correlation coefficient.

(b) Coherence.

Figure 4.36: Cross-correlation coefficient and coherence between bubble volume and separation shock location signals for case $\mathcal{P}$.

Also the coherence between the two signals is shown in Figure 4.35 and Figure 4.36. The coherence can be understood as the cross-correlation over the frequency spectrum. For the quantities presented it means that the two signals are more correlated at lower frequencies, associated with Strouhal numbers of $St_{L_{sep}} \approx 0.03 - 0.04$ and also at $St_{L_{sep}} \approx 0.1$, reaching values as high as 0.8. For the remaining high-frequency spectrum, the data shows a lot of oscillations, that for this analysis are interpreted as noise given the small data set used to compute the Fourier transform and the large variance not captured as indicated in Table 4.3.

4.3.1 Considerations on the Unsteady Mechanism

A similar analysis can be performed among all variables of interest to describe the STBLI unsteadiness. By doing that one can obtain the various cross-correlation coefficients as well as the non-dimensional time shifts between each two of the interest variables. The plots for the cross-correlations and coherences between all dynamic properties considered can be found in Appendix G and Appendix H, for $\mathcal{F}$ and $\mathcal{P}$, respectively.

The outcomes of this analysis will be presented separately for each case since each analysis provides information on case-specific observed phenomena, that make sense in the particular context of each interaction.

Reference Case

A diagram is presented in Figure 4.37 with a summary of the time shifts between the dynamic variables considered as the strenght of the correlation between them. The diagram presented suggests that variations in the bubble height trigger the remaining events, namely the change in volume, followed by a change in the separation length, proceeded at last by the motion of the separation shock. The time shifts found between the variables are coherent despite not matching perfectly, strongly suggesting that the order presented is the one determining the unsteady behaviour of SWTBLIs.

The strongest correlations are found between the variation in height and volume of the recirculation bubble and between the latter and the shock location. These are the links that can be considered more relevant given their magnitude.

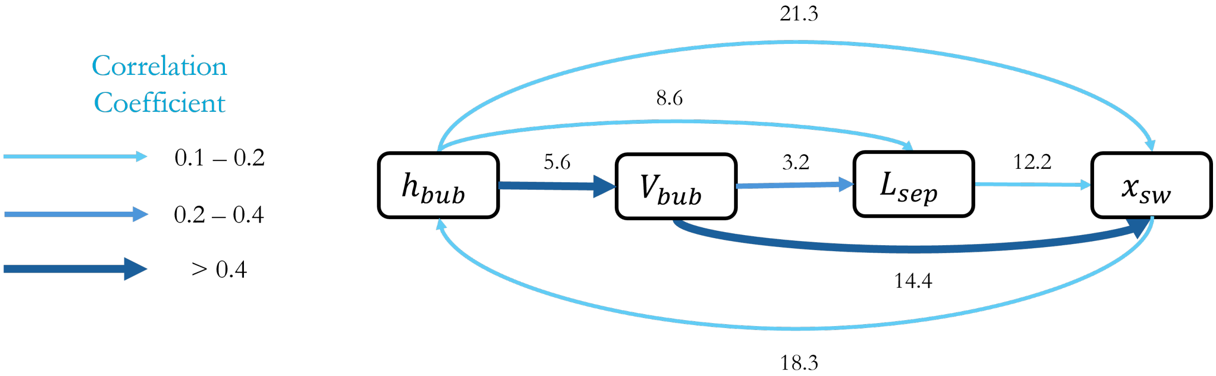

Figure 4.37: Diagram of the relation between bubble properties and separation shock location, based on the non-dimensionalised time shift $\tau = \Delta t \frac{u_\infty}{\delta_\infty}$ between time signals for reference case $\mathcal{F}$.

Note that two arrows connect h_{bub} and x_{sw}. This is because the cross-correlation between these two variables presents two peaks around $\tau = 0$: a positive and a negative (see Figure G.61 in Appendix G). This fact showcases the cyclical dynamic of the interaction with periodic breathing motions of the bubble along with periodic shock excursions in the streamwise direction. The exact mechanism linking the two events is not clear, though. However, the coherence found between the variables consider may shed light on the sequence of events driving the unsteadiness of SWTBLIs.

Another argument that further strengthens this relation between the quantities and points to the importance of these observations is the acoustic propagation time between the bubble apex (related to the bubble height, h_{bub}) and the separation and reattachment points. Based on the average speed over the points in each portion of the dividing streamline and the distance between the points time shifts of 8.9 and 5.6 were computed in the upstream and downstream directions, respectively (see Figure 4.38). Returning to Figure 4.37 one can notice that these values coincide almost perfectly with the time shifts between the bubble height and the separation length and bubble volume signals, respectively. Given this fact, it is plausible to hypothesise that a movement of the reattachment point causes a variation in the bubble volume, preceding the movement of the separation point and causing a change in the separation length. Furthermore, given the fact that both these shifts are computed with respect to the bubble apex, it is also plausible to consider that the interaction of the detached shear layer with the impinging shock (that occurs close to the apex) is leading all the dynamics.

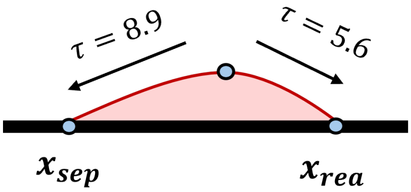

Figure 4.38: Schematics of bubbles acoustic propagation time between bubble apex and separation and reattachment points for reference case $\mathcal{F}$.

A good way to better verify the hypothesis presented would be to compute the cross-correlation and coherence between the separation and reattachment locations and the quantities presented in Figure 4.37. This study was carried out. However, the results found in terms of time shifts were not coherent with the ones presented. This is due to the difficulty to accurately determine the separation and reattachment point for each snapshot. Three different ways were tested. The first was based on the position where $\langle C_f \rangle_z$ crosses zero; the second was based on the locations where the dividing streamline y-coordinates gradient becomes constant; the third relied on the identification position where the pressure would cross the mean separation and reattachment pressure thresholds.

Figure 4.39 presents the cross-correlation coefficients and coherence between the separation point, computed in the three different ways mentioned, and the separation shock location signals. As observed, each of the three ways of determining the separation point yields a different correlation peak magnitude, time shift and even coherence distribution. Hence, none of these methods seems to be reliable for a time analysis. Despite not being shown here, this lack of agreement was also verified between the separation point and all the other quantities. The same was observed for the reattachment point. The plots showing it can be consulted in Appendix G

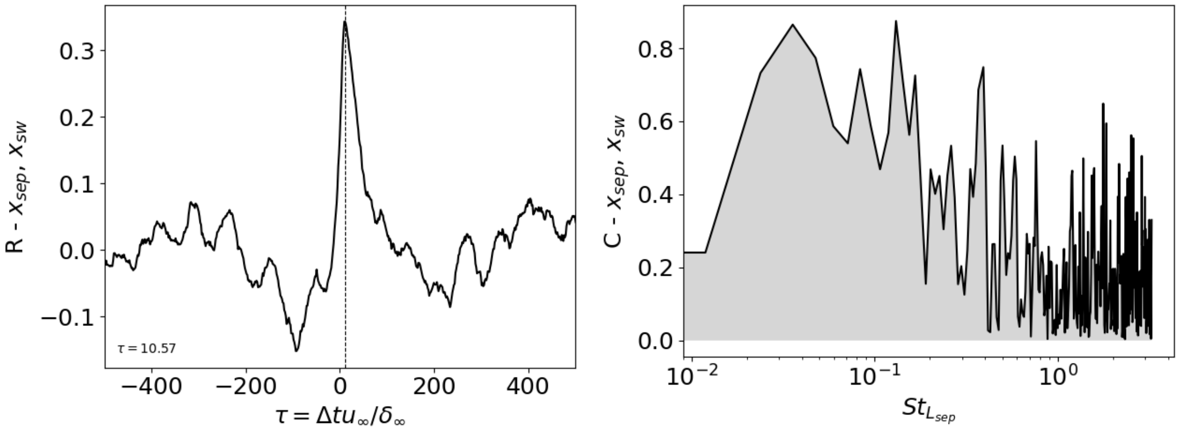

(a)

(b)

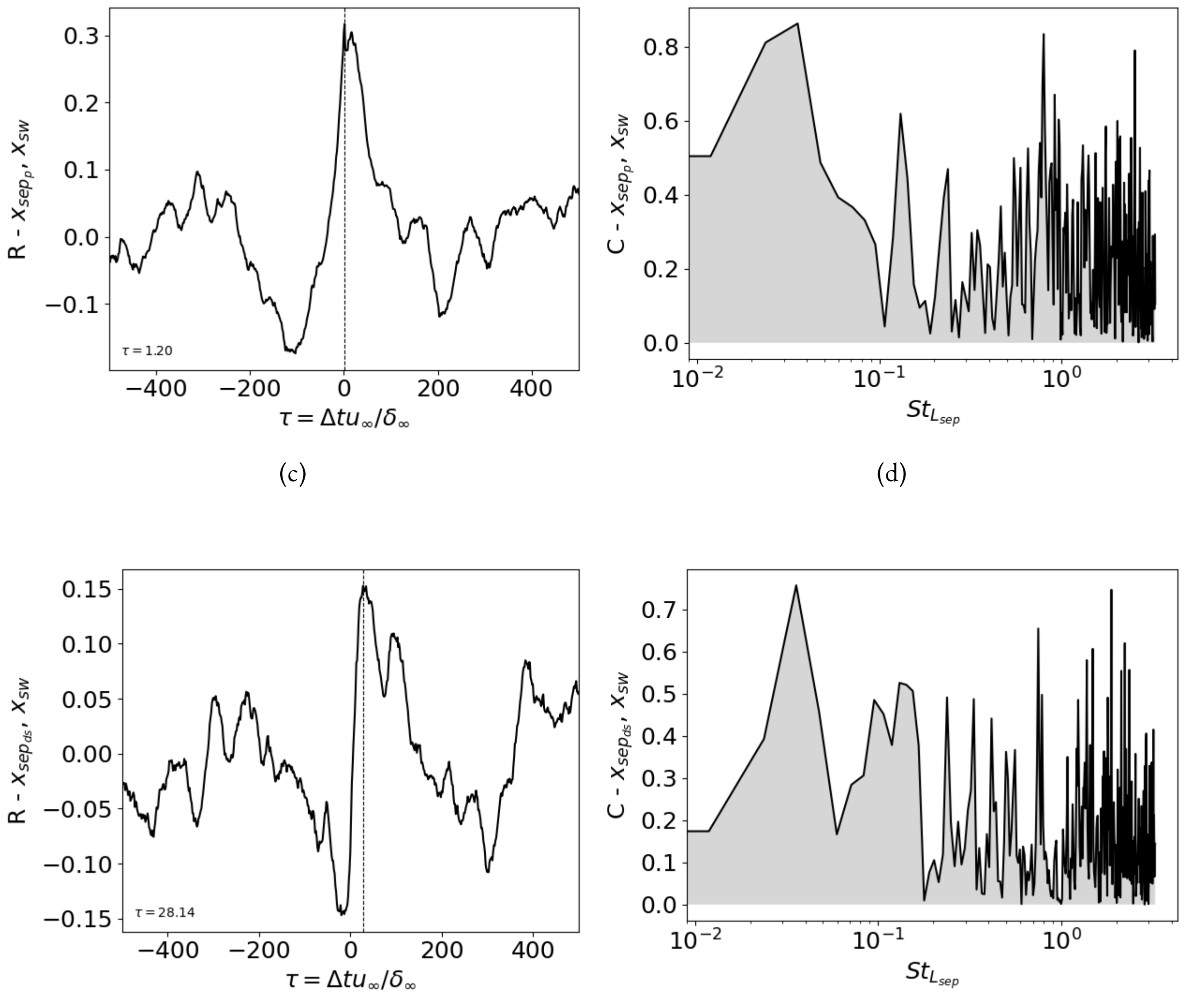

(c) (d)

(e) (f)

Figure 4.39: Cross-correlation coefficient and coherence between separation point and separation shock location signals.

As a final remark, it is important to stress that as can be inferred from Figure 4.37, not all cross-correlation coefficients have as high magnitudes as desired to strengthen the conclusions drawn. Likewise, another important aspect to keep in mind is that correlation is not causality. Hence the exact succession of dynamic events may occur in a slightly different way than the one suggested. However, despite all these precautions, the coherence found is striking and gives a clear clue into the mechanism driving the unsteadiness in SWTBLIs.

Controlled Case

In a similar way to what was done for the reference case, a similar study was carried out for the controlled interaction. The diagram containing the time shifts is shown in Figure 4.40. Several differences can be noted from what was observed for the flat plate configuration.

The first difference is that the cross-correlation between h_{bub} and x_{sw} is no longer anti-symmetric around $\tau = 0$. Hence, only one arrow connects both quantities. The second difference is the increase in correlation coefficient between the two previously mentioned quantities and the decrease between V_{bub} and L_{sep}. Lastly, the most important variation has to do with the lack of coherence between the time shifts. While all time shifts seemed to be related and in agreement with the reference case, in this case, no relation is found anymore.

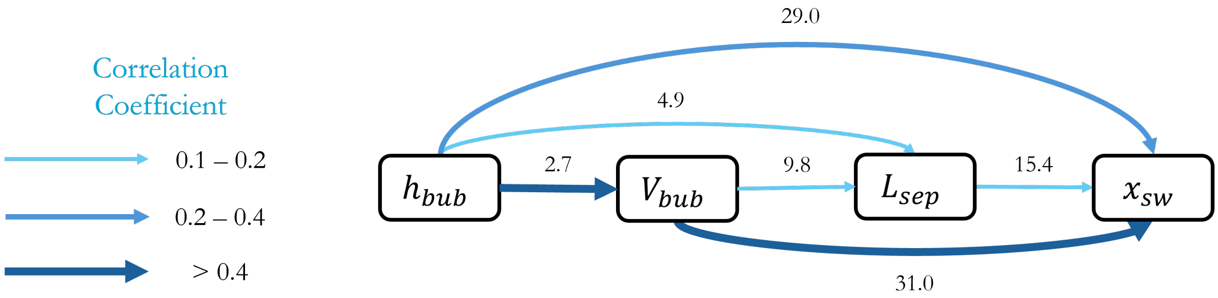

Figure 4.40: Diagram of the relation between bubble properties and separation shock location, based on the non-dimensionalised time shift $\tau = \Delta t \frac{u_\infty}{\delta_\infty}$ between time signals for study case $\mathcal{P}$.

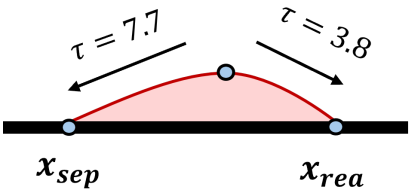

Figure 4.41: Schematics of bubbles acoustic propagation time between bubble apex and separation and reattachment points for study case $\mathcal{P}$.

However, when analysing the acoustic propagation speed of a perturbation from the bubble apex to the separation and reattachment points (as shown in Figure 4.41) the value found for the propagation to the reattachment point is almost the same as the time shift between V_{bub} and h_{bub}. This observation suggests that the mechanisms associated with reattachment still play a significant role in the STBLI dynamics, while the ones related to separation are now decoupled. This observation is in agreement to what was previously documented in Figure 4.34. The hypothesis grows even stronger if one recalls the peaks found in the PSD contours for the pressure and wall-normal velocity fluctuations close to reattachment as well as the agreement of these peaks with the most energetic frequencies found for the shock motion and the bubble volume signals.

CHAPTER 5

Conclusions & Recommendations

In this thesis a passive control method for a Mach 2 shock wave turbulent boundary layer interaction has been presented. Wall-resolved large-eddy simulations were performed for both the uncontrolled and the controlled interactions. The uncontrolled case consisted of a canonical impinging shock flat plate interaction, while the controlled case included a wall with perforations placed over two separated Helmholtz-like resonator cavities. The goal of this thesis was to gain further insight into the flat plate canonical interaction as well as to determine whether the passive control method implemented would bring any benefits in terms of flow separation reduction and reflected shock low-frequency unsteadiness mitigation.

For the reference case ($\mathcal{F}$), similar results were found to the ones obtained by Laguarda et al. (2024b). Without any control, the adverse pressure gradient imposed by the impinging shock to the incoming boundary layer leads to flow separation and to the formation of a recirculation bubble. After the shock foot, the shear layer detaches and growth in the turbulent structures is observed up to the bubble apex. There, turbulence is damped, before being re-amplified further downstream at reattachment, as the boundary layer starts recovering. The Reynolds stress components present high magnitudes in particular in the region of the detached shear layer, with the location of the maxima varying depending on the specific component.

The skin-friction coefficient presents a shape characteristic of moderate friction Reynolds numbers, which is a combination of a W-shaped curve (typical of low Reynolds numbers) and a plateau-like curve (typical of high Reynolds numbers). The bubble closely resembles a perfect isosceles triangle with its upstream portion being very similar to the downstream one. The thermodynamic properties along the wall agree with previous literature, with the maxima for the RMS being located after the shock foot, before the mean separation point.

In terms of unsteady behaviour, low-frequency unsteadiness is observed at $St_{L_{sep}} \approx 0.03$, for both the reflected shock and the bubble breathing motions. Along the centerline the low-frequencies are particularly concentrated in the region close to the shock foot, increasing downstream to $St_{L_{sep}} \approx 0.1 - 1$, which are related to the flow entrainment mechanisms and the shear layer reattachment dynamics. Based on the time analysis performed, a sequence of events was suggested for the unsteady mechanism, with bubble height variations leading the unsteady behaviour that is then acoustically propagated to the separation and reattachment points, making other dynamic properties vary. The variation in bubble height is closely related to the interaction between the impinging shock and the detached shear layer close to the bubble apex.

With regard to the controlled interaction (case $\mathcal{P}$), analysis of the instantaneous shows that the dampening of the turbulent structures at the bubble apex is more significant. For the mean flow, one could observe that the intersection between the reflected shock and the impinging shock happened further downstream and further away from the wall, when compared with the reference case. This is due to the postponement of the separation onset due to the re-energizing of the boundary layer after crossing the reflected shock foot. The re-energizing of the boundary layer is possible due to the suction/blowing mechanism created by the pressure gradients between the extremities of each cavity sucking air from downstream and blowing it upstream. Regarding the Reynolds stress normal components, their distributions closely resembled those obtained for the baseline but, a displacement of the maxima was observed to the rear part of the second cavity below the wall. This was attributed to the reattachment of the shear layer near that region.

Overall, there was a minor increase in the total pressure recovery factor, while the total drag increased by $\approx 20\%$. Despite the separation bubble decrease and the more negative values of C_f found, the pressure drag created by the cavities exceeds the improvements from the reduced separation region. One could also notice very intense oscillations in all wall-related properties (even when spanwise averaged), due to the perforations on the wall, mostly concentrated at the suction portion of each cavity.

The bubble topology changed considerably, to better resemble a right triangle displaying more accentuated contours due to the bigger strength of the reattachment compression fan. Overall, the interaction influence region increased while the benefits of a reduced separation length were contradicted by higher pressure drag and unsteadiness, in particular in the wall properties. Two plateau curves were found for both mean pressure and density instead of the single plateau curve, typical of SWTBLIs, each of the plateaus being associated with a cavity. At separation, the RMS values of the thermodynamic properties decreased, but close to the rear portion of each cavity large peaks were found largely surpassing the highest peak found for the uncontrolled case.

Regarding the unsteadiness, a more tonal behaviour was found within the cavities region at higher Strouhal numbers than expected. Even though the cavities were designed to resonate at $St_{L_{sep}} \approx 0.03$, the PSDs of pressure and wall-normal velocity fluctuations, above and below the wall highlight strong dynamics in the $St_{L_{sep}} \approx 0.3$ region. The same Strouhal numbers were found associated with the bubble breathing motion (related to changes in volume), which kept a peak close to $St_{L_{sep}} \approx 0.03$, while for the shock motion, the PSD revealed a tonal dynamic behaviour at $St_{L_{sep}} \approx 0.3$. This suggests that, despite resonating at a non-desired frequency, the cavity can indeed influence the dynamics of the SWTBLI. A great preponderance of the reattachment dynamics was found to influence the unsteady behaviour of the SWTBLI as pointed out by the wall-pressure and wall-normal velocity fluctuations PSDs in the cavities regions as well as by the cross-correlation analysis between the relevant dynamic properties.

Lastly, the previously suggested sequence of events driving the unsteadiness, could not be verified anymore for the controlled interaction. Following the reasoning presented, only the dynamics associated with the reattachment point seemed to keep coherence with the remaining dynamic properties evaluated.

Recommendations

Based on the results obtained, several recommendations can be made for future studies. These include improvements in the methodology, but also in the analysis tools, as well as suggestions regarding possible new control methods that could better control the interaction between the shock system and the boundary layer.

- **Grid:** Regarding the grid used in the simulations, it was verified that close to the domain outlet y^+ slightly exceeded 1. Even though no impact was observed in the results, one should make sure that it stays below 1 for the entire extension of the domain. To do so, one could either refine the cells in that region close to the wall or use a higher domain to completely avoid any effects from the expansion wave resulting from the artificial shock generator.

- **Inflow Conditions:** If possible, a faster adapting inflow method should be used to decrease the domain extension required for inflow stabilisation/convergence, which would diminish the number of cells required in the grid. Consequently, the computational cost of each simulation would be reduced, making them more affordable and allowing for more flow/geometry iterations and bigger simulation times.

- **Data Extraction:** The sampling rates/integration time used for the snapshots sufficed for the present analysis. However, higher sampling rates/integration times would be desired to better capture the low-frequency unsteadiness, allowing better resolution in the low-frequency spectrum of the time analysis, namely when computing Fourier Transforms.

- **Cavity Dimensioning:** If more work is to be done using resonant cavities, it is suggested that more reliable expressions are used to compute the resulting resonant frequency that also take into account the pressure gradient inside the cavity. If possible, iterate the geometry using a canonical interaction, until the correct resonant frequency is achieved. Furthermore, the impact of a dividing wall between cavities should be further investigated, not only in terms of its impact in achieving the correct resonant frequency but more importantly, its impact on how the flow develops over the wall.

- **Flow analysis:** The shear layer reattachment process seems to be a big source of unsteadiness. Further analysis should be carried out to better understand the sequence of events that drive the unsteady behaviour of the interaction, with a special focus on the reattachment region. It is recommended to try to isolate each of the physical parameters evaluated in this thesis 'Unsteadiness' section (h_{bub}, V_{bub}, L_{sep} and x_{sw}) to determine what is their impact and role in the unsteadiness mechanism. Likewise, a better method to determine mean separation and reattachment points locations for each individual snapshot is required (increased domain span could facilitate this). Moreover, it would be interesting to study the interaction of the detached shear layer with the impinging shock, as it plays an important a role in the separation bubble topology and in the unsteadiness of the interaction.

- **Suggested control methods:** A control method that fixes the reflected shock location should be tried (for example, using a micro ramp). Likewise, methods for controlling and fixing the reattachment location would also be advantageous.

References

Adrian, R. J. (2007). Hairpin vortex organization in wall turbulence. *Physics of Fluids*, *19*(4). https://doi.org/10.1063/1.2717527

Anderson, B., Tinapple, J., & Surber, L. (2006). Optimal control of shock wave turbulent boundary layer interactions using micro-array actuation. *3rd AIAA Flow Control Conference*. https://doi.org/10.2514/6.2006-3197

Anderson, J. (2020, March). *Modern compressible flow: With historical perspective* (4th ed.). McGraw-Hill Education.

Andreopoulos, J., & Muck, K. C. (1987). Some new aspects of the shock-wave/boundary-layer interaction in compression-ramp flows. *J. Fluid Mech.*, *180*(-1), 405.

Aubard, G., Gloerfelt, X., & Robinet, J.-C. (2013). Large-eddy simulation of broadband unsteadiness in a shock/boundary-layer interaction. *AIAA Journal*, *51*(10), 2395–2409. https://doi.org/10.2514/1.j052249

Babinsky, H., Li, Y., & Ford, C. W. P. (2009). Microramp control of supersonic oblique shock-wave/boundary-layer interactions. *AIAA Journal*, *47*(3), 668–675. https://doi.org/10.2514/1.38022

Babinsky, H., & Harvey, J. K. (2011, September). *Shock wave-boundary-layer interactions*. Cambridge University Press.

Ben-Dor, G. (2007, September). *Shock wave reflection phenomena* (2nd ed.). Springer Berlin, Heidelberg. https://doi.org/https://doi.org/10.1007/978-3-540-71382-1

Beresh, S., Clemens, N., Dolling, D., Comninos, M., Beresh, S., Clemens, N., Dolling, D., & Comninos, M. (1997). Investigation of the causes of large-scale unsteadiness of shock-induced separated flow using planar laser imaging. *35th Aerospace Sciences Meeting and Exhibit*. https://doi.org/10.2514/6.1997-64

Beresh, S., Comninos, M., Clemens, N., & Dolling, D. (1998). The effects of the incoming turbulent boundary layer structure on a shock-induced separated flow. *36th AIAA Aerospace Sciences Meeting and Exhibit*. https://doi.org/10.2514/6.1998-620

Beresh, S. J., Clemens, N. T., & Dolling, D. S. (2002). Relationship between upstream turbulent boundary-layer velocity fluctuations and separation shock unsteadiness. *AIAA Journal*, *40*(12), 2412–2422. https://doi.org/10.2514/2.1609

Carrière, P., Sirieix, M., & Solignac, J.-L. (1969). Similarity properties of the laminar or turbulent separation phenomena in a non-uniform supersonic flow. In *Applied mechanics* (pp. 145–157). Springer Berlin Heidelberg. https://doi.org/10.1007/978-3-642-85640-2_11

Chanaud, R. (1994). Effects of geometry on the resonance frequency of helmholtz resonators. *Journal of Sound and Vibration*, *178*(3), 337–348. https://doi.org/10.1006/jsvi.1994.1490

Chapman, D. R., Kuehn, D. M., & Larson, H. K. (1958). Investigation of separated flows in supersonic and subsonic streams with emphasis on the effect of transition [Document ID: 19930092343]. *NTRS - NASA Technical Reports Server*.

Clemens, N. T., & Narayanaswamy, V. (2014). Low-frequency unsteadiness of shock wave/turbulent boundary layer interactions. *Annual Review of Fluid Mechanics*, *46*(1), 469–492. https://doi.org/10.1146/annurev-fluid-010313-141346

Cogo, M., Salvadore, F., Picano, F., & Bernardini, M. (2022). Direct numerical simulation of supersonic and hypersonic turbulent boundary layers at moderate-high reynolds numbers and isothermal wall condition [Cited by: 20; All Open Access, Green Open Access, Hybrid Gold Open Access]. *Journal of Fluid Mechanics*, *945*. https://doi.org/10.1017/jfm.2022.574

Cousteix, J. (2003). Aircraft aerodynamic boundary layers. In *Encyclopedia of physical science and technology* (pp. 301–317). Elsevier. https://doi.org/10.1016/b0-12-227410-5/00906-6

D'Aguanno, A. (2023). *Physics and control of transonic buffet* [Doctoral dissertation, Delft University of Technology]. https://doi.org/10.4233/UUID:7E4F868B-7716-4C36-8FA0-B55572D1572B

Delery, J., & Marvin, J. G. (1986). *Shock-wave boundary layer interactions* [AGARD-AG-280]. Advisory Group for Aerospace Research and Development.

(DHPC), D. H. P. C. C. (2024). DelftBlue Supercomputer. https://www.tudelft.nl/dhpc/system

DiGregorio, N. J., Drozda, T. G., & Madnia, C. K. (2019). Comparison of boundary layer similarity transformations for high mach number flows. *AIAA Scitech 2019 Forum*. https://doi.org/10.2514/6.2019-1390

Dolling, D. S., & Or, C. T. (1985). Unsteadiness of the shock wave structure in attached and separated compression ramp flows. *Experiments in Fluids*, *3*(1), 24–32. https://doi.org/10.1007/bf00285267

Dolling, D. S., & Murphy, M. T. (1983). Unsteadiness of the separation shock wave structure in a supersonic compression ramp flowfield. *AIAA Journal*, *21*, 1628–1634. https://api.semanticscholar.org/CorpusID:121413529

Dores, F., Hickel, S., & Laguarda, L. (2024). Supplementary material to the msc thesis "passive control of shock wave turbulent boundary layer interaction over a perforated wall". *4TU.ResearchData*. https://doi.org/https://doi.org/10.4121/2935d3cc-06dd-4a64-ad0f-e0b1a4beb590

Dupont, P., Haddad, C., & Debiève, J. F. (2006). Space and time organization in a shock-induced separated boundary layer. *Journal of Fluid Mechanics*, *559*, 255. https://doi.org/10.1017/s0022112006000267

Dussauge, J.-P., Dupont, P., & Debiève, J.-F. (2006). Unsteadiness in shock wave boundary layer interactions with separation. *Aerospace Science and Technology*, *10*(2), 85–91. https://doi.org/10.1016/j.ast.2005.09.006

Erengil, M. E., & Dolling, D. S. (1991). Correlation of separation shock motion with pressure fluctuations in the incoming boundary layer. *AIAA J.*, *29*(11), 1868–1877.

Erengil, M. E. (1993, January). *Physical causes of separation shock unsteadiness in shock wave/turbulent boundary layer interactions* [Doctoral dissertation, University of Texas, Austin].

Farabee, T. M., & Casarella, M. J. (1991). Spectral features of wall pressure fluctuations beneath turbulent boundary layers. *Physics of Fluids A: Fluid Dynamics*, *3*(10), 2410–2420. https://doi.org/10.1063/1.858179

Fedotov, E. S., Kustov, O. Y., & Bulbovich, R. V. (2018). Determination of end correction of helmholtz resonator based on numerical simulation. *AIP Conference Proceedings*. https://doi.org/10.1063/1.5065186

Freedman, D., & Diaconis, P. (1981). On the histogram as a density estimator:l 2 theory. *Zeitschrift für Wahrscheinlichkeitstheorie und Verwandte Gebiete*, *57*(4), 453–476. https://doi.org/10.1007/bf01025868

Gaitonde, D. V. (2015). Progress in shock wave/boundary layer interactions. *Progress in Aerospace Sciences*, *72*, 80–99. https://doi.org/10.1016/j.paerosci.2014.09.002

Gaitonde, D. V., & Adler, M. C. (2023). Dynamics of three-dimensional shock-wave/boundary-layer interactions. *Annual Review of Fluid Mechanics*, *55*(1), 291–321. https://doi.org/10.1146/annurev-fluid-120720-022542

Ganapathisubramani, B., Clemens, N. T., & Dolling, D. S. (2007). Effects of upstream boundary layer on the unsteadiness of shock-induced separation. *Journal of Fluid Mechanics*, *585*, 369–394. https://doi.org/10.1017/s0022112007006799

Gonsalez, J., & Dolling, D. (1993). Correlation of interaction sweepback effects on unsteady shock-induced turbulent separation. *31st Aerospace Sciences Meeting*. https://doi.org/10.2514/6.1993-776

Gottlieb, S., & Shu, C.-W. (1998). Total variation diminishing runge-kutta schemes. *Mathematics of Computation*, *67*(221), 73–85. https://doi.org/10.1090/s0025-5718-98-00913-2

Griffin, K. P., Fu, L., & Moin, P. (2021). Velocity transformation for compressible wall-bounded turbulent flows with and without heat transfer [Cited by: 58; All Open Access, Bronze Open Access, Green Open Access]. *Proceedings of the National Academy of Sciences of the United States of America*, *118*(34). https://doi.org/10.1073/pnas.2111144118

Grilli, M., Hickel, S., & Adams, N. A. (2013). Large-eddy simulation of a supersonic turbulent boundary layer over a compression–expansion ramp. *International Journal of Heat and Fluid Flow*, *42*, 79–93. https://doi.org/10.1016/j.ijheatfluidflow.2012.12.006

Guiho, F., Alizard, F., & Robinet, J.-C. (2016). Instabilities in oblique shock wave/laminar boundary-layer interactions. *Journal of Fluid Mechanics*, *789*, 1–35. https://doi.org/10.1017/jfm.2015.729

Hadjadj, A., Ben-Nasr, O., Shadloo, M., & Chaudhuri, A. (2015). Effect of wall temperature in supersonic turbulent boundary layers: A numerical study. *International Journal of Heat and Mass Transfer*, *81*, 426–438. https://doi.org/10.1016/j.ijheatmasstransfer.2014.10.025

Helm, C. M., & Martín, M. P. (2021). Scaling of hypersonic shock/turbulent boundary layer interactions. *Physical Review Fluids*, *6*(7). https://doi.org/10.1103/physrevfluids.6.074607

Hickel, S., Egerer, C. P., & Larsson, J. (2014). Subgrid-scale modeling for implicit large eddy simulation of compressible flows and shock-turbulence interaction. *Physics of Fluids*, *26*(10). https://doi.org/10.1063/1.4898641

Holden, H. A., & Babinsky, H. (2005). Separated shock-boundary-layer interaction control using streamwise slots. *Journal of Aircraft*, *42*(1), 166–171. https://doi.org/10.2514/1.4687

Hu, W., Hickel, S., & van Oudheusden, B. W. (2021). Low-frequency unsteadiness mechanisms in shock wave/turbulent boundary layer interactions over a backward-facing step. *Journal of Fluid Mechanics*, *915*. https://doi.org/10.1017/jfm.2021.95

Huang, J., Duan, L., & Choudhari, M. M. (2022). Direct numerical simulation of hypersonic turbulent boundary layers: Effect of spatial evolution and reynolds number. *Journal of Fluid Mechanics*, *937*, A3. https://doi.org/10.1017/jfm.2022.80

Huang, W., Wu, H., Yang, Y.-g., Yan, L., & Li, S.-b. (2020). Recent advances in the shock wave/boundary layer interaction and its control in internal and external flows. *Acta Astronautica*, *174*, 103–122. https://doi.org/10.1016/j.actaastro.2020.05.001

Humble, R. A., Elsinga, G. E., Scarano, F., & van Oudheusden, B. W. (2009). Three-dimensional instantaneous structure of a shock wave/turbulent boundary layer interaction. *Journal of Fluid Mechanics*, *622*, 33–62. https://doi.org/10.1017/s0022112008005090

Hunt, D., & Nixon, D. (1995). A very large eddy simulation of an unsteady shock wave/turbulent boundary layer interaction. *Fluid Dynamics Conference*. https://doi.org/10.2514/6.1995-2212

Jana, T., Thillaikumar, T., & Kaushik, M. (2020). Assessment of cavity covered with porous surface in controlling shock/boundary-layer interactions in hypersonic intake. *International Journal of Aeronautical and Space Sciences*, *21*(4), 924–941. https://doi.org/10.1007/s42405-020-00269-4

Kang, Y., & Lee, S. (2024). Direct numerical simulation of turbulence amplification in a strong shock-wave/turbulent boundary layer interaction. *Physics of Fluids*, *36*(1). https://doi.org/10.1063/5.0180077

Kinefuchi, K., Starikovskiy, A., & Miles, R. (2016). Control of shock wave - boundary layer interaction using nanosecond dielectric barrier discharge plasma actuators. *52nd AIAA/SAE/ASEE Joint Propulsion Conference*. https://doi.org/10.2514/6.2016-5070

Kistler, A. L. (1964). Fluctuating wall pressure under a separated supersonic flow. *The Journal of the Acoustical Society of America*, *36*(3), 543–550. https://doi.org/10.1121/1.1918998

Laguarda, L., Hickel, S., Schrijer, F., & van Oudheusden, B. High-reynolds number effects in shock-wave/turbulent boundary-layer interactions. In: 2022. https://www.scopus.com/inward/record.uri?eid=2-s2.0-85143839460&partnerID=40&md5=31d38987adff1bb94b0e3b6b5810d56b

Laguarda, L., Hickel, S., Schrijer, F., & van Oudheusden, B. (2024a). Assessment of reynolds number effects in supersonic turbulent boundary layers. *International Journal of Heat and Fluid Flow*, *105*, 109234. https://doi.org/10.1016/j.ijheatfluidflow.2023.109234

Laguarda, L., Hickel, S., Schrijer, F., & van Oudheusden, B. (2024b). Reynolds number effects in shock-wave/turbulent boundary-layer interactions. *Journal of Fluid Mechanics*, *989*. https://doi.org/10.1017/jfm.2024.361

Laguarda, L., & Hickel, S. (2024). Low-frequency dynamics of turbulent recirculation bubbles. *Physics of Fluids*, *36*(8). https://doi.org/10.1063/5.0227332

Langfeldt, F., Hoppen, H., & Gleine, W. (2019). Resonance frequencies and sound absorption of helmholtz resonators with multiple necks. *Applied Acoustics*, *145*, 314–319. https://doi.org/10.1016/j.apacoust.2018.10.021

Lee, S., & Loth, E. (2009). Supersonic boundary layer interactions with various micro-vortex generator geometries. *39th AIAA Fluid Dynamics Conference*. https://doi.org/10.2514/6.2009-3712

Leishman, G. (2022). *Introduction to aerospace flight vehicles*. Embry-Riddle Aeronautical University. https://doi.org/10.15394/eaglepub.2022.1066

Li, W., & Liu, H. (2019). Large-eddy simulation of shock-wave/boundary-layer interaction control using a backward facing step. *Aerospace Science and Technology*, *84*, 1011–1019. https://doi.org/10.1016/j.ast.2018.11.005

Lindgren, E. R. (1965). *Experimental study on turbulent pipe flows of distilled water* [Report 1AD621071]. Oklahoma State University, Civil Engineering Dept.

Loginov, M. S., Adams, N. A., & Zheltovodov, A. A. (2006). Large-eddy simulation of shock-wave/turbulent-boundary-layer interaction. *Journal of Fluid Mechanics*, *565*, 135. https://doi.org/10.1017/s0022112006000930

Martis, R. R., & Misra, A. (2013). Effect of height of microvortex generators on swept shock wave boundary layer interactions. *CEAS Aeronautical Journal*, *4*(3), 315–326. https://doi.org/10.1007/s13272-013-0075-y

Matheis, J., & Hickel, S. (2015). On the transition between regular and irregular shock patterns of shock-wave/boundary-layer interactions. *Journal of Fluid Mechanics*, *776*, 200–234. https://doi.org/10.1017/jfm.2015.319

McCormick, D. C. (1993). Shock/boundary-layer interaction control with vortex generators and passive cavity. *AIAA Journal*, *31*(1), 91–96. https://doi.org/10.2514/3.11323

Morgan, B., Duraisamy, K., Nguyen, N., Kawai, S., & Lele, S. K. (2013). Flow physics and rans modelling of oblique shock/turbulent boundary layer interaction. *Journal of Fluid Mechanics*, *729*, 231–284. https://doi.org/10.1017/jfm.2013.301

Muck, K.-C., Andreopoulos, J., & Dussauge, J.-P. (1988). Unsteady nature of shock-wave/turbulent boundary-layer interaction. *AIAA Journal*, *26*(2), 179–187. https://doi.org/10.2514/3.9870

Narayanaswamy, V., Raja, L. L., & Clemens, N. T. (2012). Control of unsteadiness of a shock wave/-turbulent boundary layer interaction by using a pulsed-plasma-jet actuator. *Physics of Fluids*, *24*(7). https://doi.org/10.1063/1.4731292

Nishioka, M. (2009). Rotta skin friction law and schoenherr formula. *Fluid Dynamics Research*, *41*(4), 045509. https://doi.org/10.1088/0169-5983/41/4/045509

Pasquariello, V., Grilli, M., Hickel, S., & Adams, N. A. (2014). Large-eddy simulation of passive shock-wave/boundary-layer interaction control. *International Journal of Heat and Fluid Flow*, *49*, 116–127. https://doi.org/10.1016/j.ijheatfluidflow.2014.04.005

Pasquariello, V., Hickel, S., & Adams, N. A. (2017). Unsteady effects of strong shock-wave/boundary-layer interaction at high reynolds number. *Journal of Fluid Mechanics*, *823*, 617–657. https://doi.org/10.1017/jfm.2017.308

Piponniau, S., Dussauge, J. P., Debiève, J. F., & Dupont, P. (2009). A simple model for low-frequency unsteadiness in shock-induced separation. *Journal of Fluid Mechanics*, *629*, 87–108. https://doi.org/10.1017/s0022112009006417

Pirozzoli, S., & Bernardini, M. (2011). Turbulence in supersonic boundary layers at moderate reynolds number. *Journal of Fluid Mechanics*, *688*, 120–168. https://doi.org/10.1017/jfm.2011.368

Pirozzoli, S., & Bernardini, M. (2013). Probing high-reynolds-number effects in numerical boundary layers [Cited by: 86]. *Physics of Fluids*, *25*(2). https://doi.org/10.1063/1.4792164

Pirozzoli, S., & Grasso, F. (2006). Direct numerical simulation of impinging shock wave/turbulent boundary layer interaction at m=2.25. *Physics of Fluids*, *18*(6). https://doi.org/10.1063/1.2216989

Poinsot, T., & Lelef, S. (1992). Boundary conditions for direct simulations of compressible viscous flows. *Journal of Computational Physics*, *101*(1), 104–129. https://doi.org/10.1016/0021-9991(92)90046-2

Priebe, S., Wu, M., & Martín, M. P. (2009). Direct numerical simulation of a reflected-shock-wave/turbulent-boundary-layer interaction. *AIAA Journal*, *47*(5), 1173–1185. https://doi.org/10.2514/1.38821

Priebe, S., & Martín, M. P. (2012). Low-frequency unsteadiness in shock wave–turbulent boundary layer interaction. *Journal of Fluid Mechanics*, *699*, 1–49. https://doi.org/10.1017/jfm.2011.560

Priebe, S., Tu, J. H., Rowley, C. W., & Martín, M. P. (2016). Low-frequency dynamics in a shock-induced separated flow. *Journal of Fluid Mechanics*, *807*, 441–477. https://doi.org/10.1017/jfm.2016.557

Raja sekar, K., Jegadheeswaran, S., Kannan, R., & Manigandan, P. (2019). Perforated wall in controlling the separation bubble due to shock wave –boundary layer interaction. *International Journal of Turbo amp; Jet-Engines*, *39*(2), 223–231. https://doi.org/10.1515/tjj-2018-0048

Ringuette, M. J., Bookey, P., Wyckham, C., & Smits, A. J. (2009). Experimental study of a mach 3 compression ramp interaction at retheta = 2400. *AIAA Journal*, *47*(2), 373–385. https://doi.org/10.2514/1.38248

Ringuette, M. J., Wu, M., & Martín, M. P. (2007). Coherent structures in direct numerical simulation of turbulent boundary layers at mach 3. *Journal of Fluid Mechanics*, *594*, 59–69. https://doi.org/10.1017/s0022112007009020

Sandham, N. D. (2016). Effects of compressibility and shock-wave interactions on turbulent shear flows. *Flow, Turbulence and Combustion*, *97*(1), 1–25. https://doi.org/10.1007/s10494-016-9733-6

Schlichting, H., & Gersten, K. (2017). *Boundary-layer theory*. Springer Berlin Heidelberg. https://doi.org/10.1007/978-3-662-52919-5

Schreyer, A.-M., Sahoo, D., Williams, O. J. H., & Smits, A. J. (2021). Influence of a microramp array on a hypersonic shock-wave/turbulent boundary-layer interaction. *AIAA Journal*, *59*(6), 1924–1939. https://doi.org/10.2514/1.j059925

Schülein, E., & Trofimov, V. M. (2011). Steady longitudinal vortices in supersonic turbulent separated flows. *Journal of Fluid Mechanics*, *672*, 451–476. https://doi.org/10.1017/s0022112010006105

Scott, D. W. (1979). On optimal and data-based histograms. *Biometrika*, *66*(3), 605–610. https://doi.org/10.1093/biomet/66.3.605

Sepahi-Younsi, J., & Esmaeili, S. (2023). Source of buzz instability in a supersonic air inlet. *Aerospace Science and Technology*, *138*, 108334. https://doi.org/10.1016/j.ast.2023.108334

Shahab, M. F., Lehnasch, G., Gatski, T. B., & Comte, P. (2011). Statistical characteristics of an isothermal, supersonic developing boundary layer flow from dns data. *Flow, Turbulence and Combustion*, *86*(3–4), 369–397. https://doi.org/10.1007/s10494-011-9329-0

Shahzad, H., Hickel, S., & Modesti, D. (2024). Physics-informed acoustic liner optimization: Balancing drag and noise. *AIAA Journal*, 1–9. https://doi.org/10.2514/1.j063677

Smits, A. J., Matheson, N., & Joubert, P. N. (1983). Low-reynolds-number turbulent boundary layers in zero and favorable pressure gradients. *Journal of Ship Research*, *27*(03), 147–157. https://doi.org/10.5957/jsr.1983.27.3.147

Smits, A. J., & Dussauge, J.-P. (2006, January). *Turbulent shear layers in supersonic flow* (2nd ed.). Springer. https://doi.org/https://doi.org/10.1007/b137383

Souverein, L. J., Bakker, P. G., & Dupont, P. (2013). A scaling analysis for turbulent shock-wave/boundary-layer interactions. *Journal of Fluid Mechanics*, *714*, 505–535. https://doi.org/10.1017/jfm.2012.495

Souverein, L. J., & Debiève, J.-F. (2010). Effect of air jet vortex generators on a shock wave boundary layer interaction. *Experiments in Fluids*, *49*(5), 1053–1064. https://doi.org/10.1007/s00348-010-0854-8

Spalding, D. B. (1961). A single formula for the “law of the wall”. *Journal of Applied Mechanics*, *28*(3), 455–458. https://doi.org/10.1115/1.3641728

Sun, Q., Li, Y., Cui, W., Cheng, B., Li, J., & Dai, H. (2014). Shock wave-boundary layer interactions control by plasma aerodynamic actuation. *Science China Technological Sciences*, *57*(7), 1335–1341. https://doi.org/10.1007/s11431-014-5586-1

Sun, Z., Schrijer, F. F. J., Scarano, F., & van Oudheusden, B. W. (2012). The three-dimensional flow organization past a micro-ramp in a supersonic boundary layer. *Physics of Fluids*, *24*(5). https://doi.org/10.1063/1.4711372

Threadgill, J. A., & Bruce, P. J. (2016). Shock wave boundary layer interaction unsteadiness: The effects of configuration and strength. *54th AIAA Aerospace Sciences Meeting*. https://doi.org/10.2514/6.2016-0077

Titchener, N., & Babinsky, H. (2013). Shock wave/boundary-layer interaction control using a combination of vortex generators and bleed. *AIAA Journal*, *51*(5), 1221–1233. https://doi.org/10.2514/1.j052079

Touber, E., & Sandham, N. D. (2009). Large-eddy simulation of low-frequency unsteadiness in a turbulent shock-induced separation bubble. *Theoretical and Computational Fluid Dynamics*, *23*(2), 79–107. https://doi.org/10.1007/s00162-009-0103-z

Touber, E., & Sandham, N. D. (2011). Low-order stochastic modelling of low-frequency motions in reflected shock-wave/boundary-layer interactions. *Journal of Fluid Mechanics*, *671*, 417–465. https://doi.org/10.1017/s0022112010005811

Trettel, A., & Larsson, J. (2016). Mean velocity scaling for compressible wall turbulence with heat transfer. *Physics of Fluids*, *28*. https://doi.org/10.1063/1.4942022

Ünalmis, O., & Dolling, D. (1994). Decay of wall pressure field and structure of a mach 5 adiabatic turbulent boundary layer. *Fluid Dynamics Conference*. https://doi.org/10.2514/6.1994-2363

van Driest, E. R. (1951). Turbulent boundary layer in compressible fluids. *Journal of the Aeronautical Sciences*, *18*(3), 145–160. https://doi.org/10.2514/8.1895

van Driest, E. R. (1956). The problem of aerodynamic heating. *Institute of the Aeronautical Sciences*, 26–41.

Vyas, M. A., Waindim, M., & Gaitonde, D. V. (2016). Budget of turbulent kinetic energy in a shock wave/boundary-layer interaction. *46th AIAA Fluid Dynamics Conference*. https://doi.org/10.2514/6.2016-3187

Wang, H., Hu, W., Xie, F., Li, J., Jia, Y., & Yang, Y. (2022). Control effects of a high-frequency pulsed discharge on a hypersonic separated flow. *Physics of Fluids*, *34*(6). https://doi.org/10.1063/5.0094186

White, F., & Majdalani, J. (2021, April). *Viscous fluid flow ISE* (4th ed.). McGraw-Hill Education.

Wu, M., & Martín, M. P. (2007). Analysis of shock motion in shockwave and turbulent boundary layer interaction using direct numerical simulation data. *Journal of Fluid Mechanics*, *594*, 71–83. https://doi.org/10.1017/s0022112007009044

Wu, W., Laguarda, L., Modesti, D., & Hickel, S. (2024). Passive control of shock-wave/turbulent boundary-layer interaction using spanwise heterogeneous roughness. *Flow, Turbulence and Combustion*. https://doi.org/10.1007/s10494-024-00580-0

Xie, Z.-T., & Castro, I. P. (2008). Efficient generation of inflow conditions for large eddy simulation of street-scale flows. *Flow, Turbulence and Combustion*, *81*(3), 449–470. https://doi.org/10.1007/s10494-008-9151-5

Yan, L., Wu, H., Huang, W., Li, S.-b., & Liu, J. (2020). Shock wave/turbulence boundary layer interaction control with the secondary recirculation jet in a supersonic flow. *Acta Astronautica*, *173*, 131–138. https://doi.org/10.1016/j.actaastro.2020.04.003

Yan, Y., Li, Q., Liu, C., Pierce, A., Lu, F., & Lu, P. (2012). Numerical discovery and experimental confirmation of vortex ring generation by microramp vortex generator. *Applied Mathematical Modelling*, *36*(11), 5700–5708. https://doi.org/10.1016/j.apm.2012.01.015

Zhai, J., Zhang, C.-A., Wang, F.-M., & Zhang, W.-W. (2022). Control of shock-wave/boundary-layer interaction using a backward-facing step. *Aerospace Science and Technology*, *126*, 107665. https://doi.org/10.1016/j.ast.2022.107665

Zukoski, E. E. (1967). Turbulent boundary-layer separation in front of a forward-facing step. *AIAA Journal*, *5*(10), 1746–1753. https://doi.org/10.2514/3.4299

Appendix A

Gas Dynamics

In this chapter shocks and expansion waves, as well as the inviscid interaction between shocks (shock reflections) is discussed.

Note: In this section the symbols in Nomenclature should not be considered. All variables are represented by their standard symbols. Hence, take ϕ as the turning angle, θ as the flow deflection angle, instead of the BL momentum thickness, ν as the Prandtl-Meyer angle instead of kinematic viscosity and μ as the Mach angle instead of as dynamic viscosity as identified in Nomenclature.

For reference, the isentropic flow relations are presented next:

$$\frac{p}{p_0} = \left(1 + \frac{\gamma - 1}{2} M^2\right)^{-\frac{\gamma}{\gamma-1}}, \tag{A.1}$$

$$\frac{\rho}{\rho_0} = \left(1 + \frac{\gamma - 1}{2} M^2\right)^{-\frac{1}{\gamma-1}}, \tag{A.2}$$

$$\frac{T}{T_0} = \left(1 + \frac{\gamma - 1}{2} M^2\right)^{-1}, \tag{A.3}$$

$$\left(\frac{p}{p_0}\right) = \left(\frac{\rho}{\rho_0}\right)^{\gamma} = \left(\frac{T}{T_0}\right)^{\frac{\gamma}{\gamma-1}}. \tag{A.4}$$

A.1 Shock Waves

Shock waves are thin regions of space, usually modelled as discontinuities, over which the main dynamic and thermodynamic properties vary almost instantly. Pressure, density and temperature increase and velocity and Mach number decrease across shock waves. Also, total pressure decreases due to the increase of entropy. Only total temperature remains constant, given the adiabatic character of shock waves when assuming a calorically perfect gas. Depending on the orientation of the shock with respect to the flow, shocks can be termed normal or oblique.

A.1.1 Normal Shocks

Normal shocks are perpendicular to the flow direction. These are the strongest shocks that can be produced. Behind a normal shock, the flow is always subsonic. These shocks do not introduce any deflection to the flow direction. The normal shock relations are as follows:

$$M_2^2 = \frac{1 + [(\gamma - 1)/2]M_1^2}{\gamma M_1^2 - (\gamma - 1)/2}, \tag{A.5}$$

$$\frac{p_2}{p_1} = 1 + \frac{2\gamma}{\gamma + 1}\left(M_1^2 - 1\right), \tag{A.6}$$

$$\frac{p_{0_2}}{p_{0_1}} = \left[\frac{(\gamma + 1)M_1^2}{(\gamma - 1)M_1^2 + 2}\right]^{\frac{\gamma}{\gamma - 1}} \left[\frac{\gamma + 1}{2\gamma M_1^2 - (\gamma - 1)}\right]^{\frac{1}{\gamma - 1}}, \tag{A.7}$$

$$\frac{\rho_2}{\rho_1} = \frac{u_1}{u_2} = \frac{(\gamma + 1)M_1^2}{2 + (\gamma - 1)M_1^2}, \tag{A.8}$$

$$\frac{T_2}{T_1} = \frac{[2\gamma M_1^2 - (\gamma - 1)][(\gamma - 1)M_1^2 + 2]}{(\gamma + 1)^2 M_1^2}. \tag{A.9}$$

A.1.2 Oblique Shocks

Regarding oblique shocks, these are at an angle β with the flow direction. Since they are not as strong as the normal shocks, the flow behind them can be either subsonic or supersonic (see dashed lines in Figure A.1), depending on the kind of solution allowed for a specific Mach number and flow deflection angle θ. It can be a weak or a strong solution. The $\theta - \beta - M$ diagram in Figure A.1 shows the different possibilities.

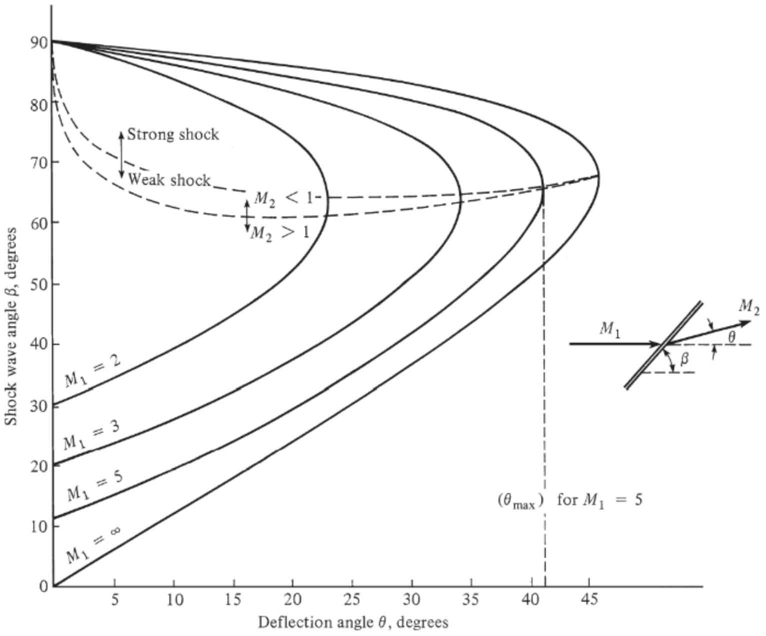

Figure A.1: $\theta - \beta - M$ curves. (J. Anderson, 2020)

The equations for the variation of the properties across an oblique shock are shown next:

$$M_{n_1} = M_1 \sin\beta, \tag{A.10}$$

$$\tan\theta = 2\cot\beta \left[\frac{M_1^2 \sin^2\beta - 1}{M_1^2(\gamma + \cos 2\beta) + 2}\right], \tag{A.11}$$

$$M_2 = \frac{M_{n_2}}{\sin(\beta - \theta)}. \tag{A.12}$$

The relations for pressure, stagnation pressure, density and temperature are the same as for normal shocks (Appendix A.1.1), but with M_1 and M_2 substituted by their components normal to the shock, namely M_{n_1} and M_{n_2}, respectively.

A.2 Expansion Waves

An expansion wave is an entity over which the Mach number increases while, density, static pressure and static temperature decrease. When a supersonic flow is turned in a convex corner or surface an infinite amount of these waves appear to form an expansion fan, also known as a *Prandtl-Meyer (PM) expansion fan*. This phenomenon is isentropic, meaning that both total temperature and pressure are kept constant. The inclination of each wave follows the Mach angle, defined as

$$\mu = \arcsin\left(\frac{1}{M}\right), \tag{A.13}$$

and the first and last wave inclinations depend on the initial and final Mach numbers, the latter depending on the flow deflection angle.

The Prandtl-Meyer angle ν gives the relation between the turn angle ϕ and the two Mach numbers, M_1 and M_2,

$$\phi = \nu(M_2) - \nu(M_1), \tag{A.14}$$

$$\nu(M) = \sqrt{\frac{\gamma+1}{\gamma-1}} \arctan \sqrt{\frac{\gamma-1}{\gamma+1}(M^2-1)} - \arctan\sqrt{M^2-1}. \tag{A.15}$$

The maximum turn angle ($\phi_{max} = \nu_{max} - \nu(M_1)$) is determined by pressure considerations and is given by

$$\nu_{max} = \frac{\pi}{2}\left(\sqrt{\frac{\gamma+1}{\gamma-1}} - 1\right). \tag{A.16}$$

The final static properties as a function of the initial conditions and the final Mach number for a Prandtl-Meyer expansion fan are:

$$\frac{p_2}{p_1} = \left(\frac{1+\frac{\gamma-1}{2}M_1^2}{1+\frac{\gamma-1}{2}M_2^2}\right)^{\frac{\gamma}{\gamma-1}}, \tag{A.17}$$

$$\frac{\rho_2}{\rho_1} = \left(\frac{1+\frac{\gamma-1}{2}M_1^2}{1+\frac{\gamma-1}{2}M_2^2}\right)^{\frac{1}{\gamma-1}}, \tag{A.18}$$

$$\frac{T_2}{T_1} = \left(\frac{1+\frac{\gamma-1}{2}M_1^2}{1+\frac{\gamma-1}{2}M_2^2}\right). \tag{A.19}$$

A.3 Inviscid Shock-Shock Interactions

When a shock interacts with a surface, another shock or other discontinuity is reflected. The structure of this reflection depends on the initial flow conditions and can be either regular or irregular.

A.3.1 Regular Reflection (RR)

A reflection is said to be regular when it is composed of only two shocks: an incident, i, and a reflected shock, r, that meet at the reflection point, R located on the reflection surface (Ben-Dor, 2007). When supersonic flow encounters a shock (i) it is deflected. Since the flow cannot go through the wall it must realign with the wall direction. In order for that to happen a new shock is generated (r) - see Figure A.2a.

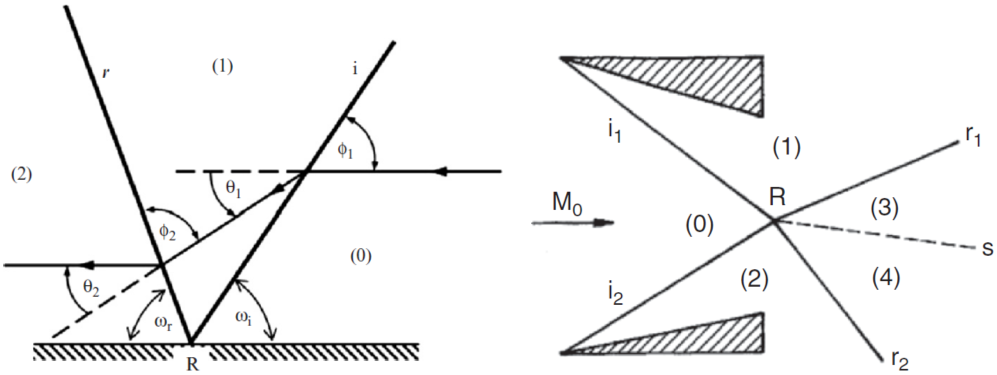

(a) Wall reflection

(b) Shock interaction

Figure A.2: Schematics of RR. (Ben-Dor, 2007)

Apart from the most common reflections that can occur on a physical surface, shocks can also reflect on shear layers or as a result of the interaction between two shocks. Figure A.2b shows an example of this kind of interaction for shocks with different inclination angles. In this case, viscosity will play an important role, particularly in the slipstream that is created given the different post-shock conditions (3) and (4).

A.3.2 Irregular Reflection (IR)

Moving to the IR the most common one is the Mach reflection (MR), which will be the only one addressed here. The MR is characterized by the convergence of 4 different discontinuities: an incident shock, i, a reflected shock, r, a Mach stem, m and a slipstream, s. These discontinuities converge at the so-called triple point, T (see Figure A.3a).

Note that there is a clear discontinuity in the slope between the incident shock and the Mach stem. Furthermore, the foot of the Mach steam is always perpendicular to the wall.

The MR can be further subdivided into 3 different categories (see Figure A.3b) depending on the direction of propagation of the triple point with respect to the reflecting surface. If it moves away from the surface it is called a direct MR, when it moves towards the surface is called inverse MR and when it is parallel is termed stationary MR (Ben-Dor, 2007).

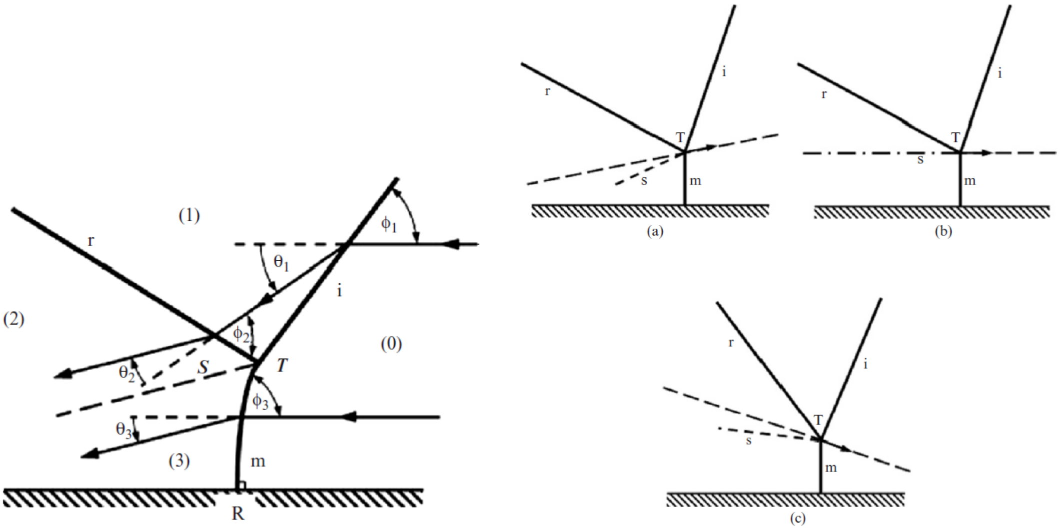

(a) (b)

Figure A.3: Representations of MR on a wall. (a): general schematics, (b)-(a): direct MR, DiMR, (b)-(b): stationary MR, StMR, (b)-(c): inverse MR, InMR. (Ben-Dor, 2007)

Appendix B

$\langle y^+ \rangle$

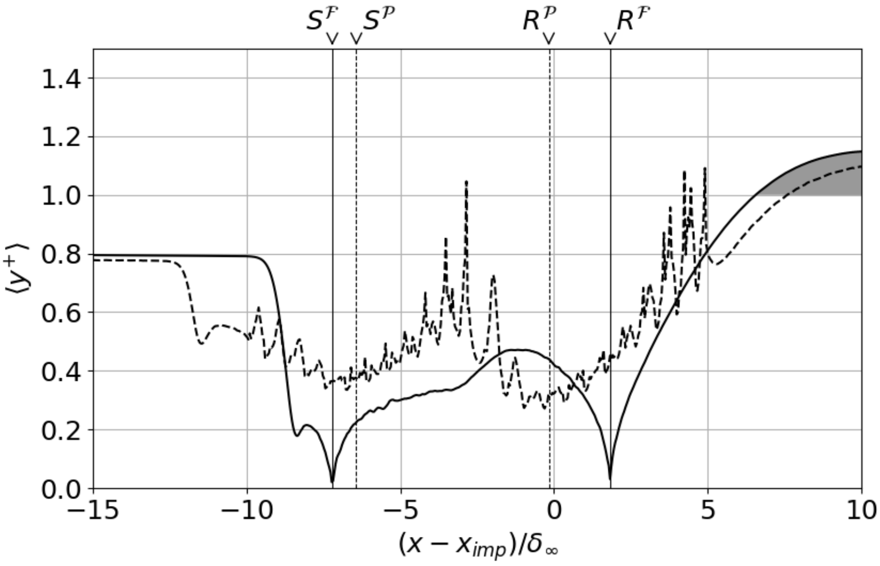

Figure B.1: Time- and span-averaged y^+ over the domain centerline, computed based on l^+_{min}.

Appendix C

Cross-correlation coefficient between thermodynamic quantities ($\mathscr{F}$)

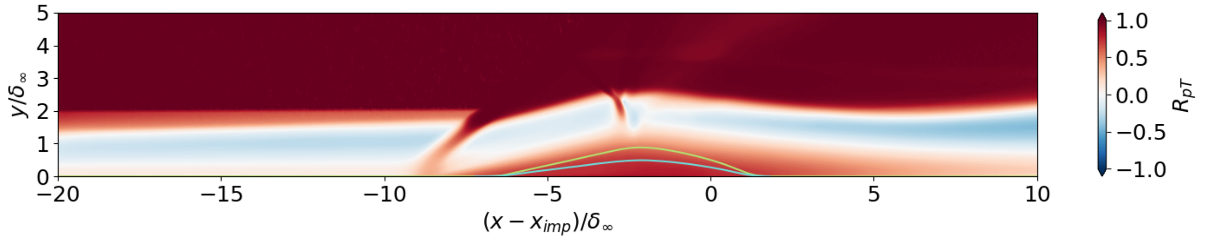

(a) Pressure - temperature.

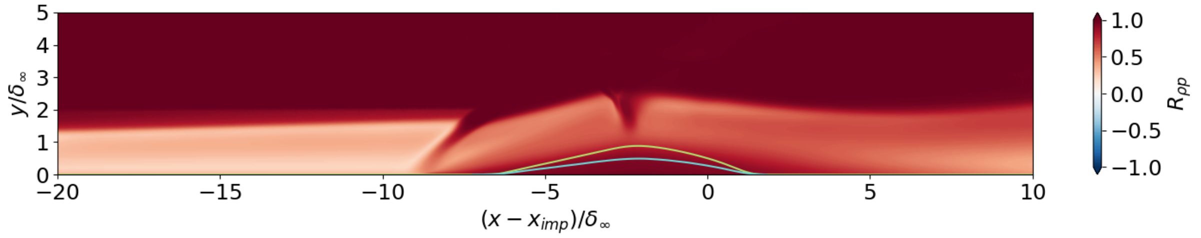

(b) Density - pressure.

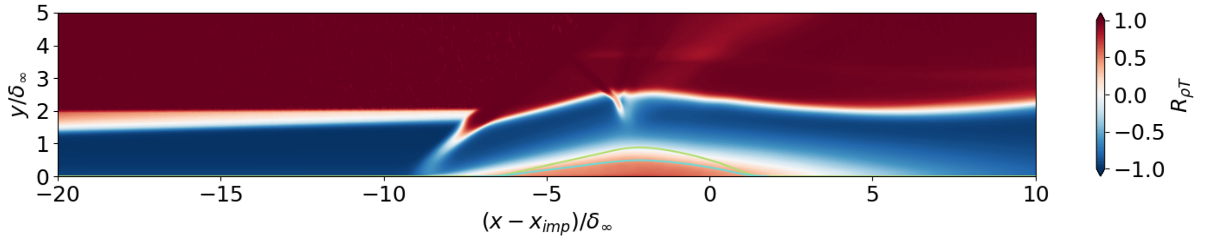

(c) Density - temperature.

Figure C.1: Time-averaged cross-correlation coefficient between thermodynamic quantities fluctuations. (—) $\langle u \rangle = 0$. (—) dividing streamline: $\left\{(x, y_{ds}) \mid \int_0^{y_{ds}} \langle \rho u \rangle \, dy = 0\right\}$.

Appendix D

Cross-correlation coefficient between thermodynamic quantities at $x = x_{imp}$

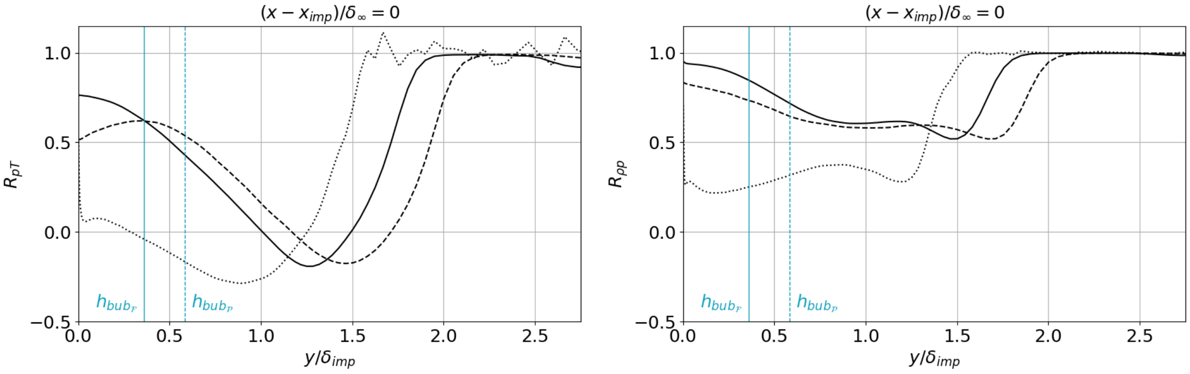

(a) Pressure - temperature.

(b) Density - pressure.

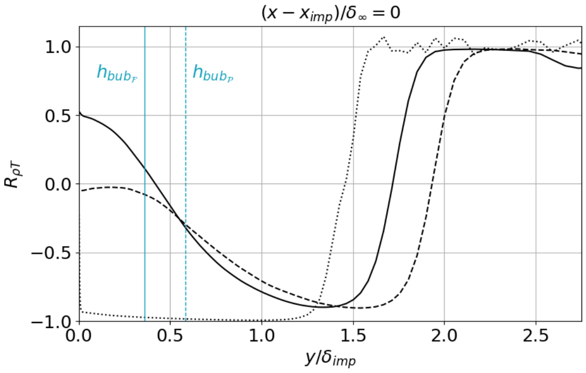

(c) Density - temperature.

Figure D.1: Span- and time-averaged cross-correlation coefficient between thermodynamic properties fluctuations at $x = x_{imp}$. $(\cdots\cdots)$ undisturbed boundary layer. h_{bub}, mean bubble height.

Appendix E

Power Spectral Density (PSD) of dynamic quantities ($\mathcal{F}$)

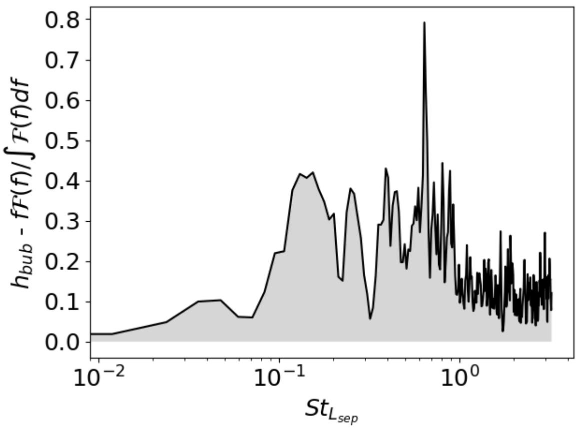

(a) Bubble height.

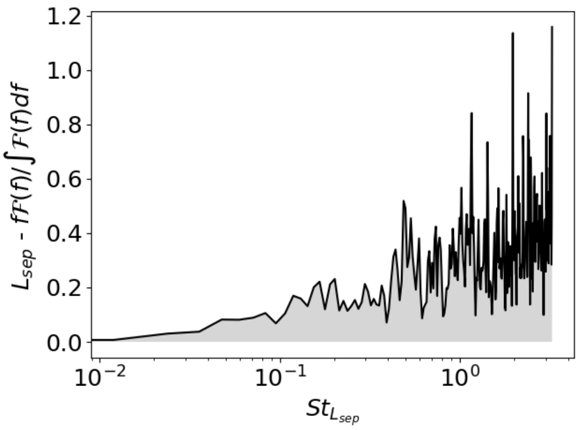

(b) Separation length.

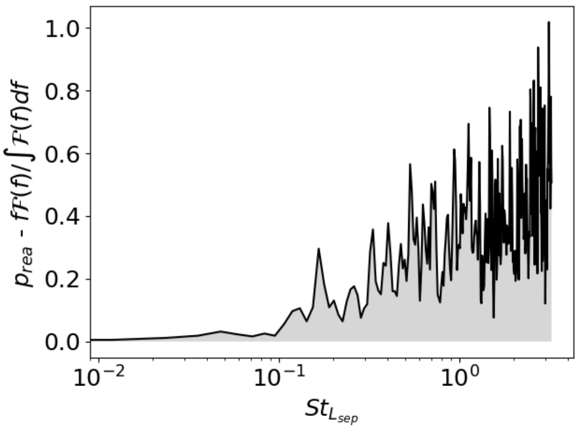

(c) Pressure at reattachment point.

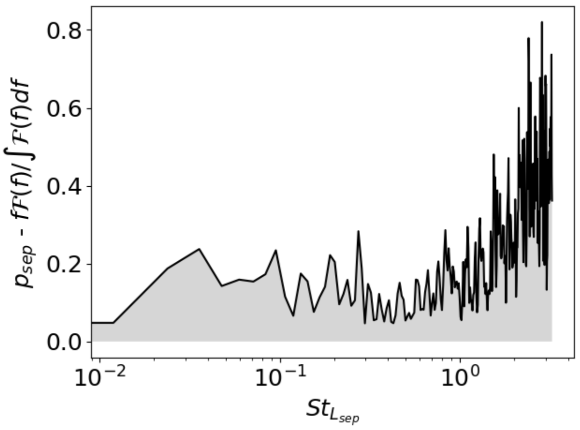

(d) Pressure at separation point.

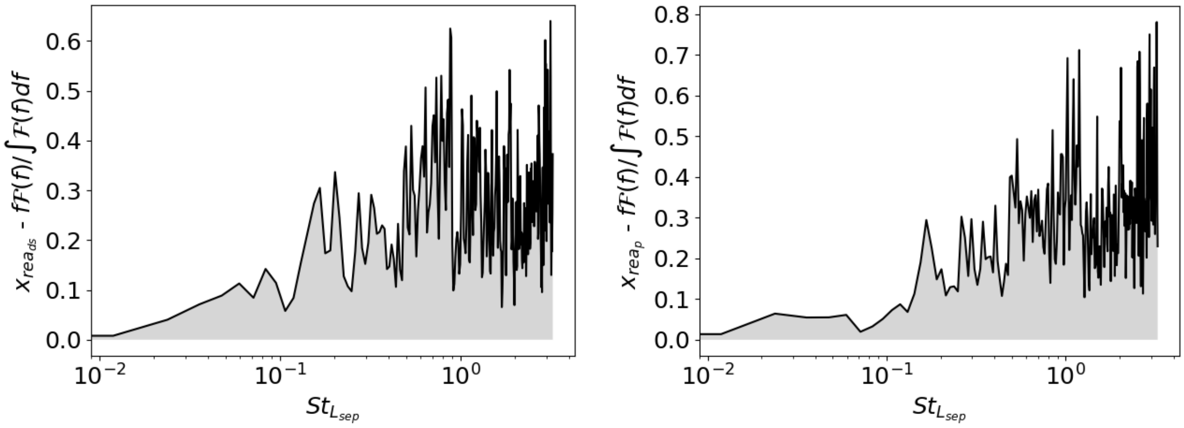

(e) Reattachment point computed based on dividing streamline (explanation on the computation method in Section 4.3).

(f) Reattachment point computed based on threshold pressure (explanation on the computation method in Section 4.3).

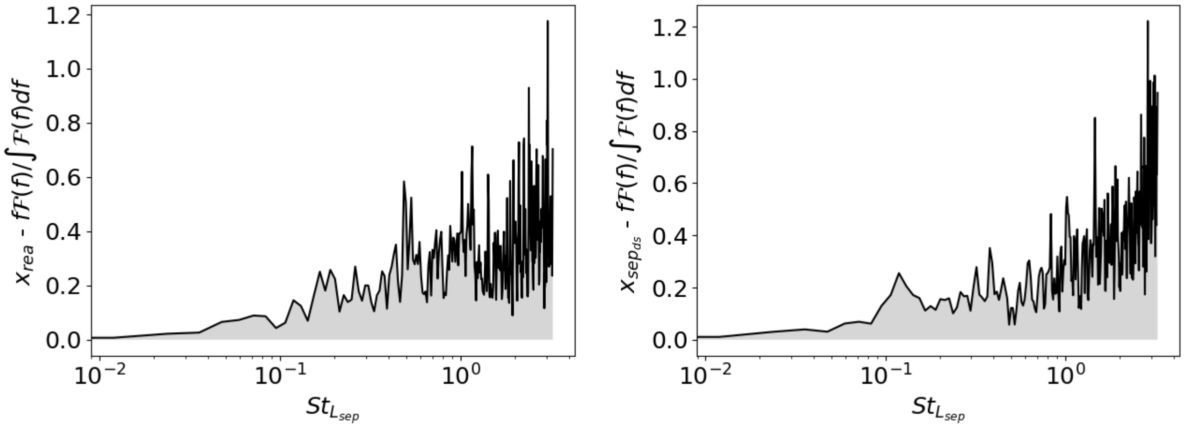

(g) Reattachment point computed based on skin-friction coefficient (explanation on the computation method in Section 4.3).

(h) Separation point computed based on dividing streamline (explanation on the computation method in Section 4.3).

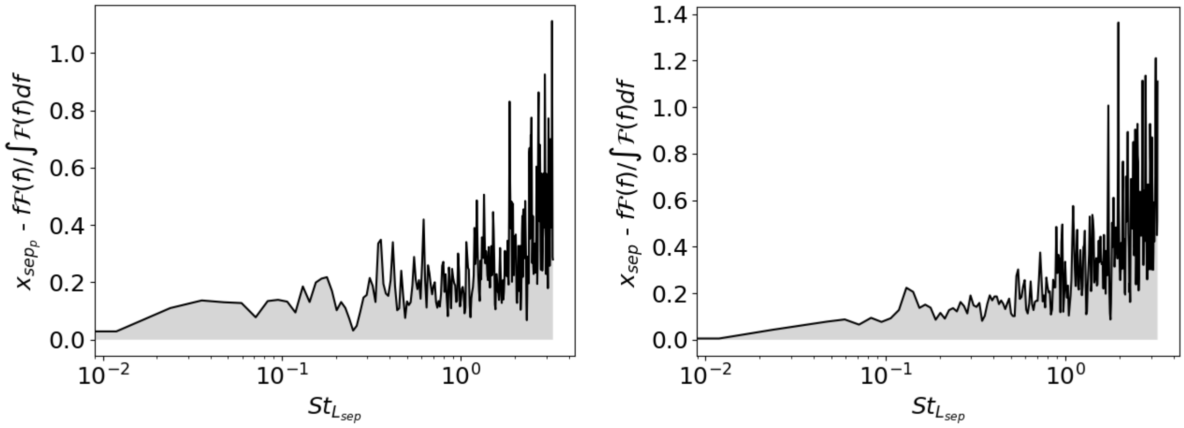

(i) Separation point computed based on threshold pressure (explanation on the computation method in Section 4.3).

(j) Separation point computed based on skin-friction coefficient (explanation on the computation method in Section 4.3).

Figure E.1: Normalised pre-multiplied power spectral density of STBLI dynamic properties.

Appendix F

Power Spectral Density (PSD) of dynamic quantities ($\mathcal{P}$)

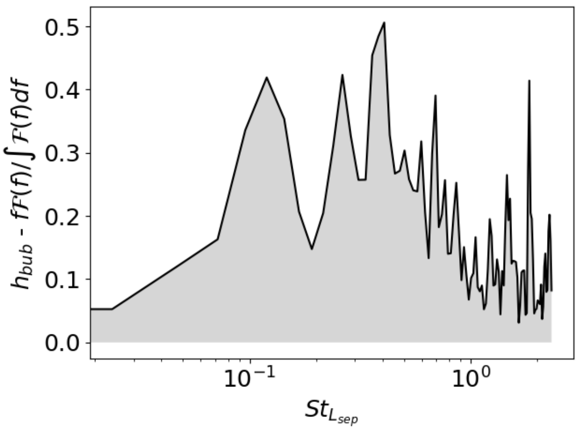

(a) Bubble height.

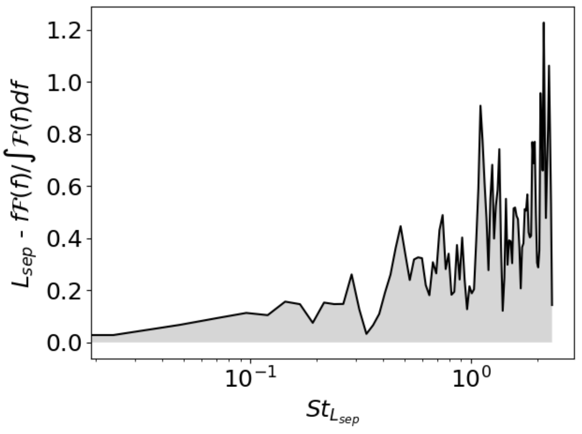

(b) Separation length.

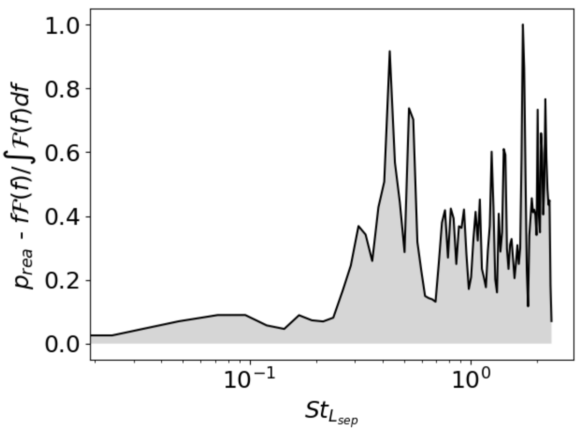

(c) Pressure at reattachment point.

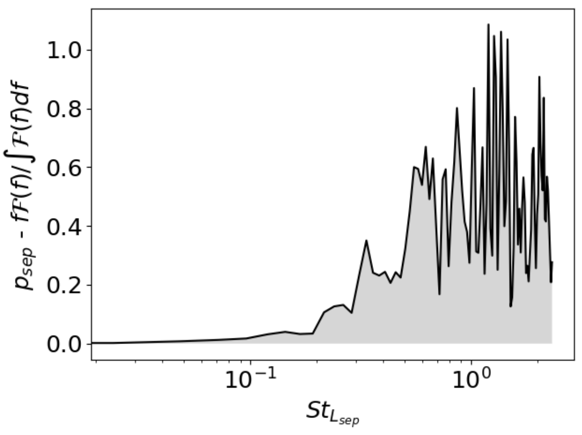

(d) Pressure at separation point.

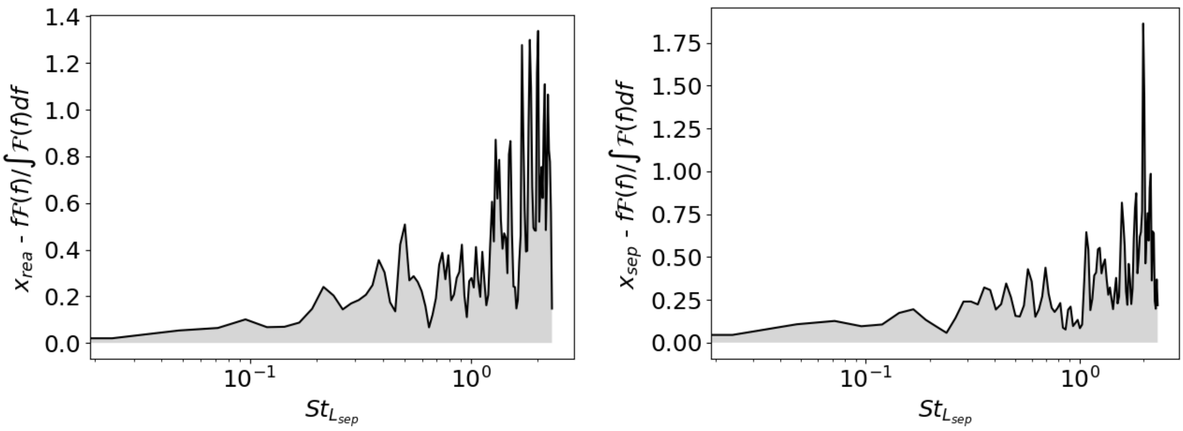

(e) Reattachment point computed based on skin-friction coefficient (explanation on the computation method in Section 4.3).

(f) Separation point computed based on skin-friction coefficient (explanation on the computation method in Section 4.3).

Appendix G

Cross-correlation & coherence between dynamic quantities ($\mathcal{F}$)

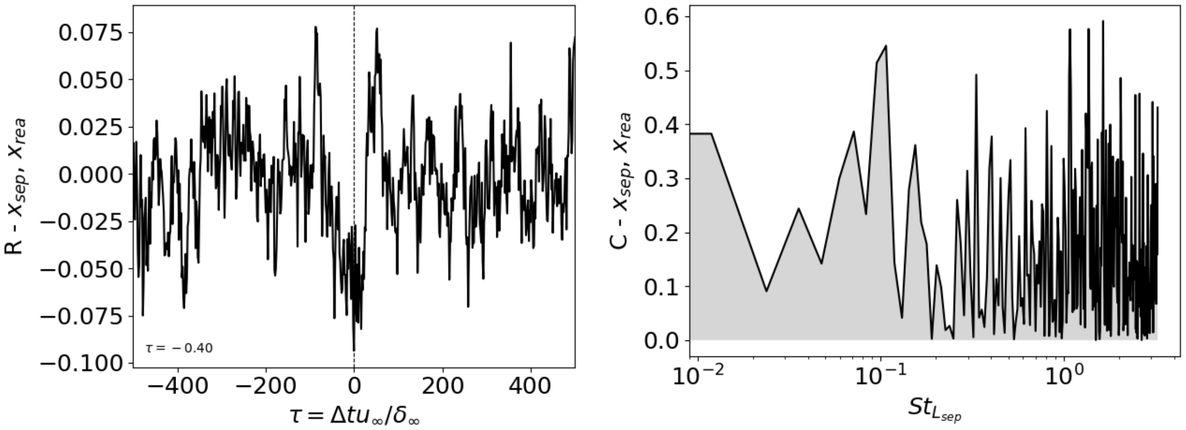

(a) Cross-correlation coefficient.

(b) Coherence.

Figure G.1: Separation point (skin-friction based) and reattachment point (skin-friction based).

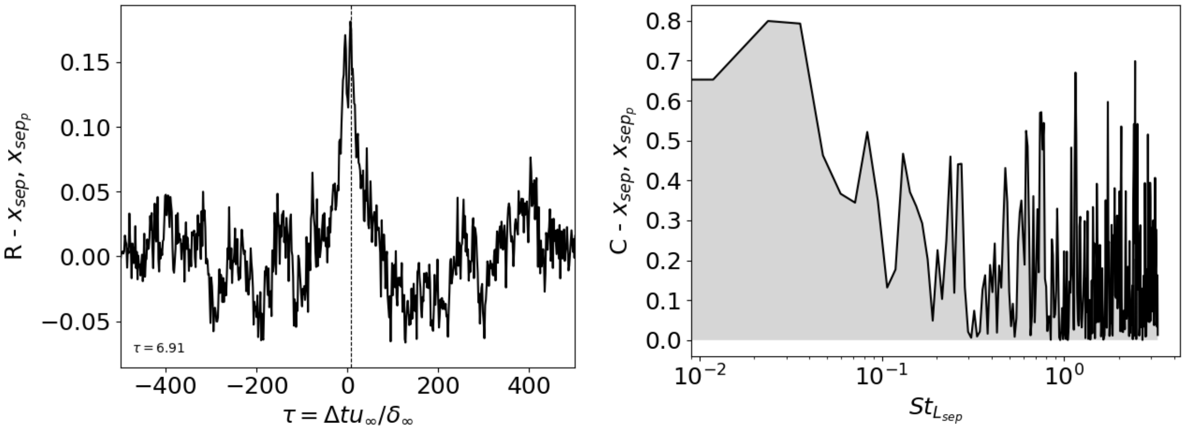

(a) Cross-correlation coefficient.

(b) Coherence.

Figure G.2: Separation point (skin-friction based) and separation point (pressure based).

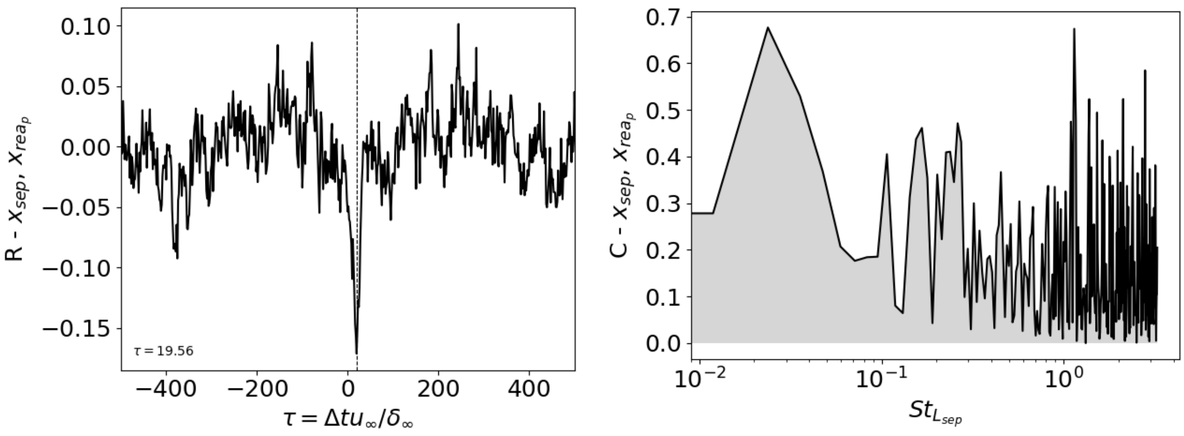

(a) Cross-correlation coefficient.

(b) Coherence.

Figure G.3: Separation point (skin-friction based) and reattachment point (pressure based).

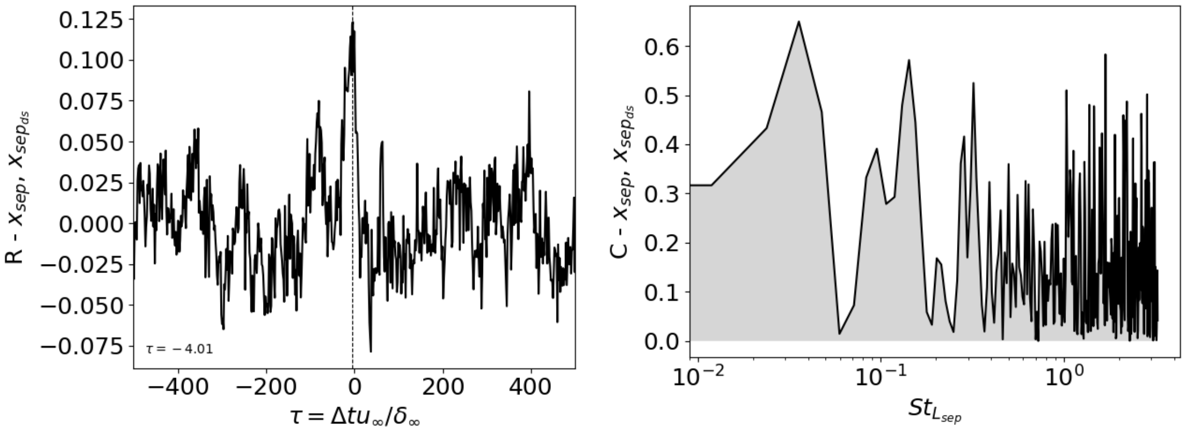

(a) Cross-correlation coefficient.

(b) Coherence.

Figure G.4: Separation point (skin-friction based) and separation point (dividing streamline based).

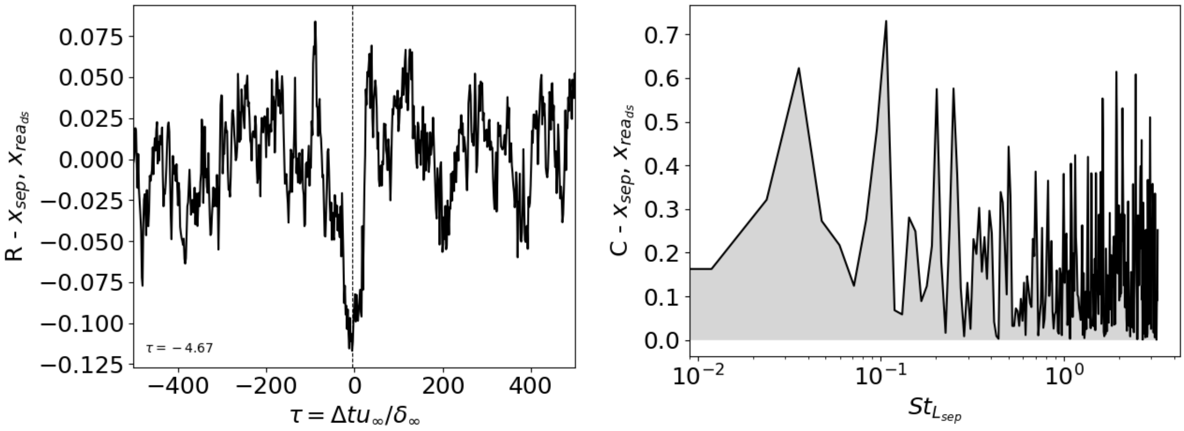

(a) Cross-correlation coefficient.

(b) Coherence.

Figure G.5: Separation point (skin-friction based) and reattachment point (dividing streamline based).

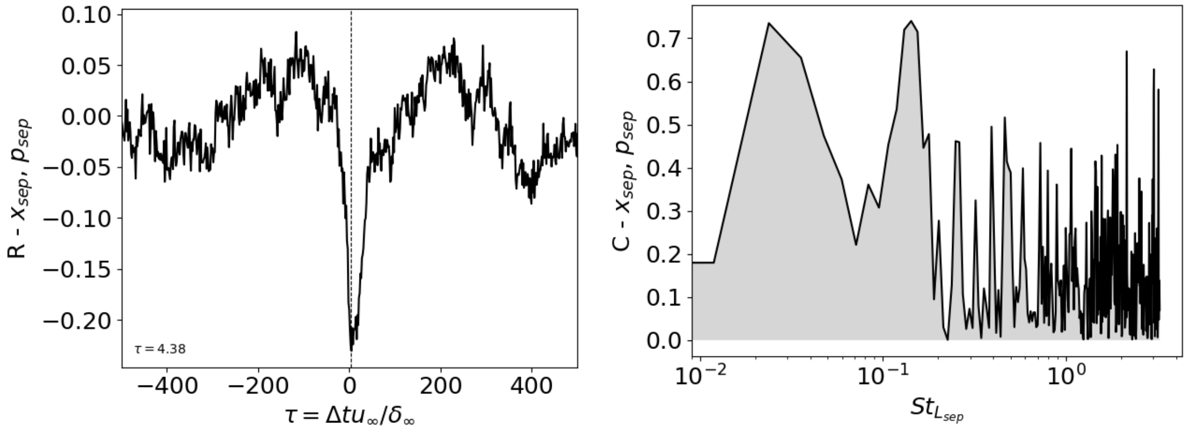

(a) Cross-correlation coefficient.

(b) Coherence.

Figure G.6: Separation point (skin-friction based) and pressure at separation location.

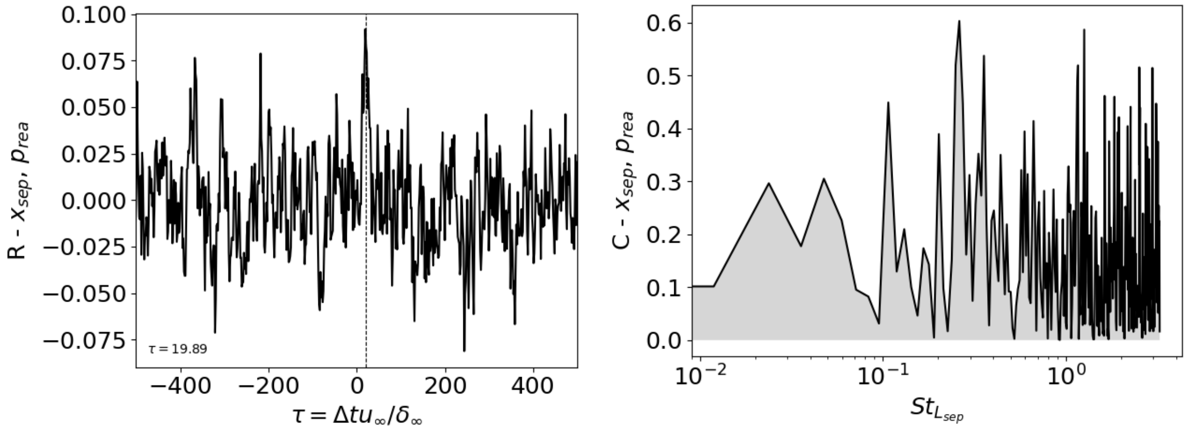

(a) Cross-correlation coefficient.

(b) Coherence.

Figure G.7: Separation point (skin-friction based) and pressure at reattachment location.

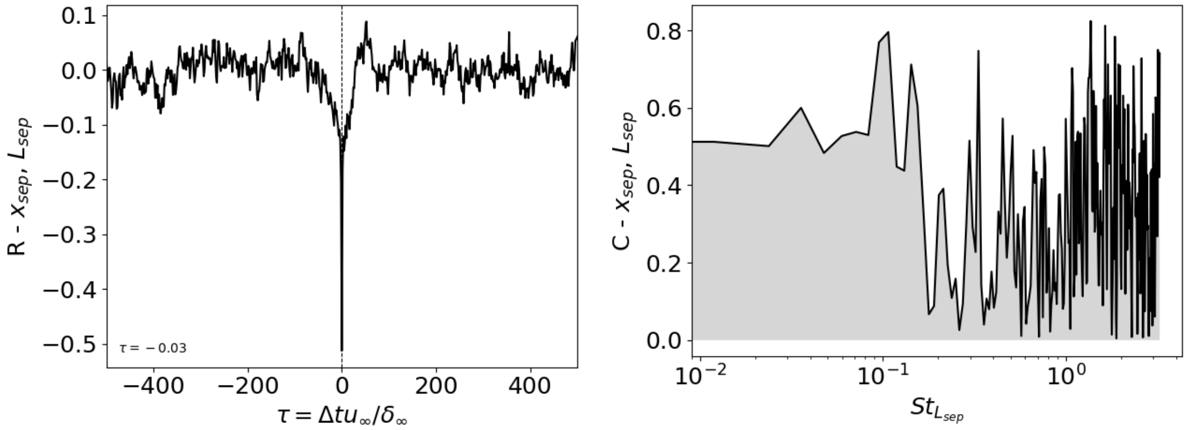

(a) Cross-correlation coefficient.

(b) Coherence.

Figure G.8: Separation point (skin-friction based) and separation length.

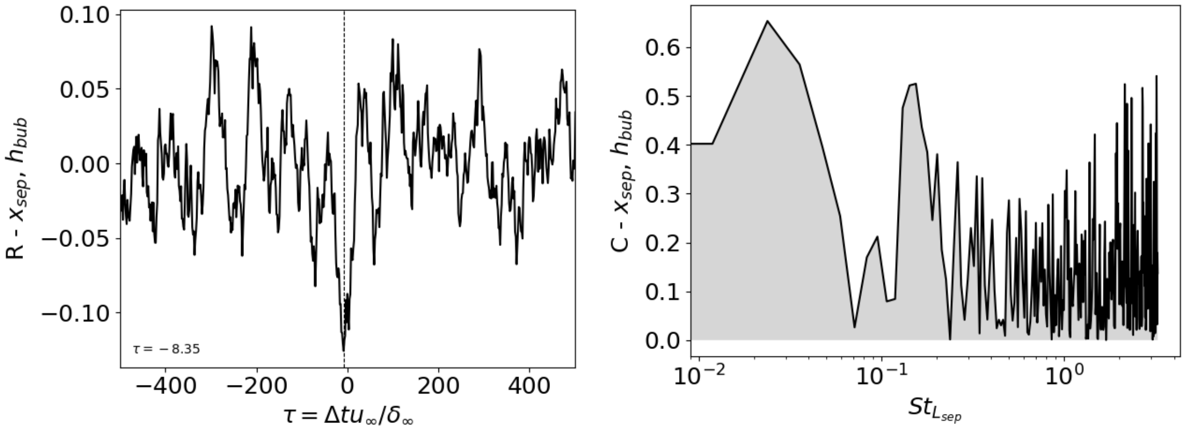

(a) Cross-correlation coefficient.

(b) Coherence.

Figure G.9: Separation point (skin-friction based) and bubble height.

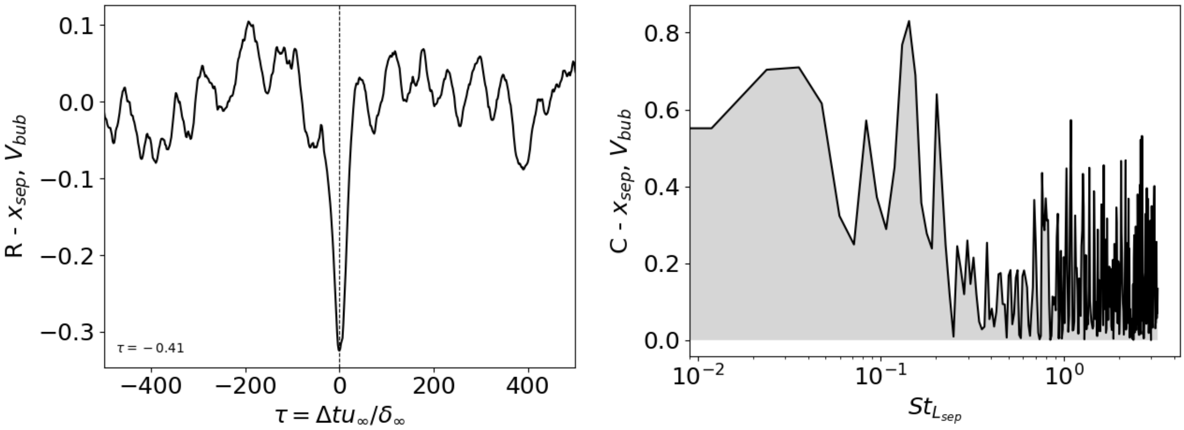

(a) Cross-correlation coefficient.

(b) Coherence.

Figure G.10: Separation point (skin-friction based) and bubble volume.

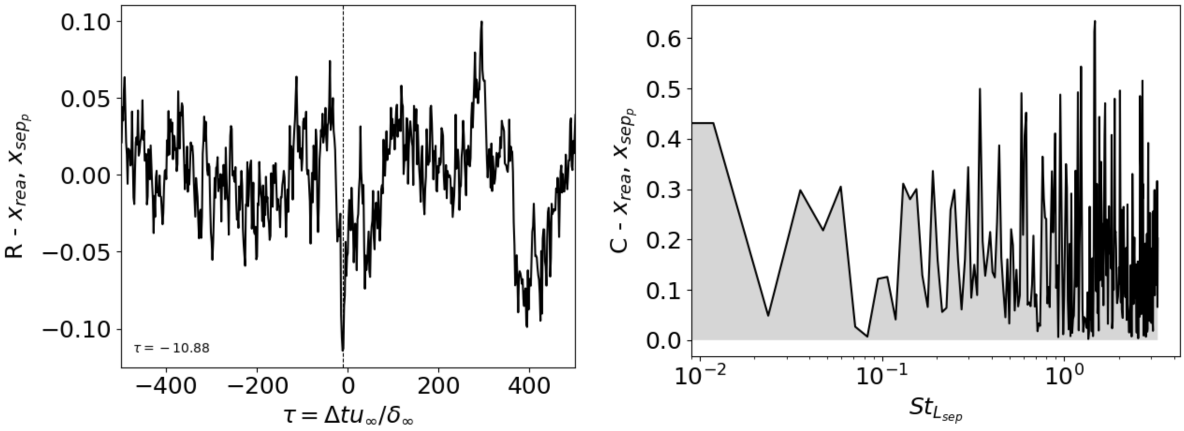

(a) Cross-correlation coefficient.

(b) Coherence.

Figure G.11: Reattachment point (skin-friction based) and separation point (pressure based).

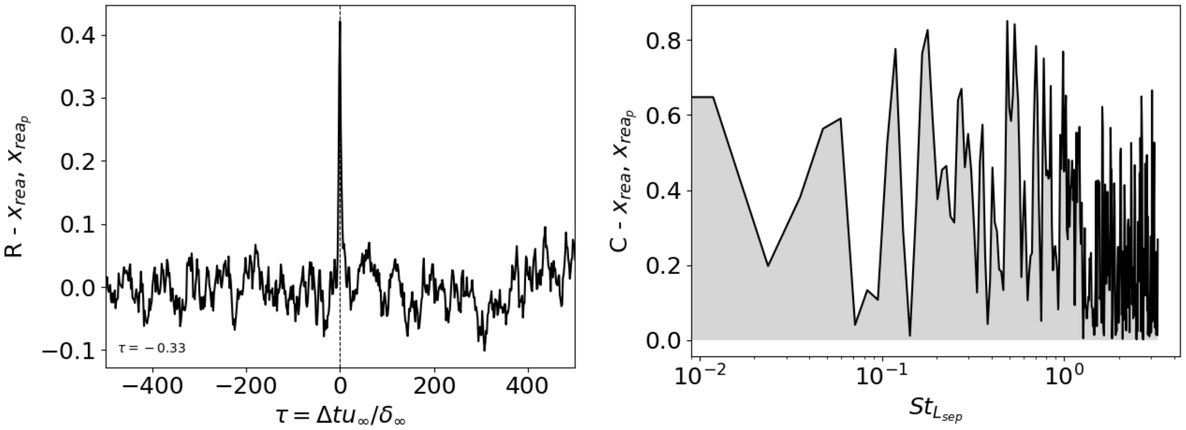

(a) Cross-correlation coefficient.

(b) Coherence.

Figure G.12: Reattachment point (skin-friction based) and reattachment point (pressure based).

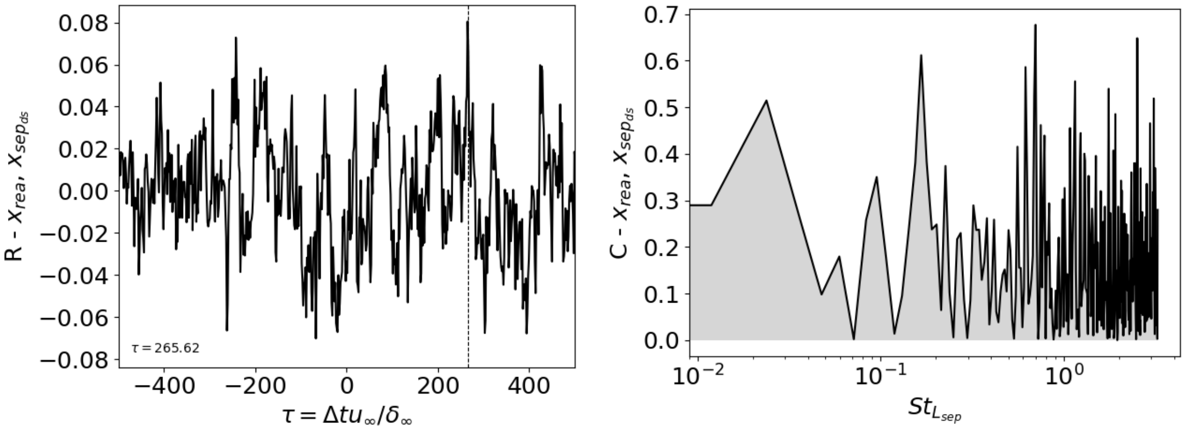

(a) Cross-correlation coefficient.

(b) Coherence.

Figure G.13: Reattachment point (skin-friction based) and separation point (dividing streamline based).

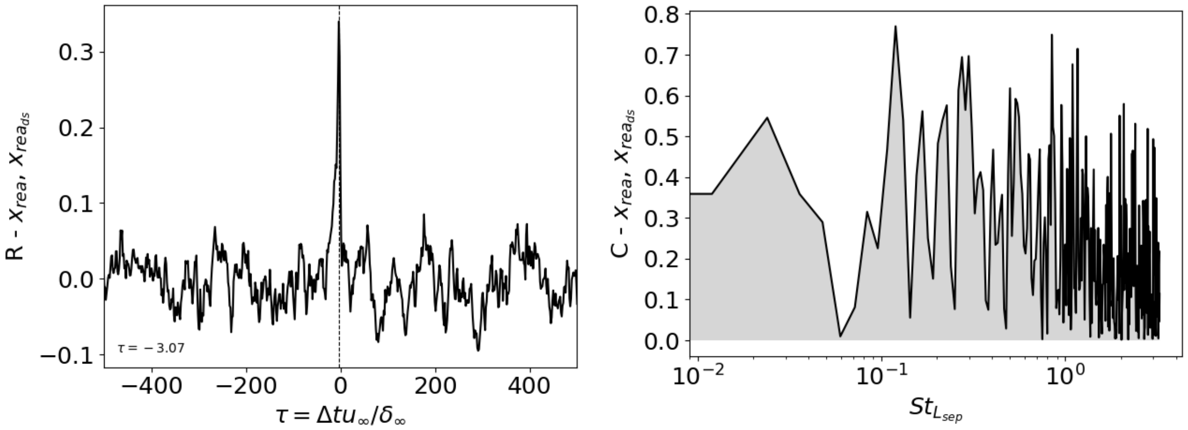

(a) Cross-correlation coefficient.

(b) Coherence.

Figure G.14: Reattachment point (skin-friction based) and reattachment point (dividing streamline based).

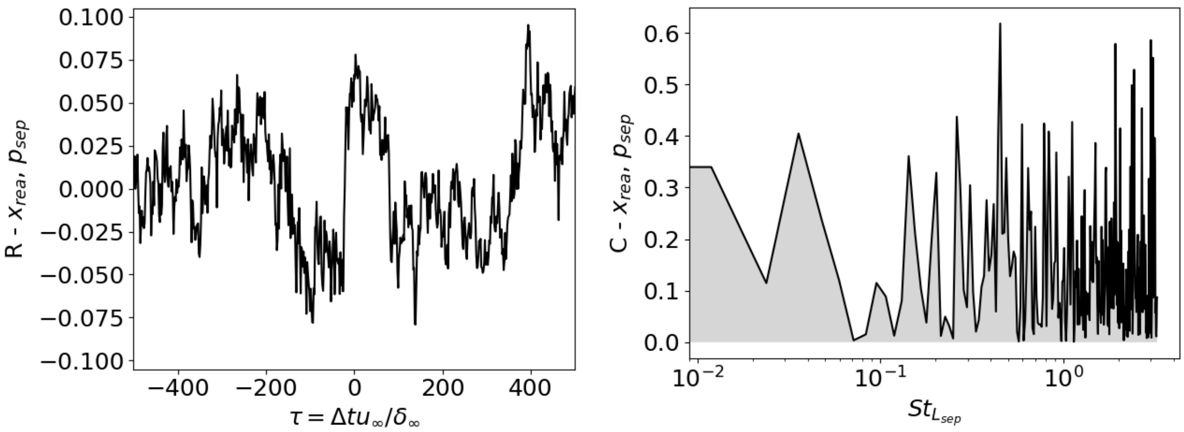

(a) Cross-correlation coefficient.

(b) Coherence.

Figure G.15: Reattachment point (skin-friction based) and pressure at separation location.

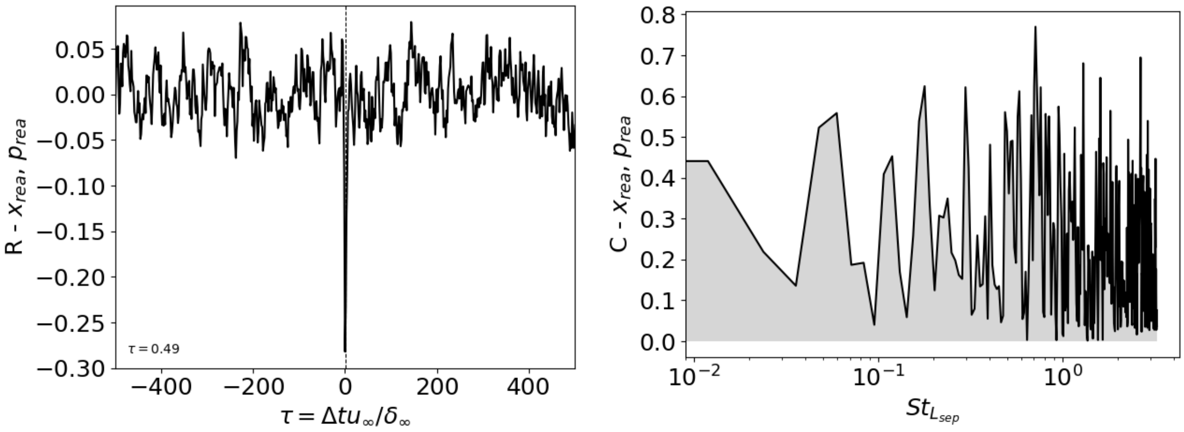

(a) Cross-correlation coefficient.

(b) Coherence.

Figure G.16: Reattachment point (skin-friction based) and pressure at reattachment location.

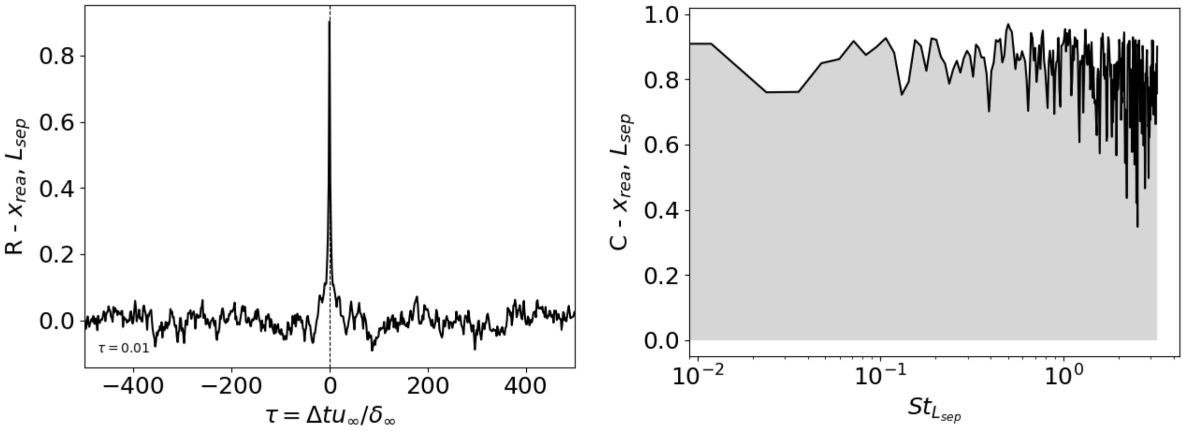

(a) Cross-correlation coefficient.

(b) Coherence.

Figure G.17: Reattachment point (skin-friction based) and separation length.

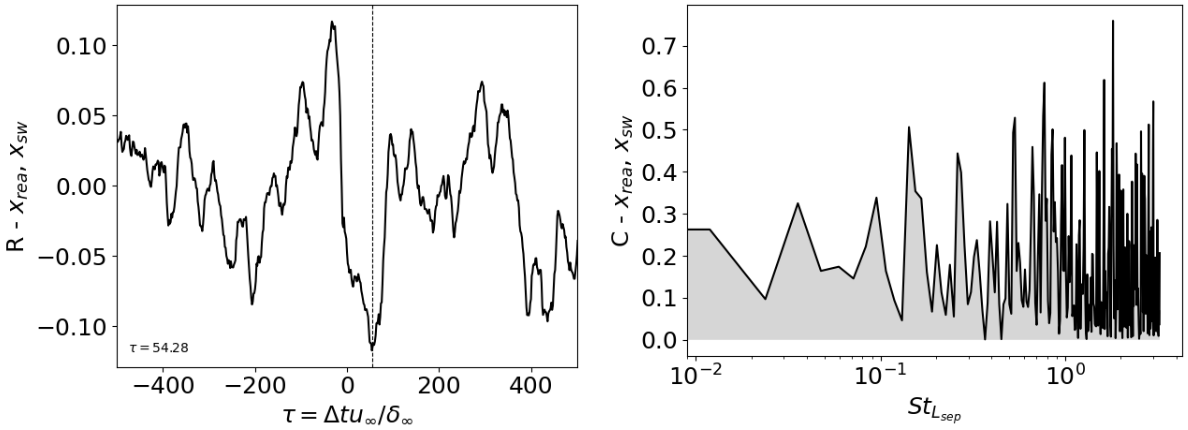

(a) Cross-correlation coefficient.

(b) Coherence.

Figure G.18: Reattachment point (skin-friction based) and reflected shock location.

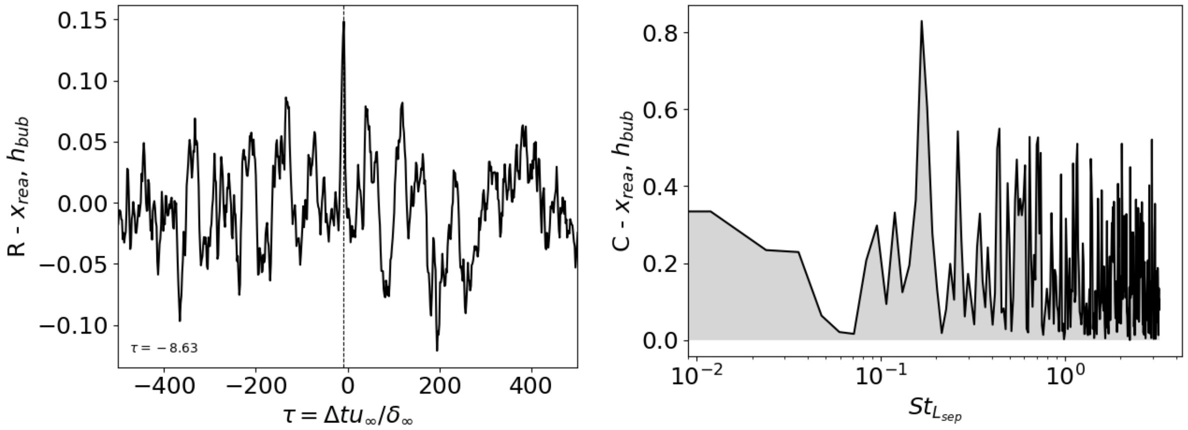

(a) Cross-correlation coefficient.

(b) Coherence.

Figure G.19: Reattachment point (skin-friction based) and bubble height.

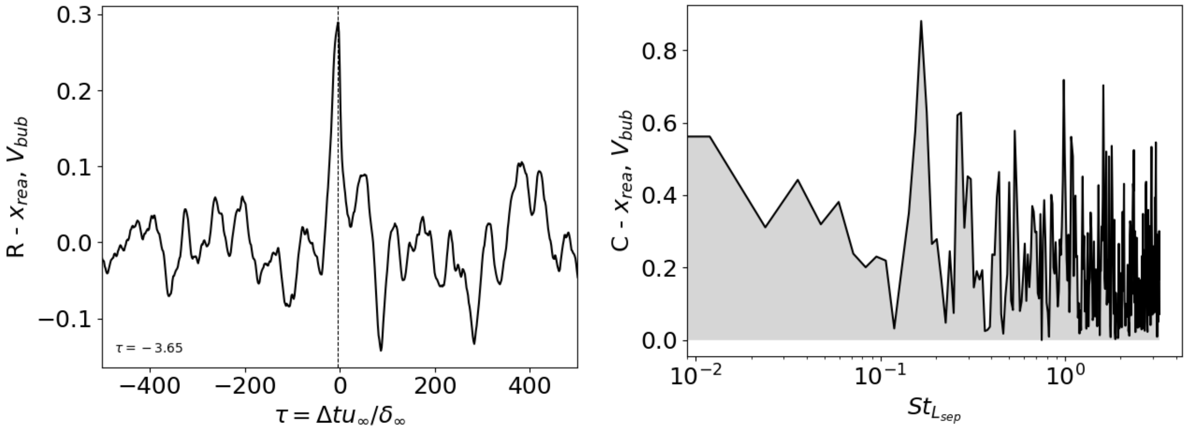

(a) Cross-correlation coefficient.

(b) Coherence.

Figure G.20: Reattachment point (skin-friction based) and bubble volume.

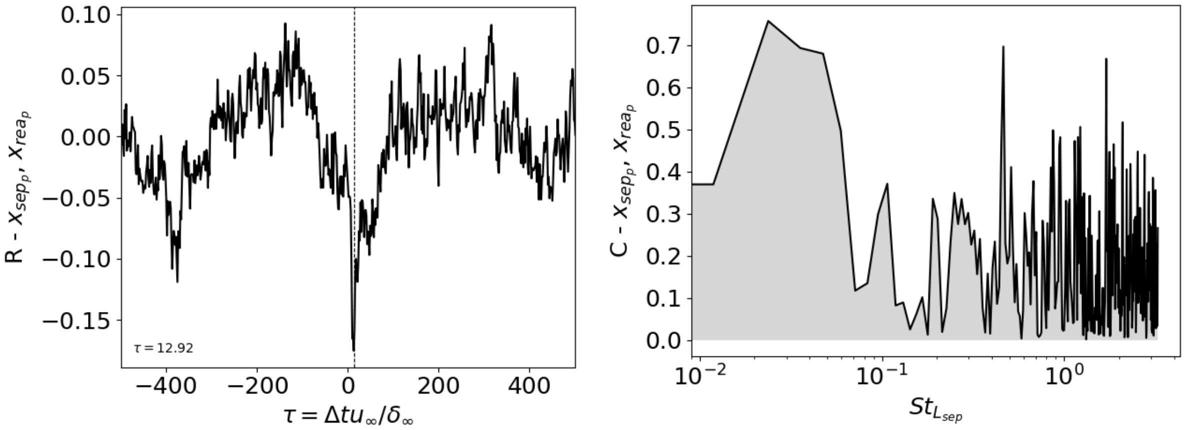

(a) Cross-correlation coefficient.

(b) Coherence.

Figure G.21: Separation point (pressure based) and reattachment point (pressure based).

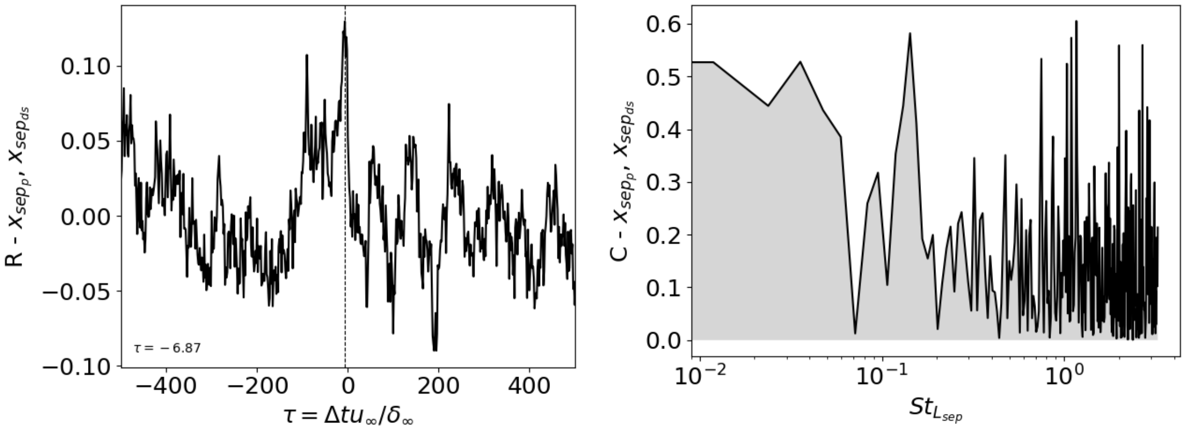

(a) Cross-correlation coefficient.

(b) Coherence.

Figure G.22: Separation point (pressure based) and separation point (dividing streamline based).

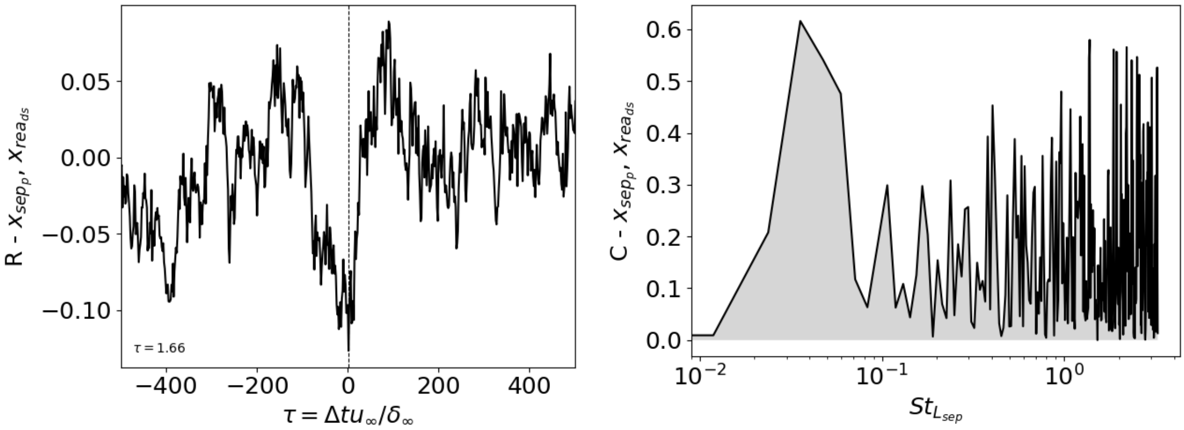

(a) Cross-correlation coefficient.

(b) Coherence.

Figure G.23: Separation point (pressure based) and reattachment point (dividing streamline based).

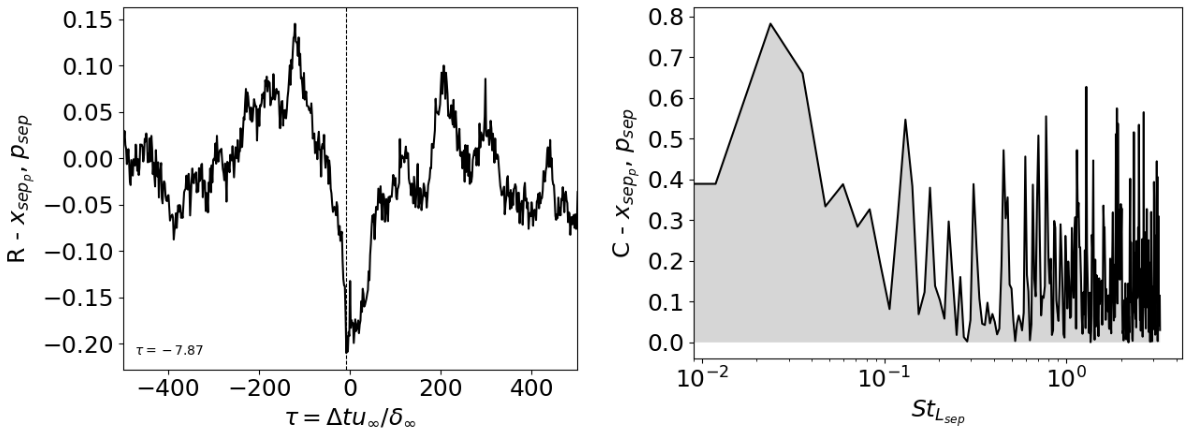

(a) Cross-correlation coefficient.

(b) Coherence.

Figure G.24: Separation point (pressure based) and pressure at separation point.

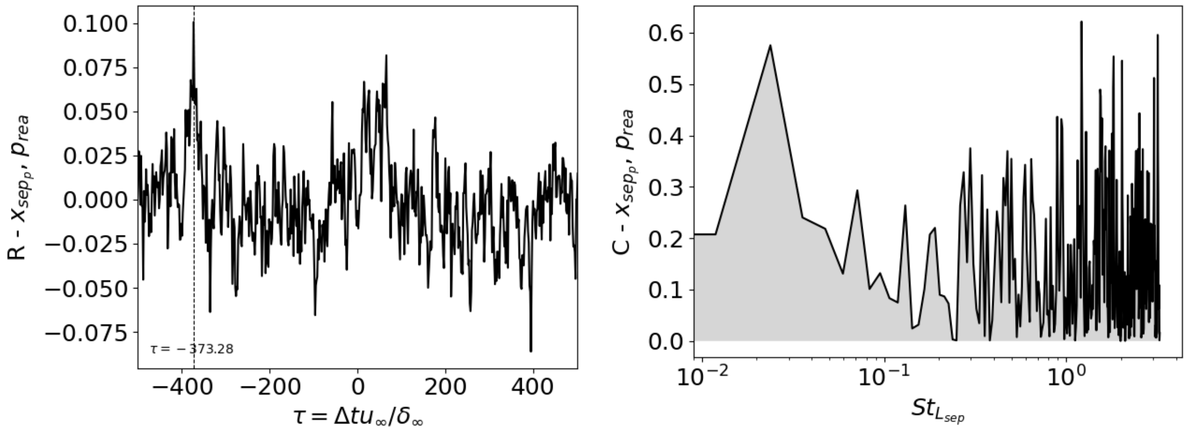

(a) Cross-correlation coefficient.

(b) Coherence.

Figure G.25: Separation point (pressure based) and pressure at reattachment point.

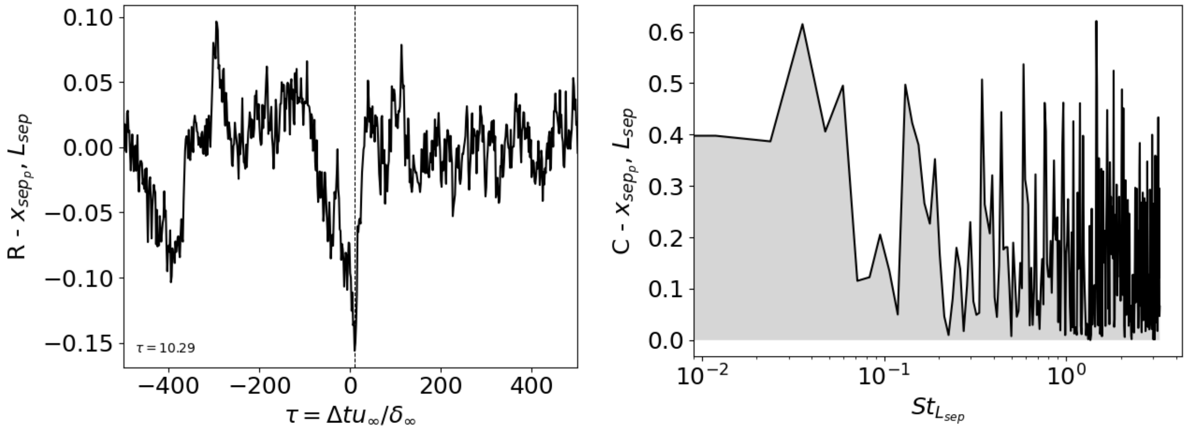

(a) Cross-correlation coefficient.

(b) Coherence.

Figure G.26: Separation point (pressure based) and separation length.

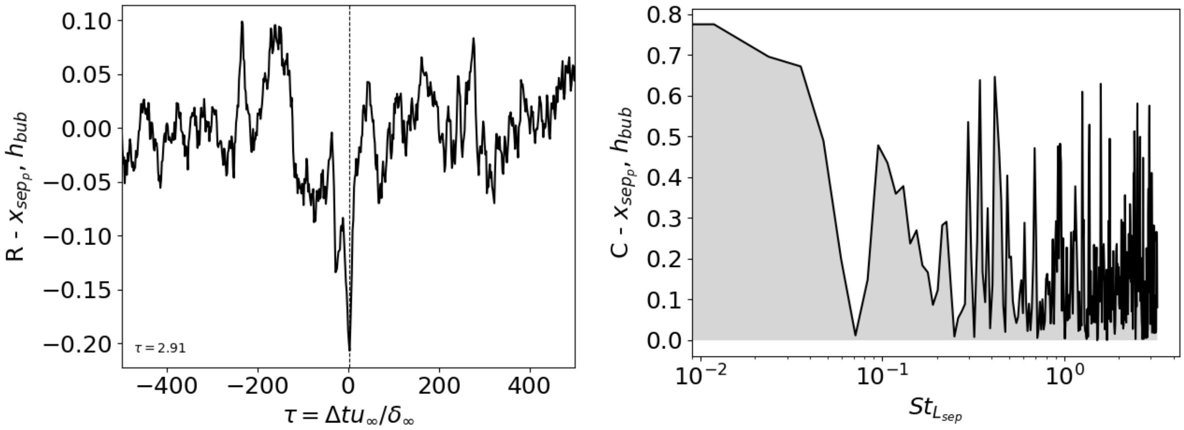

(a) Cross-correlation coefficient.

(b) Coherence.

Figure G.27: Separation point (pressure based) and bubble height.

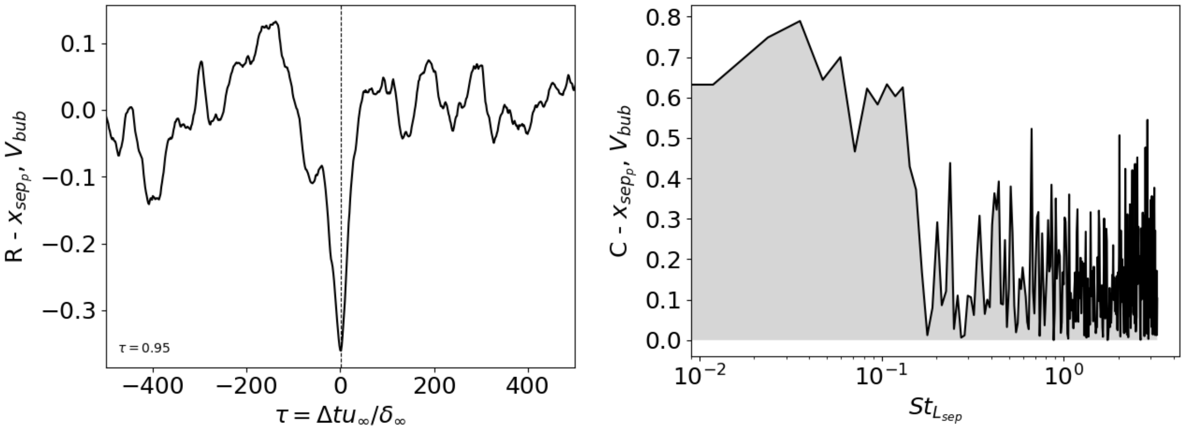

(a) Cross-correlation coefficient.

(b) Coherence.

Figure G.28: Separation point (pressure based) and bubble volume.

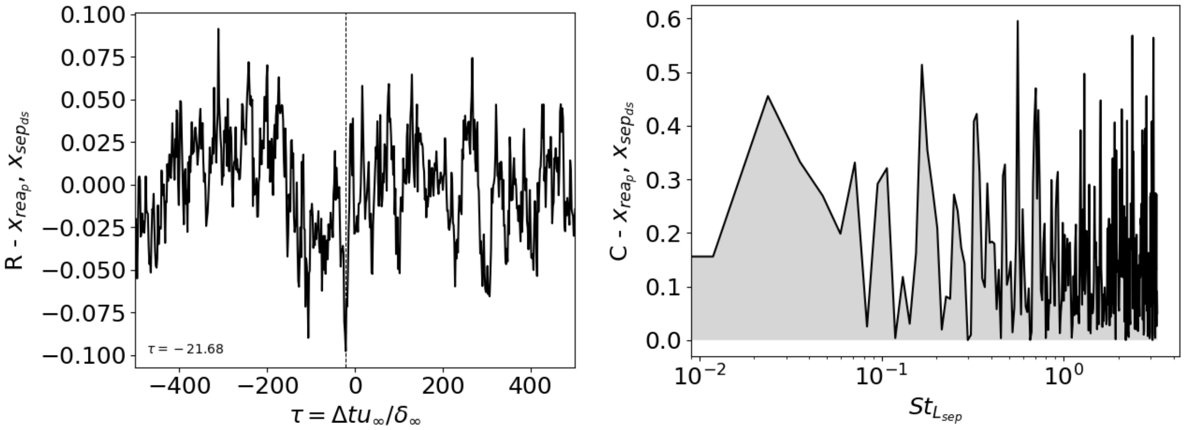

(a) Cross-correlation coefficient.

(b) Coherence.

Figure G.29: Reattachment point (pressure based) and separation point (dividing streamline based).

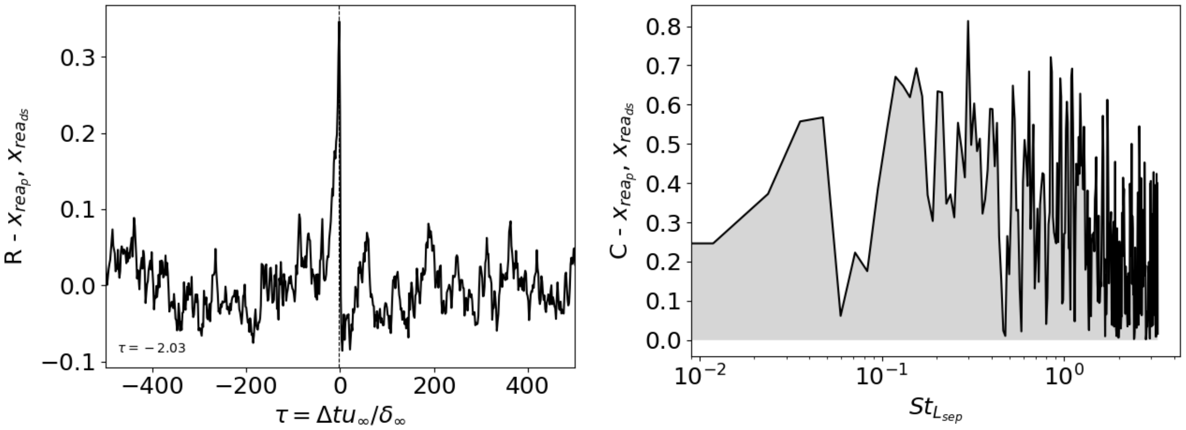

(a) Cross-correlation coefficient.

(b) Coherence.

Figure G.30: Reattachment point (pressure based) and reattachment point (dividing streamline based).

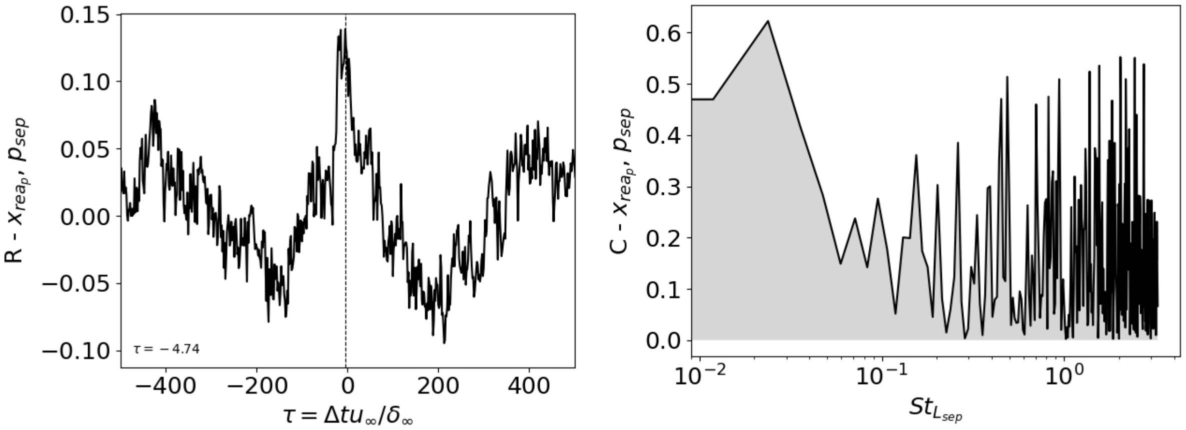

(a) Cross-correlation coefficient.

(b) Coherence.

Figure G.31: Reattachment point (pressure based) and pressure at separation point.

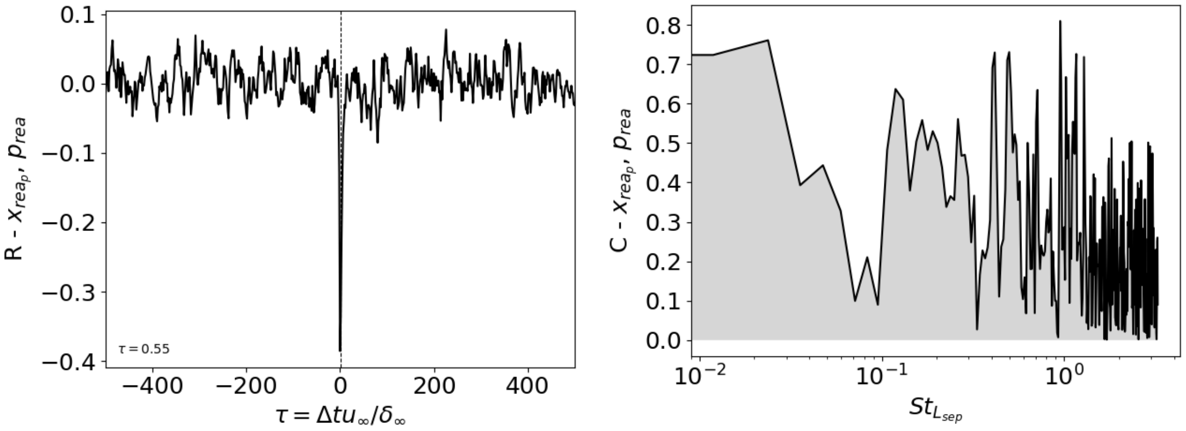

(a) Cross-correlation coefficient.

(b) Coherence.

Figure G.32: Reattachment point (pressure based) and pressure at reattachment point.

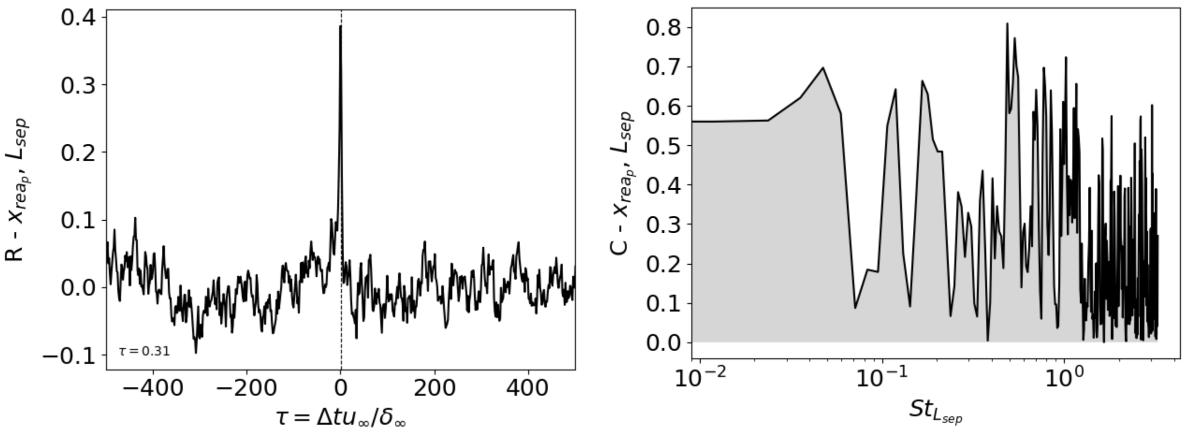

(a) Cross-correlation coefficient.

(b) Coherence.

Figure G.33: Reattachment point (pressure based) and separation length.

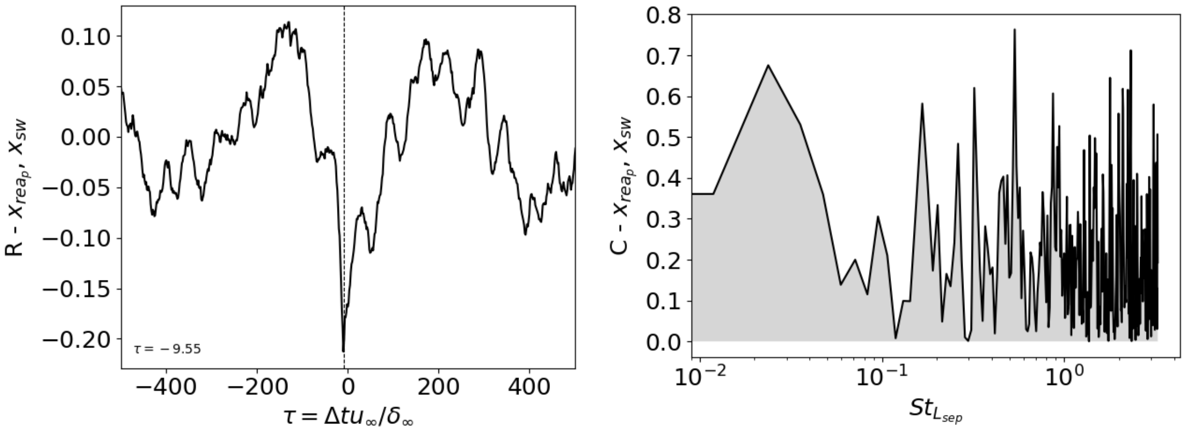

(a) Cross-correlation coefficient.

(b) Coherence.

Figure G.34: Reattachment point (pressure based) and reflected shock location.

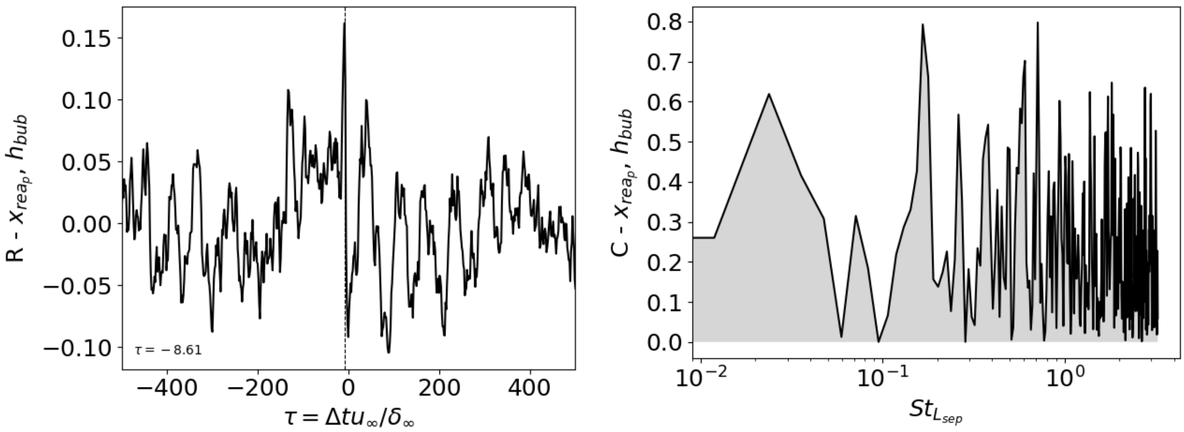

(a) Cross-correlation coefficient.

(b) Coherence.

Figure G.35: Reattachment point (pressure based) and bubble height.

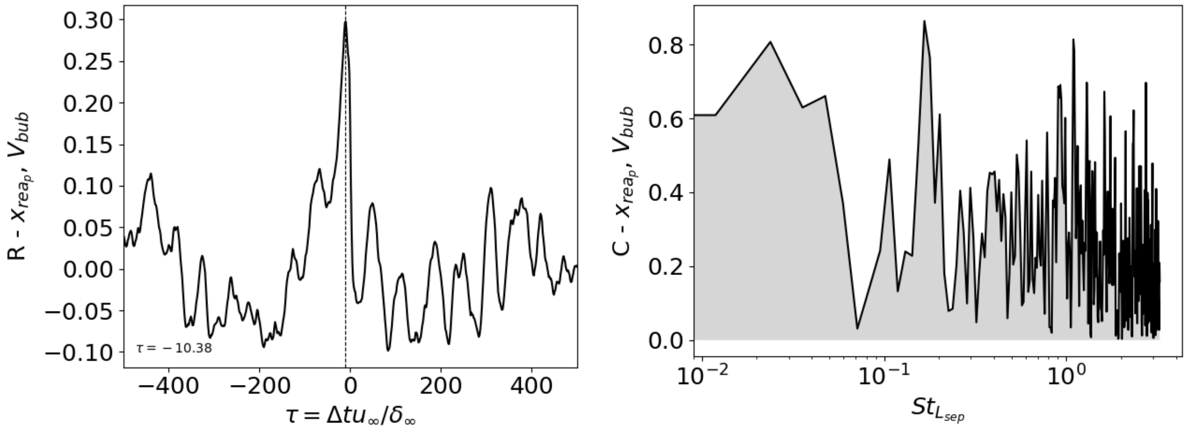

(a) Cross-correlation coefficient.

(b) Coherence.

Figure G.36: Reattachment point (pressure based) and bubble volume.

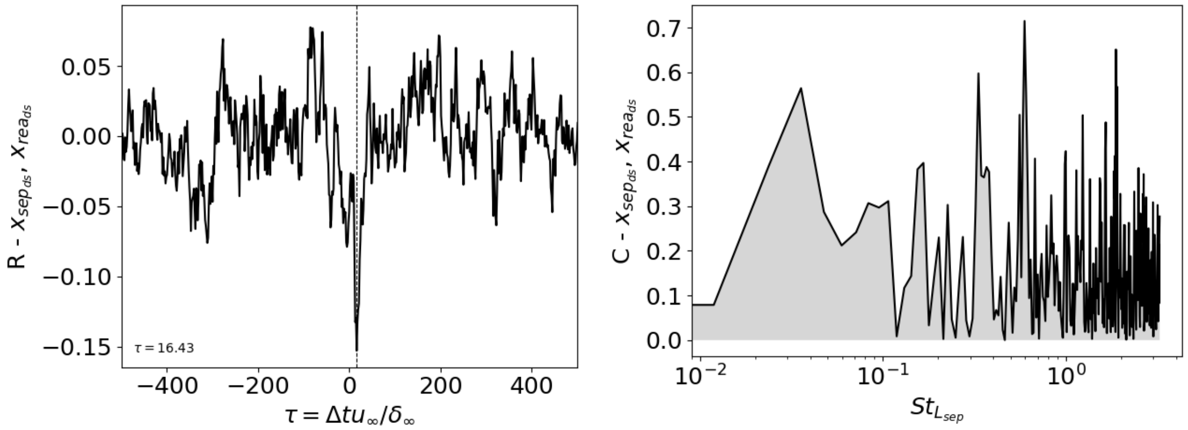

(a) Cross-correlation coefficient.

(b) Coherence.

Figure G.37: Separation point (dividing streamline based) and reattachment point (dividing streamline based).

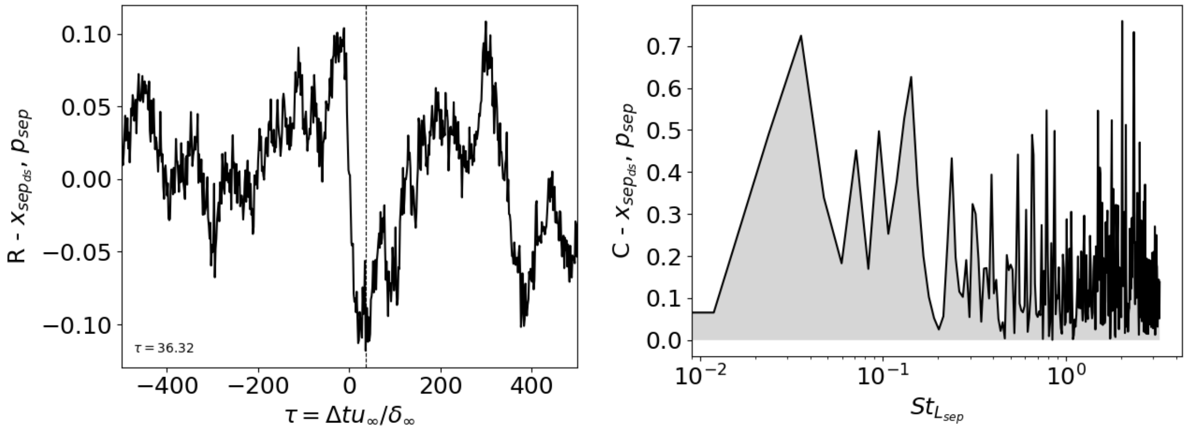

(a) Cross-correlation coefficient.

(b) Coherence.

Figure G.38: Separation point (dividing streamline based) and pressure at separation point.

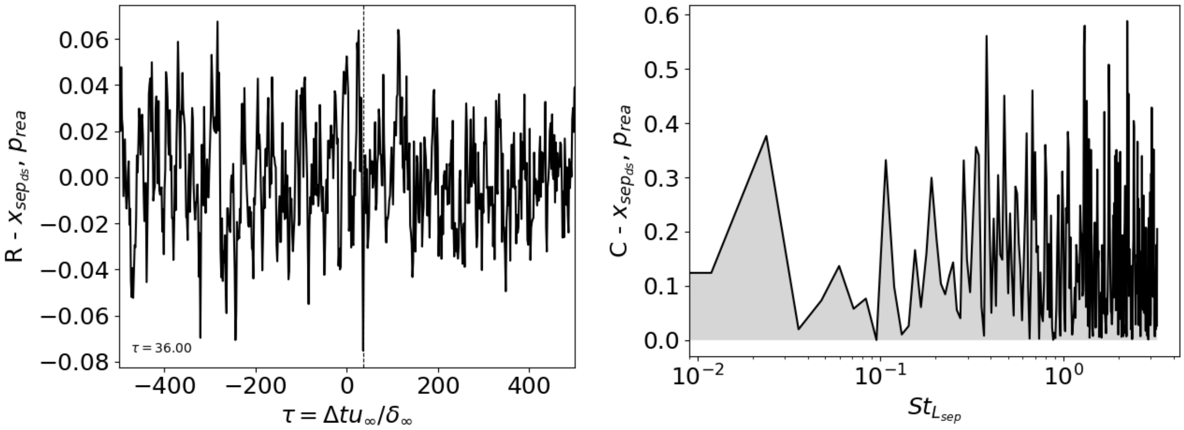

(a) Cross-correlation coefficient.

(b) Coherence.

Figure G.39: Separation point (dividing streamline based) and pressure at reattachment point.

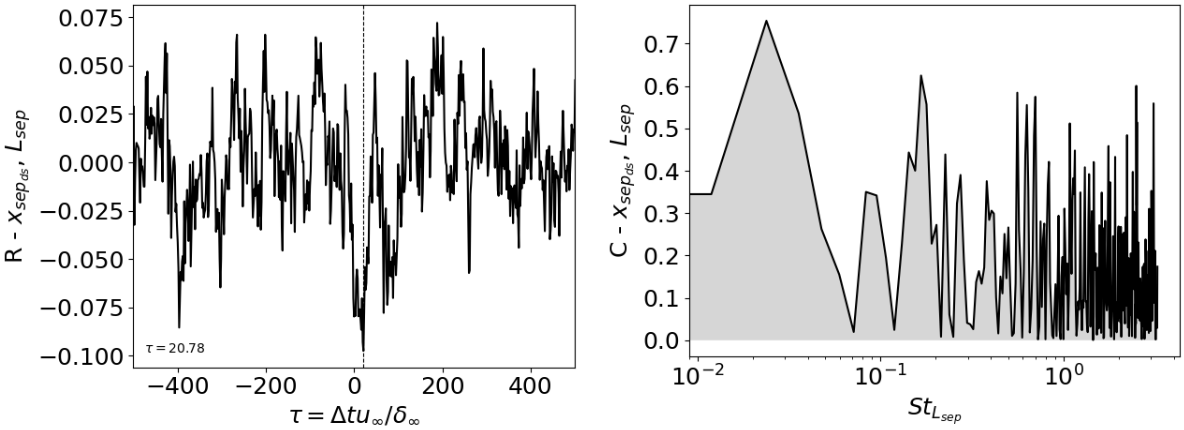

(a) Cross-correlation coefficient.

(b) Coherence.

Figure G.40: Separation point (dividing streamline based) and separation length.

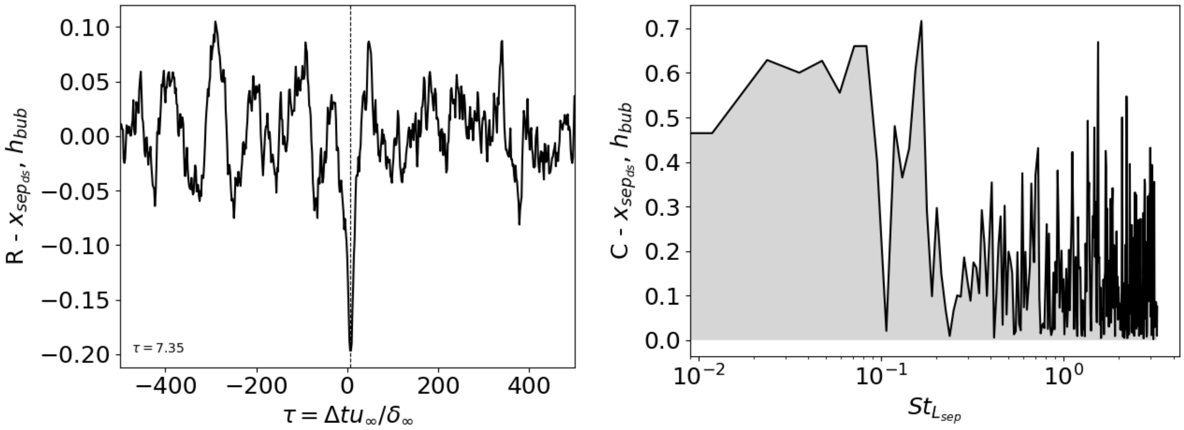

(a) Cross-correlation coefficient.

(b) Coherence.

Figure G.41: Separation point (dividing streamline based) and bubble height.

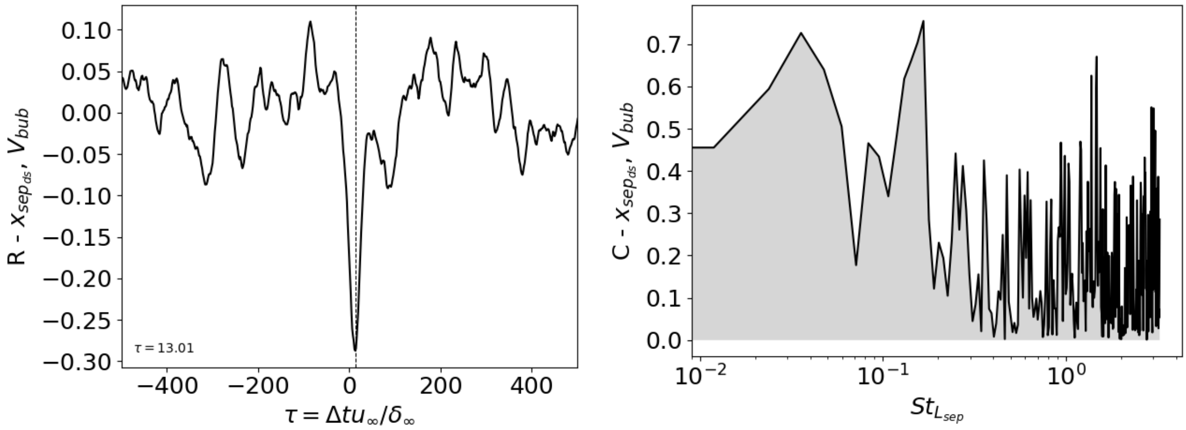

(a) Cross-correlation coefficient.

(b) Coherence.

Figure G.42: Separation point (dividing streamline based) and bubble volume.

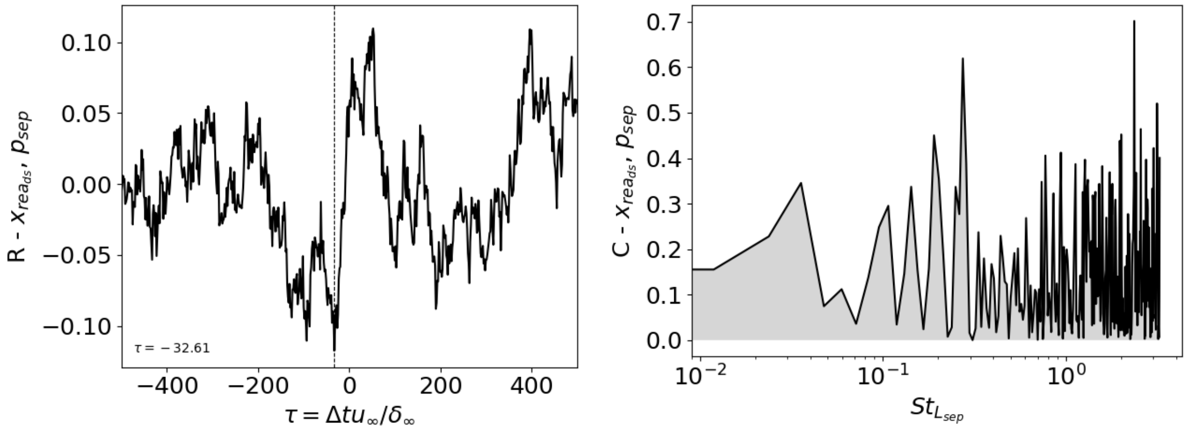

(a) Cross-correlation coefficient.

(b) Coherence.

Figure G.43: Reattachment point (dividing streamline based) and pressure at separation point.

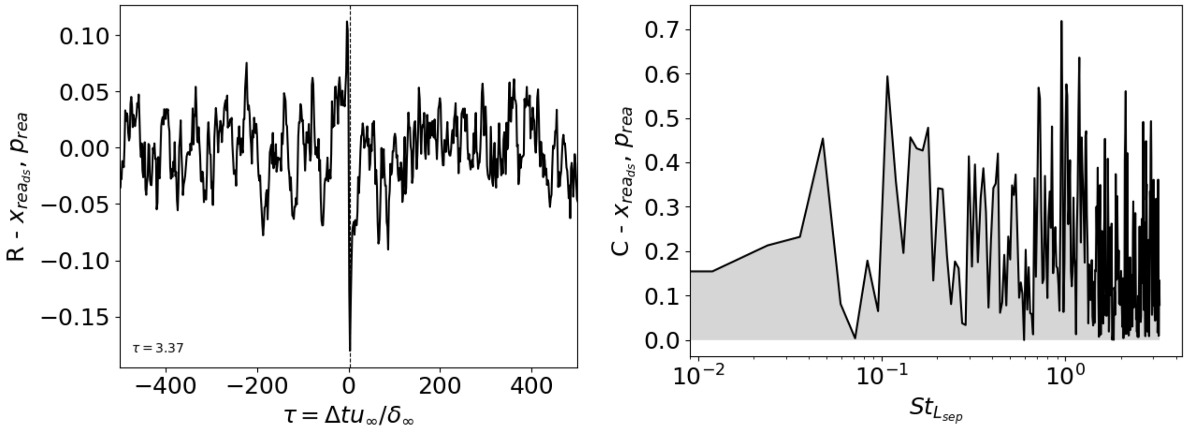

(a) Cross-correlation coefficient.

(b) Coherence.

Figure G.44: Reattachment point (dividing streamline based) and pressure at reattachment point.

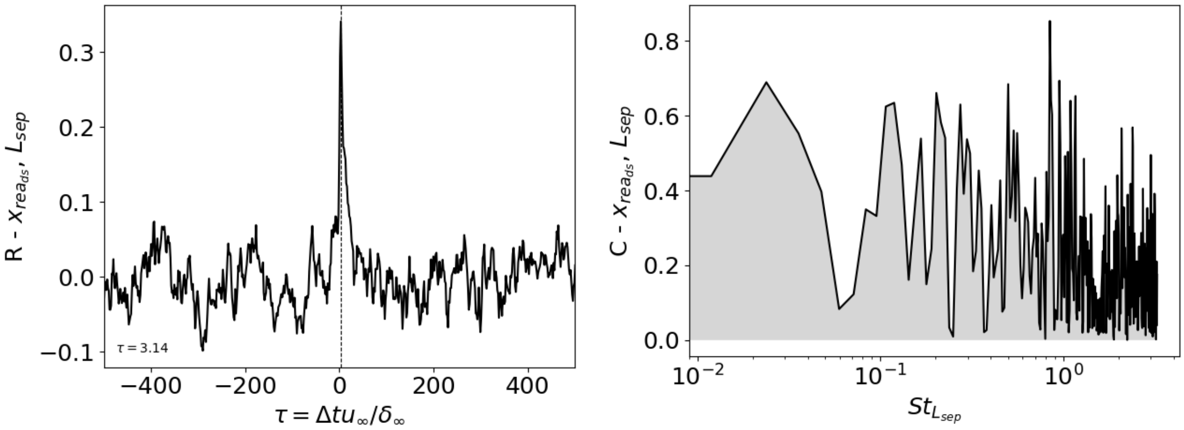

(a) Cross-correlation coefficient.

(b) Coherence.

Figure G.45: Reattachment point (dividing streamline based) and separation length.

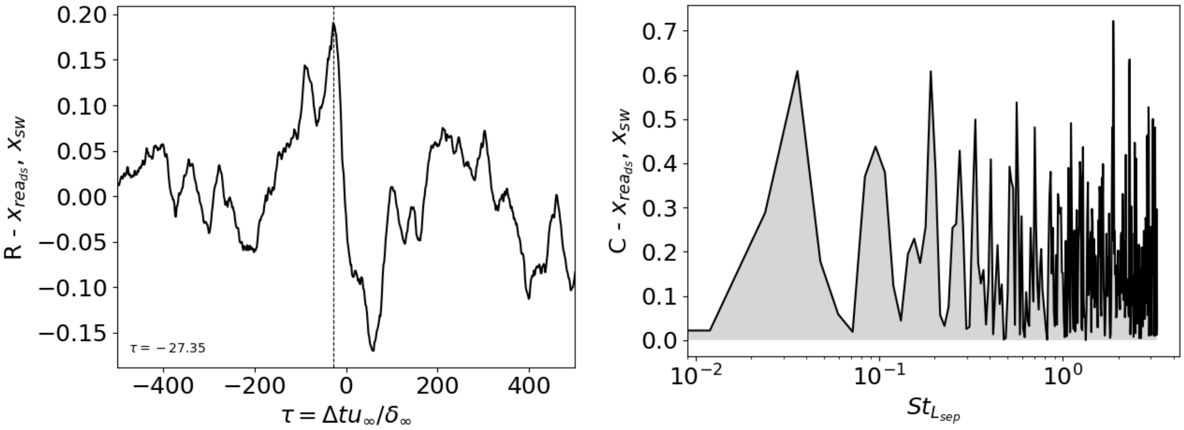

(a) Cross-correlation coefficient.

(b) Coherence.

Figure G.46: Reattachment point (dividing streamline based) and reflected shock location.

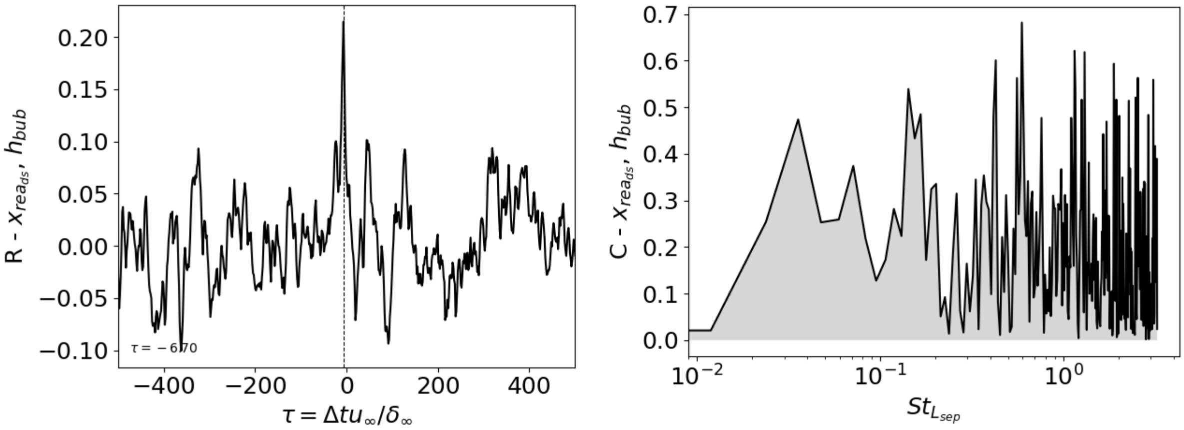

(a) Cross-correlation coefficient.

(b) Coherence.

Figure G.47: Reattachment point (dividing streamline based) and bubble height.

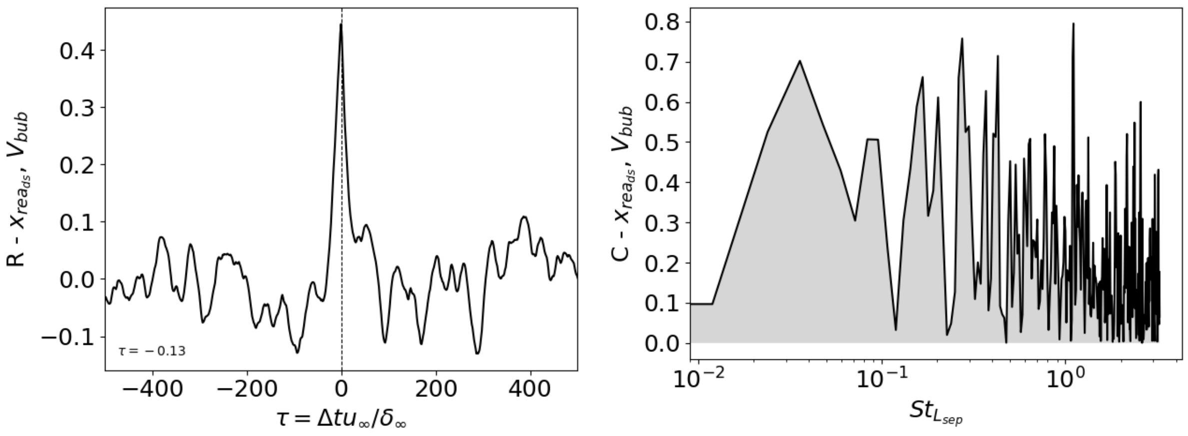

(a) Cross-correlation coefficient.

(b) Coherence.

Figure G.48: Reattachment point (dividing streamline based) and bubble volume.

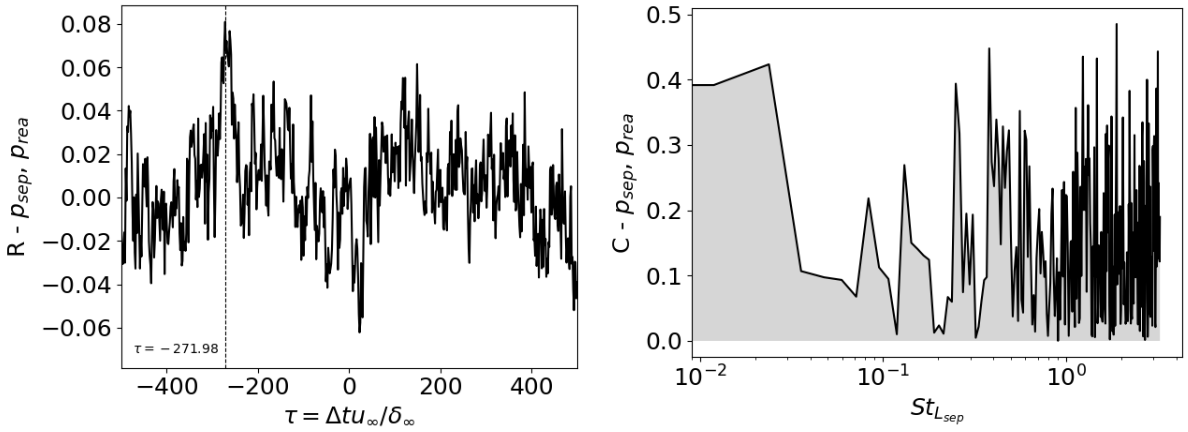

(a) Cross-correlation coefficient.

(b) Coherence.

Figure G.49: Pressure at separation location and pressure at reattachment location.

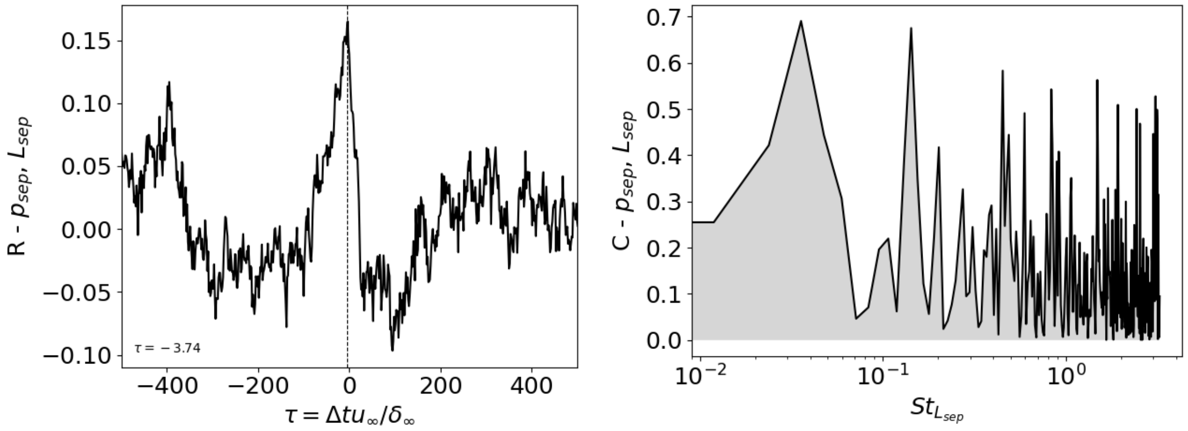

(a) Cross-correlation coefficient.

(b) Coherence.

Figure G.50: Pressure at separation location and separation length.

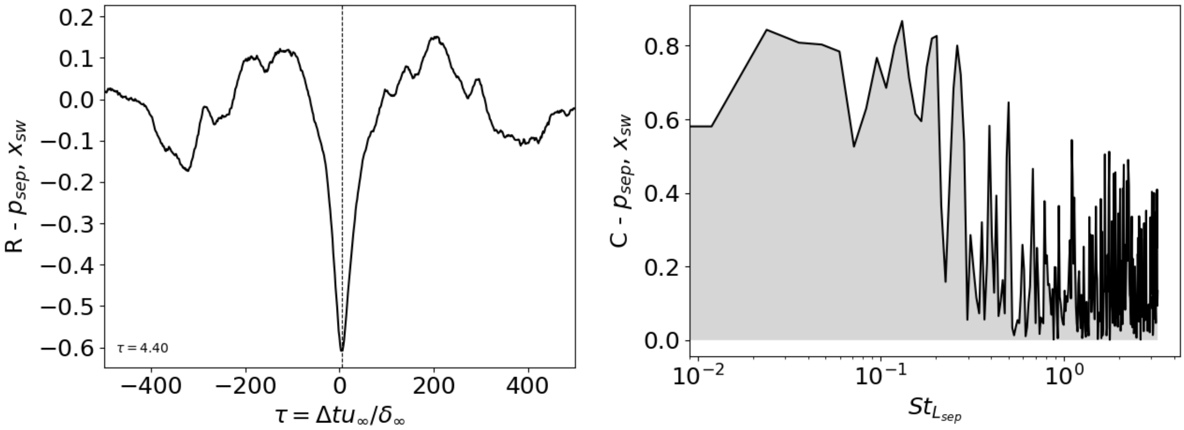

(a) Cross-correlation coefficient.

(b) Coherence.

Figure G.51: Pressure at separation location and reflected shock location.

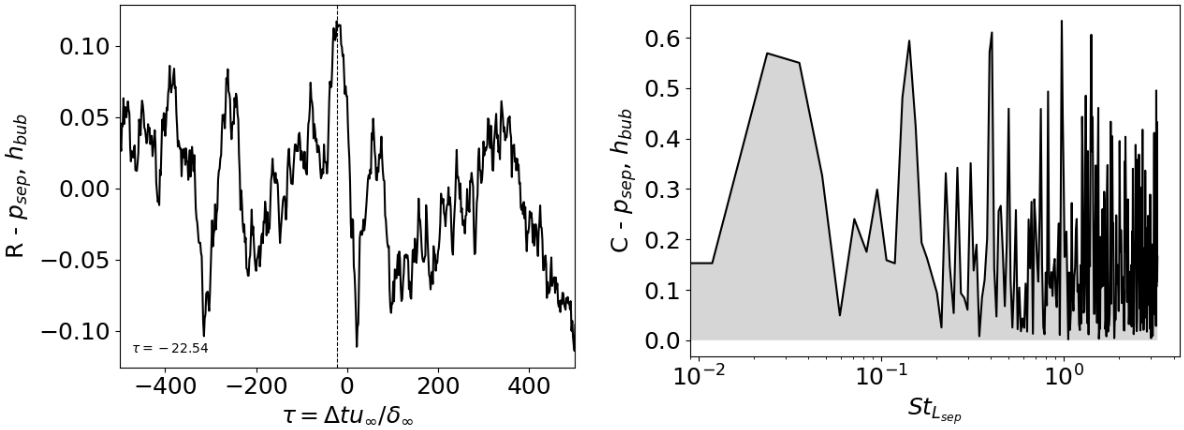

(a) Cross-correlation coefficient.

(b) Coherence.

Figure G.52: Pressure at separation location and bubble height.

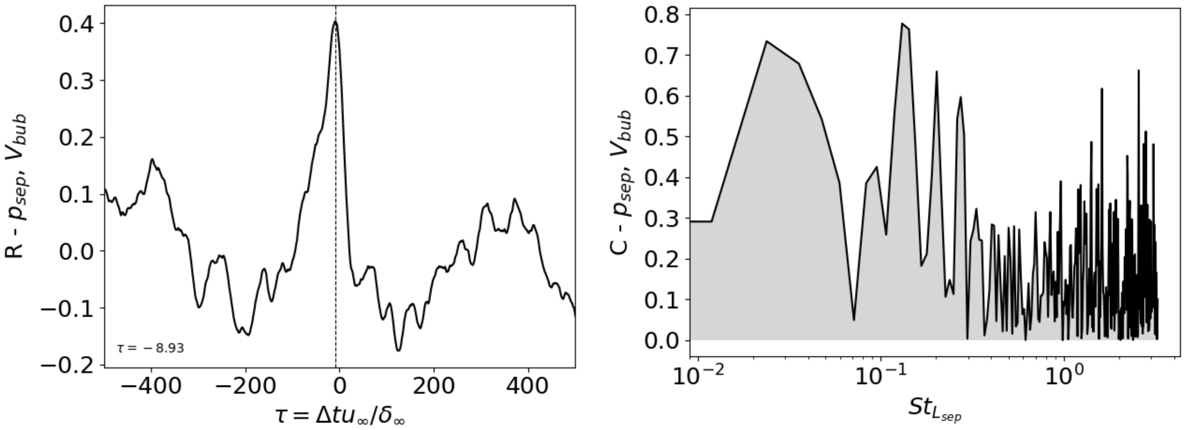

(a) Cross-correlation coefficient.

(b) Coherence.

Figure G.53: Pressure at separation location and bubble volume.

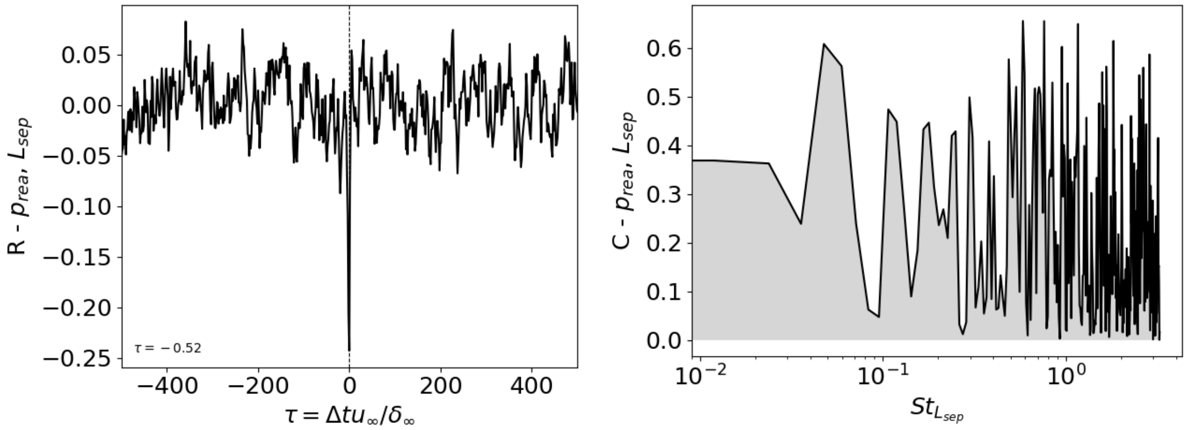

(a) Cross-correlation coefficient.

(b) Coherence.

Figure G.54: Pressure at reattachment location and separation length.

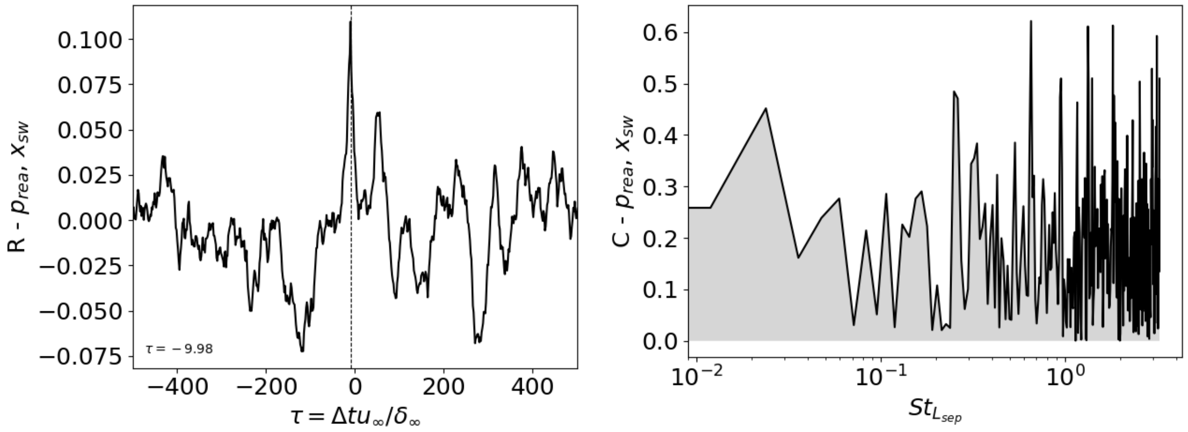

(a) Cross-correlation coefficient.

(b) Coherence.

Figure G.55: Pressure at reattachment location and reflected shock location.

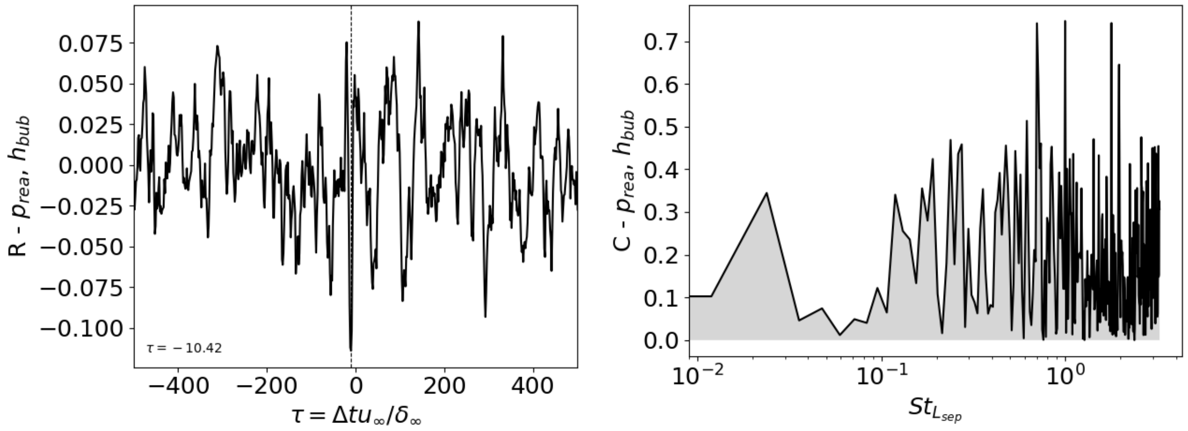

(a) Cross-correlation coefficient.

(b) Coherence.

Figure G.56: Pressure at reattachment location and bubble height.

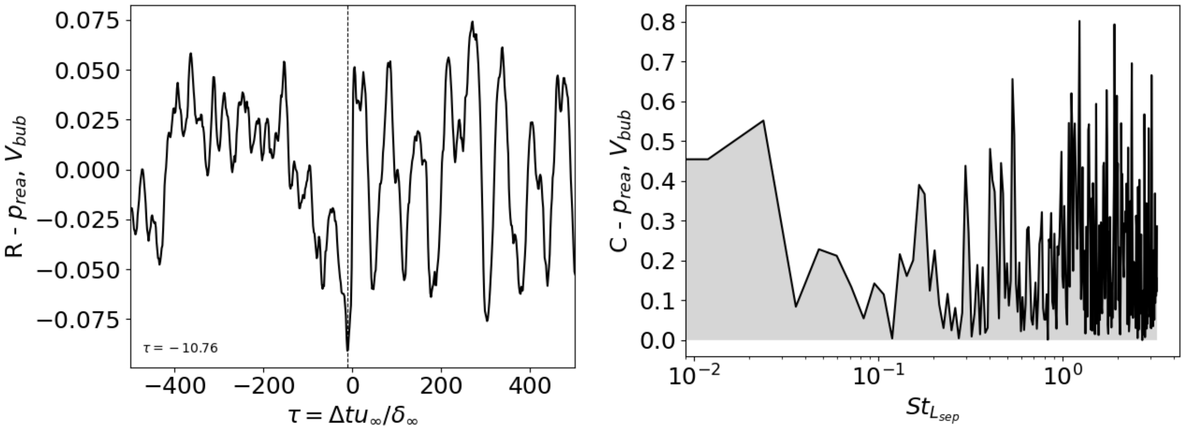

(a) Cross-correlation coefficient.

(b) Coherence.

Figure G.57: Pressure at reattachment location and bubble volume.

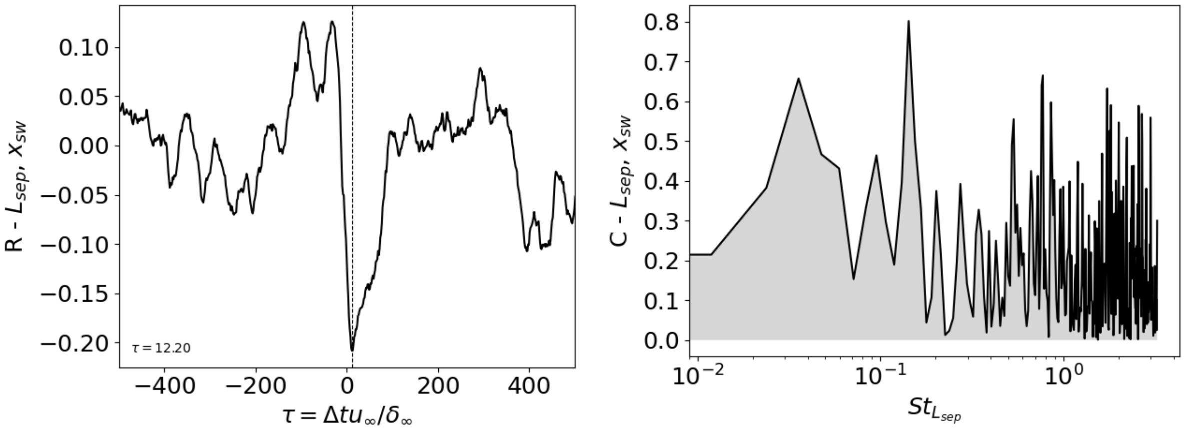

(a) Cross-correlation coefficient.

(b) Coherence.

Figure G.58: Separation length and reflected shock location.

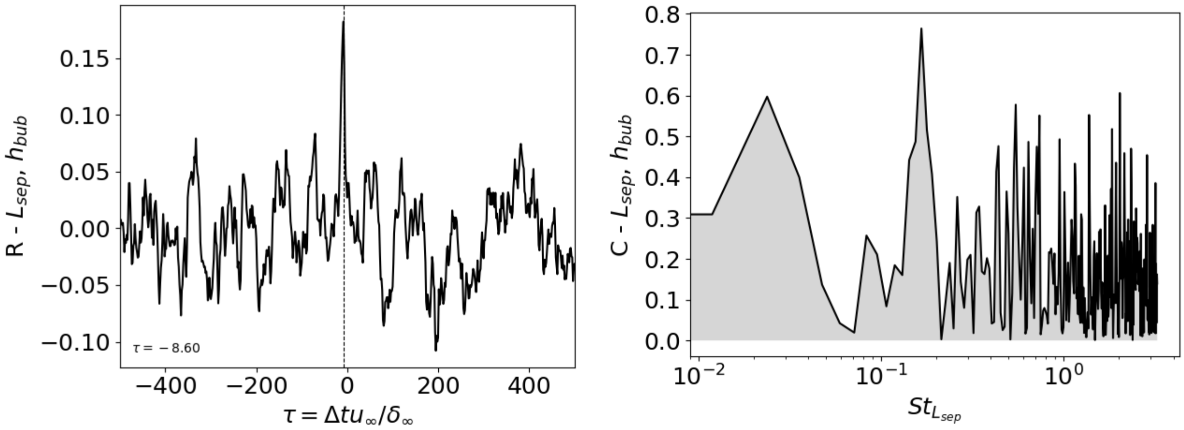

(a) Cross-correlation coefficient.

(b) Coherence.

Figure G.59: Separation length and bubble height.

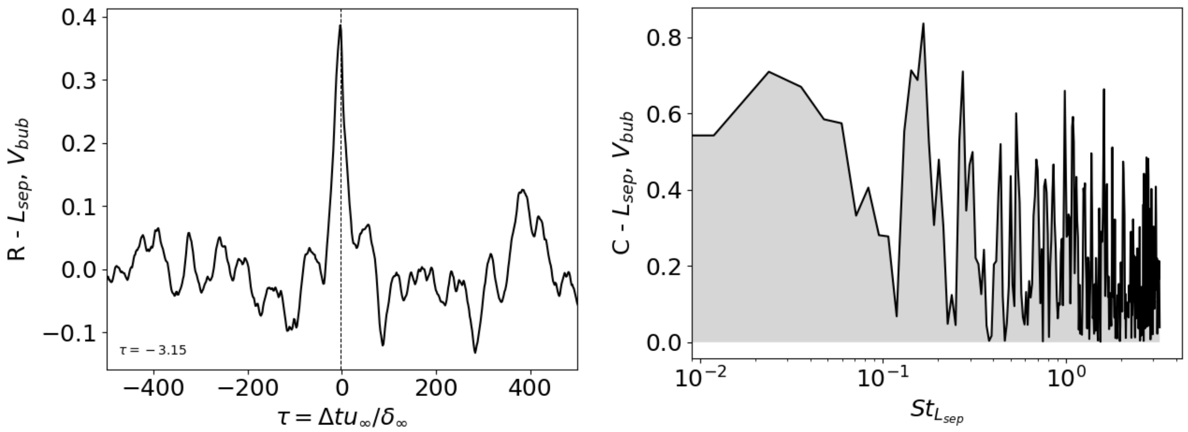

(a) Cross-correlation coefficient.

(b) Coherence.

Figure G.60: Separation length and bubble volume.

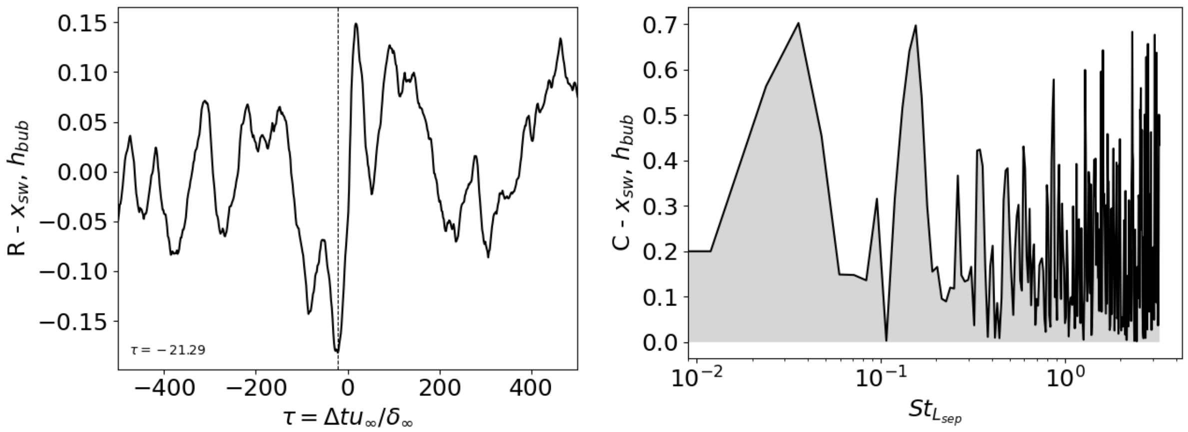

(a) Cross-correlation coefficient.

(b) Coherence.

Figure G.61: Reflected shock location and bubble height.

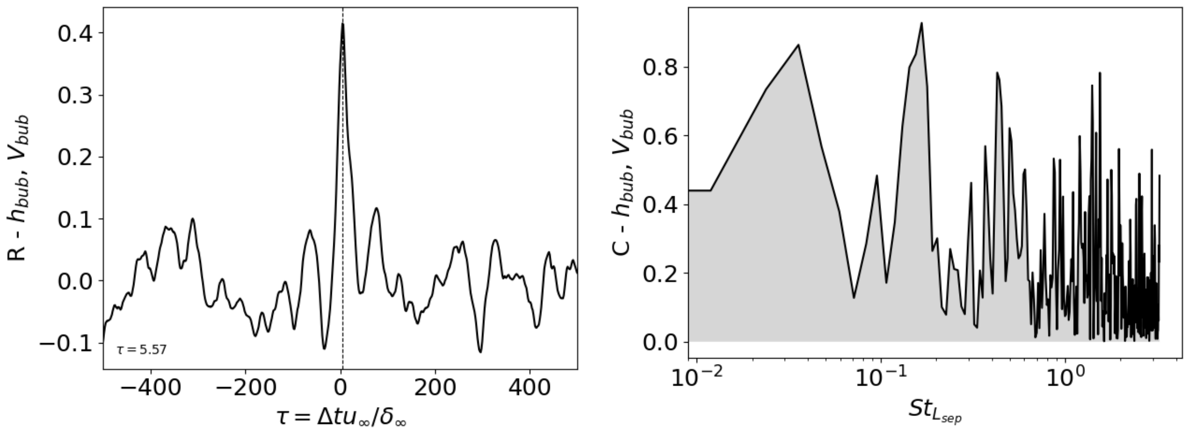

(a) Cross-correlation coefficient.

(b) Coherence.

Figure G.62: Bubble height and bubble volume.

Appendix H

Cross-correlation & coherence between dynamic quantities ($\mathcal{P}$)

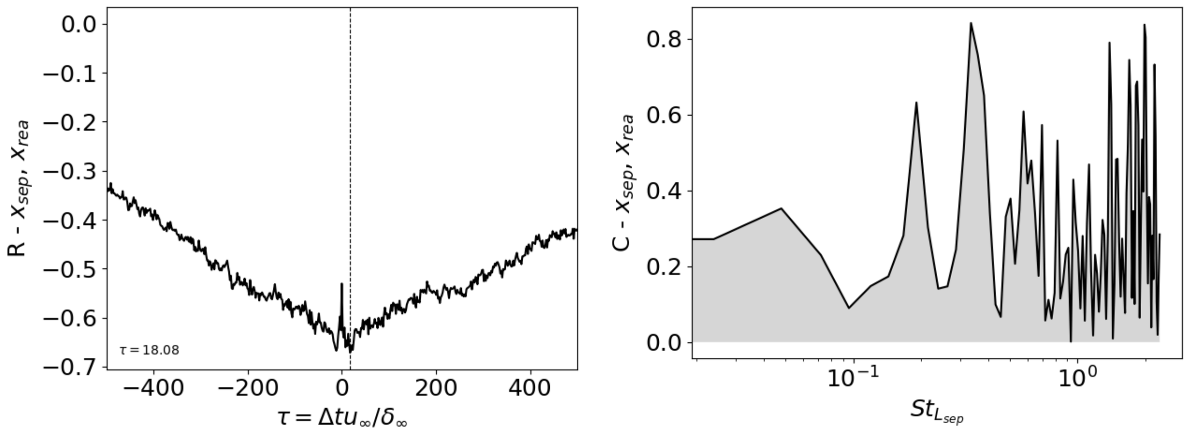

(a) Cross-correlation coefficient.

(b) Coherence.

Figure H.1: Separation point (skin-friction based) and reattachment point (skin-friction based).

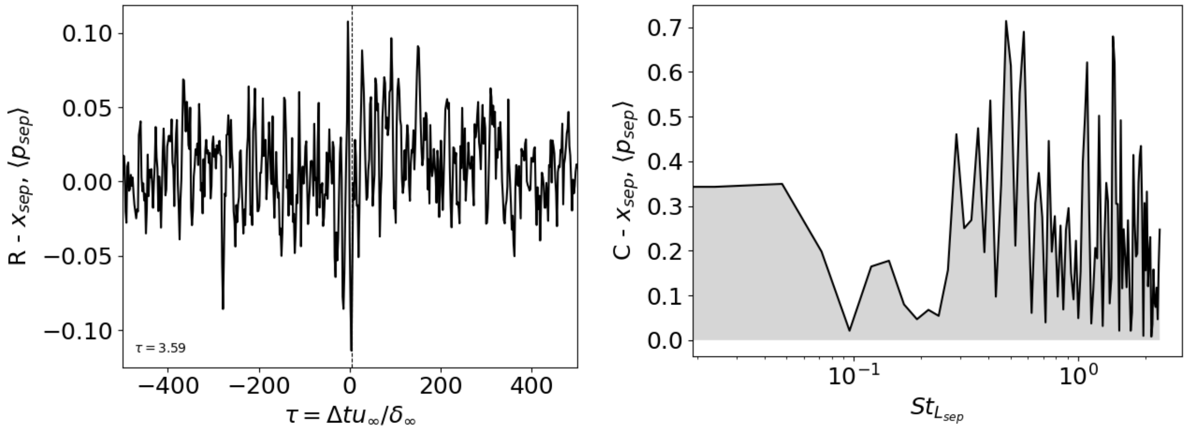

(a) Cross-correlation coefficient.

(b) Coherence.

Figure H.2: Separation point (skin-friction based) and span-averaged pressure at separation location.

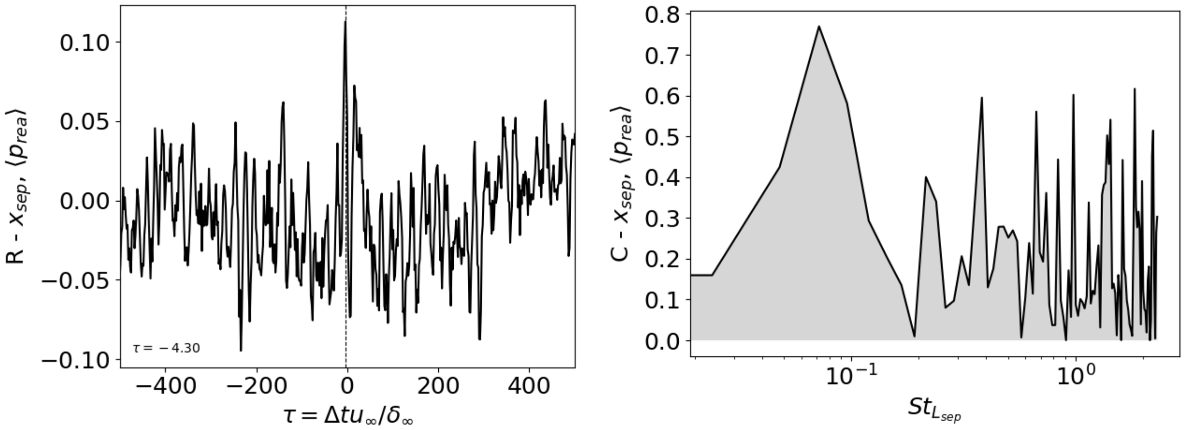

(a) Cross-correlation coefficient.

(b) Coherence.

Figure H.3: Separation point (skin-friction based) and span-averaged pressure at reattachment location.

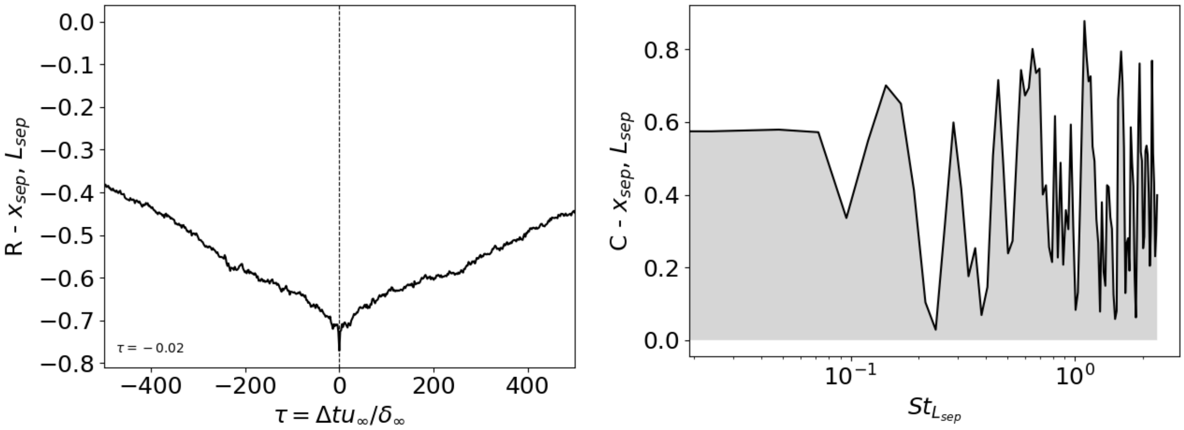

(a) Cross-correlation coefficient.

(b) Coherence.

Figure H.4: Separation point (skin-friction based) and separation length.

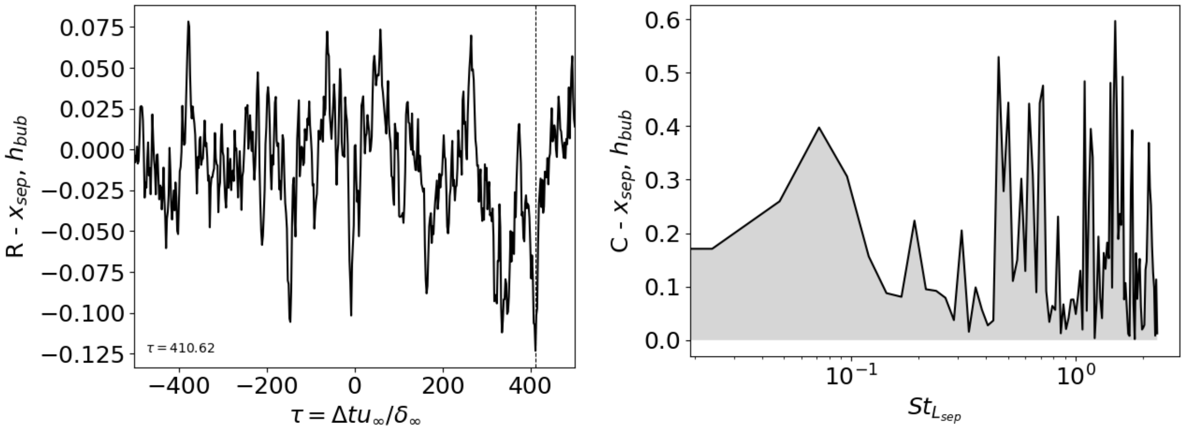

(a) Cross-correlation coefficient.

(b) Coherence.

Figure H.5: Separation point (skin-friction based) and bubble height.

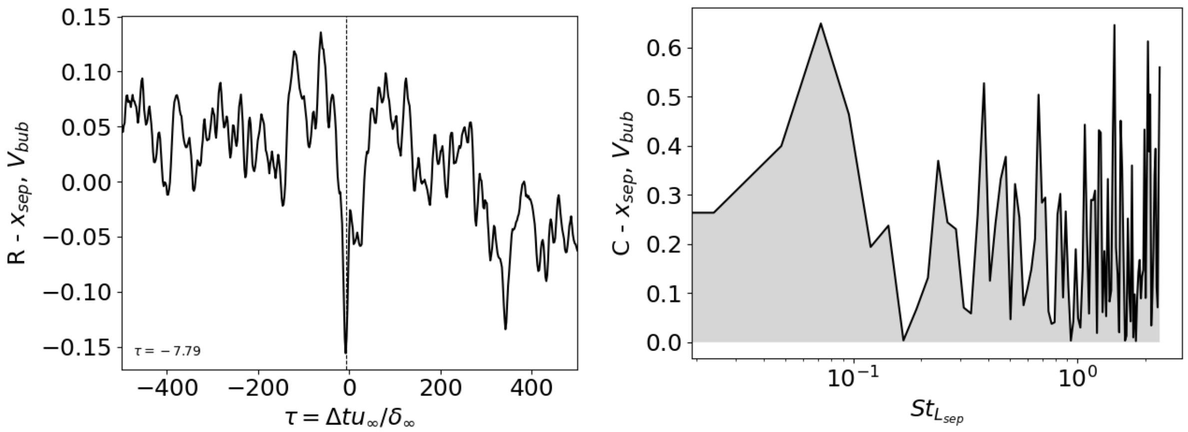

(a) Cross-correlation coefficient.

(b) Coherence.

Figure H.6: Separation point (skin-friction based) and bubble volume.

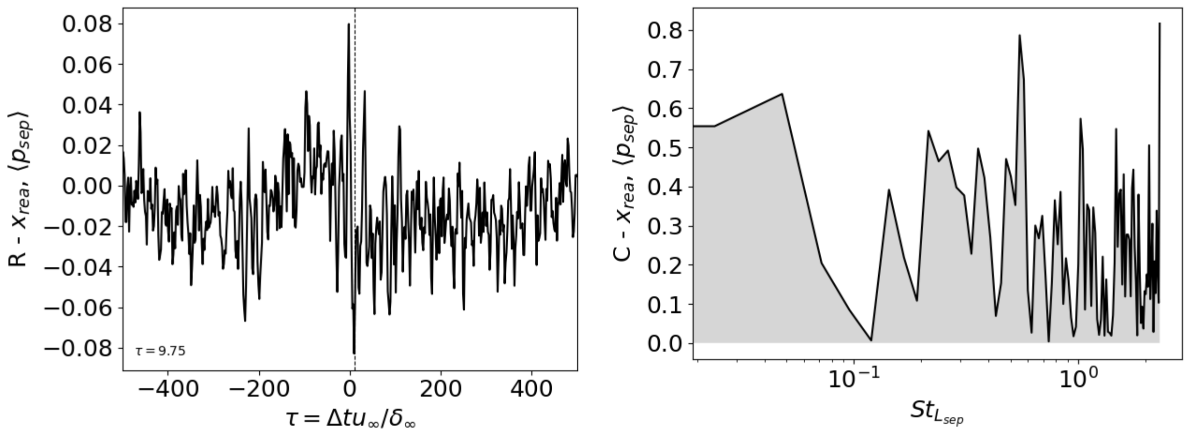

(a) Cross-correlation coefficient.

(b) Coherence.

Figure H.7: Reattachment point (skin-friction based) and span-averaged pressure at separation location.

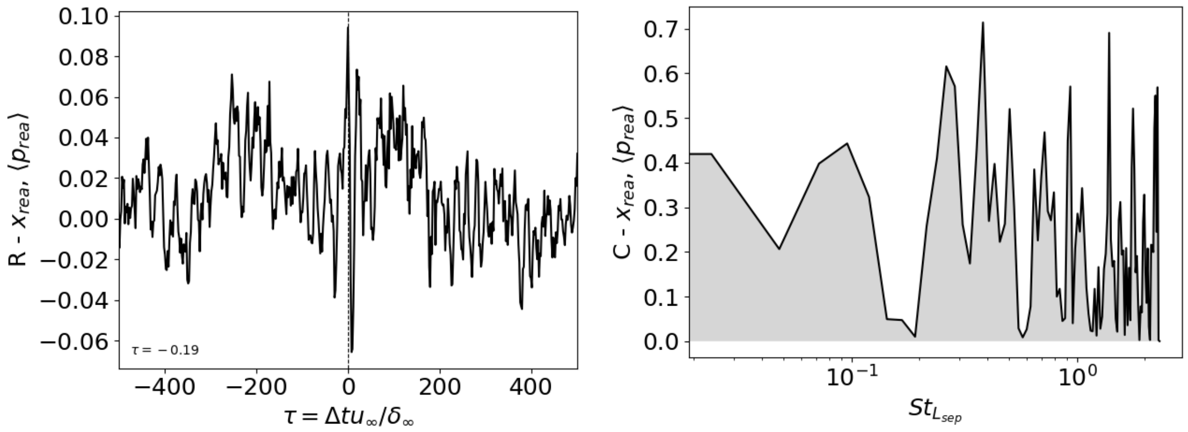

(a) Cross-correlation coefficient.

(b) Coherence.

Figure H.8: Reattachment point (skin-friction based) and span-averaged pressure at reattachment location.

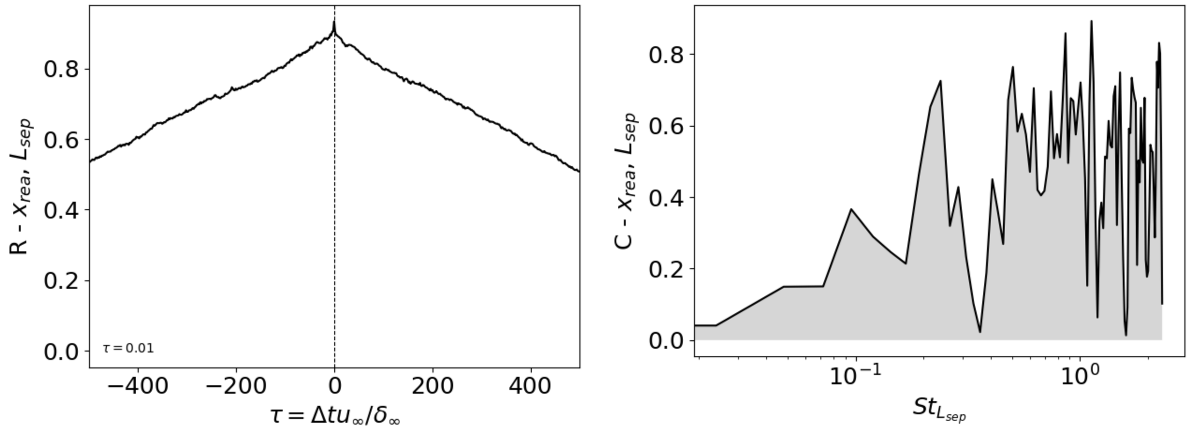

(a) Cross-correlation coefficient.

(b) Coherence.

Figure H.9: Reattachment point (skin-friction based) and separation length.

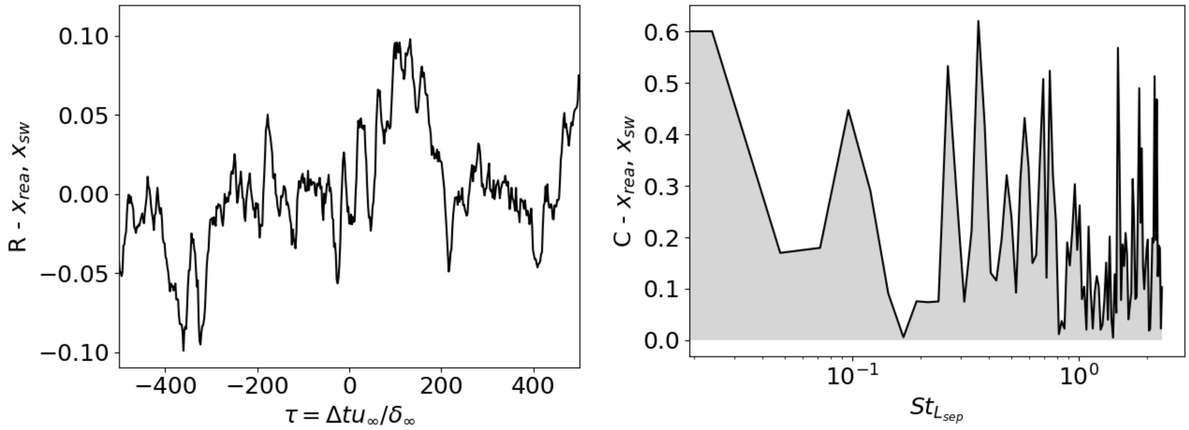

(a) Cross-correlation coefficient.

(b) Coherence.

Figure H.10: Reattachment point (skin-friction based) and reflected shock location.

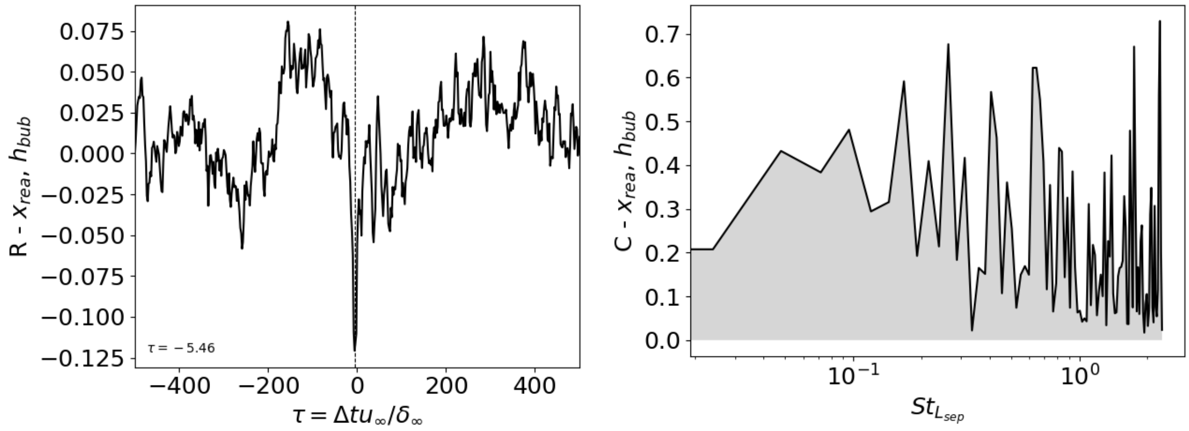

(a) Cross-correlation coefficient.

(b) Coherence.

Figure H.11: Reattachment point (skin-friction based) and bubble height.

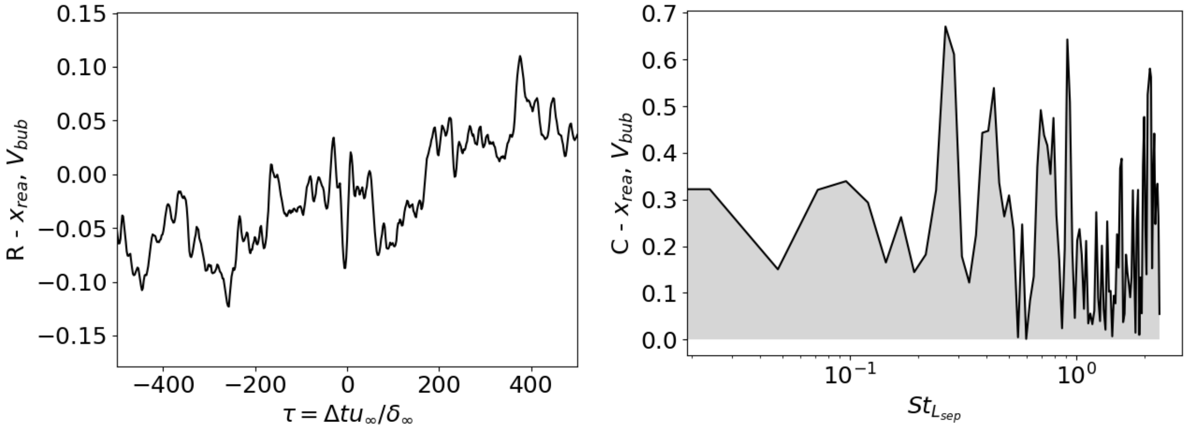

(a) Cross-correlation coefficient.

(b) Coherence.

Figure H.12: Reattachment point (skin-friction based) and bubble volume.

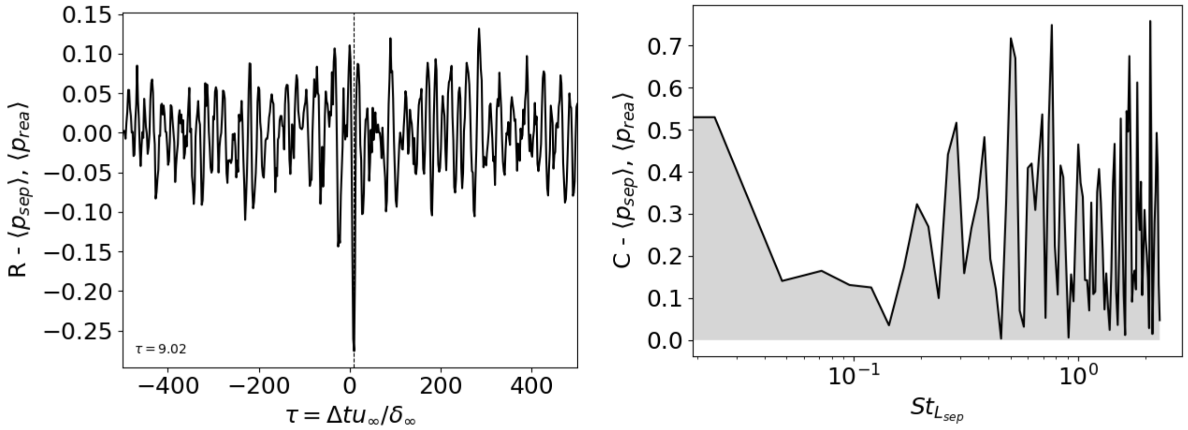

(a) Cross-correlation coefficient.

(b) Coherence.

Figure H.13: Span-averaged pressure at separation location and span-averaged pressure at reattachment location.

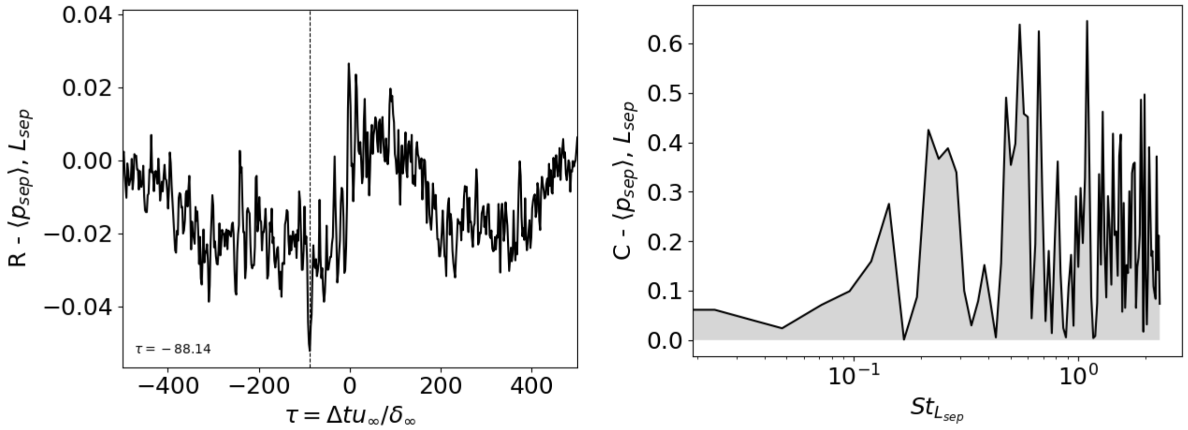

(a) Cross-correlation coefficient.

(b) Coherence.

Figure H.14: Span-averaged pressure at separation location and separation length.

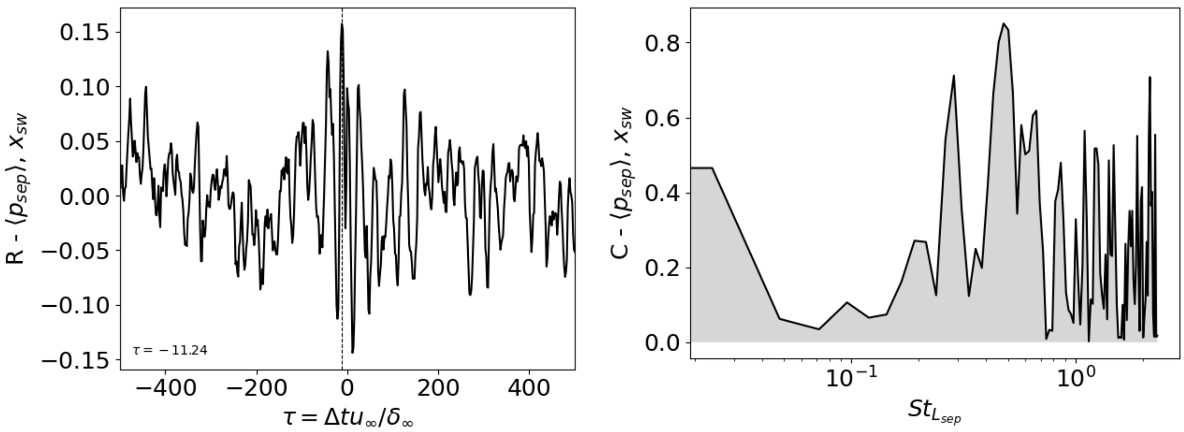

(a) Cross-correlation coefficient.

(b) Coherence.

Figure H.15: Span-averaged pressure at separation location and reflected shock location.

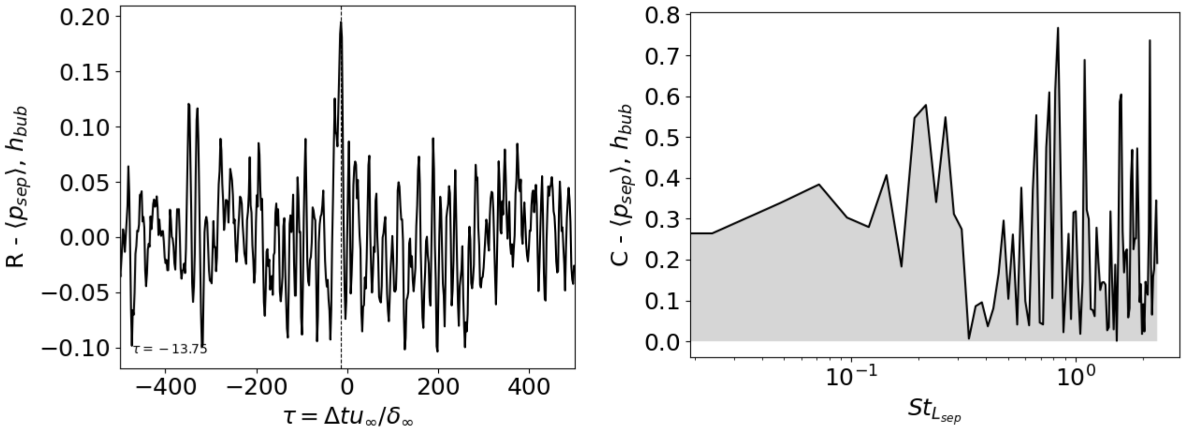

(a) Cross-correlation coefficient.

(b) Coherence.

Figure H.16: Span-averaged pressure at separation location and bubble height.

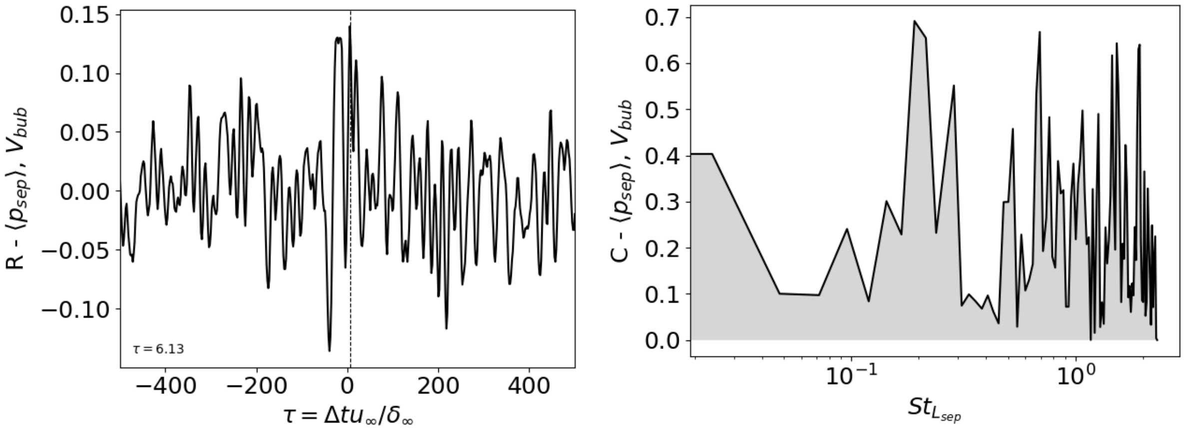

(a) Cross-correlation coefficient.

(b) Coherence.

Figure H.17: Span-averaged pressure at separation location and bubble volume.

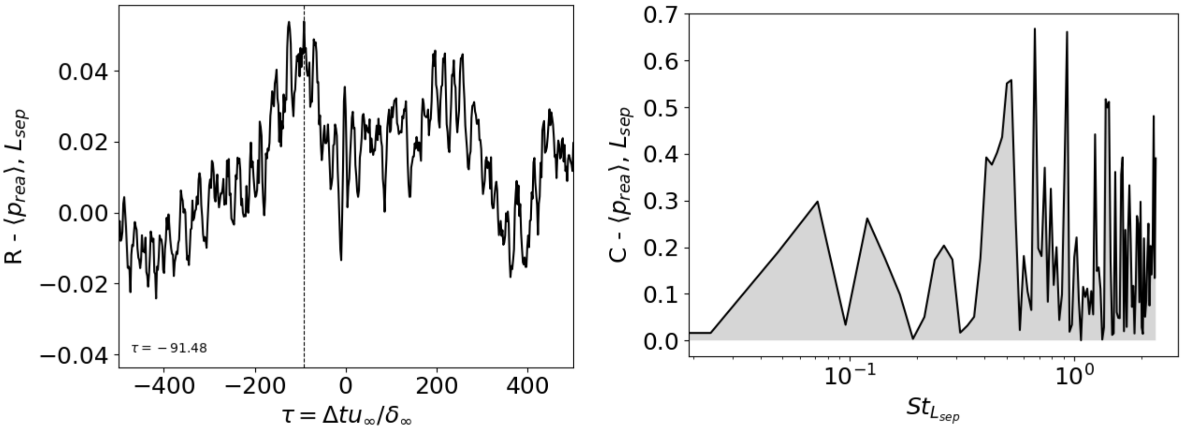

(a) Cross-correlation coefficient.

(b) Coherence.

Figure H.18: Span-averaged pressure at reattachment location and separation length.

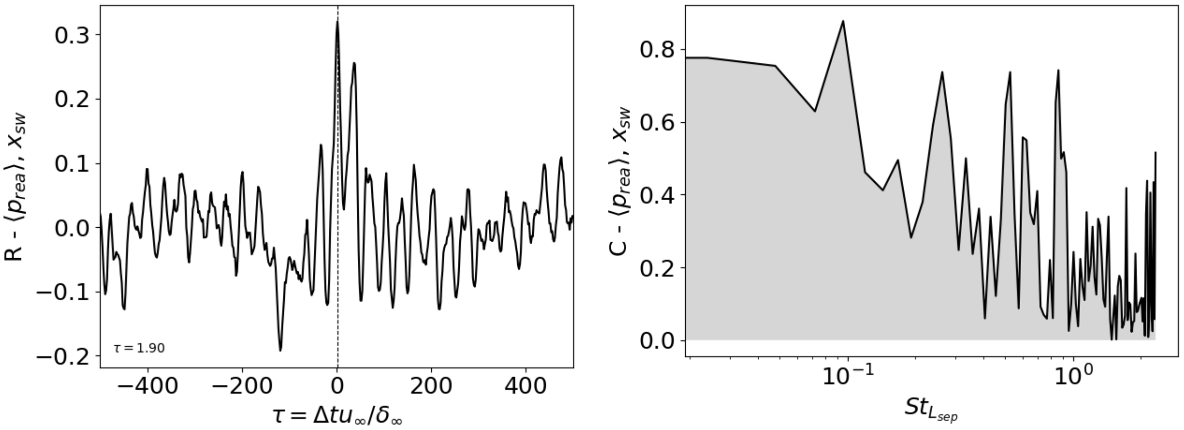

(a) Cross-correlation coefficient.

(b) Coherence.

Figure H.19: Span-averaged pressure at reattachment location and reflected shock location.

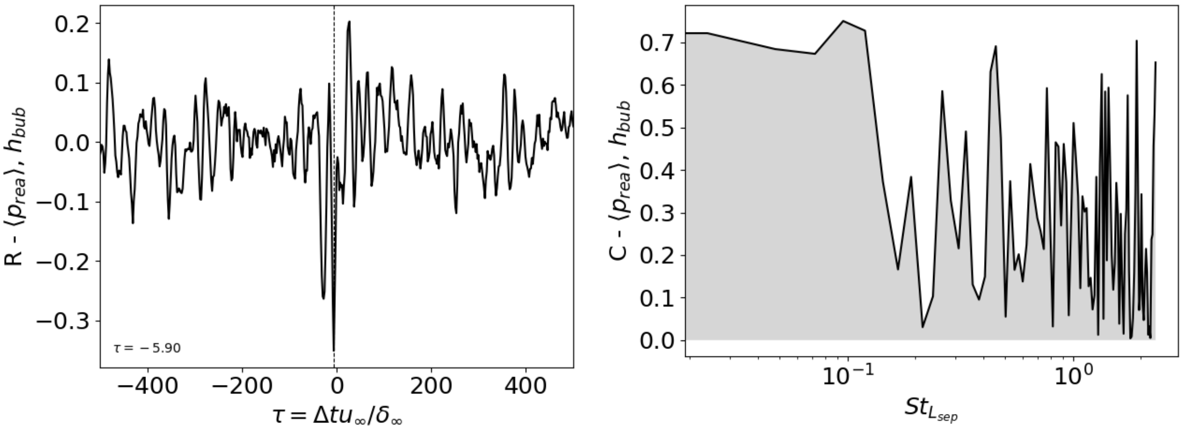

(a) Cross-correlation coefficient.

(b) Coherence.

Figure H.20: Span-averaged pressure at reattachment location and bubble height.

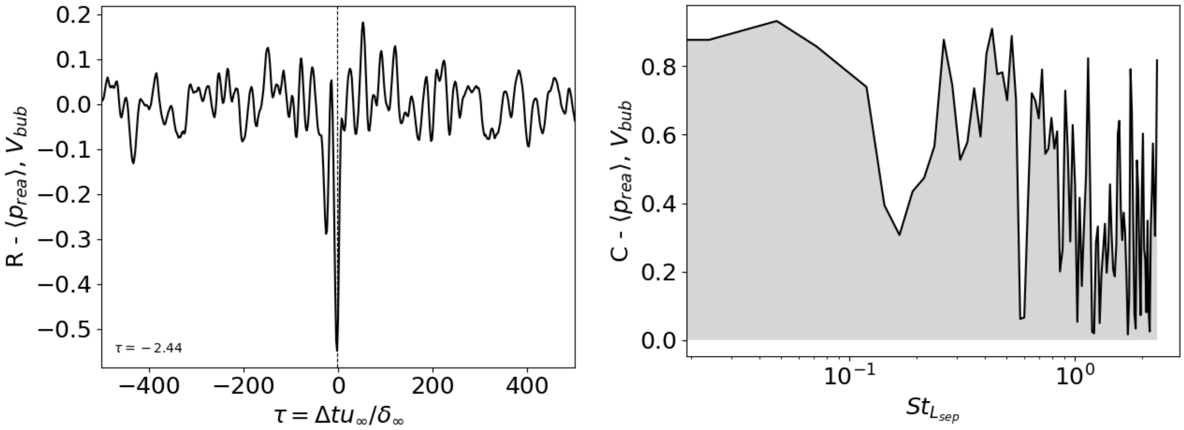

(a) Cross-correlation coefficient.

(b) Coherence.

Figure H.21: Span-averaged pressure at reattachment location and bubble volume.

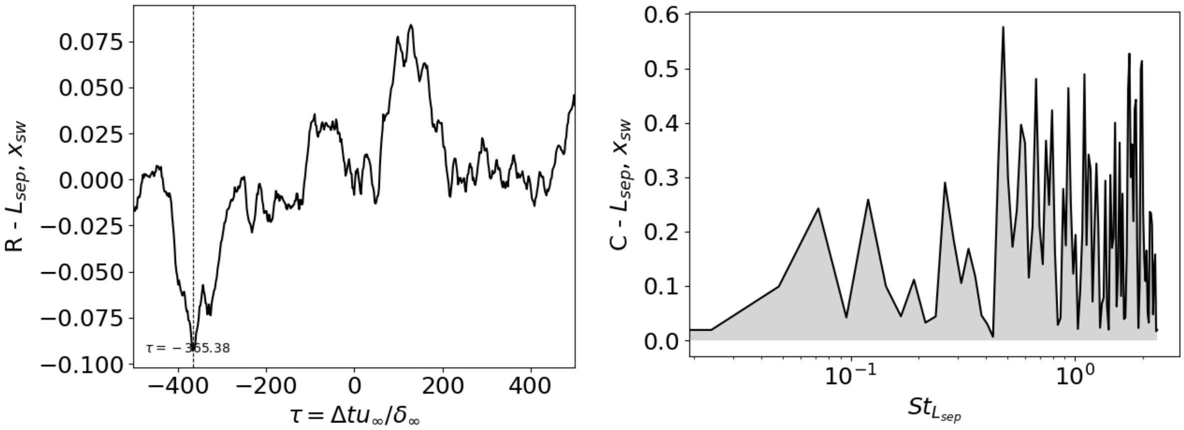

(a) Cross-correlation coefficient.

(b) Coherence.

Figure H.22: Separation length and reflected shock location.

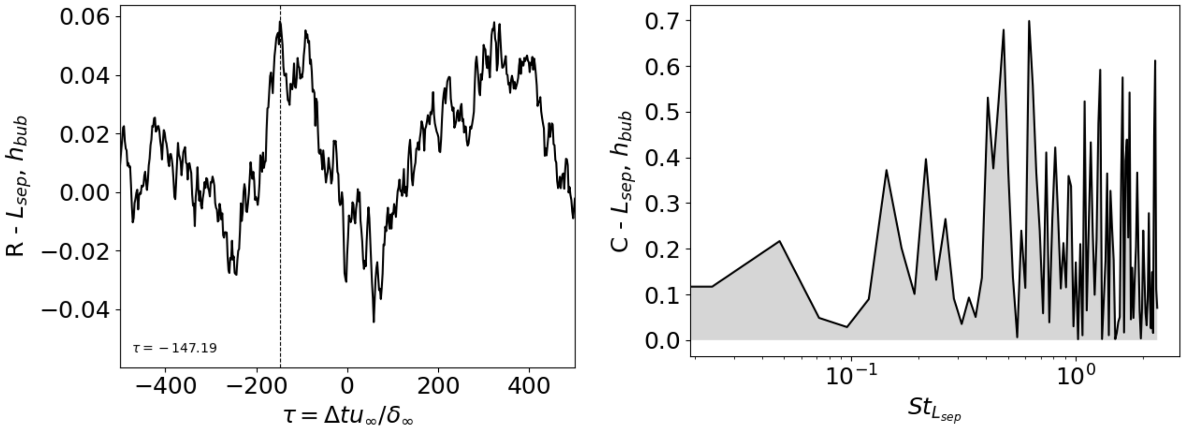

(a) Cross-correlation coefficient.

(b) Coherence.

Figure H.23: Separation length and bubble height.

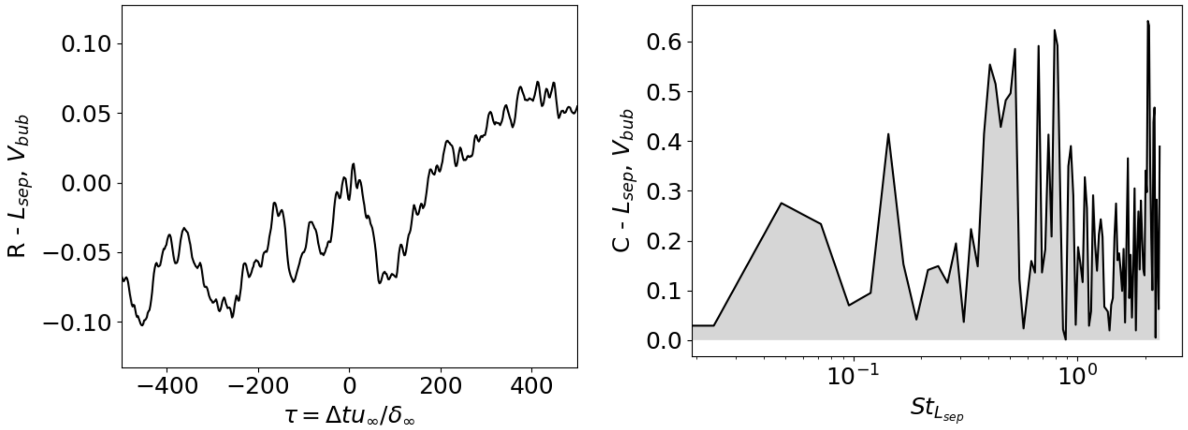

(a) Cross-correlation coefficient.

(b) Coherence.

Figure H.24: Separation length and bubble volume.

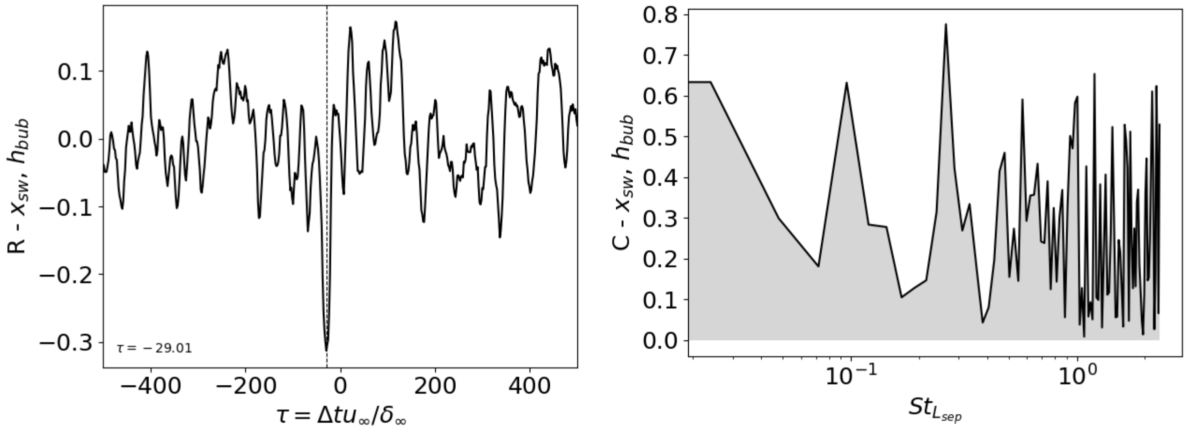

(a) Cross-correlation coefficient.

(b) Coherence.

Figure H.25: Reflected shock location and bubble height.

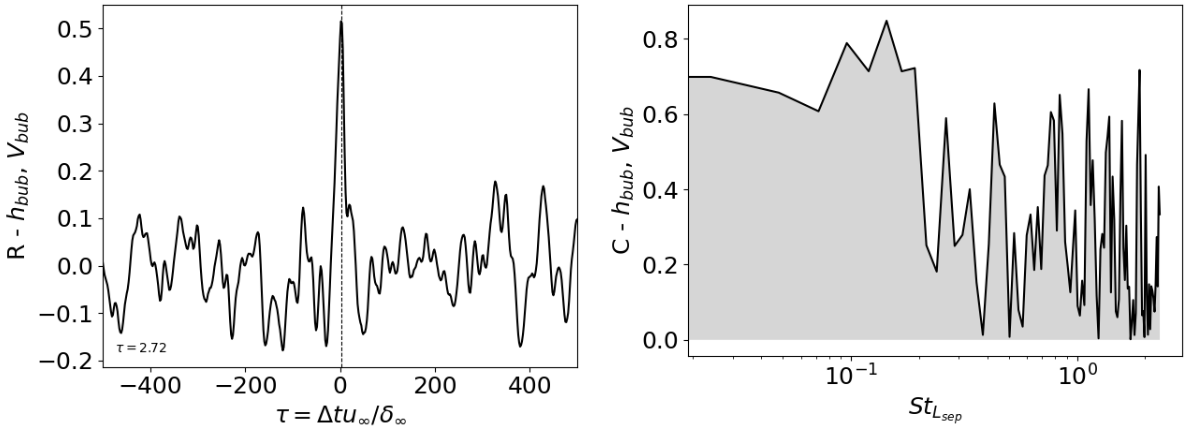

(a) Cross-correlation coefficient.

(b) Coherence.

Figure H.26: Bubble height and bubble volume.